**INAUGURAL - DISSERTATION**
**zur**
**Erlangung des Doktorwürde**
**der**
**Naturwissenschaftlich–Mathematischen**
**Gesamtfakultät**
**der Ruprecht–Karls–Universität**
**Heidelberg**

**vorgelegt von**

**Asja Pfaffenberger, M.Sc.**
**aus Berlin–Neukölln**

**Tag der mündlichen Prüfung: 24.01.2013**

# Dose Calculation Algorithms for Radiation Therapy with an MRI-Integrated Radiation Device

**Gutachter:** **Prof. Dr. Uwe Oelfke**
**Prof. Dr. Wolfgang Schlegel**

# Zusammenfassung


**Dosisberechnungsalgorithmen für die Strahlentherapie mit MRT-integrierten Bestrahlungsgeräten**

Bildgeführte adaptive Strahlentherapie (IGART) hat zum Ziel, durch genauere Kenntis der anatomischen und physiologischen Situation während der Behandlung den Therapieerfolg zu verbessern. Mit der Magnetresonanzbildgebung (MRT) wird ein Verfahren integriert, mit Hilfe dessen das zu bestrahlende Zielvolumen besser vom umliegenden, gesunden Gewebe abgegrenzt werden kann und sich Veränderungen zwischen oder auch während Therapiefraktionen berücksichtigen lassen. Dadurch wird eine Voraussetzung geschaffen, um auch die gewebeschädigende Strahlendosis besser auf das Zielvolumen beschränken zu können, um sowohl Heilungschancen zu erhöhen als auch Nebenwirkungen zu reduzieren. Dies erfordert eine präzise Berechnung der Strahlendosis im Magnetfeld, dem der Patient in diesen Bestrahlungsgeräten ausgesetzt ist. Echtzeitanpassung des Bestrahlungsplans wird angestrebt, was eine schnelle Dosisberechung voraussetzt. Hierfür bieten sich kernbasierte Methoden an, die aber bisher nur für die Strahlentherapie ohne Magnetfeld existieren. Im Rahmen dieser Arbeit werden zwei Ansätze für kernbasierte Dosiberechnungsalgorithmen vorgeschlagen und untersucht, von denen einer bis zur Anwendung in der Bestrahlungsplanoptimierung in vier klinischen Fällen gebracht wird.


# Abstract


**Dose Calculation Algorithms for Radiation Therapy with an MRI-Integrated Radiation Device**

Image-guided adaptive radiation therapy (IGART) aims at improving therapy outcome on the basis of more precise knowledge of the anatomical and physiological situation during treatment. By integration of magnetic resonance imaging (MRI), better differentiation is possible between the target volume to be irradiated and healthy surrounding tissues. In addition, changes that occur either between or during treatment fractions can be taken into account. On the basis of this information, a better conformation of radiation dose to the target volume may be achieved, which may in turn improve prognosis and reduce radiation side effects. This requires a precise calculation of radiation dose in a magnetic field that is present in these integrated irradiation devices. Real-time adaptation of the treatment plan is aimed at for which fast dose calculation is needed. Kernel-based methods are good candidates to achieve short calculation times; however, they presently only exist for radiation therapy in the absence of magnetic fields. This work suggests and investigates two approaches towards kernel-based dose calculation algorithms. One of them is integrated into treatment plan optimisation and applied to four clinical cases.

# Contents

# Part I

# Introduction and Background

# Chapter 1

# Introduction

## 1.1 Objective

In this work, methods of photon dose calculation in a magnetic field are sought that can serve as alternatives to computationally expensive Monte Carlo (MC) simulations. Magnetic fields are present in radiation therapy devices that integrate magnetic resonance (MR) imaging for online image guidance. Prototypes of these integrated devices exist but none is clinically used yet. MR-integrated radiation therapy devices are discussed in more detail in section 4.2.

MC engines currently present the most precise method for dose calculation in radiation therapy, and, in a magnetic field, the only one. They are described in section 3.1. For radiation therapy without magnetic fields, other, kernel-based methods are also employed in treatment planning which are described in section 3.2, and which are generally faster than MC techniques. The need for having a fast method at hand comes from the fact that in inverse planning, which is the state-of-the-art planning technique and which is reported on in section 1.3, dose calculation has to be performed multiple times, in order to solve an optimisation problem aimed at finding the best compromise between delivery of a high dose to the target and sparing of healthy tissues.

For conventional treatment planning which is based on one planning computed tomograph (CT) acquired generally a few days before treatment starts, the main time constraint is given by how much time a treatment planner can afford to spend on a single treatment plan, and this is again determined by the number of patients to be treated, the number of treatment planners employed for this task, and the number of computer work stations that the clinic is equipped with. Thus for conventional treatment planning, time frames of minutes for the dose optimisation procedure can generally be acceptable; however, considering the online adaptation of plans, i.e. adaptation during the treatment procedure, to anatomical or physiological changes that are monitored by online imaging, time requirements will be higher. Especially with respect to organ motion that occurs while the patient is being treated, a real-time adaptation is desired.

MC simulations are also increasing in speed with increasing computational power and the usage of parallel processing [1]. However, MC simulations are based on modelling the interactions of single particles in the medium and achieve their high precision only by a high number of statistical events. Therefore investigation of kernel-based alternative methods which summarise multiple events already and have the potential of being faster than a MC simulation is considered valuable.

Two approaches towards kernel-based methods are studied in this work and compared with MC simulations in terms of quality of dose calculation. The analytical approach described in part II uses a parameterisation of the tracks of Compton electrons for the generation of photon point-interaction kernels, while the dose warping approach described in part III maps a conventional dose distribution that is generated in the absence of any magnetic field, to a dose distribution that would be generated inside a magnetic field.

## 1.2 Image-Guided Adaptive Radiation Therapy

Research in medical physics for radiation therapy aims at developing more and more precise techniques to increase radiation damage to the limited region of tumour cell presence and at the same time, sustain the integrity and function of surrounding healthy tissues. The aim of image-guided adaptive radiation therapy is to modify the treatment on the basis of images acquired during the treatment process, and it is hoped that in this manner, cure rates and quality of life of the patients can be improved.

The information contained in the images may be of purely anatomical kind, and monitor changes that occur from one treatment fraction to the other, where usually, around 30 fractions of treatment are applied on an almost daily basis, with each fraction taking around 10-20 minutes. Beside errors in set up when re-positioning the patient each day, the patient may lose or, more seldomly, gain weight over the treatment period. What is more, some organs have a variable filling like the stomach, bladder and intestine, or change their exact location like the prostate, seminal vesicles and intestinal loops. Also may the tumour mass shrink or grow over the treatment course. These changes that occur from one treatment fraction to the other are termed interfractional changes. The second group of anatomical changes is that of intrafractional motion, which occurs during one single treatment fraction. This term encompasses changes due to breathing, swallowing or heartbeat motion, but also the drifting of abdominal organs due to passage of intestinal air which is observed in treatment of the prostate [2][3].

On the other hand, radiosensitivity of cells and tissues changes with the oxygenation level, the cell-cycle position they are in, and is influences by signalling, repair processes are triggered by irradiation, and cellular proliferation is again dependent on hormonal levels and the availability of resources in the vicinity of the cells. Many of these processes are not fully understood yet; however, efforts exist to include more and more of this functional information into treatment planning [4].

Traditionally, offline techniques are used for imaging as the basis for diagnosis or for treatment planning: Prior to treatment, images are acquired by means of CT (computed tomography) and, in order to obtain functional information, they may be combined with other modalities like PET (positron emission tomography), SPECT (single photon emission computed tomography), two-dimensional gamma camera images, or MRI (magnetic resonance imaging). On these images, regions are segmented into belonging to or being infiltrated by the tumour, and into healthy tissues that need to be spared from irradiation. In the past years, relying on a single set of images which was acquired prior to treatment, is not considered appropriate anymore in view of the changes described above. When imaging only prior to treatment, interfractional and intrafractional changes have to be taken into consideration by the introduction of appropriate margins [5][6] around the target volume, by which healthy tissues will be irradiated and may be harmed. Further, already the possible time gap between image acquisition and treatment may alter the tumour size significantly. Using imaging procedures more excessively throughout the whole course of treatment, it is hoped that margins can be reduced and radiation more precisely restricted to the tumour tissue to be damaged.

Different approaches exist with respect to the actual frequency at which imaging is applied or the way the imaging information is used. While in order to assess the tumour size, a weekly image may suffice, the correction of positioning errors rather makes sense if applied online, i.e. when the patient is in treatment position. Other anatomical information that is acquired online may be used offline to verify whether the dose delivered in the actual anatomical situation is in agreement with the planned dose, and adapt the treatment plan for the next fraction accordingly. Functional imaging may also be applied prior to or after each fraction and the treatment plan adapted such as to compensate for the changes. And finally, online image information may be used directly online to adapt the treatment plan, and maybe even in real-time. For online adaption of treatment plans, fast image acquisition and processing is required, fast automated structure recognition and tools to actually change the treatment plan, including dose calculation and optimisation.

Strategies currently employed or investigated for the incorporation of motion into the treatment process range from the use of time-resolved images for the definition of margins as mentioned above, to gating and tracking approaches, where the former decides to restrict irradiation to times in which the anatomy is in agreement with the anatomy used for planning, and the latter attempts to follow the tumour motion throughout the treatment. Tools employed are external surface detection, either by projection of laser specles or by the use of markers, and breath detection by means of spirometers or pressure belts. Both these external surrogates need to be correlated with internal tumour motion in order to be applicable, and still, the determination of the correlation is another issue as well as the validity of the set of images that the correlation is based on. The implantation of radioopaque markers into the tumour to be detected on fluoroscopic x-ray images, or the implantation of tiny coils that can be detected by means of electromagnetic signals, is a more precise option for online detection of the tumour position. In order to obtain volumetric information of the whole region irradiated, cone-beam CT's may also be integrated with radiation devices, or a modified therapy beam be used for CT acquisition prior to radiation delivery. Tracking approaches further require means to adapt the therapy beam to the actual target position and projection and need to rely on prediction models to compensate for system lag times [3].

Any application of additional imaging needs to be motivated, however, by an expected benefit for the patient from the imaging procedure. Especially should the benefit prevail over the risk from the procedure. One major constraint in increasing the frequency of imaging for radiation treatment is therefore the harm that the imaging techniques may do to the patient. For imaging techniques which involve ionising radiation, the overall radiation dose may be of concern as well as the dose to certain tissues [7]. X-ray based techniques like fluoroscopy or CT are therefore generally restricted in terms of frequency and, during acquisition, to the overall imaging time. This is one reason why the integration of MRI with radiation devices is considered beneficial. Other arguments are the improved soft-tissue contrast when compared with x-ray based techniques, and the capability of acquiring functional information. These expected benefits are discussed further in chapter 4 where also the approaches by different groups working on MR integration with radiation devices are presented.

## 1.3 IMRT and Inverse Planning

Radiation therapy generally chooses several directions from which the patient will be irradiated such that a high dose of radiation is delivered to the target volume while surrounding organs at risk are spared. Techniques exist where the photon fluence of the beam is constant across the beam, while in intensity-modulated radiation therapy (IMRT) a modulation of the fluence is used in order to obtain a better confinement of the dose to the target.

Figure 1.1 shows a screenshot from a treatment planning software, where the 3D visualisation of a target volume and organs at risk is seen along with eight of nine equiangular beams that irradiate the target volume (one beam is hidden). The patient contour and other organs are not visualised, nor are the medical linear accelerator to produce the beams or its gantry to transport the beams to the nine treatment angles. The beams are shaped by means of multi-leaf collimators (MLC's) in which two opposing banks of attenuating leaves can be positioned independently. In the figure, the MLC's are collimated to the outer contour of the radiation beams.

For creation of the modulated fluence patterns, different shapes are formed by these leaves with variable opening times while the beam is on. The smallest subunits that the fluence patterns are composed of is termed a bixel or beamlet and is basically given by the MLC leaf width. Examples of such fluence patterns are also displayed in the figure.

With the number of subfields ranging up to several hundreds and each of them having their own weighting factor or beamlet weight, the number of degrees of freedom in the treatment planning process motivated

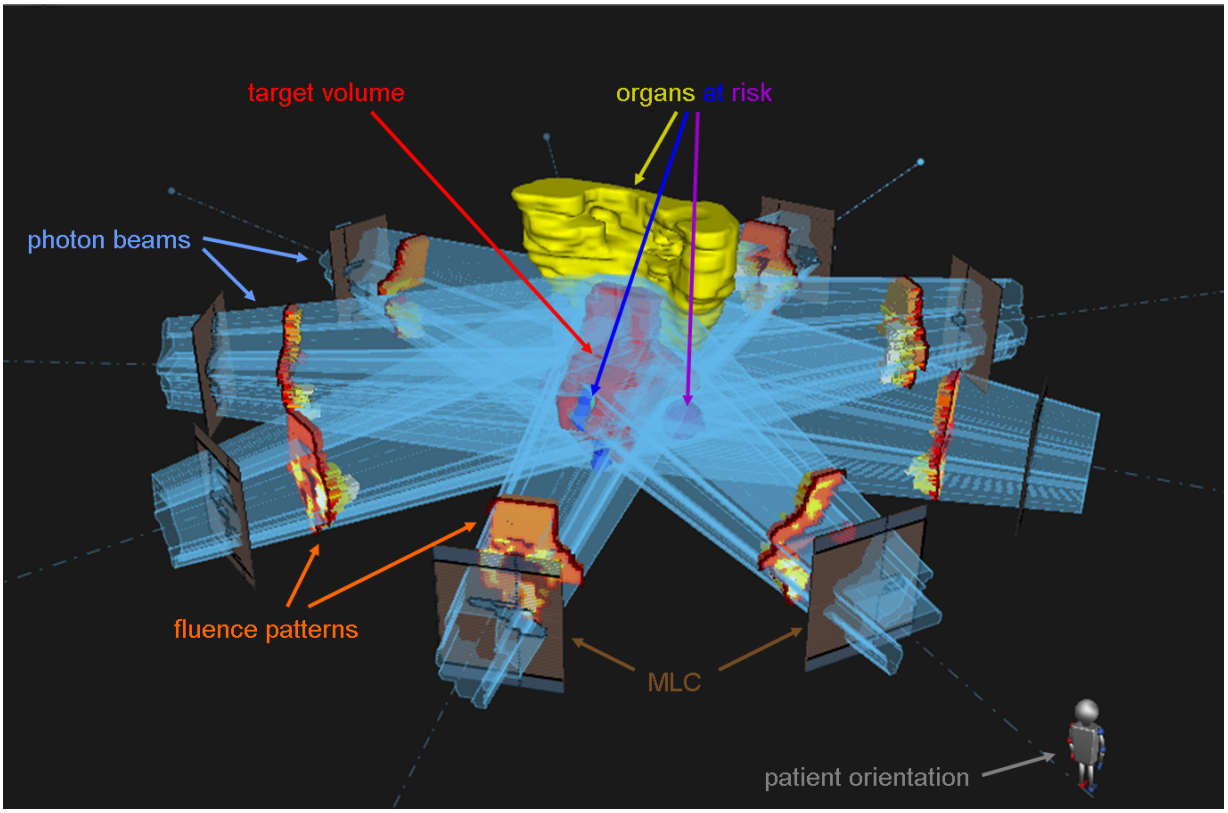


**Figure 1.1** IMRT treatment by nine equiangular coplanar beams (one hidden by target/organs at risk). Screenshot from the RayStation treatment planning software v3.0.0.253 [8], with labels added.

the inverse planning approach. In inverse planning as performed in the DKFZ inverse planning module KonRadXP [9][10], a set of beamlet weights is determined that minimises a quadratic objective function in which constraints for the target volume and for the organs at risk are coded [11]. The objective function is evaluated in an iterative algorithm which varies treatment parameters such as to find the set of parameters that minimise the value of it. In each iteration, the dose for the new set of parameters has to be calculated, and the procedure continues until a termination condition is reached [11].

The dose $d_i$ in any voxel $i$ is given by a linear superposition of the contributions from all beamlets $j$ to that voxel, weighted by the beamlet weight $w_j$, as

$$d_i = \sum_{j=1}^{N_j} D_{ij} w_j \tag{1.1}$$

where $N_j$ is the number of beamlets. Knowing the matrix element $D_{ij}$, the optimisation is performed on the basis of the beamlet weights [12].

# Chapter 2

# Physics Background

The photon energies in radiation therapy with x-rays are generally in the 1 to 20 MeV range. By convention, in the radiation therapy community photon spectra of linear accelerators are given in units of "MV" instead of "MeV", where a 6 MV spectrum is dosimetrically equivalent to a spectrum that was historically generated by the production of bremsstrahlung x-rays from electrons accelerated to a potential of 6 megavolts, i.e. having gained 6 MeV when interacting with the target for bremsstrahlung production. A 6 MeV beam, in contrast, refers to a monoenergetic beam of 6 MeV. These conventions are adopted in the text.

"Dose" or "dose of radiation" used in the text without further specifications refers to the absorbed dose given by

$$D = \frac{d\bar{\epsilon}}{dm} = \frac{1}{\rho}\frac{d\bar{\epsilon}}{dV} = -\frac{1}{\rho}\vec{\nabla}\cdot\vec{\Psi}(\vec{r}), \tag{2.1}$$

where $d\bar{\epsilon}$ is the mean energy imparted by ionising radiation in a volume element $dV$, $dm = \rho dV$ is the mass of the material with density $\rho$ in this volume element, and $\vec{\nabla}\cdot\vec{\Psi}(\vec{r})$ is the divergence of the vectorial energy fluence (Reich [13]). Absorbed dose is measured in units of gray (Gy), where 1 Gy=1 J/kg, and in a voxelised geometry, it will generally be given as the energy absorbed in the finite voxel, divided by the mass of the material in this voxel.

## 2.1 Relevant Photon Interactions

Photon attenuation of a narrow monoenergetic beam of initial energy fluence $\Psi(h\nu, 0)$ penetrating a layer of material of thickness z is given by

$$\Psi(h\nu, z) = \Psi(h\nu, 0)\mathrm{e}^{-\mu z} \tag{2.2}$$

where $\mu$ is the attenuation coefficient. The mass attenuation coefficient of a material with density $\rho$ is given as $\frac{\mu}{\rho}$ [13]. The total mass attenuation coefficient is related with the total cross section per atom $\sigma_{\mathrm{tot}}$ as $\mu/\rho = \sigma_{\mathrm{tot}}/uA$, where $u$ is the atomic mass unit and A is the relative atomic mass of the element [14].

The total cross section is given as the sum of the cross sections of the underlying principal interactions in the MeV range as

$$\sigma_{\mathrm{tot}} = \sigma_{\mathrm{pe}} + \sigma_{\mathrm{coh}} + \sigma_{\mathrm{incoh}} + \sigma_{\mathrm{pair}}, \tag{2.3}$$

where $\sigma_{\mathrm{pe}}$, $\sigma_{\mathrm{coh}}$, $\sigma_{\mathrm{incoh}}$ and $\sigma_{\mathrm{pair}}$ are the cross sections of the photoelectric absorption, coherent and incoherent (Compton) scatter as well as of pair production, respectively [14]. The most dominant cross section in the energy range given is the Compton cross section and it may be referred to [14] for values.

Compton effect (incoherent scatter) is the only interaction explicitly used in this work. Therefore, formulae are only given for this effect in the following. In incoherent scatter, an incident photon interacts

with a shell electron. Its energy is decreased by the binding energy of the electron and by kinetic energy that is transferred to the electron. The photon scatter angle $\theta_\gamma$ and the electron scatter angle $\theta_{el}$ after the interaction of an incident photon of energy $E = h\nu$ are related by

$$\theta_\gamma = 2arctan\left(\frac{\cot(\theta_{el})}{(1+\frac{E}{m_0c^2})}\right), \tag{2.4}$$

where this equation is equation (5.21) of [15], re-arranged, and $m_0c^2$ is the rest energy of the electron. The photon angle varies between ]0°,180°] with respect to the incident photon direction, while the electron angle lies between [0°,90°[, where the electron scatter is forward (0°) when the photon is scattered back (180°). This dependency is depicted in figure A.1 of the appendix for a 6 MeV incident photon.

The energy of the scattered electron $E_{el}$ is given in terms of the photon scatter angle $\theta_\gamma$ according to equation (6-9a) of [16] as

$$E_{el} = h\nu\frac{\alpha(1-cos(\theta_\gamma))}{1+\alpha(1-cos(\theta_\gamma))} \tag{2.5}$$

with $\alpha = \frac{h\nu}{m_0c^2}$, or in terms of the electron scatter angle $\theta_{el}$ using 2.4 and $\cos\theta = \cos^2(\frac{\theta}{2}) - sin^2(\frac{\theta}{2})$ and as given in [17]:

$$E_{el} = h\nu\frac{2\alpha\cos^2\theta_{el}}{1+2\alpha+\alpha^2\sin^2\theta_{el}}. \tag{2.6}$$

The differential cross section for every photon angle is given as

$$\frac{d\sigma}{d\theta_\gamma} = \frac{r_0^2}{2}(1+cos^2\theta_\gamma)\left\{\frac{1}{1+\alpha(1-cos\theta_\gamma)}\right\}^2\left\{1+\frac{\alpha^2(1-cos\theta_\gamma)^2}{[1+\alpha(1-cos\theta_\gamma)](1+cos^2\theta_\gamma)}\right\} * 2\pi sin\theta_\gamma, \tag{2.7}$$

according to [16], equation (6-11) and with $d\Omega = 2\pi sin\theta d\theta$, where $r_0 = 2.81794 \times 10^{-13}$ cm is the classical electron radius and $\alpha = \frac{h\nu}{m_0c^2}$.

The energy transfer coefficient $\sigma_{tr}$ is given as

$$\begin{aligned}\sigma_{tr} = {} & 2\pi r_0^2\left\{\frac{2(1+\alpha)^2}{\alpha^2(1+2\alpha)} - \frac{(1+3\alpha)}{(1+2\alpha)^2} + \frac{(1+\alpha)(1+2\alpha-2\alpha^2)}{\alpha^2(1+2\alpha)^2}\right\} \\ & -2\pi r_0^2\left\{\frac{4\alpha^2}{3(1+2\alpha)^3} + \left(\frac{1+\alpha}{\alpha^3} - \frac{1}{2\alpha} + \frac{1}{2\alpha^3}\right) ln(1+2\alpha)\right\}\end{aligned} \tag{2.8}$$

with the classical electron radius $r_0 = 2.81794 \times 10^{-13}$ cm, and $\alpha = \frac{h\nu}{m_0c^2}$, according to equations (6-6) and (6-13) of [16].

## 2.2 Relevant Electron Interactions

The secondary electrons produced in Compton interaction undergo further collisions or produce bremsstrahlung x-rays. For these interactions, the total mass stopping power is described in section 2.2.1 of the ICRU report 35 [18] to include "the total energy loss, $dE$, by collision and radiation for a pathlength, $dl$, in matter of density $\rho$" and is given as

$$\frac{1}{\rho}\left(\frac{dE}{dl}\right)_{\text{tot}} = \left(\frac{S}{\rho}\right)_{\text{tot}} = \left(\frac{S}{\rho}\right)_{\text{col}} + \left(\frac{S}{\rho}\right)_{\text{rad}}. \tag{2.9}$$

The mass collision stopping power $\left(\frac{S}{\rho}\right)_{\text{col}}$ "includes all energy losses in particle collision which directly produce secondary electrons and atomic excitations", whereas the radiative stopping power $\left(\frac{S}{\rho}\right)_{\text{rad}}$ "includes all energy losses of the primary electron which lead to bremsstrahlung production" [18].

The same report defines the "csda range" or "mean path length for an electron of initial energy $E_0$" as the integral of the reciprocal of the stopping power as

$$r_0 = \int_0^{E_0} \left(\frac{S(E)}{\rho}\right)_{\text{tot}}^{-1} dE \tag{2.10}$$

in section 2.2.5 [18], where csda stands for the continuous-slowing-down approximation. In this approximation, energy loss fluctuation are neglected and instead, it is assumed that the energy loss is always equal to the mean rate of energy loss. The report remarks further that "the csda range represents the path length and not the depth of penetration in a given direction" [18].

# Chapter 3

# Dose Calculation Methods for Radiation Therapy

## 3.1 Monte Carlo Dose Calculation Methods

The most precise method currently available for calculation of three-dimensional dose distributions are Monte-Carlo based methods which will be described in the following. Other, kernel-based techniques are sketched in section 3.2.

The report of the Task Group 105 of the American Association of Physicists in Medicine (AAPM) "Issues associated with clinical implementation of Monte Carlo-based photon and electron external beam treatment planning" describes the Monte Carlo (MC) method to accurately calculate dose distributions for clinical radiotherapy, "particularly in heterogeneous patient tissues where the effects of electron transport cannot be accurately handled with conventional, deterministic dose algorithms". They further report that while previously, the long calculation times prevented the use of MC methods in clinical routine, recently more and more also commercial treatment planning systems include MC algorithms, since "the development of faster codes optimized for radiotherapy calculations and improvements in computer processor technology have substantially reduced calculation times to, in some instances, within minutes on a single processor" [19].

Various aspects of Monte-Carlo dose calculations are covered in the above-mentioned report, and it may be referred to this document for further details. For explanation of the general idea, the report itself quotes a publication by Rogers and Bielajew who describe the basic idea of modelling particle transport as "The Monte Carlo technique for the simulation of the transport of electrons and photons through bulk media consists of using knowledge of the probability distributions governing the individual interactions of electrons and photons in materials to simulate the random trajectories of individual particles. One keeps track of physical quantities of interest for a large number of histories to provide the required information about the average quantities." [20] For the use in medical physics, the energy deposition is the most relevant quantity to be stored, and through it, the dose.

In this work, it was decided to use the Geant4 simulation toolkit [21][22], based on a publication of Raaymakers et al., who were the first to publish on their design of a MRI-integrated medical linear accelerator (cf. section 4). They compare several Monte Carlo codes used in medical physics, i.e. MCNP (Briesmeister 1997 [23]), EGS4 (Nelson et al. 1985 [24]) and EGSnrc (Kawrakow 2000 [25]), and report that the "mutual differences for heterogeneous media were smaller than 5% and the difference with measurements was smaller than 4%. The literature on experimental validation with the incorporation of a magnetic field has only been reported for EGS4 and did not show fair correspondence between calculation and experiment (Litzenberg et al 2001 [26])" [27]. Raaymaker et al. further state that a validation of the inclusion of magnetic fields in Monte Carlo calculations is not the goal of their paper but they include experimental data for their specific set up and find their measurements to be in agreement with the Geant4 results [27].

The Geant4 code is the slowest Monte Carlo dose calculation algorithm in a comparison of the AAPM task group report summarising results from other studies, with 193 minutes, compared with 0.9 minutes for the fastest code VMC++ which, however, does not incorporate transport in a magnetic field. Since the simulations in this work serve as reference and time was not focussed on for the reference simulations, this was accepted.

For dose calculations to be used with a MRI-integrated linear accelerator (cf. chapter 4), Bol et al. have recently published their work on MC-based treatment planning using parallelisation on GPU architecture. They use their Monte-Carlo implementation to calculate the dose distribution due to each beamlet to be subsequently employed in the IMRT optimisation, and report the total calculation time to stay below 2.5 minutes for the rather large clinical case of a cervix, seven beam plan, if the same number of GPU is used as there are beam angles. This value is for a 1.5 T magnetic field, for which they report the simulation to take twice as long as for 0 T. The actual IMRT optimisation they apply after the precalculation of the beamlets is described to stay well within 7 s. The dose is calculated on the basis of CT data to be registered with the MR image which, in the case of rigid registration, can also be performed with seconds [1].

## 3.2 Kernel-Based Dose Calculation Methods

Aside from Monte-Carlo based methods, other techniques exist for dose calculation that are based on two-dimensional or three-dimensional convolutions. Two-dimensional convolution methods use a convolution kernel that is derived from the dose deposition due to an infinitely narrow photon beam and which is termed a differential pencil beam [28]. Three-dimensional convolution techniques are also referred to as superposition methods and use the dose deposition due to a photon point interaction as a convolution kernel [29][30]. In the following, one implementation of a pencil beam algorithm will be sketched which is used in the inverse planning module of the DKFZ employed in chapter 11, along with the superposition approach that the analytical approach presented in part II was intended to be used in.

### Pencil Beam Algorithm

Using the dose distribution from an infinitely narrow beam of radiation, the basic idea of a pencil beam algorithm is that the three-dimensional dose distribution of a radiation field can be determined by a two-dimensional, lateral convolution of this narrow pencil beam kernel at different depths, with the primary fluence. The method implemented for calculation of the dose contributions from the beamlets for IMRT optimisation (cf. section 1.3) in the DKFZ treatment planning software which is used in chapter 11, is based on a work by Bortfeld et al. [31], where also a more detailed description is found. Relevant for understanding the use of an infinite source-to-axis distance (SAD) in section 11.1 is the fan-line coordinate system employed, and it is reproduced in figure 3.1a in analogy to an illustration in the publication by Bortfeld et al. In the fan-line coordinate system, all rays are in parallel, in contrast to the actual gantry system where a divergent beam is produced at the radiation source.

In the fan-line coordinate system, the convolution integral to calculate the dose $D'_{irreg}(x_p, y_p, d)$ at a point $(x_p, y_p, d)$ is given as

$$D'_{irreg}(x_p, y_p, d) = \int_{-\infty}^{\infty} \int_{-\infty}^{\infty} \Psi'(x, y) F(x, y) K(x - x_p, y - y_p, d)\, dxdy, \tag{3.1}$$

where $\Psi'(x, y)$ is the energy fluence in air in the absence of any beam modifying devices, $F(x, y)$ is the transmission factor describing the effect of beam modification, e.g. by means of an MLC (cf. section 1.3), $K(x, y, d)$ is the pencil beam kernel, i.e. the dose due to an infinitely narrow beam in a semi-infinite slab, and the primes ($'$) indicate an implicit dependence on the source-to-surface distance (SSD). The authors refer to numerous other publications with similar formulations [31].

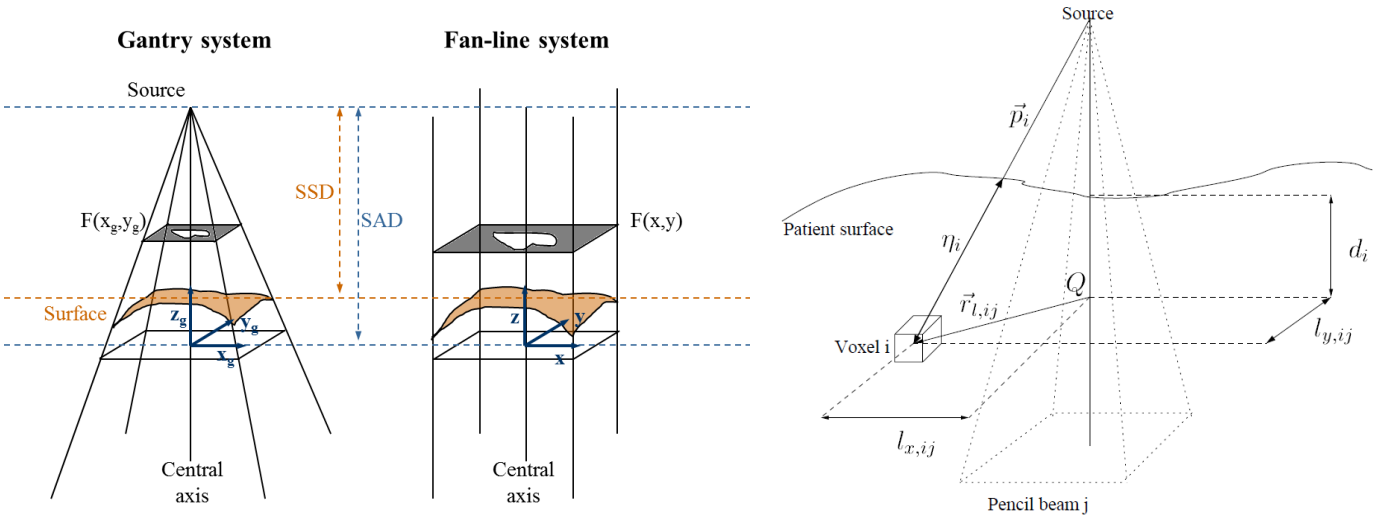


**(a)** Gantry system and fan-line system according to and as illustrated in Bortfeld et al. [31].

**(b)** Geometric set up for dose calculation algorithm. Courtesy of S. Nill, originally found in [12].

**Figure 3.1** Geometries for dose calculation.

The actual pencil beam algorithm developed in the very publication and implemented in the treatment planning system employed in this work, decomposes the pencil beam kernel into terms that depend only on the depth and others that depend only on the lateral position. In that manner, the number of two-dimensional convolutions can be reduced to three for the calculation of the whole three-dimensional dose distribution for all depth. The dose in then given by

$$D'_{irreg}(x_p, y_p, d) \approx \sum_{i=1}^{3} D'_i(d) \int_{-\infty}^{\infty}\int_{-\infty}^{\infty} \Psi'(x,y) F(x,y) w_i(x - x_p, y - y_p)\, dxdy, \tag{3.2}$$

which accelerates the calculation significantly [31].

By means of the pencil beam convolution described, the dose distribution for a beamlet to be used in optimisation is generated, still in the fan-line system, i.e. for an infinite SSD which would imply parallel rays. It was found that the finite pencil beam created in this manner, i.e. in the fan-line system, is sufficient to calculate dose also for other values of SSD. In order to calculate the contribution from one beamlet $j$ to the dose in voxel $i$, so the element of the $D_{ij}$ matrix (cf. optimisation section 1.3), in the actual divergent system with finite SSD's to the patient skin, a look-up in the stored finite fan-line pencil beam is performed with subsequent inverse square correction. The exact algorithm is described by Nill [12], which is used as a reference in the following. Figure 3.1b from the same work illustrates the geometry of dose calculation, depicting voxel $i$ and finite pencil beam $j$, both in an actual divergent system of coordinates. For the look-up, the lateral coordinates $l_{x,ij}$ and $l_{y,ij}$ in the divergent system are transformed into the fan-line coordinates as

$$\begin{aligned} l^f_{x,ij} &= l_{x,ij} \frac{SAD}{SAD + d_i} \qquad \text{and} \\ l^f_{y,ij} &= l_{y,ij} \frac{SAD}{SAD + d_i}, \end{aligned} \tag{3.3}$$

and the water equivalent pathlength, or radiological depth, $\eta_i$ along the ray from the surface of the patient to voxel $i$ is calculated as

$$\eta_i = \sum_r \rho_r \Delta x_r, \tag{3.4}$$

with $\rho_r$ being the relative electron density for voxel $r$ on the path of the ray through matter, and $\Delta x_r$ being the distance traversed in voxel $r$. For lookup in the precalculated finite pencil beam $D_{pb}$, bi-linear

interpolation is performed, and with the inverse square correction, the $D_{ij}$ matrix element (cf. equation 1.1) is then given by

$$D_{ij} = D_{pb}(\eta_i, l^f_{x,ij}, l^f_{y,ij}) \left[\frac{SAD}{SAD + d_i}\right]^2 f_{c,j} \tag{3.5}$$

where $f_{c,j}$ is a correction factor that may account for the primary fluence distribution [12].

By the pencil beam method, heterogeneities on the beam path are taken into account by the radiological depth scaling; however, lateral heterogeneities cannot be handled. The accuracy of the algorithm is documented in Scholz et al.: "Since the respective dose kernels are derived from measured dose distributions in water, this algorithm leads to exact dose distributions well before and behind tissue inhomogeneities, but inside or close to media different from water deviations to measurements of up to 20% on the central axis of small fields were observed. Aside from these regions, inside homogeneous, water-equivalent material this algorithm calculates very quickly three-dimensional distributions of absolute dose for arbitrary field shapes within 2% deviations from measurements" [32].

In terms of computational speed, a recent study by Siggel et al. investigates the performance of a re-engineered multithreaded implementation of the pencil beam algorithm and finds times for raytracing and dose calculation to range from less than 0.4 seconds for 18 threads employed in a 7 beam prostate case to around 11 seconds for a single thread employed in a 9 beam head-and-neck case [33].

### Superposition Algorithm

In the superposition method, instead of using the dose due to an infinitely narrow photon beam in a two-dimensional convolution, the dose deposition due to a photon point interaction is employed in a three-dimensional convolution. According to Ahnejö et al. [34], the point spread function or point kernel $h(\vec{r}, \vec{s})$ describes the energy transferred to point $\vec{r}$ due to a point interaction at source point $\vec{s}$. And the **T**otal **E**nergy **R**eleased per unit **MA**ss (TERMA) at the interaction point is given by the product of the mass attenuation coefficient $\frac{\mu}{\rho}(E, \vec{s})$ of the primary photons of energy $E$ at this point $\vec{s}$, the energy and primary photon fluence differential in energy $\Phi_E(\vec{s})$ at the same point as

$$T_E(\vec{s}) = \frac{\mu}{\rho}(E, \vec{s}) E \Phi_E(\vec{s}). \tag{3.6}$$

For a monoenergetic photon beam and in a homogeneous medium, the dose $D_E(\vec{r})$ is computed by a convolution of the TERMA with the point kernel that actually only depends on the difference $(\vec{r} - \vec{s})$, as

$$D_E(\vec{r}) = \int_V T_E(\vec{s}) h_E(\vec{r} - \vec{s}) d^3 s, \qquad \text{where} \int_V h_E(\vec{r} - \vec{s}) d^3 \vec{s} = 1 \ \ [34]. \tag{3.7}$$

The point kernel is generally determined in water, but in order to account for heterogeneous tissues with varying densities, a scaling is applied according to a proposition by Mohan et al. [35] that is based on O'Connor's theorem [36]: The water dose deposition kernel $h_{E,H_2O}$ is scaled by the relative electron density to water $\rho_{rel}(\vec{s}) = \rho(\vec{s})/\rho_{H_2O}$ at the point of interaction $\vec{s}$, and by the average electron density $\overline{\rho}_{rel}(\vec{s}, \vec{r})$ between the point of interaction $\vec{s}$ and the point the energy is transferred to $\vec{r}$, such that

$$\begin{aligned} h_{E,inhom}(\vec{s}, \vec{r}) = \rho_{rel}(\vec{s})\ \overline{\rho}^2_{rel}(\vec{s}, \vec{r})\ h_{E,H_2O}\ (\overline{\rho}_{rel}(\vec{s}, \vec{r}) \cdot (\vec{r} - \vec{s})), \\ \text{where}\ \ \overline{\rho}_{rel}(\vec{s}, \vec{r}) = |\vec{r} - \vec{s}|^{-1} \int_{\vec{s}}^{\vec{r}} \rho_{rel}(\vec{s'})\ ds', \end{aligned} \tag{3.8}$$

which assumes a linear energy propagation between $\vec{s}$ and $\vec{r}$. The density scaling leads to a deformation of the point kernel, such that in directions of lower electron density, it is extended whereas in directions of higher electron density, it is contracted.

The extension from monoenergetic photon beams to the spectrum of a medical linear accelerator is achieved by use of a weighted sum of the dose contributions from discrete energies as

$$D(\vec{r}) = \sum_i \alpha_i \int_V T_{E_i}(\vec{s}) h_{E_i,inhom}(\vec{s},\vec{r}) d^3s, \tag{3.9}$$

where the $\alpha_i$ are the weights for the contributions from the respective bins with energies $E_i$. This sketch of the basic principles of the superposition method followed a description by Scholz [37].

The accuracy of the superposition algorithm is reported to be within 2 % also in heterogeneous tissues for the set up investigated by Scholz et al. [32]. Recent figures reported for the calculation speed by a GPU-based implementation of a superposition algorithm are 2.8 seconds per beam [38].

# Chapter 4

# MRI-integrated Radiation Devices

Five groups worldwide have worked or are working on concepts for integrated devices that combine medical linear accelerators or cobalt-60 irradiation units with onboard magnetic resonance imaging. In this chapter, their visions on the potential of these devices are presented in section 4.1 along with the existing plans and prototypes in section 4.2 and finally the effects on the dose deposition that have been observed by these groups (section 4.3).

The first group to publish their concept is located at the University Medical Centre Utrecht in the Netherlands (Lagendijk et al. 2002 [39], Raaymakers et al. [27]) who have built a prototype combining a cylindrical MR-scanner with a medical linear accelerator. A different set up has been built by the ViewRay™ company having its origins in the Universities of Florida and Washington, USA, where three cobalt-60 sources are mounted on a ring gantry around the MR-Scanner (Dempsey et al. [40], [41]), very similar to the design proposed in a publication from the Peter MacCallum Cancer Centre in Melbourne, Australia, where with two rotating cobalt-60 sources, a helical tomotherapy system is proposed (Kron et al. [42]). At the Cross Cancer Institute in Edmonton, Canada, a bi-planar MRI is combined with a medical linear accelerator (Fallone et al. [43], Kirkby et al. [44]) which is also the design chosen by a collaboration of several Australian universities and Stanford University, USA (Constantin et al. [45], Australian MRI-Linac Program [46]).

## 4.1 The Potential of MRI-Integrated Radiation Devices

The most frequent reason given in publications of the groups working on MRI-integrated radiation devices is the onboard availability of anatomical information. Lagendijk et al. see a possible "breakthrough in accurate position verification in radiotherapy" with the capability of such a system to "make fast 2D images of soft tissues with orientation along and perpendicular to the field axis, allowing continuous imaging at critical locations" [39], and the same group envisions "online optimization of the treatment plan" [27]. In a recent work, they emphasise the superiority of MRI over other modalities as offering "unequalled soft-tissue contrast for direct visualization of the target volume and the surrounding organs at risk" (Stam et al. [47]).

The same reasoning is followed by Constantin et al. where they focus again on the direct availability in the treatment situation and characterise the "ideal image guidance strategy in radiation therapy" as "to have real-time volumetric and position information of the tumor and surrounding healthy tissue during the treatment itself". They describe MRI as a "compelling approach" since it is capable of the latter with "exquisite soft tissue contrast to differentiate cancerous from healthy tissue" and due to its non-invasiveness [45].

Fallone et al. comment further on the use of this information for "real-time tracking of the tumor and healthy tissues during irradiation by the treatment beam" [43] and the group has evaluated an autocontouring algorithm for lung tumour tracking in a phantom study (Yun et al. [48]). Also the Utrecht group

has published on gating and tracking approaches using what they term pencil-beam navigators that can follow tissue boundaries and may be used in combination with 2D images (Crijns et al. [49], Stam et al. [47]).

Kron et al. stress the use of "information from multiple imaging modalities for target definition during treatment planning" and delivery to account for variations of the target position. They mention MRI and positron emission tomography (PET) explicitly as modalities providing "essential information, which improves target outlining in many clinical scenarios". In PET imaging they see the difficulty though "to perform daily PET scans with radioactive tracers" and recommend MRI for image guidance due to its "excellent soft tissue contrast" which makes MRI especially useful for brain and pelvic lesions, and due to MRI's capability to provide images on "flow or metabolic activity" [42].

Especially could daily time-resolved information on hypoxic regions be of interest for radiation therapy since these are known to be more radio-resistant than well-oxygenated cells and the regions are known to change both shape and position (Nehmeh et al. [50]). MR spectroscopy is another method that can help in tumour diagnostics [51] and its frequent use may help understand tumour response to radiation better. In general, onboard MR imaging could be used in research activities aimed at monitoring and understanding radiobiological processes over the course of treatment by providing a couple of additional functional scans to be evaluated offline in every fraction. One can envision perspectives in terms of personalised medicine like creating individual fractionation schemes based on images visualising reoxygenation patterns, radiosensitivity markers, information on accelerated repopulation that may become apparent 3 to 4 weeks after treatment start or, in case of hypofractionated treatments, repair processes that occur 4-24 hours after irradiation (cf. "Time-dose-fractionation" [52]).

Ultimately, it is clear that MR-integration with radiation therapy devices will provide information on anatomical and functional changes online, i.e. during the time of treatment. Its potential, however, only arises from the intelligent use of this information for adaptation of the treatment. The online information may influence two aspects of treatment plan adaptation: On the one hand, the actual delineation and classification of structures may change in terms of where radiation damage is desired, where it is tolerated and where it is to be avoided, but also in terms of prescription, i.e. how much dose should be applied to a certain structures, given sufficient knowledge for auch a decision is available. This adaptation to the daily functional circumstances will probably need to be done once at the beginning of or prior to the treatment. On the other hand, anatomical changes may also occur intrafractional, throughout the radiation treatment. For these, gating or tracking, as mentioned above, may be the methods of choice, but also real-time dose calculation and optimisation may be thought of, aiming at treating each individual patient with the best achievable dose distribution in order to maximise his or her personal therapeutic success.

## 4.2 Plans and Prototypes

Kirkby et al. from the Edmonton group distinguish between two basic geometries of MRI-integrated radiation therapy devices and their categorisation is adopted here. The first geometry that they term "fixed cylindrical (FC)" [44] is displayed in figure 4.1 (a) and (b). It consists of a cylindrical body coil which creates a $B_0$ field parallel to the patient's cranio-caudal axis, and a radiation source that can rotate around that axis on the outside of the MR coil. Its rotation direction is depicted in (a), while (b) shows the direction of treatment couch translation.

The FC geometry is implemented in the prototype of the UMC Utrecht, where a modified 1.5 T MR-scanner is combined with a modified 6 MV medical linear accelerator that is mounted on a ring gantry around the scanner (Raaymakers et al. [53]). Also the two designs involving cobalt-60 sources are FC devices, but they use split solenoids and place the cobalt-60 sources in the gap between them. The design by Kron et al. involves two cobalt-60 sources on opposing sides of the gap [42], while in the design of the ViewRay™ company three cobalt-60 source are arranged at 120° angle from each other, all focussing towards the centre

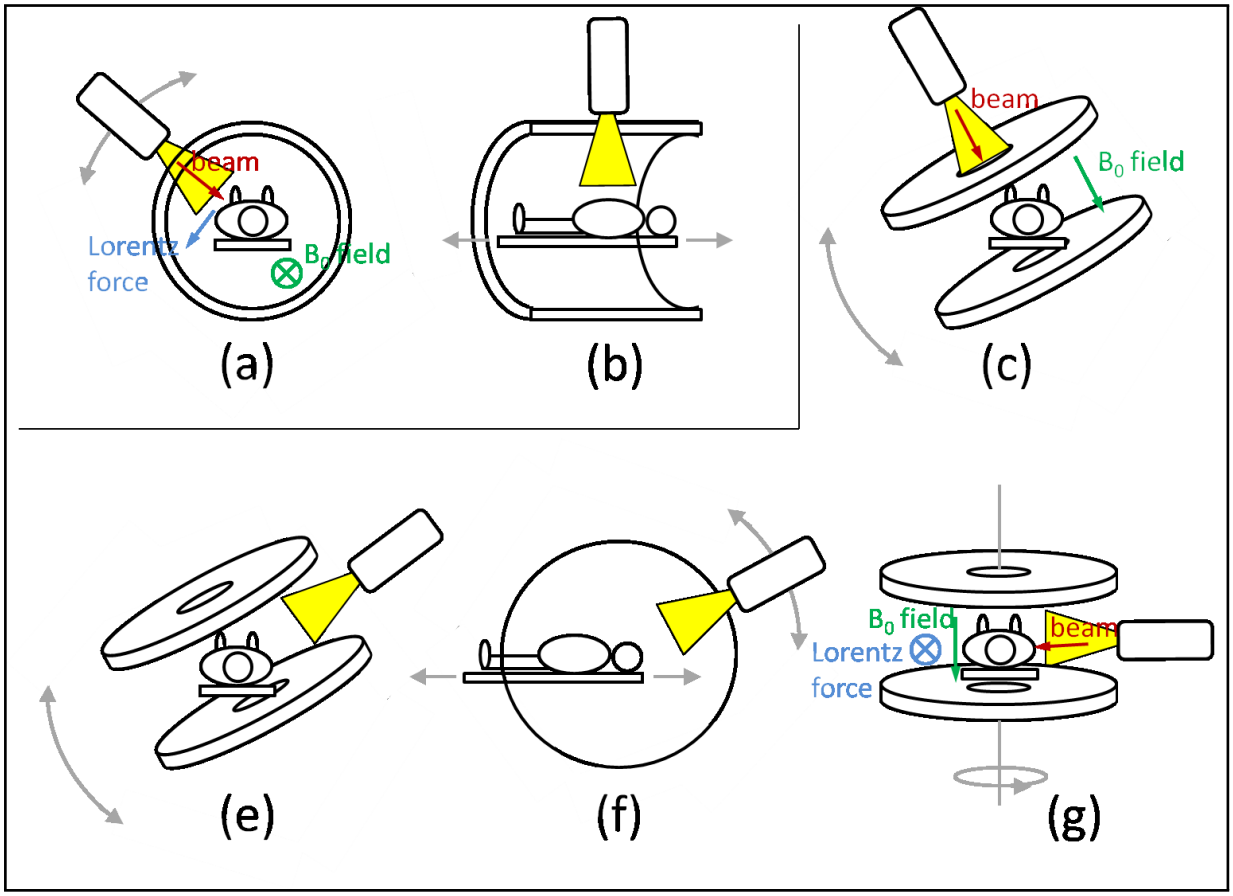


**Figure 4.1** Designs of MRI-integrated irradiation devices. FC design in a tranverse (a) and lateral cross-sectional view (b), in-line (c) and perpendicular (e) configuration of the RBP design; other potentional degrees of freedom in a perpendicular RBP set up when the gap between the poles is vertical (f, lateral view) or horizontal (g). Image inspired by [44] and [45].

of the coils [41]. The magnetic field suggested by Kron et al. is 0.25 T, whereas the viewray system uses 0.3 T.

In the second geometry, the irradiation device is attached to the open end of a biplanar magnet, and the complete assembly rotates around the patient cranio-caudal axis. Consequently, it is termed the "rotating biplanar (RBP) geometry" [44]. The RBP geometry is shown in (e) of figure 4.1, where the grey arrows indicate the direction of rotation of the complete assembly. Due to the shape of the magnet poles, the type of MR-scanner used in this design is also often referred to as a "double-donut" MR-scanner. Aubin et al. from the same group propose to use a second configuration, where irradiation is through a hole in the centre of one magnet pole, such that the beam and the magnetic field are in parallel as illustrated in figure 4.1 (c). Accordingly, they differentiate between the "transverse design" for the former and the "parallel design" for the latter set up [54], while Constantin et al. refer to the "perpendicular configuration" and the "in-line configuration" [45].

The RBP design in both configurations each is described by the Edmonton group and the Australian MRI-Linac Program, where Fallone et al. have decided on a magnetic field of 0.2 T [44][55], and the Australian group use fields between 0.2 T and 3 T for their simulations of a perpendicular configuration (Oborn et al. [56]) and fields between 0.2 T and 1 T for the in-line configuration (Constantin et al. [45], Oborn et al. [57]). Generally, biplanar scanner have lower magnetic fields than what is possible with cylindrical scanners.

While the treatment couch of the Edmonton design is seen only to have translational degrees of freedom [54], the Australian collaboration announces on their website that a rotating couch system is planned to be developed [46] which would add the degree of freedom depicted in (g) of figure 4.1. Another degree of

freedom that can be imagined for the RBP design is sketched in (f) of the same figure, where the irradiation device rotates in the midsagittal plane of the patient. This design would be required to deliver the non-coplanar beam in the brain case presented chapter 11.

The different designs imply different orientations of the magnetic field and the photon beam and therefore also of the direction of the Lorentz-force acting on secondary electrons produced in the patient. In the FC design the magnetic field is fixed with respect to the patient and always parallel to his or her cranio-caudal axis as shwon in figure 4.1 (a). When the irradiation device changes its position around this axis, so does the beam direction. The Lorentz force on the secondary electrons with a velocity component in direction parallel to the beam therefore also changes direction such as to stay perpendicular to both the field and the direction of motion. In contrast, in the original RBP design without couch rotations, the beam direction is fixed with respect to the magnetic field and they both rotate around the patient together, such that the Lorentz force always stays parallel to the patient cranio-caudal axis. Once couch rotation or rotation in the midsagittal plane is introduced, the direction of the Lorentz force necessarily changes as well. In the in-line configuration, both beam and field are in parallel, such that the Lorentz force merely affects electrons with velocity components perpendicular to the beam.

## 4.3 Effects on the Dose Deposition

Since in the following chapters, the effects of the magnetic field on the dose deposition can be observed in several illustrations of reference Monte Carlo simulations, only a short overview is given here. As described above, two orientations are suggested where the beam is either in parallel with or perpendicular to the magnetic field. A comparison of the effects due to both orientations is given by Kirkby et al. [58] and it it seen that effects are much smaller in a parallel field compared with a perpendicular field. Parallel fields will not be described in more detail here, since throughout the work, perpendicular fields have been used which is the orientation of the existing prototypes.

Effects on the dose distribution for MRI-integrated irradiation devices with a perpendicular orientation of beam and field were first reported on by Raaijmakers et al. and they find that due to the deflection of the secondary electrons by the Lorentz force, lateral beam profiles in water are deformed sidewards such that the penumbras on both beam edges differ, and the dose maximum is at shallower depths than if no magnetic field is present [27]. On the exit surface from tissue to air, they observe a 40 % dose increase due to what they term the electron return effect (ERE) (Raaijmakers et al. [59]) and they investigaste it further with respect to the surface orientation in (Raaijmakers et al. [60]).

The ERE can be observed in figure 4.2, where a Monte Carlo simulation of a 1.25 MeV photon beam is seen, in which only secondary electron interactions and tracks are displayed. The beam is incident from below in the figure, into PMMA material in which another cylinder of polyethylene with a small isooctane layer is embedded (liquid ionisation chamber). The white horizontal line marks the boundary to air where the ERE is observed for 0.8 T (right). While at 0 T, the eletrons produced close to this boundary continue their motion on a straight track, at 0.8 T they get bent back onto the surface. By penetrating back into the solid material, further interactions cause a dose increase as described in [59].

The path of an electron in a magnetic field depends both on the energy of the electron and the strength of the magnetic field, and the radius of its motion in vacuum is given by the relativistic gyroradius $r_g$ which is defined as

$$r_g = \frac{\gamma m_0 v}{qB} = \frac{\gamma \beta m_0 c}{qB} \tag{4.1}$$

where $\gamma = \frac{1}{\sqrt{1-\left(\frac{v}{c}\right)^2}}$ is the Lorentz factor, $m_0$ is the particle rest mass, $q$ the charge, $B$ the magnetic field, $c$ the speed of light, and $\beta = \frac{v}{c}$ is the relative velocity [61].

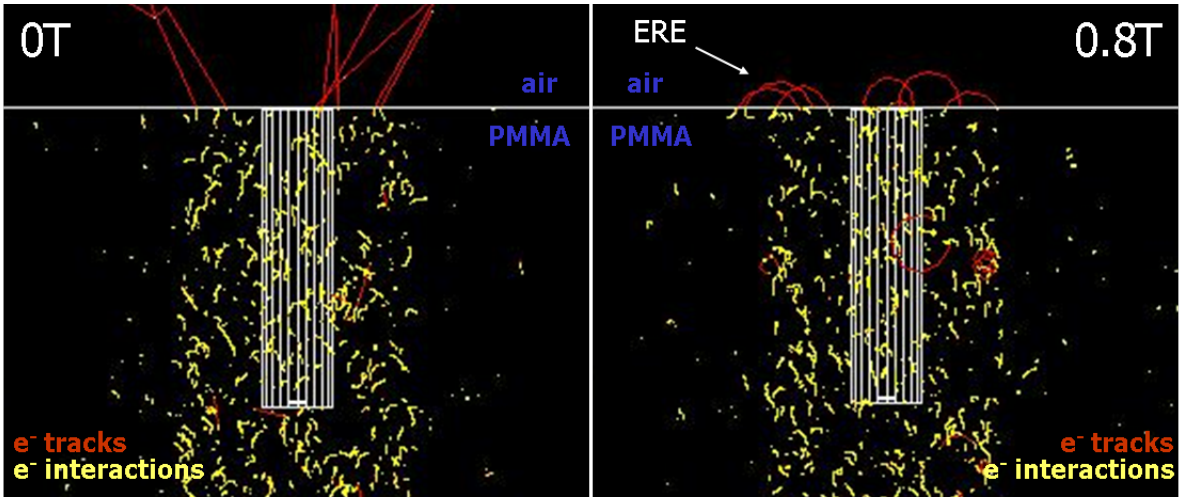


**Figure 4.2** Monte Carlo simulation of secondary electron interactions due to a 1.25 MeV photon beam incident from below. At the exit surface to air, electron are bent back for 0.8 T. In the middle of the beam a solid polyethylene cylinder with a small isooctane layer is seen. Simulation and visualisation by means of the Geant4 toolkit [21][22].

The position where the electrons return to the material, and also how far they still penetrate into the tissue to deposit dose determines what the dose increase due to the ERE looks like. While the energy chosen in 4.2 corresponds approximately to photons from cobalt-60, Raaijmakers et al. use a 6 MV photon spectrum of a medical linear accelerator in their investigation of the influence of magnetic fields of different magnitude on the dose distribution, with a different spectrum of secondary electrons produced, accordingly. Raaijmakers et al. find that dose effects due to the ERE are strongest at 0.75 T for the exit surface of a beam and at 3 T for a lateral tissue-air interface [62]. Their findings are in agreement with Kirkby et al. [44] who investigate fields of 0.2 T and 1.5 T for both cobalt-60 and 6 MV photons.

# Part II

# Analytical Approach

# Chapter 5

# Material and Methods

For dose calculation in a magnetic field, a fast and reliable method is desired (cf. chapter 1.1). In this part, it is investigated whether an analytical description of the point kernel in a magnetic field can be used in order to calculate dose in analogy to the superposition technique (cf. section 3.2).

## 5.1 Kernel Approximation by Tracking of Compton Electrons

In the superposition technique, O'Connor's theorem is employed to inversely scale the dimensions of the photon point kernel with the density of the material the secondary electrons are travelling in (cf. section 3.2). Under the influence of a magnetic field, the electrons will be systematically deflected, such that a mere scaling of the dimensions does not seem appropriate.

The energy range of the majority of primary photons in radiation therapy lies between around 100 keV and 10 MeV. In this range, the photon mass attenuation coefficient is dominated by the Compton effect (cf. section 2), and most of the dose deposited is due to the secondary electrons produced in this interaction. A set of equations, taken from Jette [63], are used to describe the tracks of these Compton electrons in matter in a magnetic field. It was hoped that by depositing dose along these tracks, point kernels in a magnetic field could be approximated, and that consequently, a density scaling along the tracks would be possible.

For this purpose, the electron tracks were described in two ways, first, following Jette in using a constant electron stopping power of 2 MeV/cm for water [64], and second, using variable stopping power values taken from the ESTAR database of NIST [65]. Both descriptions are found in section 5.1.1, while the sampling of the point kernel is sketched in section 5.1.2.

### 5.1.1 Electron tracks

#### Constant stopping power

In first approximation, Jette [63] neglects scatter and describes electron motion as a superposition of the continuous-slowing-down approximation and the influence of the Lorentz force, namely

$$\frac{d\vec{p}}{dt} = -S_T\left(E\left(s\right)\right)\frac{\vec{v}}{v} + \frac{e}{c}\vec{v}\times\vec{B}, \tag{5.1}$$

where $\frac{d\vec{p}}{dt}$ is the change of momentum in time, $S_T$ is the total (linear) stopping power, $\vec{v}$ and $v$ are the electron's velocity and speed, respectively, $e$ is its charge, $c$ is the speed of light and $\vec{B}$ is the magnetic field it travels in.

Using a constant magnetic field in y-direction, Jette arrives at equations for the coordinates of the electron tracks, in terms of the distance travelled $s$. The tracks depend on the initial position $(x_0, y_0, z_0)$,

the initial zenith and azimuthal angles $\theta_0$ and $\phi_0$ with the z-axis parallel to which the primary photon travels, and two integrals $S\left(\frac{s}{r_0}\right)$ and $C\left(\frac{s}{r_0}\right)$ which themselves depend on the initial electron energy and the magnetic field the particles are exposed to. $r_0$ is the continuous-slowing-down range (cf. equation 2.10).

$$\begin{aligned} x(s) &= x_0 + r_0\left[\cos\theta_0 S\left(\frac{s}{r_0}\right) + \sin\theta_0\cos\phi_0 C\left(\frac{s}{r_0}\right)\right], \\ y(s) &= y_0 + \sin\theta_0\sin\phi_0 s, \\ z(s) &= z_0 + r_0\left[\cos\theta_0 C\left(\frac{s}{r_0}\right) - \sin\theta_0\cos\phi_0 S\left(\frac{s}{r_0}\right)\right] \end{aligned} \tag{5.2}$$

The integrals read, as a matter of completeness,

$$\begin{aligned} C(\tau) &= \int_0^\tau cos\left[\frac{qB}{S_T} ln\left(\frac{\sqrt{\lambda(\lambda+2)}+\lambda+1}{\sqrt{\lambda(1-\tau')[\lambda(1-\tau')+2]}+\lambda(1-\tau')+1}\right)\right] d\tau' \\ S(\tau) &= \int_0^\tau sin\left[\frac{qB}{S_T} ln\left(\frac{\sqrt{\lambda(\lambda+2)}+\lambda+1}{\sqrt{\lambda(1-\tau')[\lambda(1-\tau')+2]}+\lambda(1-\tau')+1}\right)\right] d\tau' \end{aligned} \tag{5.3}$$

where $-e = q$, $\tau = \frac{s}{r_0}$, $\lambda = \frac{E_0}{mc^2}$ and $r_0 = \frac{E_0}{S_T}$, with $S_T = 2$ MeV being the constant electron stopping power.

**Variable stopping power**

Without the approximation of a constant electron stopping power Jette is using, it was also possible to obtain equations for the tracks that can be numerically evaluated. Jette first uses a non-standard spherical coordinate system in which the unit vector in the direction of electron motion $\widehat{v}$ is given by

$$\widehat{v} = \cos\xi\sin\eta\widehat{x} + \sin\xi\widehat{y} + \cos\xi\cos\eta\widehat{z}. \tag{5.4}$$

Using $\vec{B} = B\vec{y}$, he shows that $\xi$ is constant at its initial value $\xi = \xi_0$, and $\eta$ can be given by

$$\eta(s) = \eta_0 - eB\int_0^s \frac{ds'}{\sqrt{E(s')[E(s')+2mc^2]}}, \tag{5.5}$$

$\eta_0$ being the initial value of $\eta$.

The angle $\eta$ enters the coordinate equations as

$$\begin{aligned} x(s) &= x_0 + \cos\xi_0\int_0^s \sin\left[\eta(s')\right]ds' \\ y(s) &= y_0 + \sin\xi_0 s \\ z(s) &= z_0 + \cos\xi_0\int_0^s \cos\left[\eta(s')\right]ds'. \end{aligned} \tag{5.6}$$

This is the point at which Jette introduces the constant stopping power in his publication and obtains an analytical expression for $\eta(s)$. In contrast, here the stopping power is allowed to vary with energy. The values of $\eta(s)$ are therefore numerically evaluated, simulating the energy loss due to the continuous-slowing-down approximation (csda, cf. section 2) using equation 2.9 and inserting the respective values for the total linear stopping power $\left(\frac{S}{\rho}\right)_{tot}$ from the ESTAR database [65](Jette uses $S_T$ for $S$).

Now, in analogy to the procedure Jette follows, with $-e = q$ and using

$$\eta_1(s) = qB \int_0^s \frac{ds'}{\sqrt{E(s')[E(s') + 2mc^2]}} \tag{5.7}$$

as well as the trigonometric identities

$$\begin{aligned} \sin(\eta_0 + \eta_1(s)) &= \sin\eta_0 \cos\eta_1(s) + \cos\eta_0 \sin\eta_1(s) \\ \cos(\eta_0 + \eta_1(s)) &= \cos\eta_0 \cos\eta_1(s) - \sin\eta_0 \sin\eta_1(s), \end{aligned} \tag{5.8}$$

the coordinates can be expressed as

$$\begin{aligned} x(s) &= x_0 + \cos\xi_0 \left[\sin\eta_0 \int_0^s \cos\eta_1(s')ds' + \cos\eta_0 \int_0^s \sin\eta_1(s')ds'\right] \\ y(s) &= y_0 + \sin\xi_0\ s \\ z(s) &= z_0 + \cos\xi_0 \left[\cos\eta_0 \int_0^s \cos\eta_1(s')ds' - \sin\eta_0 \int_0^s \sin\eta_1(s')ds'\right]. \end{aligned} \tag{5.9}$$

The integrals are thus independent of the initial angles $\xi_0$ and $\eta_0$ and can be substituted by $\mathcal{S}(s)$ and $\mathcal{C}(s)$ such that

$$\begin{aligned} x(s) &= x_0 + \cos\xi_0 \left[\sin\eta_0 \mathcal{C}(s) + \cos\eta_0 \mathcal{S}(s)\right] \\ y(s) &= y_0 + \sin\xi_0\ s \\ z(s) &= z_0 + \cos\xi_0 \left[\cos\eta_0 \mathcal{C}(s) - \sin\eta_0 \mathcal{S}(s)\right]. \end{aligned} \tag{5.10}$$

Comparing now the unit velocity vector representation in this coordinate system as given in equation 5.4 for $(\xi = \xi_0, \eta = \eta_0)$ with the representation of the initial unit velocity vector in a spherical coordinate system $(\theta, \phi)$ where the initial photon travels parallel to the z-axis,

$$\hat{v} = \sin\theta_0 \cos\phi_0 \hat{x} + \sin\theta_0 \sin\phi_0 \hat{y} + \cos\theta_0 \hat{z}, \tag{5.11}$$

the following equalities are obtained for all initial angles

$$\begin{aligned} \cos\xi_0 \sin\eta_0 &= \sin\theta_0 \cos\phi_0 \\ \sin\xi_0 &= \sin\theta_0 \sin\phi_0 \\ \cos\xi_0 \cos\eta_0 &= \cos\theta_0. \end{aligned} \tag{5.12}$$

Substituting these in equation 5.10, the tracks can be expressed as

$$\begin{aligned} x(s) &= x_0 + \sin\theta_0 \cos\phi_0 \mathcal{C}(s) + \cos\theta_0 \mathcal{S}(s) \\ y(s) &= y_0 + \sin\theta_0 \sin\phi_0\ s \\ z(s) &= z_0 + \cos\theta_0 \mathcal{C}(s) - \sin\theta_0 \cos\phi_0 \mathcal{S}(s). \end{aligned} \tag{5.13}$$

The superposition of csda and magnetic field action yields spiral tracks in the medium, both for the constant and variable stopping power used.

### 5.1.2 Sampling of the point kernels

Practically, the point kernels were sampled in Cartesian voxels of dimension $(1\ \text{mm})^3$ in the following manner, assuming a point interaction of a photon and considering only the Compton electrons:

- Space was discretized into intervals of electron scatter angles $(\theta_0, \phi_0)$ for which the tracks are given by equations 5.2 or 5.13, respectively.
- For every interval of electron scatter angle $\Delta\theta$, the energy of the electron is given by equation 2.5, using the conversion of electron to corresponding photon angle of equation 2.4.
- The likelihood for the electron to be scattered into this interval is obtained from the differential cross section (cf. equation 2.7).
- All azimuthal angles $\phi_0$ have the same probability of $\Delta\phi/2\pi$.
- The tracks were numerically evaluated and for every integration step $\Delta s$, energy was locally deposited in the voxel the step was located in.

MATLAB [66] was employed as a tool, and for both methods, the step size $\Delta s$ for numerical integration was chosen to be 0.0001 cm, which was found to influence the final position value by less than 1%. The angular intervals $\Delta\theta$ and $\Delta\phi$ were 0.1 degree each. After verification of the energy transfer by comparison with the respective results from equation 2.8, the kernels were scaled such that the full photon energy was deposited in the volume, in accordance with the working assumption that all energy is locally transferred by the Compton electrons.

Photon kernels were generated for different combinations of magnetic field strengths (0 T, 1.5 T, 3 T) and photon energies (1 MeV, 3 MeV, 6 MeV). The values for magnetic field strength are those of clinical state-of-the-art scanners, while the photon energies represent approximate values in a cobalt-60 irradiation (1 MeV), and for the mean and the maximum of the 6 MV spectrum of the clinical linear accelerator (3 MeV and 6 MeV).

## 5.2 Reference Simulations using Monte Carlo

The Monte Carlo simulation toolkit Geant4 [21][22] was employed to generate the point kernels for comparison, using the G4LowEnergy package and version 9.3.p02. Photon point interactions were simulated in the centre of a voxelised water phantom with and without a magnetic field (G4UniformMagField), where the water phantom was represented as a parameterised volume (G4PVParameterised). The point interaction was forced by means of a wrapper process (G4WrapperProcess), which modifies the actual physical process. The wrapper process is constructed such that for the first interaction the photon undertakes, the interaction length of the underlying physical process is decreased by a factor of $10^9$. In Geant4, the process with the shortest interaction length is the one to be invoked. In this manner, all photons are forced to interact right after their production, and a point-kernel is generated.

All photons are defined to have the same initial momentum at their generation, and the magnetic field is constructed perpendicular to this momentum. Dose was scored on a voxel-basis, where the dimensions of the voxels were $(1\ \text{mm})^3$ as for the analytical point kernels.

## 5.3 Generation of Pencil Beams

For verification of whether it is possible to use the point kernels in dose calculation, pencil beam dose distributions (cf. section 3.2) were computed from the point kernels generated by the methods described above (5.1.1, 5.1.2, 5.2). For this purpose, point kernels were convolved with the TERMA from a given

photon pencil beam in depth according to section 3.2, equation 3.7, where the TERMA is an exponential function and the photon mass attenuation coefficients for water were taken from the NIST database [14].

In addition, complete pencil beams were simulated using Geant4 [21][22] by having an infinitely narrow beam of photons impinge on the surface of a voxelised water phantom and recording the dose caused by it. Except for forcing the point interaction, the same Geant4 setup is used as for generation of the point kernels. (5.2). The water phantom is surrounded by air in the simulation.

# Chapter 6

# Results

## 6.1 Point Kernels in Water

### 6.1.1 Sampling according to the analytical approach

Some properties of the point kernels for $B = 0\ T$ are shown in the appendix A. There, instead of employing the tracks from the analytical approaches, the continuous slowing down approximation (csda) was carried out along the angular segments, and details resulting from the equations given in section 2 and underlying the kernel generation, are illustrated.

Figure 6.1 shows tracks of the Compton electrons in the plane of incidence of the photon (incident from above), sampled at a 5° spacing, where the constant stopping power approach (black) and the variable stopping power approach (red) were used. Mind that their display scales differ in order to reveal enough details. All track structures are scaled to their maximum extension. Due to the increasing energy of the incident photon from top to bottom, the dimensions actually increase in this direction, while with increasing magnetic field from left to right, the dimensions decrease. Later, in figure 6.2, the kernels are displayed to scale.

From the track structures, it can be observed that for low energy electrons, the constant stopping power approach yields longer tracks than the variable stopping power approach. This is in agreement with the actual stopping power values. Below 600 keV, the total mass stopping power of electrons increases rapidly until the electrons have completely slowed down which is seen in the appendix from figure A.3.

Considering the Compton electrons produced from the 1 MeV incident photon beam and scattered into an angle of 5° from the forward direction, i.e. having an energy of around 0.8 MeV (cf. equation 2.6), the constant stopping power approach will slow them down at a rate of 0.2 MeV/mm, such that they stop at a distance of 4 mm from the point of photon interaction. In contrast, the csda range (cf. equation 2.10) given in the ESTAR database ([65]) is only 3.3 mm which is consistent with the tracks calculated using the variable stopping power approach.

Performing the energy deposition according to the csda, point kernels as seen in figure 6.2 are sampled. Here, the energy deposition in the x-z plane containing the point of photon interaction is displayed. The photon is incident from above and has energies of (from top to bottom) 1 MeV, 3 MeV and 6 MeV, while the simulated magnetic fields are (from left to right) 0 T, 1.5 T and 3 T. The kernels are normalised such that the full energy of one photon is deposited in the entire water volume, i.e. all voxels in the 1 MeV cube add up to 1 MeV etc. The kernels displayed were generated using the variable stopping power approach.

In figure 6.2, it can be observed that the main energy deposition per voxel is along the tracks resulting from forward scatter of the electron. Application of the magnetic field bends the energy deposition to spirals which also leads to the decrease in size of the kernel.

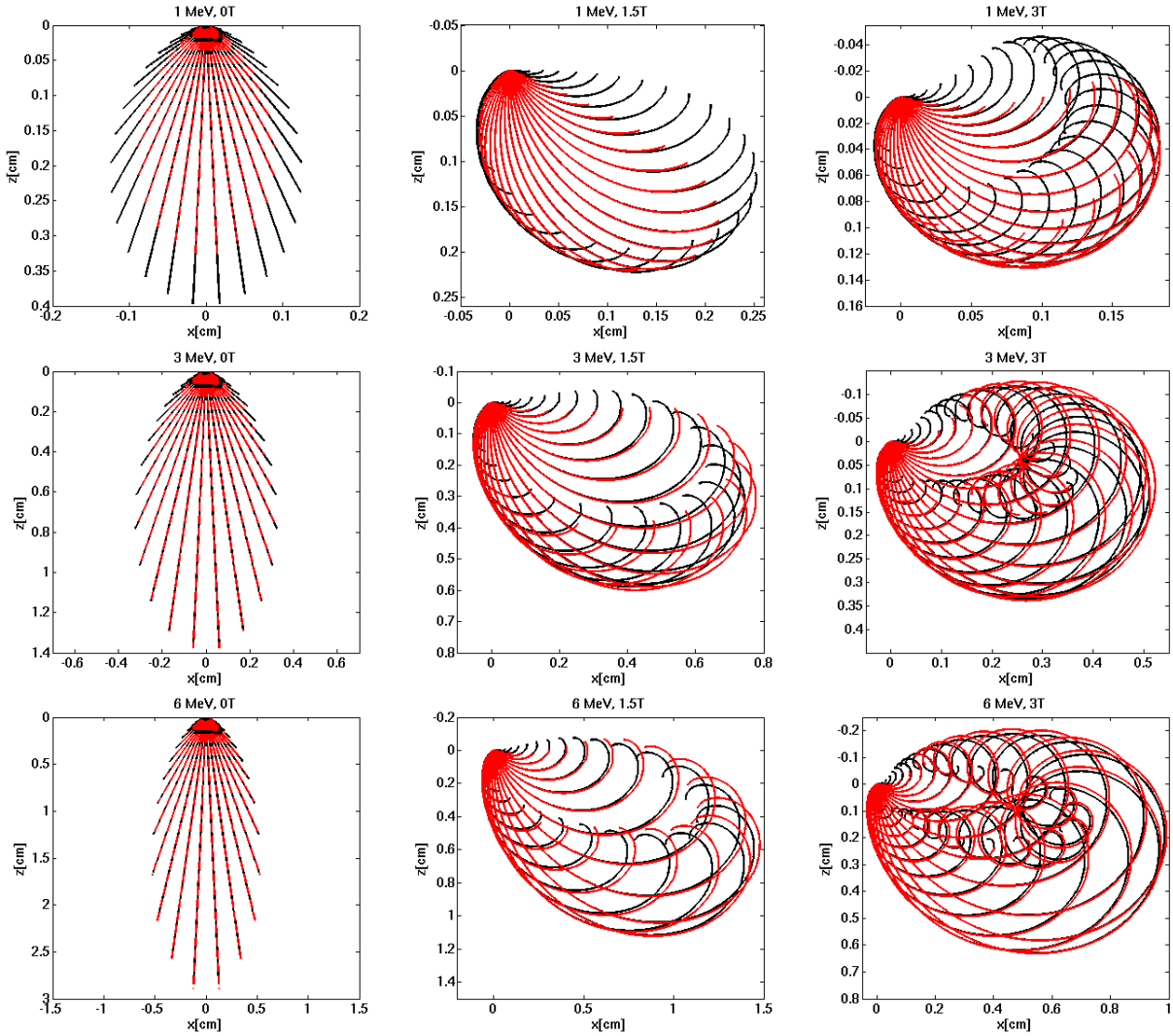


**Figure 6.1** Tracks of the electrons in the plane of incidence, sampled at $\Delta\theta_{el} = 5°$ using the constant stopping power approach (black) and the variable stopping power approach (red). Mind that the scales differ.

Note that in section 6.1.2 below, logarithmic plots of the kernels will further be shown for comparison purposes.

On visual inspection, both the kernels generated using the constant and the variable stopping power are alike, so to avoid redundance, the constant stopping power kernels are not shown here. Difference plots subtracting the kernel with the constant from the kernel with the variable stopping power are displayed in figure 6.3.

For the 3 MeV and 6 MeV kernels, it is observed that the constant stopping power approach yields a slightly higher energy deposition closer to the point of interaction, i.e. where the electrons still have a higher energy, while at the end of the range, usage of the variable stopping power leads to a higher deposition. This is again in agreement with the actual stopping power values (cf. figure A.3).

Between around 600 keV and 6 MeV, the total electron stopping power in water is slightly below 2 MeV/cm which is the value taken for the constant stopping power approach (cf. section 5.1.1). In contrast, outside that range the actual values are higher. So only after the electrons have slowed down below 600 keV, yields the variable stopping power approach higher energy deposition values. For the case of

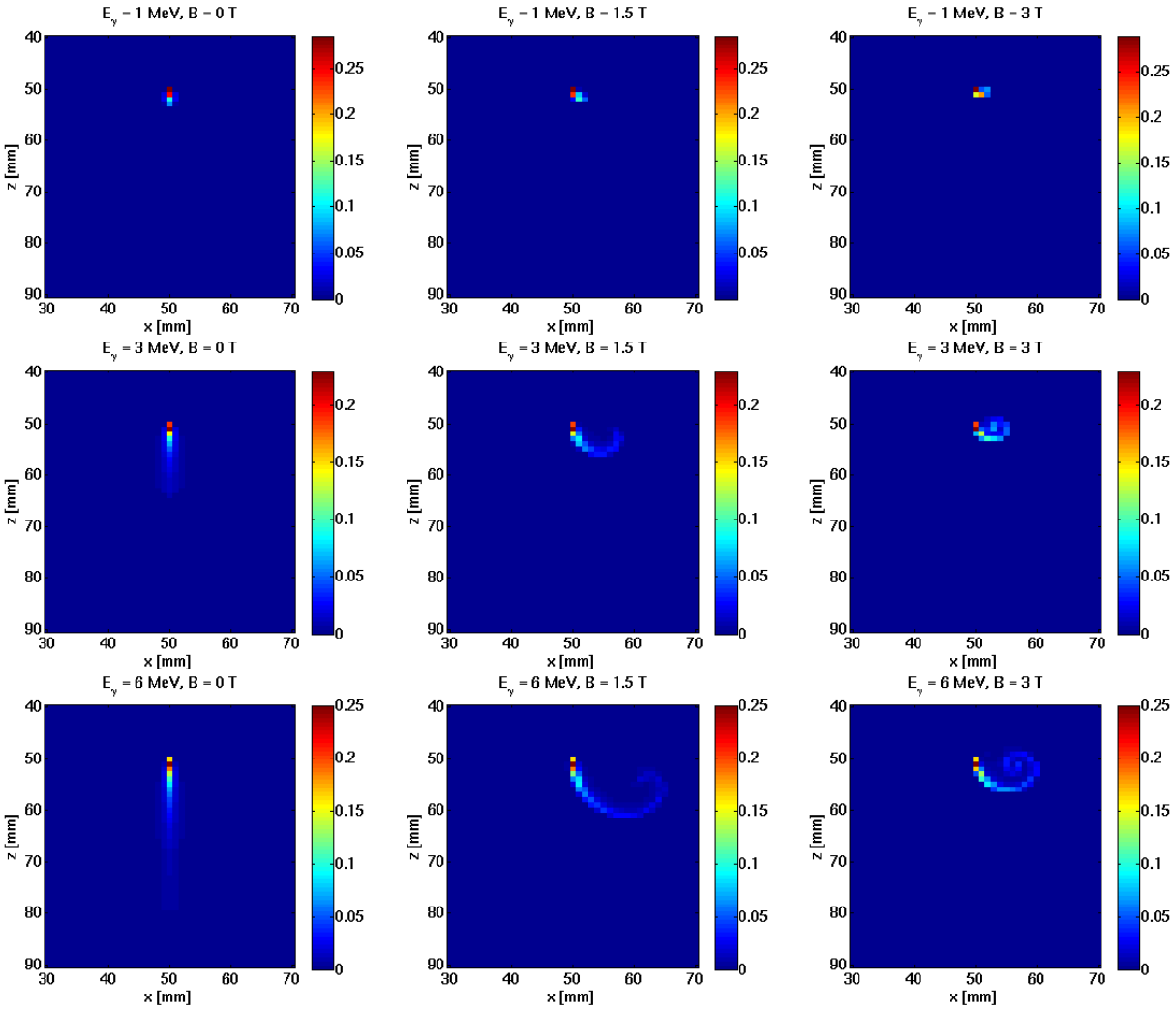


**Figure 6.2** Energy deposition due to photon point interaction in water in MeV, sampled using the variable stopping power approach. The scaling is such that 1 MeV (top), 3 MeV (middle) and 6 MeV (bottom) are deposited in the entire cube, respectively. The voxelsize is $(1\text{ mm})^3$.

1 MeV, all electrons produced have slowed down below 600 keV after maximum 1 mm as described above, and many electrons with lower initial energy values also contribute to the energy deposition, such that here, the variable stopping power approach yields higher values.

Table 6.1 lists the sum of absolute values of energy differences observed in the comparison ($(\sum_i |\Delta E_i|)$) in MeV as well as the number of voxels (n) in which the energy differs, for each combination of photon energy and magnetic field. The number of voxels corresponds approximately to the size of the kernel, in agreement with the differences observed in figure 6.3. The total misplaced energy is highest for the 1.5 T cases, where around 1/6 of the energy is not deposited consistently using the two approaches.

**Table 6.1** Total misplaced energy in MeV and number of voxels n that differ in energy, comparing constant and variable stopping power approach

| | **0 T** | **1.5 T** | **3 T** |
|---|---|---|---|
| **1 MeV** | 0.20 (n=45) | 0.17 (n=28) | 0.24 (n=18) |
| **3 MeV** | 0.29 (n=499) | 0.55 (n=286) | 0.44 (n=134) |
| **6 MeV** | 0.57 (n=2330) | 1.01 (n=1231) | 0.64 (n=533) |

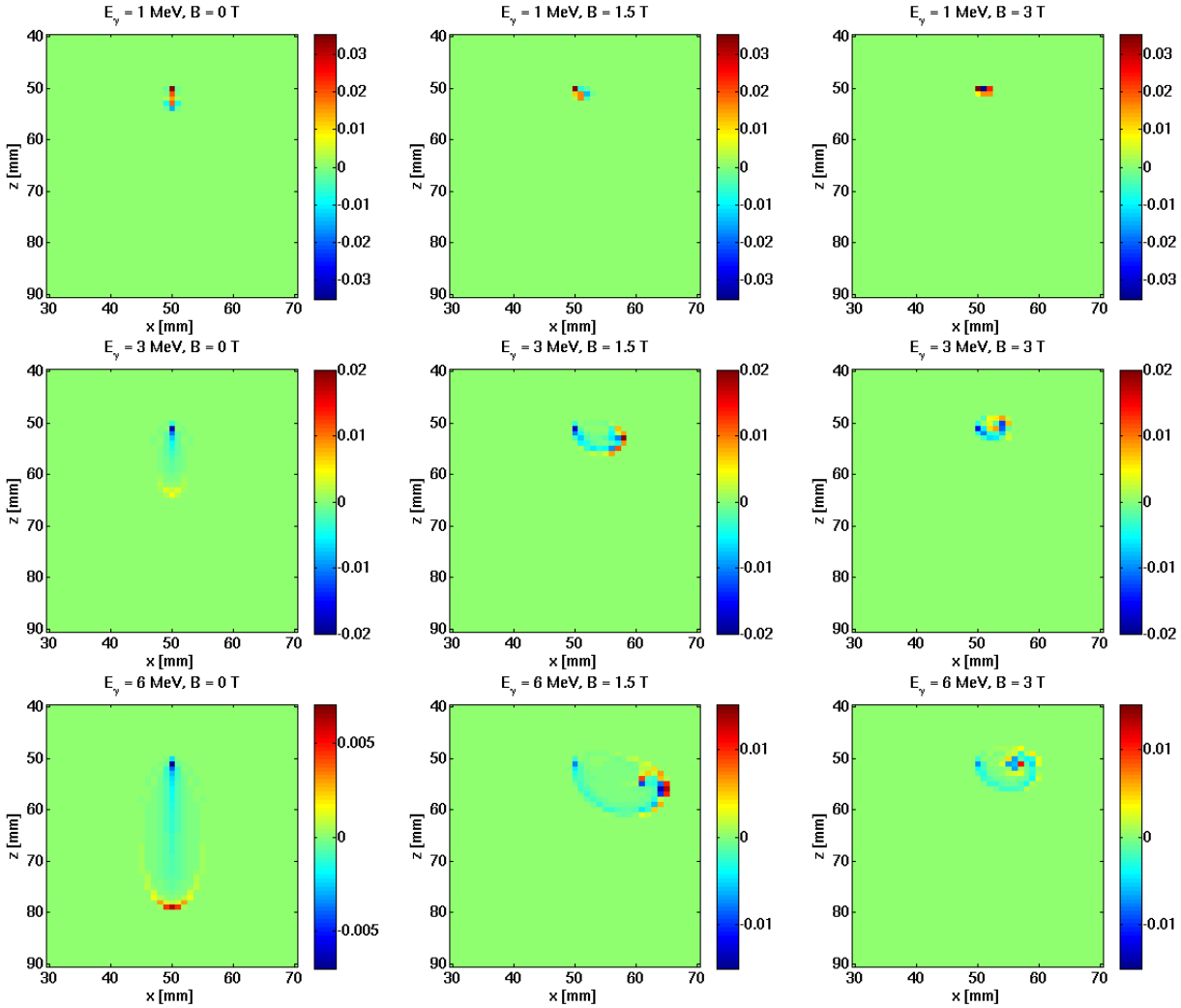


**Figure 6.3** Differences in energy deposition between the two analytical approaches. The kernel generated using the constant stopping power is subtracted from the one with the variable stopping power, such that the values are given in MeV again and can be related to the values in figure 6.2.

### 6.1.2 Analytical approach versus Monte Carlo

For all combinations of photon energy and magnetic field strength, the point kernels computed using the analytical approach show a more pronounced internal structure than their Monte-Carlo generated counterparts. This is shown in figures 6.4 to 6.6 below, using logarithmic plotting such as to display more details. While the full range of values in the analytically sampled kernels is shown to improve visibility of their inner structure, the Monte-Carlo generated kernels have been cut off below $10^{-5}$ to suppress the display of scatter in the more distant voxels.

The Monte-Carlo generated point kernels at 3 MeV, i.e. at the approximate mean energy of a 6 MV linac spectrum compare well with the kernels given in [62] for a 6 MV spectrum, both with respect to dimensions and energy fall-off.

Since scatter is neglected in the analytical approximation, the total dimensions of the kernels generated in this way are significantly smaller. Considering only the region of main energy deposition down to around $10^{-3}$, the dimensions of the magnetically deformed kernels (B=1.5 T, B=3 T) roughly agree, while for B=0 T, the analytically sampled kernels are much longer and narrower.

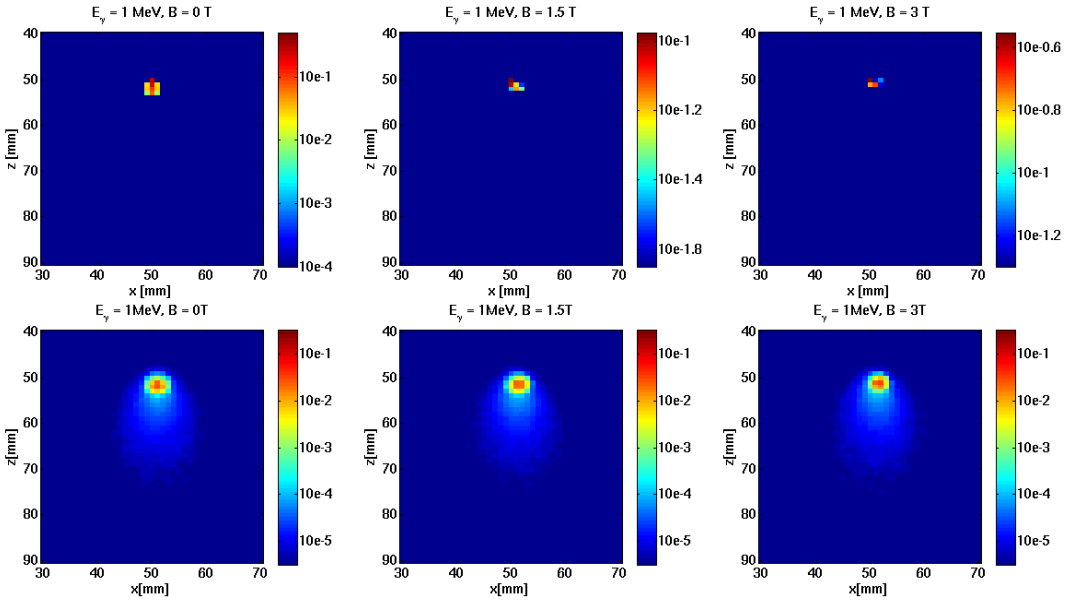


**Figure 6.4** Energy deposition kernels due to a photon point interaction, sampled analytically (top) and simulated using Monte Carlo (bottom) for different magnetic field strengths. The energy of the incident photon was 1 MeV.

It can also be remarked that the Monte Carlo simulated kernels extend into the direction backward with respect to the incident photon which is, besides interactions of Compton photons, also due to backscatter of the electrons produced in the Compton effect. The maximum angle of initial electron motion after a pure Compton effect is slightly below 90°, (cf. section 2 and appendix A). This is why no backward halo is seen in the kernels from analytical sampling. In the Monte-Carlo generated kernels of 6 MeV, 1.5 T and 6 MeV, 3 T in figure 6.6, this backward halo can be seen to be bent to the side opposite to the deflection of the forward electrons.

Observing the significant differences between the analytically generated kernels and those simulated using Geant4 [21][22], and remarking differences in the pencil beams later (cf. section 6.2), kernels were also simulated with a higher resolution of $(0.1\ \text{mm})^3$ for the voxels. For 3 MeV, they are displayed in figure 6.7. It can be seen that the basic structure of a clearly dominant track with respect to energy deposition is preserved and still the differences to the Monte Carlo simulations are significant.

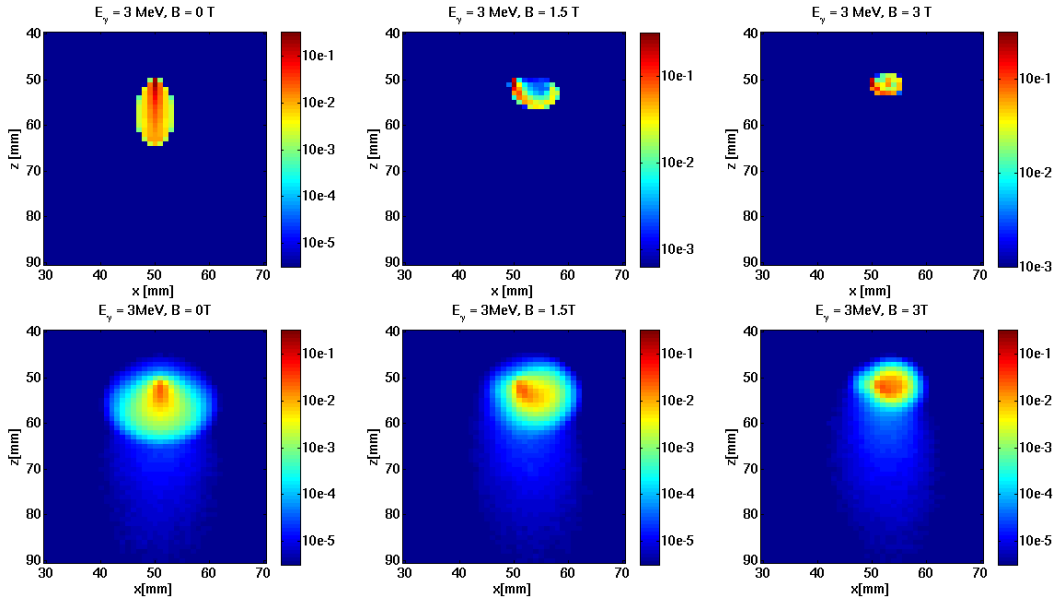


**Figure 6.5** Energy deposition kernels due to a photon point interaction, sampled analytically (top) and simulated using Monte Carlo (bottom) for different magnetic field strengths. The energy of the incident photon was 3 MeV.

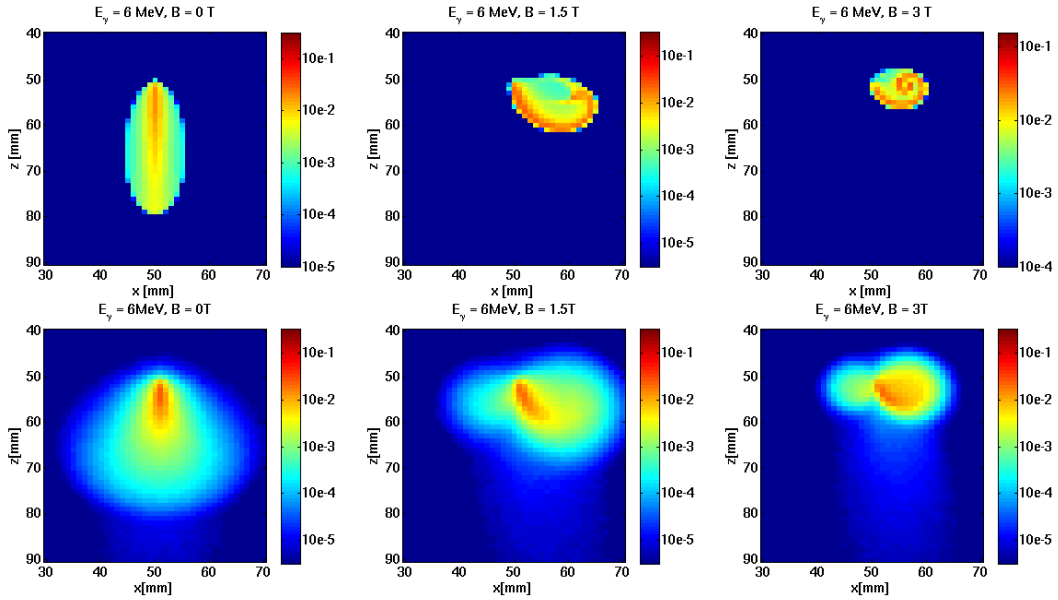


**Figure 6.6** Energy deposition kernels due to a photon point interaction, sampled analytically (top) and simulated using Monte Carlo (bottom) for different magnetic field strengths. The energy of the incident photon was 6 MeV.

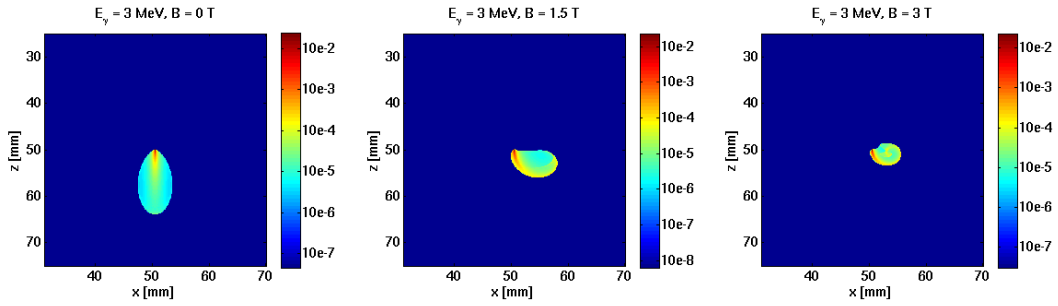


**Figure 6.7** Energy deposition kernels due to a 3 MeV photon point interaction for different magnetic field strengths, sampled analytically on a $(0.1\ \text{mm})^3$ voxel grid.

## 6.2 Pencil Beams in Water

Convolving the Monte-Carlo generated point kernels in depth with the TERMA led to the exact same depth dose behaviour (within numerical uncertainties) as the direct simulation of a narrow incident beam in Monte Carlo. This observation serves as a verification of the convolution method, and in the following, it will not be differentiated between Monte-Carlo simulation of the narrow beam and the result from convolution of the point kernel.

Qualitatively, both the analytical approach using the constant and the approach using the variable stopping power showed the same behaviour, while small quantitative differences were observed. To avoid redundancy, only the results of the variable stopping power approach are shown in the following, since all conclusions apply to both approaches in the same manner.

If no magnetic field is present, the convolution of the analytically sampled point kernels in depth with the TERMA yields rather good agreement with the Monte Carlo simulations. This is shown for 3 MeV and 6 MeV in figures 6.8 and 6.9, which are normalised to the maximum dose value occurring in the data set. In the top rows, the dose distribution in the plane of incidence is displayed for the analytically (defo) and Monte-Carlo simulated (geant) kernels as well as the difference between both (diff). The direction of photon incidence is from the top of the figure. Here already, and in the depth-dose curve in the lower right corner, it can be observed that while in the build-up region, deviations are non-negligible, the rest of the curve agrees well.

A small offset is observed which practically can be overcome by a re-normalisation to a value at a certain depth. The deviations in the build-up region are due to the lack of backscatter present in the analytically sampled kernels. The lower left and middle plots reveal the cross-sectional profiles at 2 cm and 3 cm depth, where both curves coincide rather well.

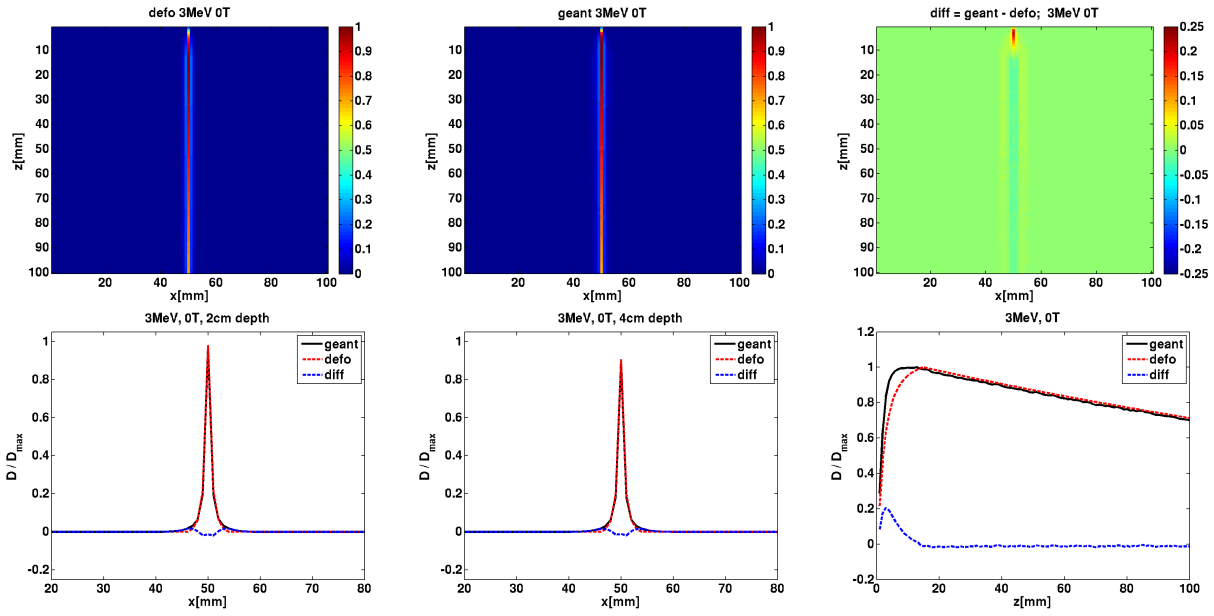


**Figure 6.8** 3 MeV, 0 T. Top: Dose deposition in the plane of incidence from convolving the TERMA with the point kernels generated by the analytical approach (defo), by Monte-Carlo simulation (geant) and the difference between both (diff). Bottom: Cross profiles at two depths and depth-dose curves.

Introducing the magnetic fields, it can be observed in figures 6.10 and 6.11 that while the Monte-Carlo simulated depth dose distribution falls off smoothly on the side the electrons get deflected to, the pencil beam composed from the analytically sampled kernel exhibits an edge. In the cross profiles the edge ap-

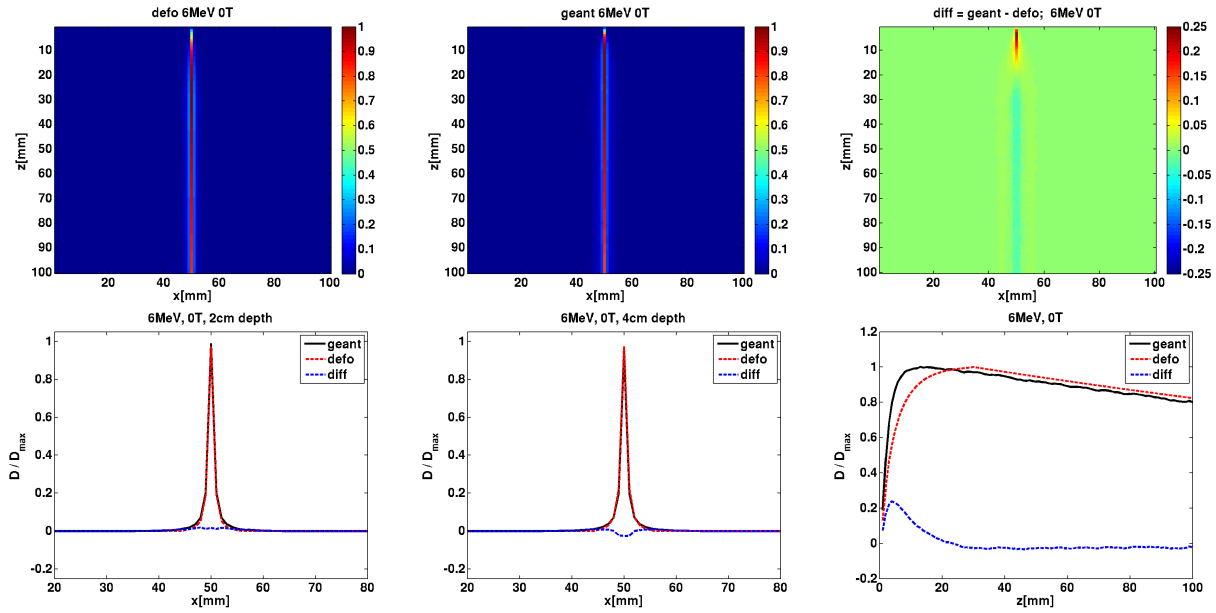


**Figure 6.9** 6 MeV, 0 T. Top: Dose deposition in the plane of incidence from convolving the TERMA with the point kernels generated by the analytical approach (defo), by Monte-Carlo simulation (geant) and the difference between both (diff). Bottom: Cross profiles at two depths and depth-dose curves.

pears as one extra peak (1.5 T) or several extra peaks (3 T, cf. figures 6.12 and 6.13) beside the central axis deposition.

Increasing the resolution does not solve the problem as can be seen in figure 6.14. In the upper row, cross profiles generated on a $(0.1\ \mathrm{mm})^3$ voxel grid are seen for 3 MeV and 0 T, 1.5 T and 3 T (from left to right), where the kernels of figure 6.7 were employed. Even though on first sight, the artifact to the side of the central axis seems to be smaller than in figures 6.10 and 6.12, this is only due to the smaller voxelsizes. Most energy is deposited right on the central axis such that using smaller voxels, the same amount of energy gets deposited in a smaller volume and therefore in less mass, which leads to an increase in dose. So using again maximum normalisation, the other dose values look relatively smaller.

In order to use the kernels on a realistic CT grid resolution of not better than $1\mathrm{mm}^2$ in the imaging planes, it would be necessary to re-bin the high resolution pencil beam dose to a $1\mathrm{mm}^2$ resolution, and the lower row of figure 6.14 shows that doing so, the artifacts from the coarser calculation are back. Cross profiles of 0 T, 1.5 T and 3 T are shown (from left to right), and it need be mentioned that the summation for generation of the plot was only over the cross profile and not three-dimensional as would be required to obtain exact values for comparison.

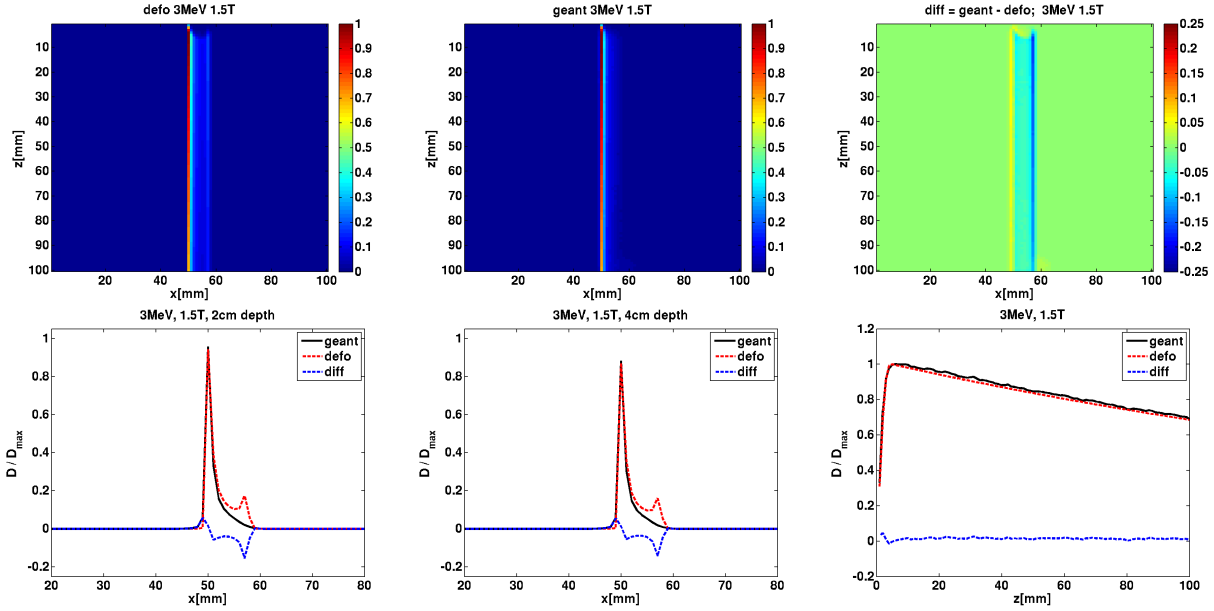


**Figure 6.10** 3 MeV, 1.5 T. Top: Dose deposition in the plane of incidence from convolving the TERMA with the point kernels generated by the analytical approach (defo), by Monte-Carlo simulation (geant) and the difference between both (diff). Bottom: Cross profiles at two depths and depth-dose curves.

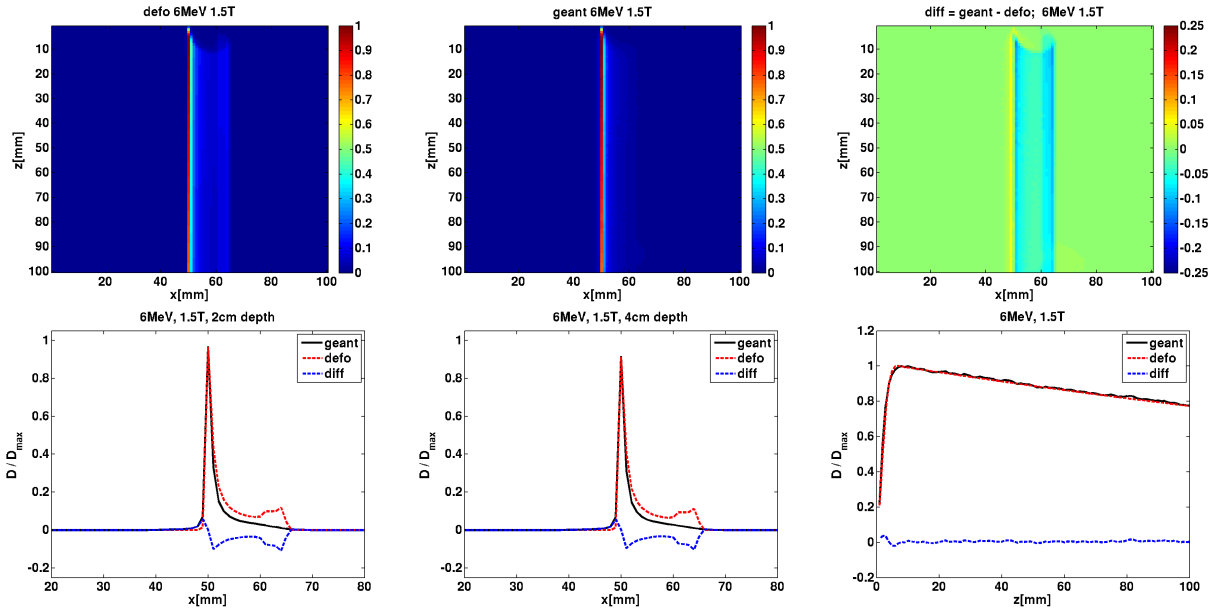


**Figure 6.11** 6 MeV, 1.5 T. Top: Dose deposition in the plane of incidence from convolving the TERMA with the point kernels generated by the analytical approach (defo), by Monte-Carlo simulation (geant) and the difference between both (diff). Bottom: Cross profiles at two depths and depth-dose curves.

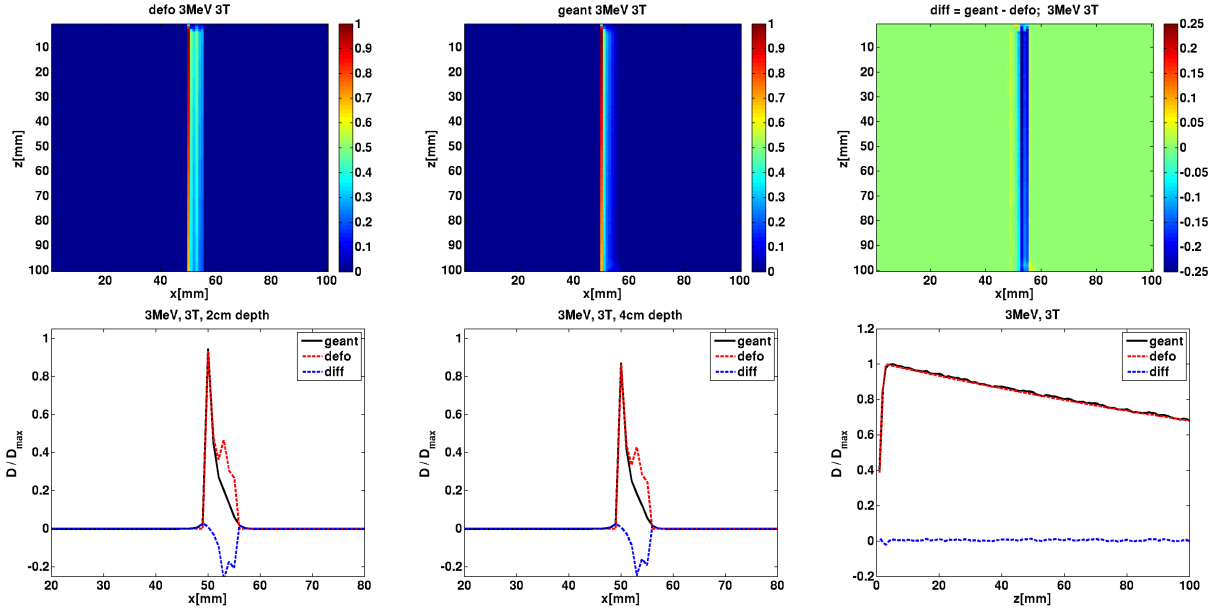


**Figure 6.12** 3 MeV, 3 T. Top: Dose deposition in the plane of incidence from convolving the TERMA with the point kernels generated by the analytical approach (defo), by Monte-Carlo simulation (geant) and the difference between both (diff). Bottom: Cross profiles at two depths and depth-dose curves.

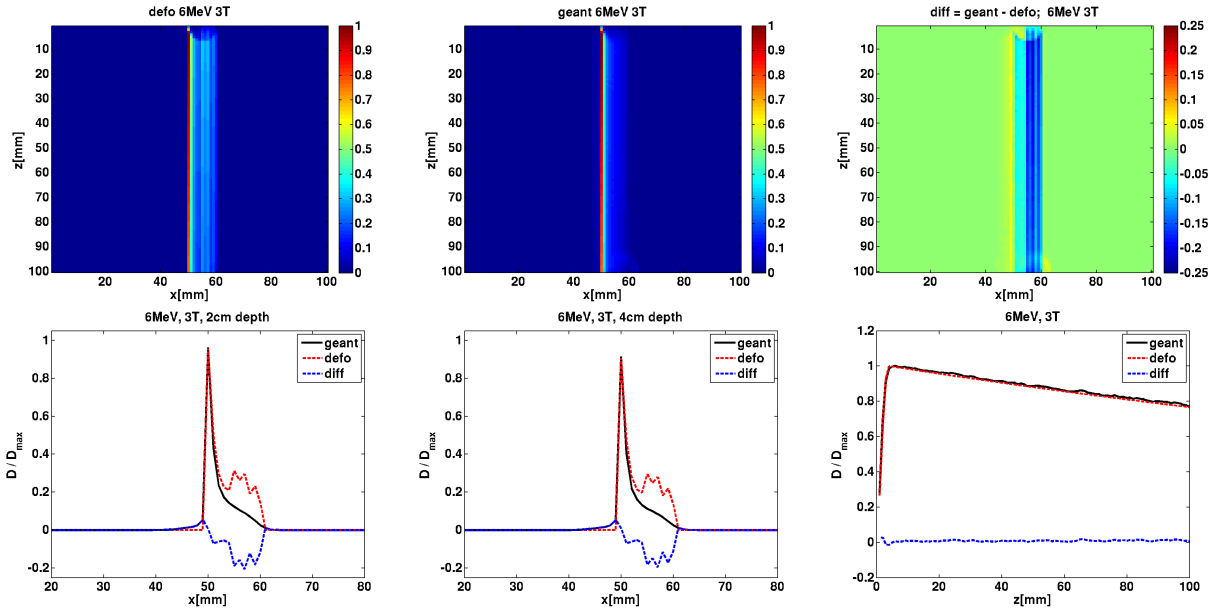


**Figure 6.13** 6 MeV, 3 T. Top: Dose deposition in the plane of incidence from convolving the TERMA with the point kernels generated by the analytical approach (defo), by Monte-Carlo simulation (geant) and the difference between both (diff). Bottom: Cross profiles at two depths and depth-dose curves.

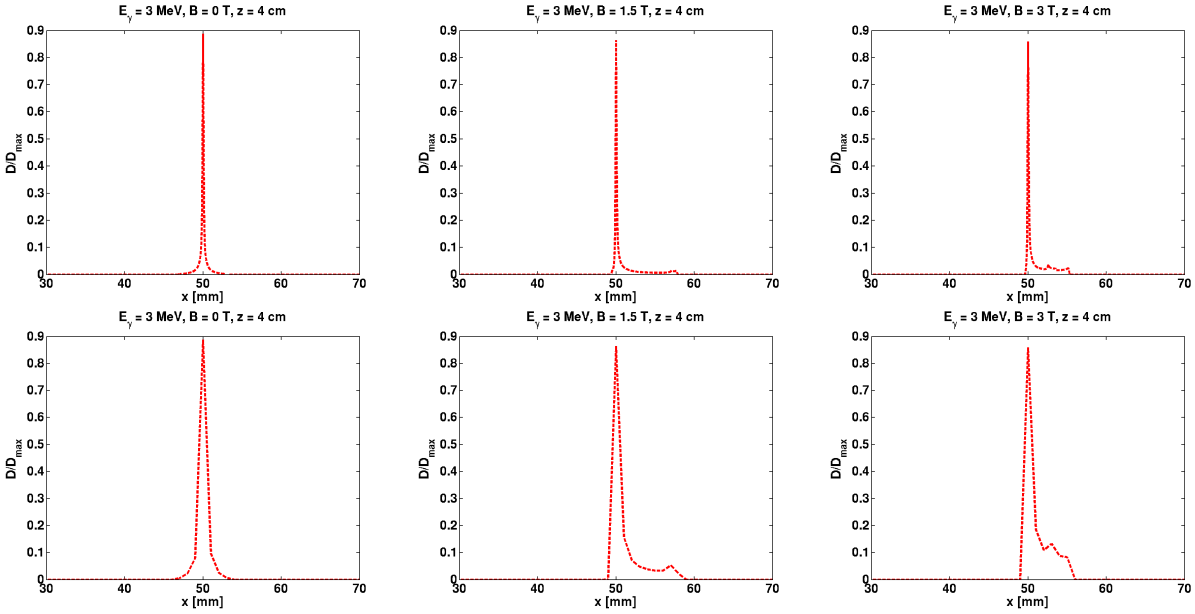


**Figure 6.14** Cross profiles from using 3 MeV variable stopping power kernels generated at a $(0.1\text{ mm})^3$ resolution. Top row: x axis in high resolution; bottom row: re-binned to a 1 mm x-axis resolution. From left to right: 0 T, 1.5 T, 3 T.

# Chapter 7

# Discussion of the Analytical Approach

The approach presented aims at modelling the dose deposition in a magnetic field based on a parameterisation of photon point interaction kernels in terms of the tracks of Compton electrons. On successful modelling, the track information was intended to be used in a method similar to the superposition technique known in photon dose calculation as described in section 3.2.

Point kernels were generated using an analytical approximation with a constant and a variable electron stopping power. Both approximations were compared with each other and with Monte Carlo simulations. The sampling following the analytical approach deposits energy according to the continuous-slowing-down approximation along the tracks of Compton electrons and assumes electron scatter does not play a dominant role with respect to the main dose deposition. Smaller differences were found between the two approximation methods, but a major discrepancy is observed comparing the analytical methods with the Monte Carlo simulations in terms of the fine structure of the kernels. In the analytically sampled kernels, a clear track structure is apparent that is washed out by scatter in the latter ones.

It is not directly evident that this inner structure will have a strong influence on the final dose deposition calculated from it, since in the dose calculation, several kernels will superimpose in close vicinity of each other and can be imagined to potentially add up to a reasonable distribution after all. Therefore, in spite of the findings, the kernels were employed for the creation of pencil beams and the results were again evaluated my means of Monte Carlo simulations.

In the absence of a magnetic field, the pencil beams generated are in good agreement with the Monte Carlo simulations. However, if a magnetic field is applied, the cross profiles of the pencil beams show extra peaks which cannot be ignored. An explanation for the difference in behaviour can be found looking again closely at figure 6.1.

While doing so, it has to be born in mind that the electron tracks of the approximation are only a virtual construct which represent hypothetical csda tracks that the electrons will not follow in reality. Any electron produced under the Compton interaction will actually take a path dominated by multiple scatter processes. Without a magnetic field, these scatter processes are known to produce a rotational symmetric widening of an initially parallel electron beam. This widening can be described by an almost linear increase of the mean square scattering angle until, after 1/3 to 1/2 of the csda range, a state of full diffusion is reached, as the ICRU report 35 [18] describes in section 2.5. The dose deposition due to this scatter behaviour is shown with the help of a Monte-Carlo simulation in the left of figure 7.1, where 3 MeV electrons with identical initial momentum are produced in one point of a water cube.

Now in the case of the 0 T kernel of figure 6.1, the scatter will transform the csda tracks into symmetric clouds of electrons. The subsequent superposition of the kernels is in forward direction, such that the amount of energy virtually lost to the side of one track due to scatter can be thought to be compensated

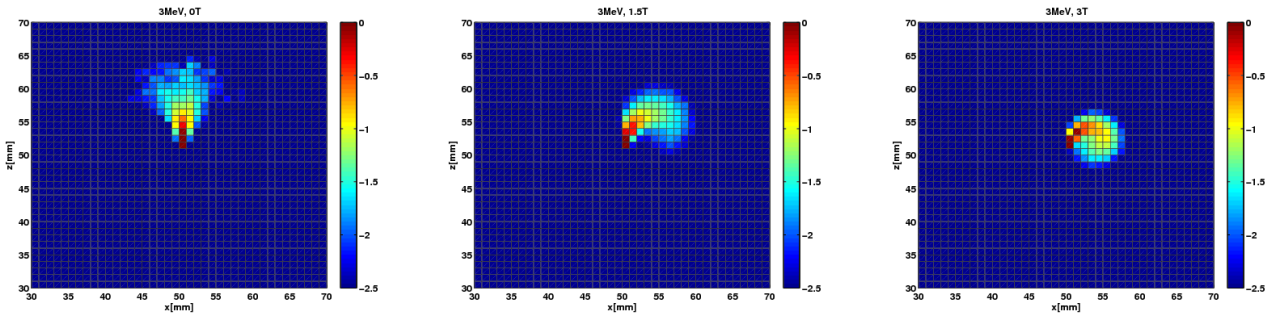


**Figure 7.1** Dose deposition due to 3 MeV electrons in 0 T, 1.5 T and 3 T (from left to right), generated at x=z=51 mm and having their initial momentum in +z direction.

by the scatter to the opposite side from a neighbouring track.

If a magnetic field is present, symmetry of the scatter is lost, as the middle (1.5 T) and right-hand (3 T) plot of figure 7.1 show. While in the figure, only one direction of incidence is shown, the deformation of the scatter halo will again change with varying angle of the direction of electron motion with respect to the magnetic field. Therefore, in the forward superposition of energy deposition kernels in a magnetic field, no compensation of scatter is expected and the irregular inner structure of the point kernels persists when they are convolved into a pencil beam.

Attempts to include the scatter in the analytical approach were not successful, since the change of geometry with relative orientation to the magnetic field poses a difficulty. The approach using the analytical modelling of the Compton electron tracks was therefore rejected as a viable means for dose calculation and another method sought which is described in part III.

# Part III

# Dose Warping

# Chapter 8

# Concept of Point-Kernel Based Warping

In the following, a method is investigated that aims at transforming (warping) the dose distribution as it would be without any magnetic field applied, to the distribution that the same photon fluence would cause in the presence of a magnetic field. If this is possible in a fast step, any existing photon dose calculation algorithm can be used and combined with the subsequent warping, in order to obtain the dose distribution in a magnetic field.

Without a magnetic field and in homogeneous media, the dose distribution $D_0(\vec{r})$ can be described as the convolution of the photon fluence $F(\vec{r})$ with a kernel $K_0(\vec{r})$ as

$$D_0(\vec{r}) = F(\vec{r}) * K_0(\vec{r}) \tag{8.1}$$

which is explained in 3.2. In a magnetic field, the dose deposition due to a photon point interaction will change but still it is assumed that it can be described in an analogous manner. The pencil beam generation from a Monte-Carlo simulated point kernel as described in section 5.3 and 6.2 serves as a verification of this assumption.

The dose distribution in a magnetic field $D_B(\vec{r})$ is then given by

$$D_B(\vec{r}) = F(\vec{r}) * K_B(\vec{r}) \tag{8.2}$$

with $K_B(\vec{r})$ being the convolution kernel in the presence of a magnetic field.

The second assumption is that a transformation from $D_0(\vec{r})$ to $D_B(\vec{r})$ exists and that it can also be described by a convolution, where the transformation kernel will be denoted as $K_0^B(\vec{r})$, such that

$$D_B(\vec{r}) = D_0(\vec{r}) * K_0^B(\vec{r}). \tag{8.3}$$

After Fourier transformation in order to reduce the convolutions to mere multiplications, equations 8.1 and 8.2 are inserted into equation 8.3 to have

$$\begin{aligned} \mathcal{F}\left(F(\vec{r})\right) \cdot \mathcal{F}\left(K_B(\vec{r})\right) &= \mathcal{F}\left(F(\vec{r})\right) \cdot \mathcal{F}\left(K_0(\vec{r})\right) \cdot \mathcal{F}\left(K_0^B(\vec{r})\right) \\ \mathcal{F}\left(K_B(\vec{r})\right) &= \mathcal{F}\left(K_0(\vec{r})\right) \cdot \mathcal{F}\left(K_0^B(\vec{r})\right) \end{aligned} \tag{8.4}$$

where $\mathcal{F}$ denotes the Fourier transform in all three dimensions.

The transformation kernel may therefore be obtained as

$$K_0^B(\vec{r}) = \mathcal{F}^{-1} \frac{\mathcal{F}\left(K_B(\vec{r})\right)}{\mathcal{F}\left(K_0(\vec{r})\right)}. \tag{8.5}$$

if both kernels $K_0(\vec{r})$ and $K_B(\vec{r})$ are known, and where $\mathcal{F}^{-1}$ is the inverse Fourier transform in three dimensions.

Using this kernel in equation 8.3, the dose in a magnetic field can then be computed from the dose in the absence of any field as

$$D_B(\vec{r}) = \mathcal{F}^{-1}\left(\mathcal{F}\left(D_0(\vec{r})\right)\frac{\mathcal{F}\left(K_B(\vec{r})\right)}{\mathcal{F}\left(K_0(\vec{r})\right)}\right), \tag{8.6}$$

which is the same as equation 8.3 but, with the use of fast fourier transforms, reduces computational complexity for numerical evaluation.

Now what remains is the determination of the kernels $K_0$ and $K_B$. In fact, the ratio of the Fourier transforms of any two dose distributions originating from the same fluence pattern and in homogeneous media could be used for determination of $K_0^B(\vec{r})$ since the fluence cancels out in equation 8.4. It is necessary though, that the media be homogeneous throughout the entire region of significant dose deposition.

Therefore, Monte-Carlo simulated point interaction kernels are chosen, i.e. the dose deposition due to photons interacting all at the same point in the medium such that the dimensions of the media can be chosen large enough to ensure homogeneity. The ideal of the corresponding fluence function is a delta function where the point interaction dose would directly give the point interaction kernel as

$$D_{\text{point}}(\vec{r}) = (\delta * K)(\vec{r}) = K(\vec{r}). \tag{8.7}$$

Practically, a Monte-Carlo simulated point deposition kernel will be of finite height, and normalisation has to be ensured by using the same number of primary photons for simulation of $D_{\text{point,0}}$ and $D_{\text{point,B}}$. The technical details of the point kernels generated are described in section 9.1.1.

# Chapter 9

# Application to Homogeneous Media

## 9.1 Material and Methods

### 9.1.1 Input Point Kernels

Photon point interaction kernels were again simulated with the Monte Carlo toolkit Geant4, using the same settings as described in section 5.2, but for different media of the human body. Both point kernels from monoenergetic photons as well as those from the inner part of a 6 MV spectrum, adapted from an implementation by Tacke et al. [67], were generated. The dimensions of the phantom in which the point interaction takes place were chosen such that the dose contribution from the boundaries was expected to be negligible, based on an investigation by Scholz [68] which finds 240 mm to be sufficient in forward direction of the photon, 84 mm sufficient in backward direction, and a radius of around 100 mm to be sufficient at a 90 degree angle with respect to the direction of photon incidence.

The kernels are generated in a 201 mm × 201 mm × 400 mm phantom with $(1\ \text{mm})^3$ resolution, where the point of interaction is at 100 mm depth, resulting in 300 mm medium in forward and 100 mm medium in backward direction. In Geant4, the medium was constructed as a solid block in the detector construction class on which a G4VScoringMesh was overlaid for recording of the deposited dose.

Point kernels were generated for water which serves as a soft-tissue equivalent in the MeV photon range (cf. section 3.2), for inhale lung and for dense bone. The material composition of water was taken from the NIST database incorporated in the Geant4 toolkit (G4_WATER), while the lung and bone composition were adopted from the Geant4 DICOM example ([21][22], example/extended/medical/DICOM) which refers to ICRU report 46 [69] for material definition. The inhale lung material was constructed with a density of 0.217 $\text{g/cm}^3$ and consisted of 9 chemical elements of the mass fraction given in table 9.1 (top). Dense bone was constructed having a density of 1.575 $\text{g/cm}^3$ and with the fractional mass values of 11 elements given in table 9.1 (bottom).

**Table 9.1** Mass fraction of chemical elements in inhale lung (top) and dense bone material (bottom)

| **H** | **C** | **N** | **O** | **Na** | **P** | **S** | **Cl** | **K** |
|---|---|---|---|---|---|---|---|---|
| 0.103 | 0.105 | 0.031 | 0.749 | 0.002 | 0.002 | 0.003 | 0.002 | 0.003 |

| **H** | **C** | **N** | **O** | **Na** | **Mg** | **P** | **S** | **Cl** | **K** | **Ca** |
|---|---|---|---|---|---|---|---|---|---|---|
| 0.056 | 0.235 | 0.050 | 0.434 | 0.001 | 0.001 | 0.072 | 0.003 | 0.001 | 0.001 | 0.146 |

In each material, point interactions were simulated for magnetic fields of 0 T, 0.2 T, 1.5 T and 3.0 T and with $10^8$ photons each, serving as the input kernels $K_B(\vec{r})$ and $K_0(\vec{r})$ for equation 8.5. Since only the ratio of the two kernels is needed and the Fourier transform is linear, no further normalisation is required in that the kernels are generated using the same number of particles, and any scaling factor will cancel out.

The multidimensional Fast Fourier Transform function fftn and its inverse ifftn of MATLAB ([66]) were employed for computation of the required transforms.

### 9.1.2 Verification in homogeneous media

The warping assumption was first tested on the dose deposition from square irradiation fields of 2 cm×2 cm width. For simplicity, the initial momenta of the photons were in parallel, and the fluence was constant over the beam.

$10^9$ photons were generated at a distance of 100 cm from the centre of a solid block of water, inhale lung or dense bone (cf. section 9.1.1), respectively, which was surrounded by air. A source-isocentre distance of 100 cm is a typical value in radiation therapy.

The solid block had dimensions of 101 mm×101 mm×100 mm on which again a G4VScoringMesh of $(1\text{ mm})^3$ resolution was overlaid for dose recording. Observing artifacts at the mesh boundaries, the mesh had to be chosen larger than the material solid such that the simulation results were valid over the full dimensions of the solid block.

The dose deposition from a photon beam incident on this set-up at 0 T, i.e. without any magnetic field applied, was used as original dose deposition $D_0(\vec{r})$ in equation 8.6, and again, the MATLAB ([66]) functions fftn and its inverse ifftn were utilised for Fourier transformation.

The resulting dose deposition $D_B(\vec{r})$ in equation 8.6 was subsequently compared with the Monte-Carlo simulation of a photon beam with magnetic field applied.

In water, both a monoenergetic photon beam of 3 MeV was used as well as photons from a 6 MV spectrum. After observing that the warping assumption principally holds both for the monoenergetic beam and the spectrum in water, the subsequent investigations in bone and lung were only carried out for the 6 MV spectrum. For consistency with the point kernel in verification, the 6 MV energy spectrum was also not varied across the beam as would be the case for a realistic linear accelerator, but the central axis spectrum was used for all photons.

## 9.2 Results

In the following, the Monte-Carlo simulated point kernels used for the warping kernels according to equation 8.5 are shown (generation cf. section 9.1.1) as well as the warping kernels. Further, the simple dose distributions used for testing the warping assumption as given in equation 8.3, and as described in section 9.1.2 are presented. The dose distributions are all simulated with the same number of primary photons ($10^9$) such that quantitative comparison is possible.

Two dimensional dose maps of the $D_0(\vec{r})$ and the transformed dose distribution from $D_B(\vec{r})$ of equation 8.6 are displayed, as well as those of the Monte-Carlo simulated $D_B^{MC}(\vec{r})$ that $D_B(\vec{r})$ is compared with, and the difference between both. Additionally, the respective cross profiles and depth-dose curves are reported.

For a better understanding of the point kernels' dimensions in the different media investigated, electron csda ranges (cf. equation 2.10) and gyroradii in magnetic fields (cf. equation 4.1) are reported in each subsection as a rough illustration.

### 9.2.1 Water and Soft Tissue

The point kernels for one monoenergetic case (3 MeV) and for the 6 MV spectrum are shown in figures 9.1 and 9.2. The dose distribution is normalised to the maximum dose in the kernel, and the colourcoding is logarithmic where values below $10^{-5.5}$ are set to zero for better visualisation. Other monoenergetic kernels were shown in figures 6.4, 6.5 and 6.6.

One cut each through the plane of photon incidence is displayed at x=101 mm, y=101 mm and z=100 mm (left to right) for magnetic fields of 0 T, 0.2 T, 1.5 T and 3 T (top to bottom), respectively. The photon's momentum is in positive z-direction, while the magnetic field has a single non-zero component in y-direction.

It can be observed that the point kernel from the 6 MV spectrum at 0 T appears to be narrower and longer than its 3 MeV counterpart which is due to higher energy components in the photon spectrum, where the distribution of momenta of the Compton electrons is more forward-peaked (cf. figure A.2) and higher energy electrons are produced with longer ranges.

The csda range of 3 MeV electrons in water is given as $r_{csda} = 1.514$ g/cm$^2$ in the ESTAR database [65], while 6 MeV electrons are listed to have $r_{csda} = 3.052$ g/cm$^2$. Dividing by the water density of $\rho = 1$ g/cm$^3$, these correspond to the respective ranges in centimeters.

The gyroradii of the same electrons in vacuum calculated according to equation 4.1 and determining the relativistic correction from $\gamma = E/(m_0c^2)$=3 MeV/0.511 MeV and $\gamma = E/(m_0c^2)$=6 MeV/0.511 MeV, are around $r_g$ =4.9 cm at 0.2 T for a 3 MeV electron and $r_g$ =10.0 cm for a 6 MeV electron.

So it is consistent with these values that in the 0.2 T simulations, effects are minor, since the electrons' trajectories are bent onto a radius of several centimeters, which is more than three times as long as their range, i.e. the curvature observed in the x-z plane is relatively small. It should be mentioned her again that a smooth, curved electron track in water is of course only a theoretical construct, and actually, any electron beam will broaden due to scatter. This was discussed in a little more detail in chapter 7.

At 1.5 T, the gyroradius in vacuum is $r_g$ =0.7 cm for a 3 MeV electron and $r_g$ =1.3 cm for a 6 MeV electron. Therefore if it were not for further scatter and slowing down, the electrons would be able to complete around the third of a circle on the circumference, such that the curvature can be considered significant in terms of its influence on the dose deposition. This is what is observed in the plots of the x-z planes at y=101 mm where the deflection of the central portion of the dose deposition kernel roughly corresponds to

these curvature values.

Also in the y-z and x-y planes of 1.5T, the influence of the magnetic field can be noticed, where electrons and therefore dose are pushed out of the y-z plane at x=101 mm and into the direction of higher x values, and on the other hand, electrons and therefore dose get pushed into the x-y plane at z=100 mm from planes of higher z values.

Gyroradii at 3 T are 0.3 cm for 3 MeV electrons and 0.7 cm for 6 MeV electrons in vacuum. Without further scatter nor slowing down, these electrons would complete the corresponding circular tracks to 70 to 80 % of the circumference, such that it is expected that the electrons are confined much more strongly than in the cases of lower magnetic fields. And indeed, most of the dose is deposited in a small circular structure in the x-z plane, not exceeding $2 \times r_g$ =0.6 cm. As for 1.5 T, electrons and dose get pushed out of the y-z plane at x=101 mm towards higher x-values, and into the x-y plane at z=100 mm from higher values of z.

Since the gyroradii in vacuum merely give a hint towards the plausibility of the point kernels, it may also be worthwhile to compare the shape of the kernels for 1.5 T and 3 T with the hypothetical electron tracks generated and described in part II and displayed in figure 6.1. Even though these tracks also lack the effects of scatter, they are considered closer to the average electron motion than a circular track in vacuum, and may help illustrate the shape of the point kernels.

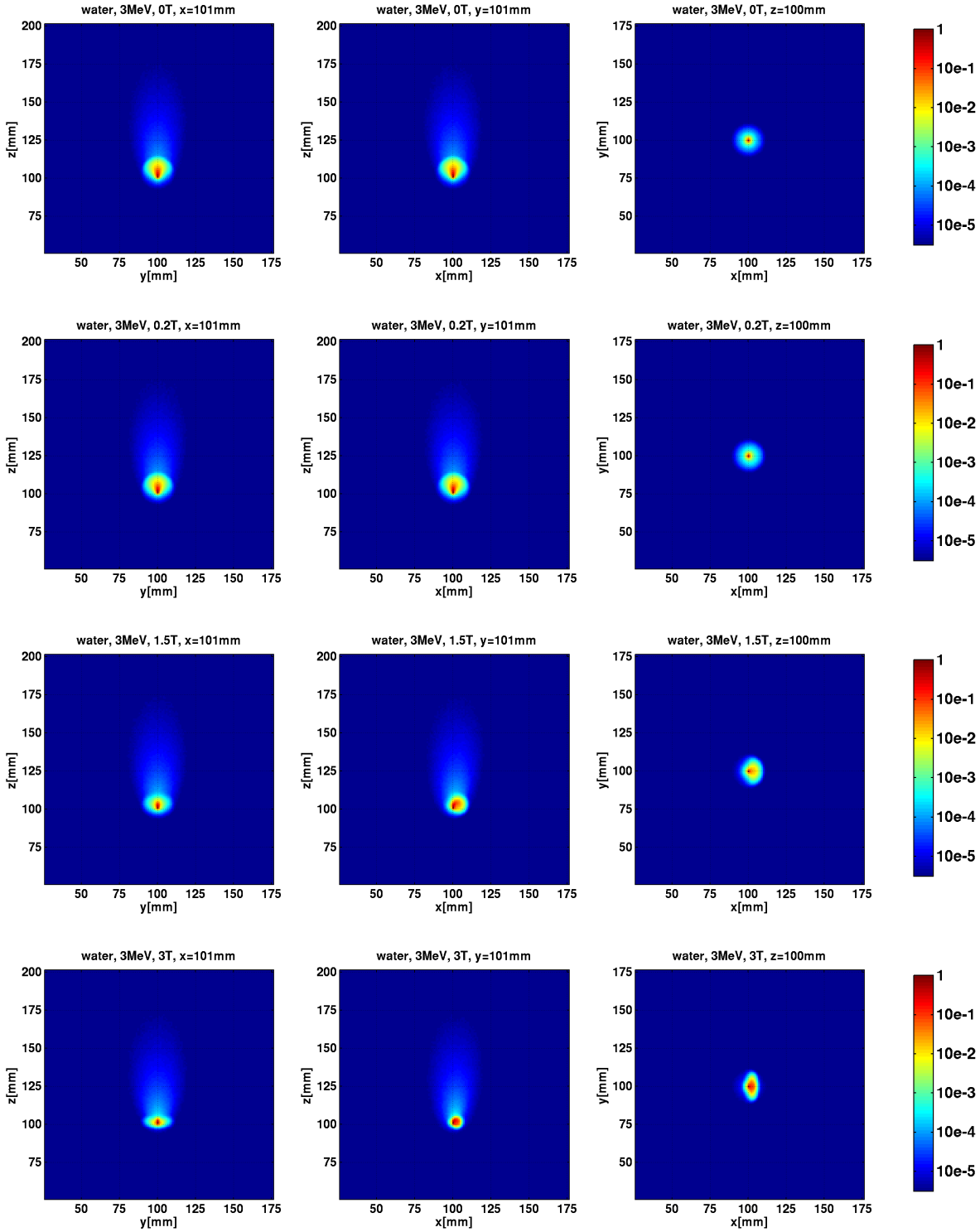


**Figure 9.1** Point kernels for 3 MeV in water.

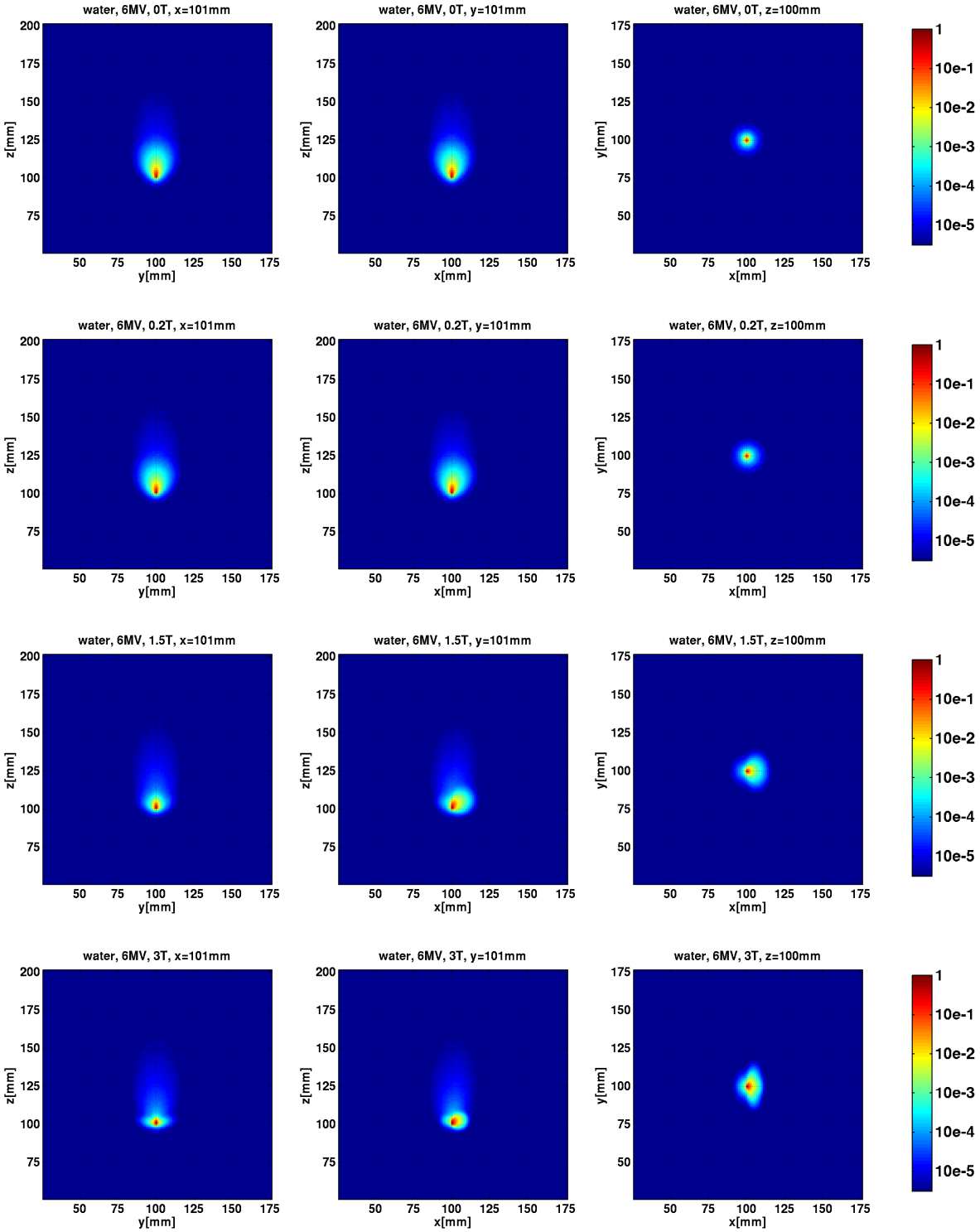


**Figure 9.2** Point kernels for 6 MV in water.

The warping kernels $K_0^B(\vec{r})$ for 3 MeV and 6 MV, determined from the point interaction kernels described above in section 9.1.1, are shown in figures 9.3 and 9.4. The values displayed represent the inverse Fourier transform of the ratio of the Fourier transforms of the two point interaction kernels according to equation 8.5 where no normalisation of the input point kernels was performed (cf. section 9.1.1). As in the point interaction kernels in figures 9.1 and 9.2, values below $10^{-5.5}$ are set to zero.

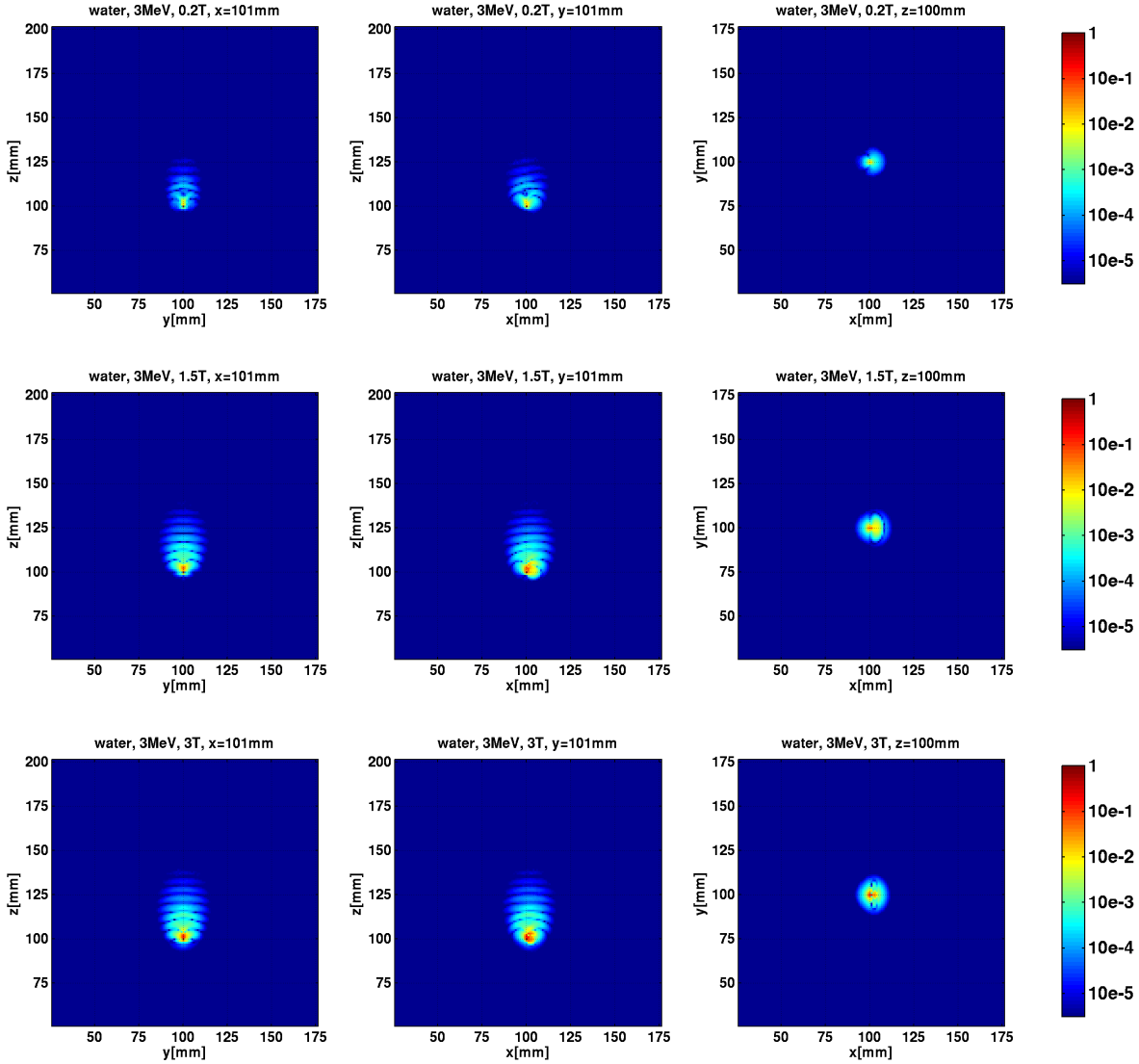


**Figure 9.3** Warping kernels for 3 MeV in water.

It can be noticed that the warping kernels for the 3 MeV photons exhibit rather extended oscillations mainly in z direction which are almost absent for 6 MV. Since the dose fall-off is sharper at 3 MeV due to the kernels being monoenergetic, the oscillations can be attributed to the Fourier transform used in kernel generation. It is consistent that they are less in x and y direction where the point kernel falls off more smoothly.

Otherwise, the warping kernels match the deformations observed in that they are small where little deflection is observed and larger where the effect is stronger.

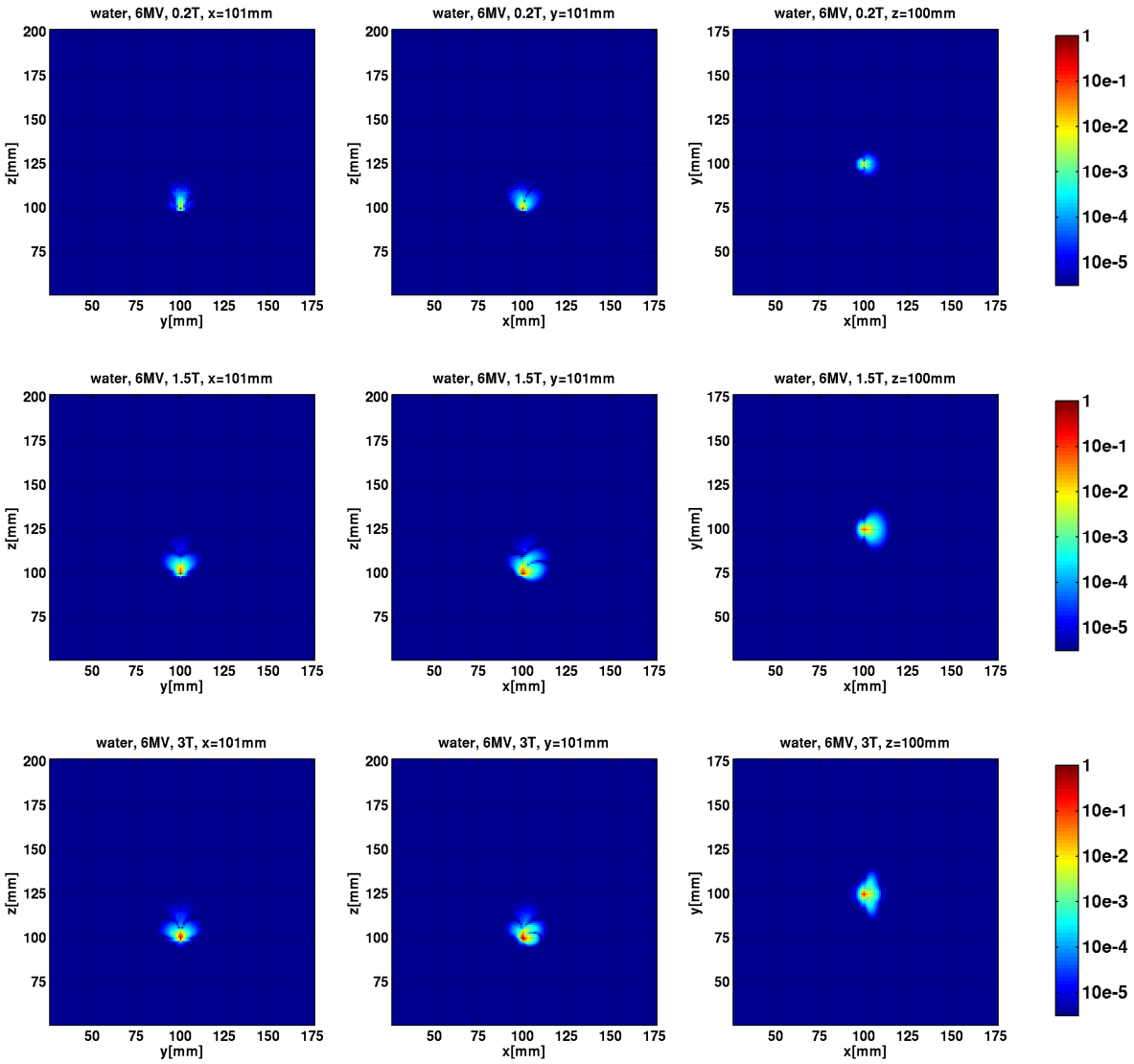


**Figure 9.4** Warping kernels for 6 MV in water.

Results from application of the monoenergetic 3 MeV warping kernels are first presented in the following, while the findings from using a spectral kernel of 6 MV are given further below.

In figure 9.5, 2D dose maps are seen of $D_0(\vec{r})$ (left top), of the transformation result from application of equation 8.6, i.e. of $D_B(\vec{r})$ for 1.5 T (right top), as well as of the Monte Carlo simulation for 1.5 T $D_B^{MC}(\vec{r})$ (left bottom) and of the difference $\left(D_B^{MC}(\vec{r}) - D_B(\vec{r})\right)$. The central plane at y=51 is displayed, where the beam travels in positive z-direction while the magnetic field is in positive y-direction.

Since the water phantom is surrounded by air, an electron return effect (ERE, cf. section 4.3) is observed at the exit surface of the beam in the Monte Carlo simulation which is also the prominent feature in the difference map.

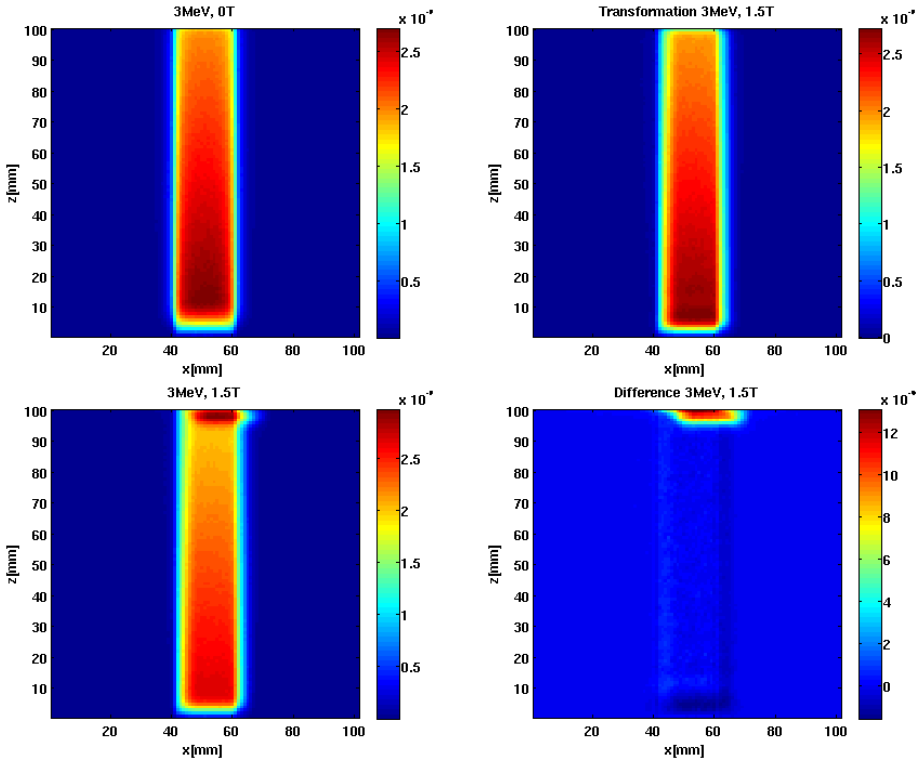


**Figure 9.5** 3 MeV water kernel in water; left the two Monte Carlo simulations (top 0 T, bottom 1.5 T), right warping result (top) and difference to Monte Carlo (bottom)

Also in the depth-dose profile through x=y=51 as seen in figure 9.6 (left), the ERE can clearly be noticed in the dose from the Monte Carlo simulation at 1.5 T, shown as a dashed red line. The warping result is represented by a black solid line, and it can be observed that except for the ERE, it coincides well with the Monte Carlo simulation. In blue, the $D_0(\vec{r})$ profile is shown as a reference.

It can also be seen that the dose maximum of both the simulation in the magnetic field and the warping result is at shallower depth than at 0 T, which is consistent with the findings reported by Raaymakers et al. in 2004 [27]. In this depth-dose maximum, a small deviation between $D_B(\vec{r})$ and $D_B^{MC}(\vec{r})$ is observed.

The same figure displays the cross profiles at depths 50 mm and 70 mm, which also agree very well except for some statistical noise in the Monte-Carlo simulations. Compared with the dose profile at 0 T, the profiles also change shape and get more rectangular.

The 2D dose maps for the warping to 3 T are omitted here since they would not reveal any qualitative difference to the 1.5 T cases. There as well, the ERE constitutes the most significant difference. However, from the depth-dose curve and the cross profiles displayed in figure 9.7 it can be seen that at any given

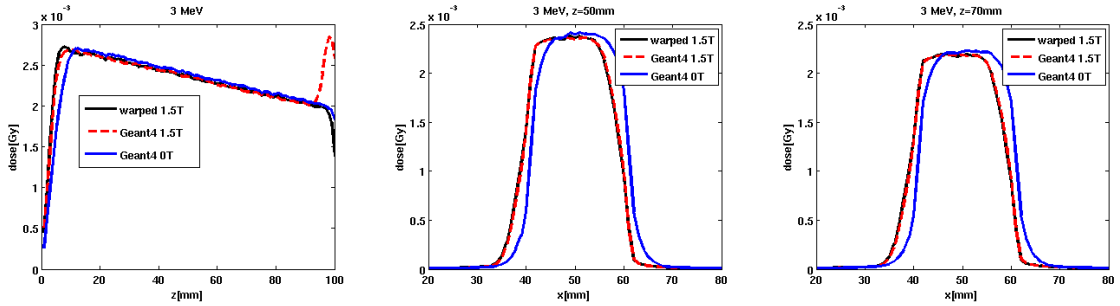


**Figure 9.6** Water, 3 MeV. Depth-dose profile (left) and cross profiles at two different depths of the Monte Carlo simulation ('Geant4', red-dashed) at 1.5 T and the warping result (black). The profile at 0 T (blue) is given for comparison.

depth beyond the depth-dose maxima, the dose deposited in a 3 T magnetic field is lower than for 0 T by around 4%.

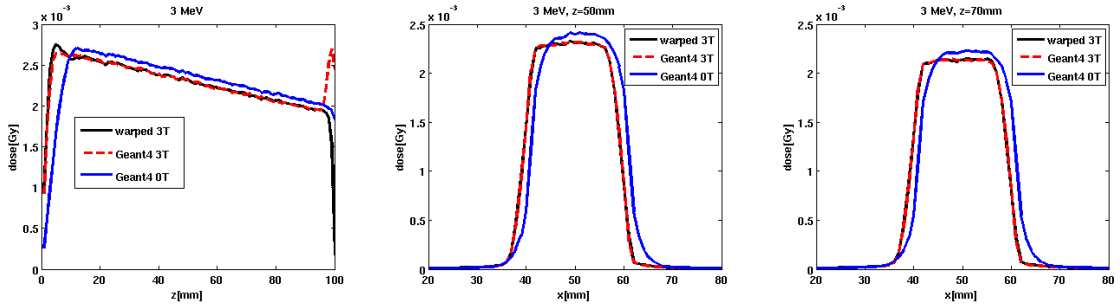


**Figure 9.7** Water, 3 MeV. Depth-dose profile (left) and cross profiles at two different depths of the Monte Carlo simulation ('Geant4', red-dashed) at 3 T and the warping result (black). The profile at 0 T (blue) is given as a reference.

This is consistent with the depth-dose maxima being at a shallower depth when a magnetic field is present. More energy is actually deposited further 'upstream' in the photon beam since the secondary electrons released by the Compton interaction are bent sideways and even back to some extent. Therefore the electrons do not transport their energy primarily downstream as for 0 T, but to the side. This behaviour is also evident from the point kernels (figures 9.1 and 9.2 above).

Looking at the corresponding plots for the 6 MV spectrum in figures 9.8 and 9.9, observations are very similar to the monoenergetic 3 MeV results.

However, the difference between $D_B(\vec{r})$ ('warped') and $D_B^{MC}(\vec{r})$ ('Geant4 1.5 T', 'Geant4 3.0 T') at the dose maximum is more pronounced for the 6 MV spectrum with respect to the 3 MeV monoenergetic beam, while dose from the ERE is lower. What is more, the cross profiles are less rectangular: on the beam edge the electrons get deflected away from (x=60 mm), there is a smooth fall off.

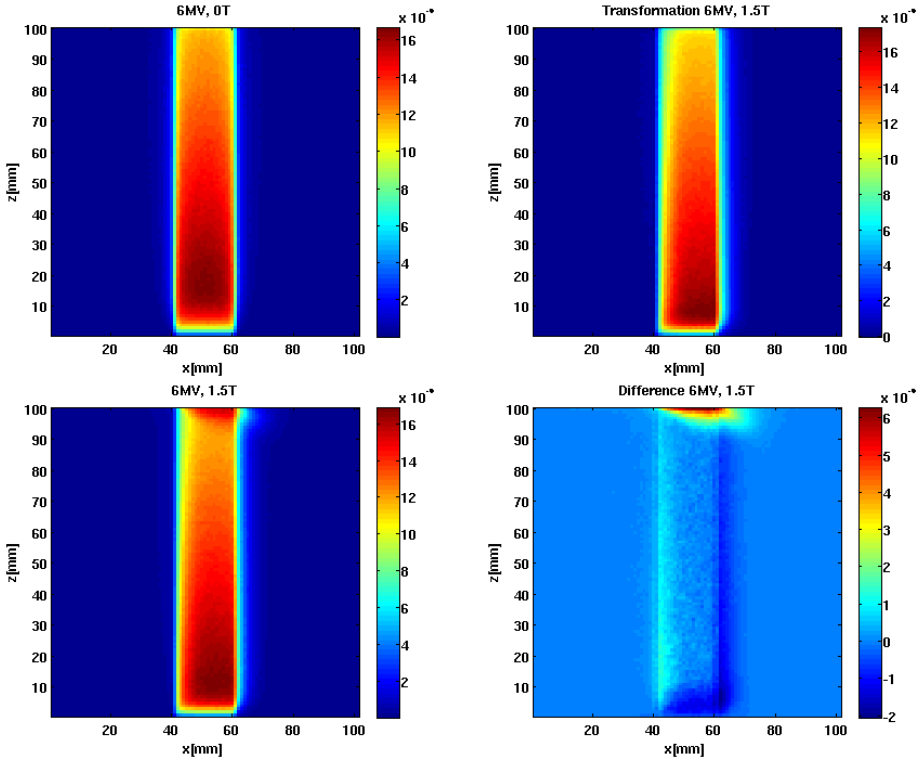


**Figure 9.8** 6 MV water kernel in water; left the two Monte Carlo simulations (top 0 T, bottom 1.5 T), right warping result (top) and difference to Monte Carlo (bottom)

This effect is due to the different ranges of secondary electrons resulting from the different incident photon energies in the spectrum. While electrons with higher energies get transported further into the centre of the beam, electrons with lower energies reach the end of their range earlier and the energy gets deposited more locally.

Close to x=60 mm, there is only contribution from low energy electrons that were generated rather close-by, whereas towards the centre of the beam, contributions from locally generated electrons and from higher energy electrons created further away superimpose. So very similar to the build-up effect of a conventional photon depth-dose curve which is also broader in case of irradiation with a spectrum, a smooth increase of dose is observed, but in this case perpendicular to the direction of incidence of the beam.

The increasing extension of the point kernels with increasing energy of the incident photons was presented in figures 6.4, 6.5 and 6.6 above.

### 9.2.2 Bone

The point interaction kernels in bone from a 6 MV photon beam are displayed in figure 9.10 for planes through x=101 mm, y=101 mm and z=100 mm (left to right) and magnetic fields of 0 T, 0.2 T, 1.5 T

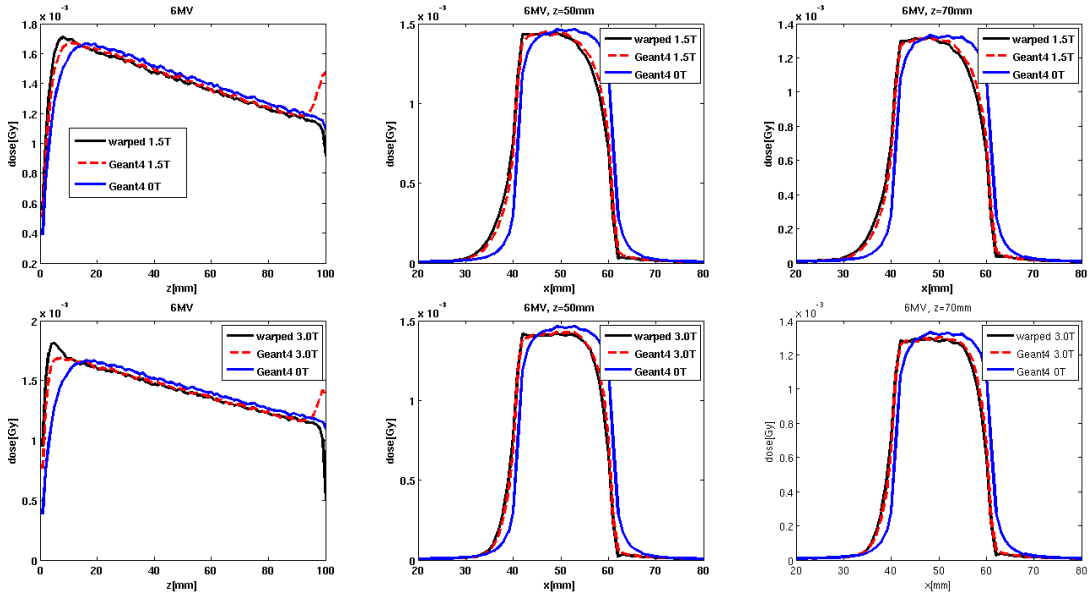


**Figure 9.9** Water, 6 MV. Depth-dose profiles (left) and cross profiles at two different depths of the Monte Carlo simulation ('Geant4', red-dashed) at 1.5 T (top) and 3 T (bottom) and the respective warping results (black). The profiles at 0 T (blue) are given as a reference.

and 3 T (top to bottom). The colourcoding is again logarithmic, where the values are normalised to the maximum dose and values below $10^{-5.5}$ are set to zero.

The dose deposition is very similar to the situation in water: Hardly any effect is observed at 0.2 T, while deformations are significant for 1.5 T and 3 T. In general, the kernels are slightly smaller than their water equivalents that were shown in figure 9.2 above. This may be explained by the smaller range of the secondary electrons in bone compared with water.

For 3 MeV, the csda range (cf. equation 2.10) in cortical bone is given in the ESTAR database [65] as $r_{csda} = 1.671$ g/cm$^2$ which corresponds to an actual range of $r_{bone} = 1.061$ cm when dividing by $\rho = 1.575$ g/cm$^3$. At 6 MeV, the corresponding values are $r_{csda} = 3.335$ g/cm$^2$ and $r_{bone} = 2.117$ cm. Therefore the actual range in bone is roughly 2/3 of the range in water which explains the smaller point interaction kernels.

What is more, the higher effective Z in bone leads to a faster increase of the mean square scatter angle of the electrons (cf. chapter 2 of [18]), such that the effect of scatter is stronger and the dose is less confined to the centre of the kernel.

The shorter electron range and the more prominent scatter lead to less electrons and therefore dose being pushed out of the y-z plane at x=101 mm to higher values of x, and being pushed into the x-y plane at z=100 mm from higher values of z, compared with the situation in water.

Consequently, the warping kernels in bone displayed in figure 9.11 are also smaller in size than the warping kernels in water which were shown in figure 9.4 above.

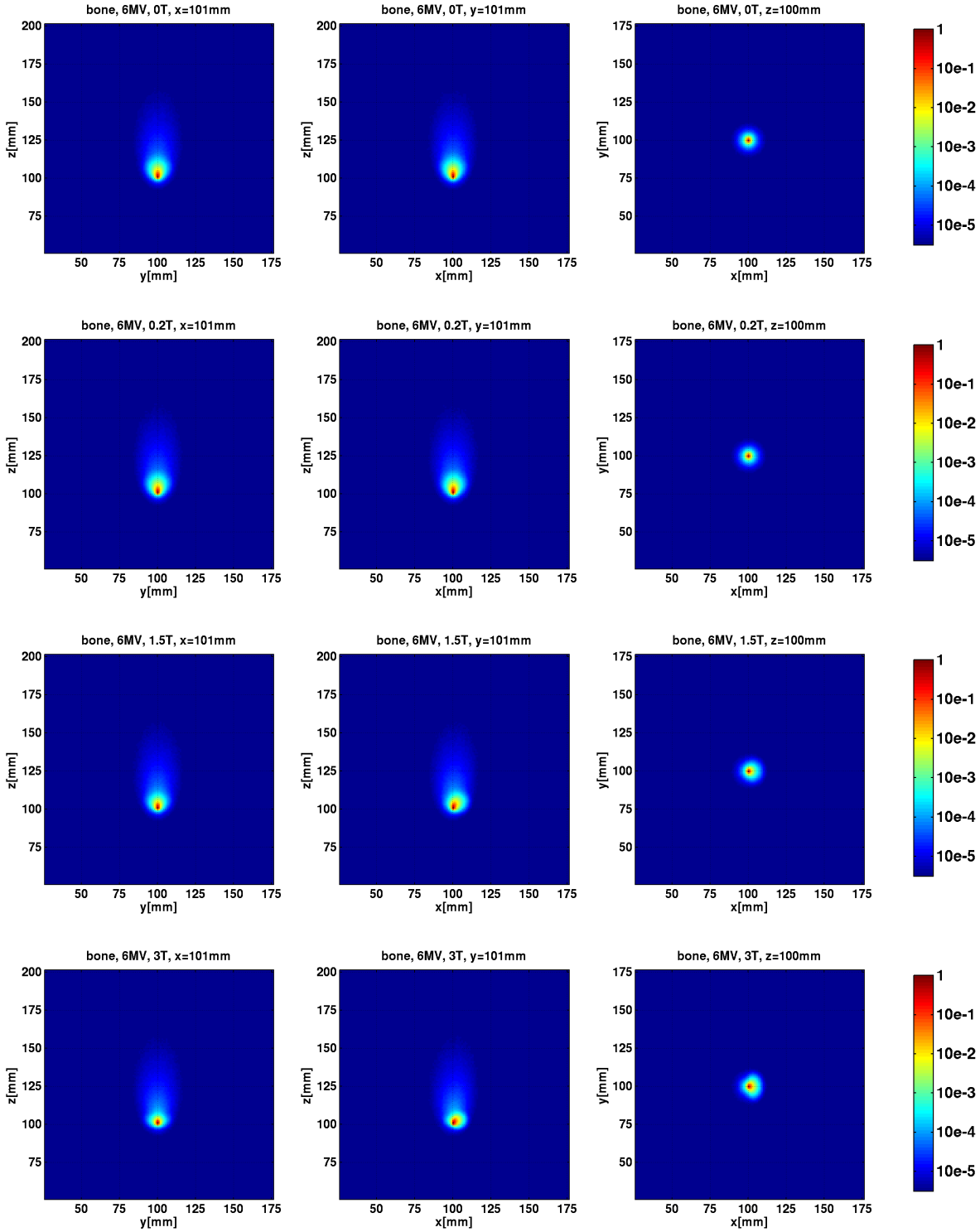


**Figure 9.10** Bone point kernels for 6 MV.

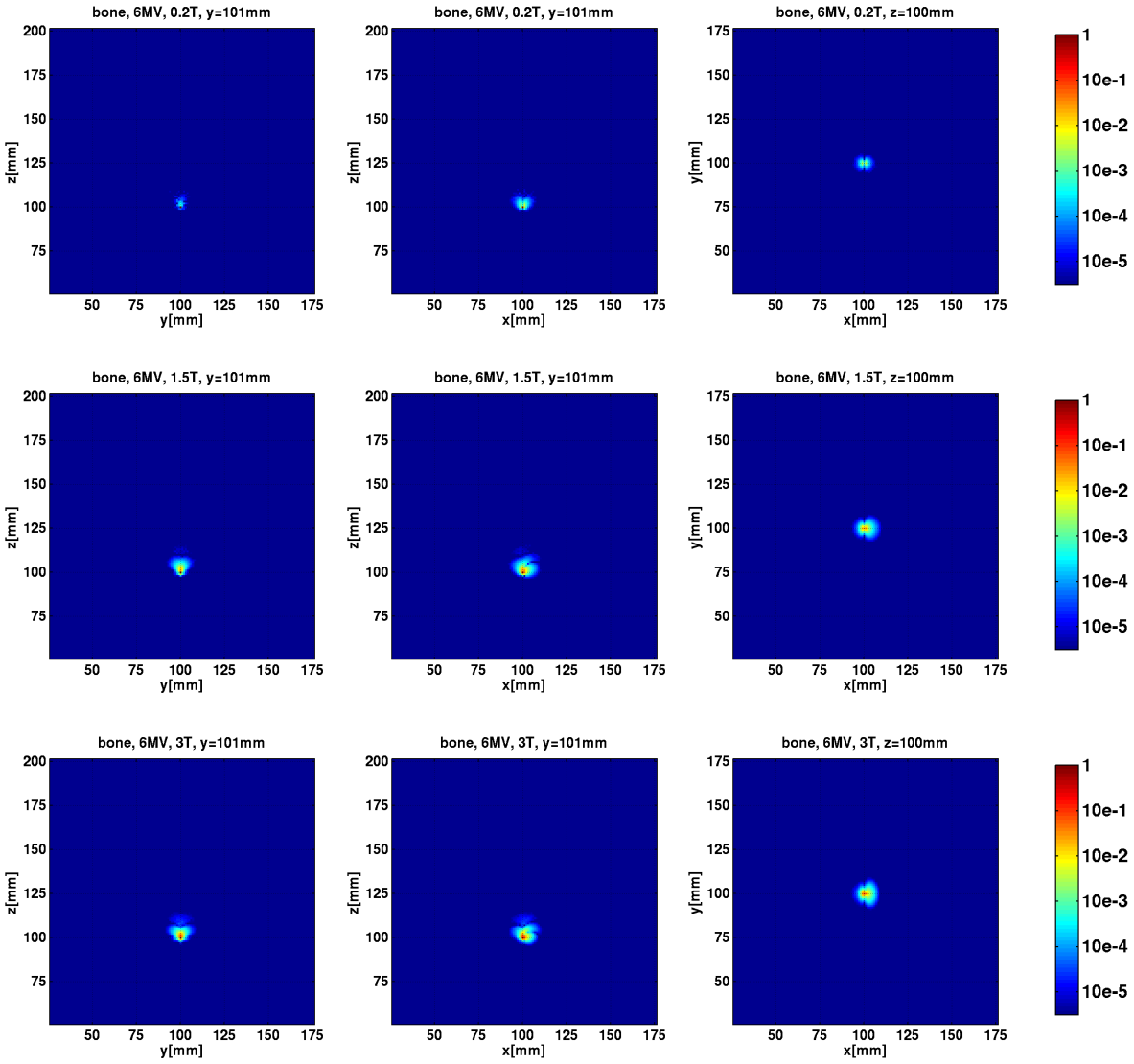


**Figure 9.11** Bone warping kernels for 6 MV.

Overall, however, differences between the water and the bone kernels are not very pronounced, and hence, the 2D dose maps of the bone simulations and of warping using the bone kernels are very similar to the water results reported above. In order to avoid redundancy, only the depth-dose profiles and cross sectional plots are shown here in figure 9.12. It can be seen that the overall effect of the magnetic field is smaller, and that especially for 0.2 T, the deviation is in the same order of magnitude as the statistical noise on the simulations.

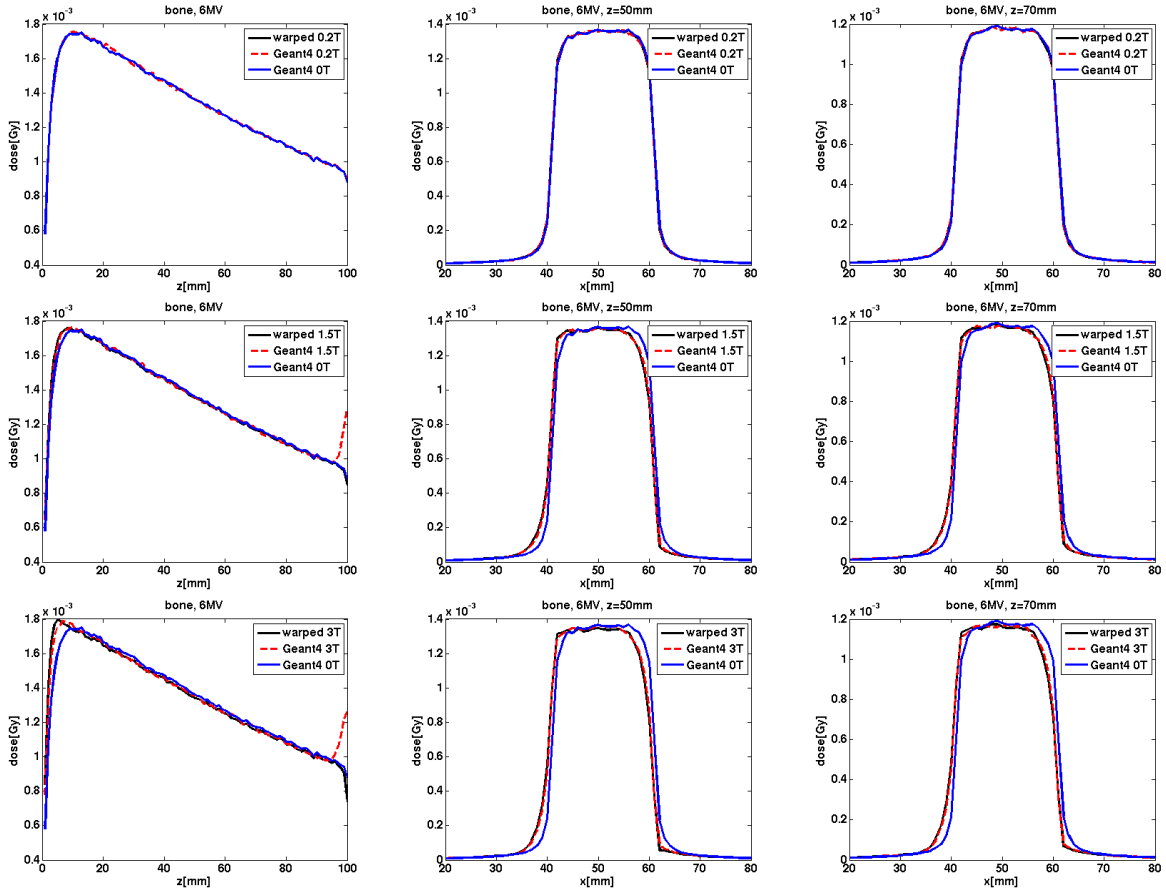


**Figure 9.12** Bone, 6 MV. Depth-dose profiles (left) and cross profiles at two different depths of the Monte Carlo simulation ('Geant4', red-dashed) at 0.2 T, 1.5 T and 3 T (top to bottom) and the respective warping results (black). The profiles at 0 T (blue) are given as a reference.

### 9.2.3 Lung

The point kernels in lung are displayed in figure 9.13, where the magnetic field again varies from top to bottom. Effects of the magnetic field are much stronger than in water and bone, and especially for the higher magnetic fields, severe deformations are observed in all dimensions of the kernels.

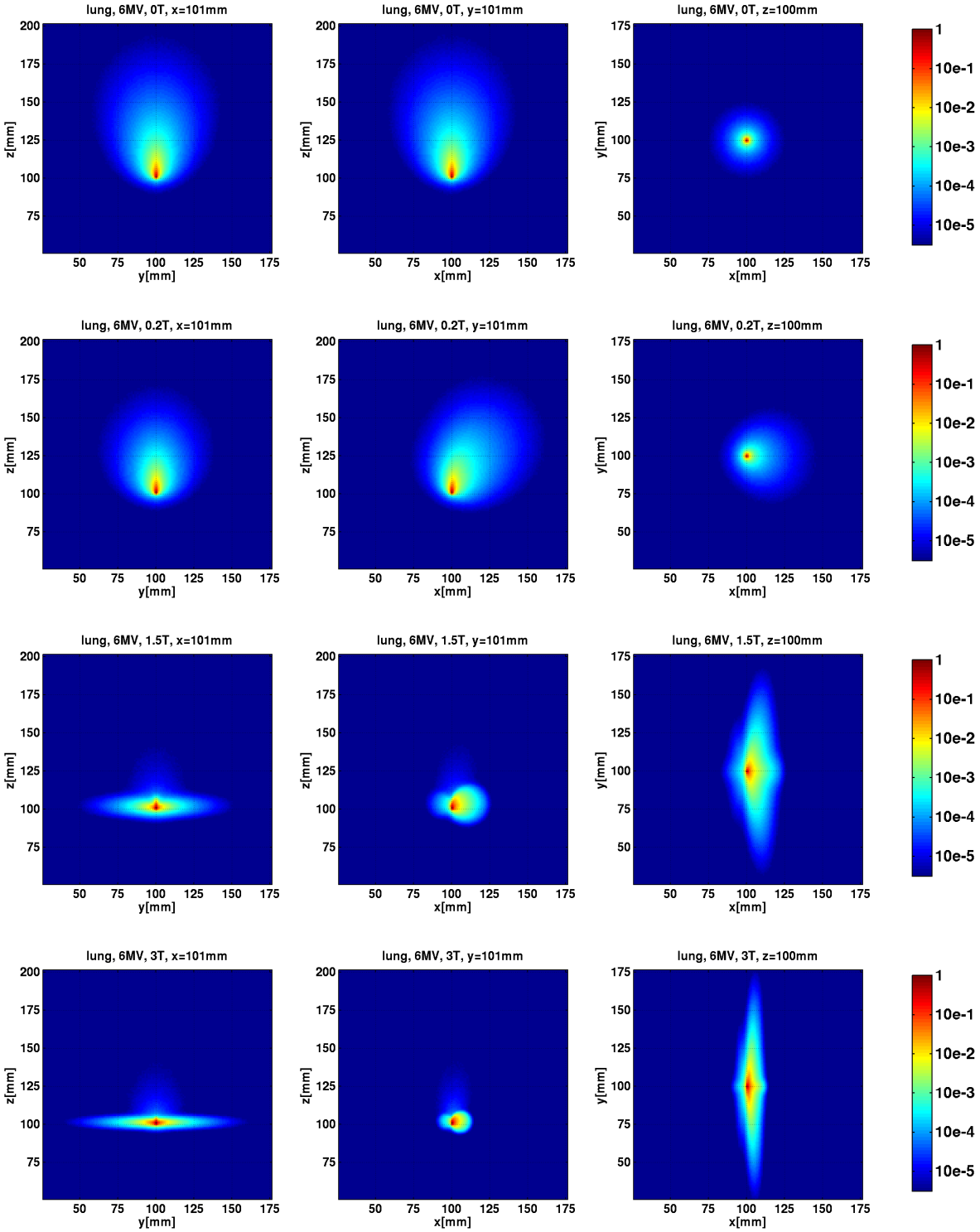


**Figure 9.13** Lung point kernels for 6 MV.

Looking first at the centre column of plots, i.e. the x-z plane in which the electron deflection takes place since the magnetic field is in y direction, a large difference in kernel size is remarked depending on the field strength. While the kernels are very extended at 0 T and 0.2 T, they become rather small at 1.5 T and 3 T.

The csda range (cf. equation 2.10) for 'Lung ICRP' is given as $r_{csda} = 1.532$ g/cm$^2$ for 3 MeV in the ESTAR database [65], and dividing it by the density of $\rho = 0.217$ g/cm$^3$ used in the lung simulations, the range of 3 MeV electrons is expected to be around 7 cm, while for 6 MeV with $r_{csda} = 3.088$ g/cm$^2$, the range is more than 14 cm. This explains the forward extension of several centimeters at 0 T.

The gyroradii (cf. equation 4.1) for 3 MeV if there were no matter present, would be around 5 cm for 0.2 T, 7 mm for 1.5 T and 3 mm for 3 T (cf. section 9.2.1). For 6 MeV, the corresponding gyroradii would be 10 cm, 13 mm and 7 mm, respectively.

These values serve as a good indication of why a curvature of several centimeters radius is observed in the point dose deposition in a magnetic field of 0.2 T while at the higher magnetic fields, much smaller circular patterns are seen. At 0.2 T, the point deposition kernel is merely deformed since the radii of the deflection that the secondary electrons are subject to, are in the same order of magnitude as the electron ranges in lung tissue.

However, at 1.5 T and 3 T, electron motion in the x-z plane is confined to radii of several millimeters, such that beyond the small circular patterns, no dose is deposited by secondary electrons, except for some scatter.

The full picture becomes clear from the plots of the y-z and x-y plane. While the electron motion is restricted in the directions perpendicular to the magnetic field, they do not experience any force in y direction. When they are produced in Compton interaction, they therefore basically retain their momentum in y direction, so that it is likely that instead of contributing to the dose ahead of the point of interaction, they get bent onto a corkscrew-like trajectory, spiralling out from their point of creation towards both positive and negative y-direction until they reach the end of their range. This leads to the elongate patterns observed at 1.5 T and 3 T in the two outer columns of the figure.

In the centre column, i.e. in the x-z plane, another effect can be noticed at 1.5 T and 3 T, namely a smaller circular structure towards lower values of x, so in the direction opposite to the main dose deposition. The same observation was already made in the monoenergetic point kernels of 6 MeV photons in water displayed in figure 6.6, and this structure is caused by electrons with a momentum having a component in negative z-direction, so which are backscattered. So for these electrons, the action of the Lorentz force is in opposite direction to those with momentum in positive z-direction, and another small tubular structure emerges.

Magnetic field effects on the kernels are much stronger in the lung kernels compared with the water kernels, due to the approximately 5-fold longer electron ranges resulting mainly from the lower density.

The lung warping kernels determined from these point kernels are displayed in figure 9.14, and it can be remarked that even though the differences in size of the point kernels at different magnetic field strengths are significant, they do not result in differences of the same extent in the warping kernels.

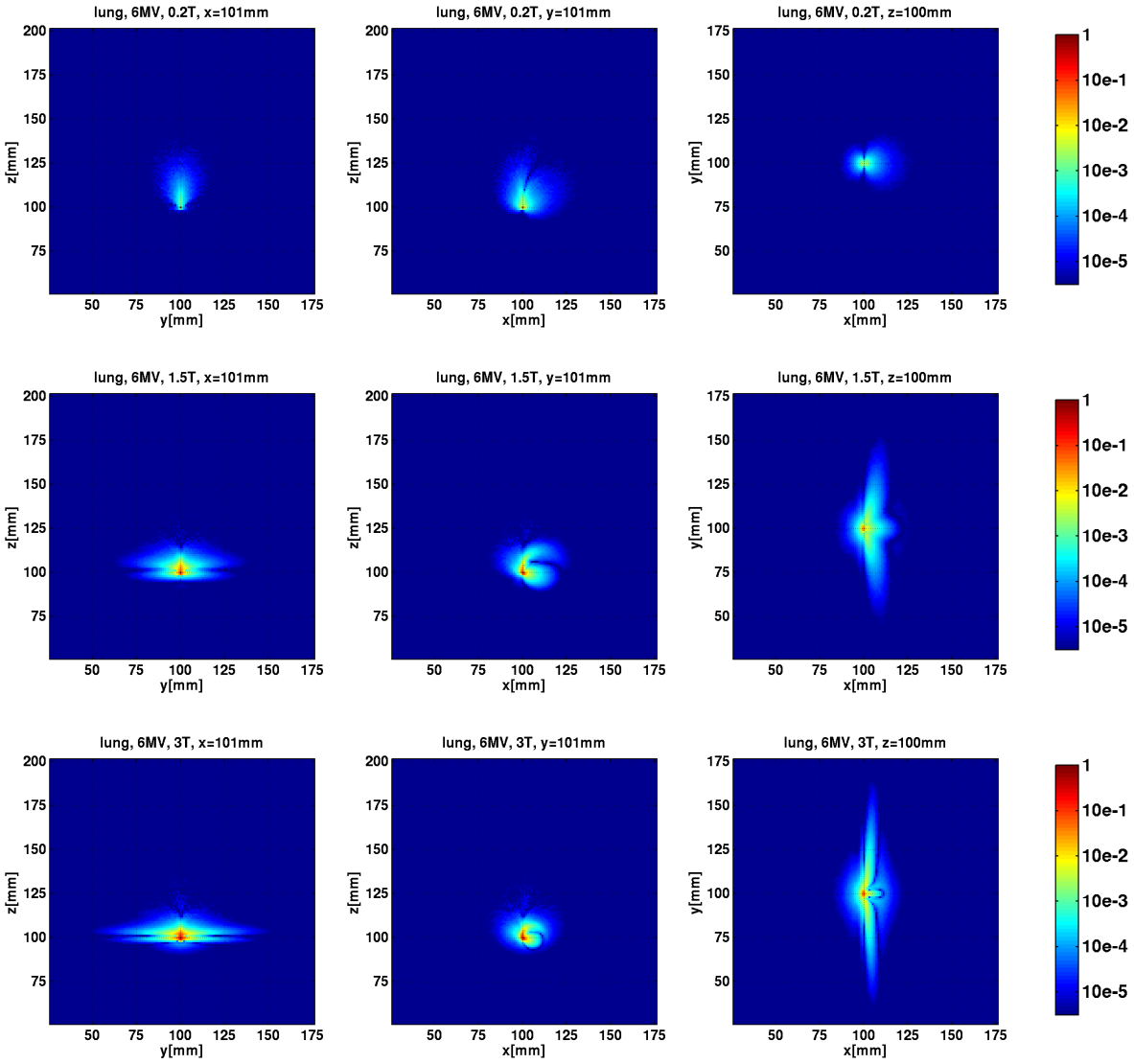


**Figure 9.14** Lung warping kernels for 6 MV.

The properties of the kernels translate directly into the dose deposition from the 2 cm×2 cm beam as can be seen from the Monte Carlo simulations displayed in figures 9.15, 9.16 and 9.17. While for 0 T and 0.2 T, build-up at the entrance surface of the beam is slow, it is fast and edgy for 1.5 T and 3 T.

The most significant difference between the warping result and the Monte Carlo generation is again the dose due to the ERE, whereas elsewhere, the agreement is rather good. Again, for the 0.2 T case, the electron returning to the exit surface of the beam deposit their dose in a curved long pattern, while at 1.5 T and 3 T, the dose deposition in confined to a narrow band close to the surface, correspoding to smaller gyroradii.

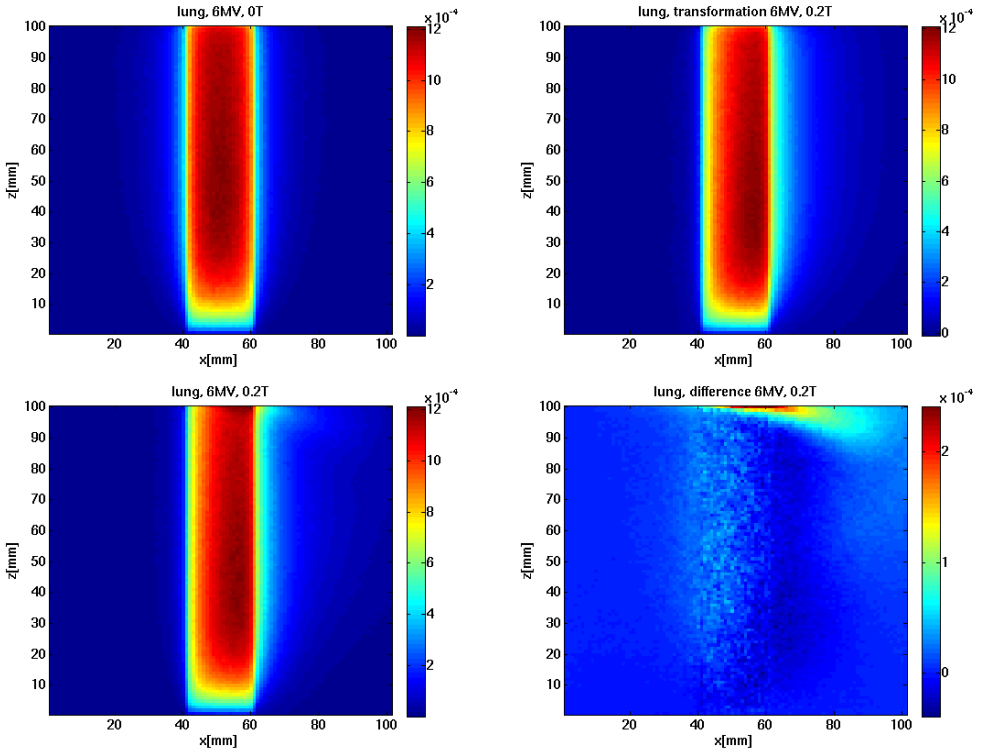


**Figure 9.15** Dose deposition in lung; left the two Monte Carlo simulations (0 T, 0.2 T), right warping result using the lung kernel (top), and difference to Monte Carlo (bottom)

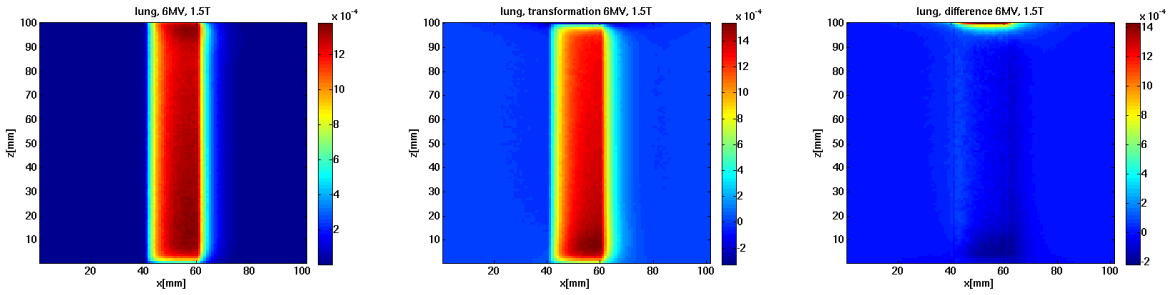


**Figure 9.16** Dose deposition in lung, 1.5 T; the Monte Carlo simulation (left), warping result using the lung kernel (center) and difference to Monte Carlo (right)

Looking at the depth-dose curves in figure 9.18, the differences in the build-up regions of 0 T and 0.2 T compared with 1.5 t and 3 T, are even more evident. It can be remarked, however, that the warping produces an overshoot for 1.5 T and 3 T.

In the cross profiles, it is seen that the general shape of the beam in the magnetic fields is modelled rather well by the warping. However, significant differences exist with respect to exact height for 1.5 T

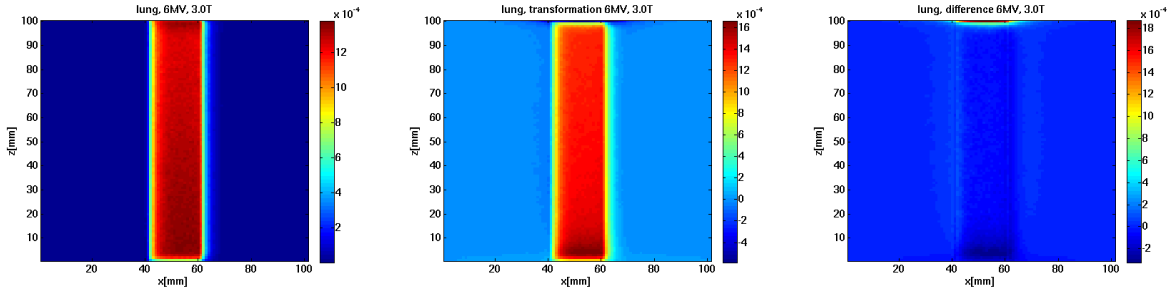


**Figure 9.17** Dose deposition in lung, 3 T; the Monte Carlo simulation (left), warping result using the lung kernel (center) and difference to Monte Carlo (right)

and 3 T. Comparing with the 0 T distribution, the magnetic field strongly affects the dose deposition, and locally a dose increase of around 10 % is observed.

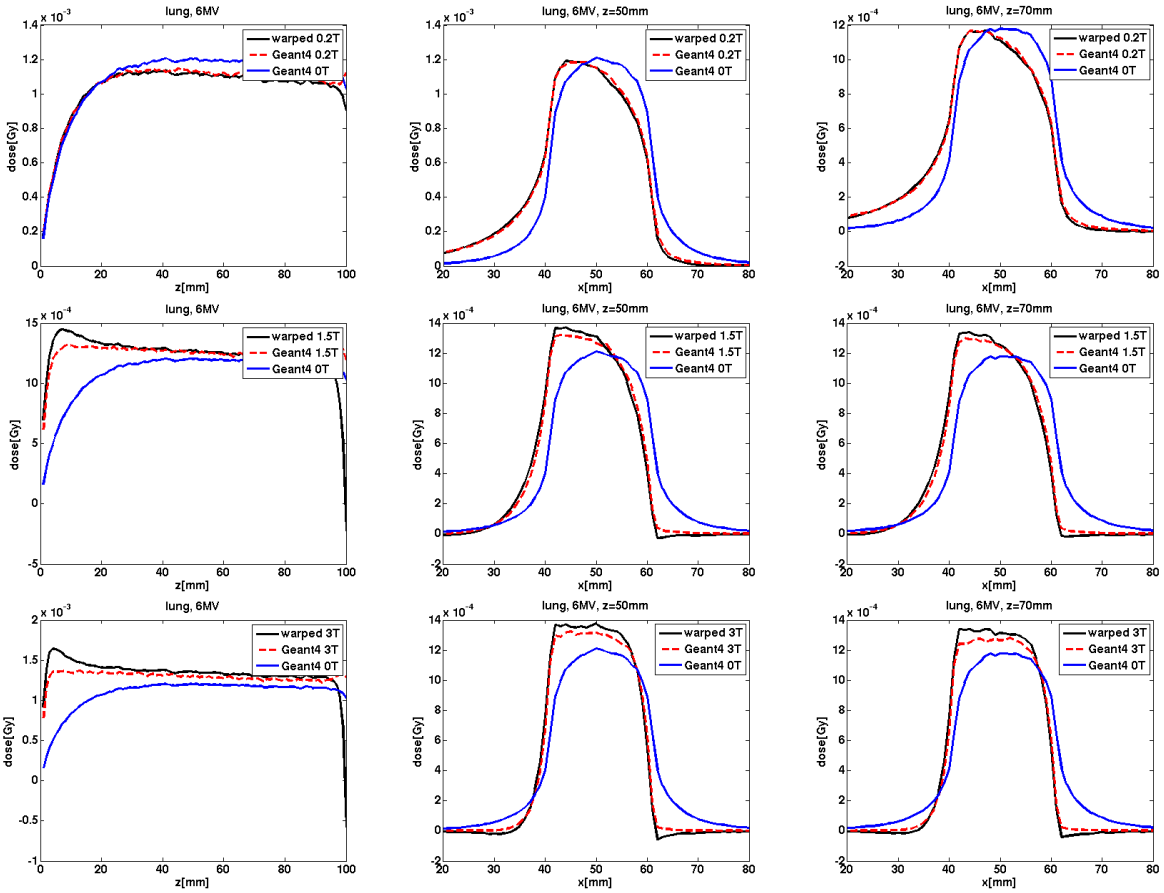


**Figure 9.18** Lung, 6 MV. Depth-dose profiles (left) and cross profiles at two different depths of the Monte Carlo simulation ('Geant4', red-dashed) at 0.2 T, 1.5 T and 3 T (top to bottom) and the respective warping results (black). The profiles at 0 T (blue) are given as a reference.

## 9.3 Summary and Conclusion

In this chapter, application of the warping method to homogeneous media was described. For this purpose, photon point interaction kernels were generated in three types of media present in the human body which are water, bone and lung tissue, and at different magnetic fields that are found in clinical MR scanners. It was seen that the dimensions and shapes of the point kernels were in good agreement with expectations from the known ranges of secondary electrons in the respective media, and from the known gyroradii of electrons in the according magnetic fields. Especially in lung tissue, the effects of the magnetic field were significant due to the long electron ranges.

From the point interaction kernels, warping kernels were determined to be applied to simulated dose distributions in homogeneous phantoms. For bone and water, basically a sideward deformation of the whole cross profiles was noticed as well as an upstream shift of the depth-dose profile, causing the depth-dose maximum to be located at shallower depths if a magnetic field is present. Consequently, the rest of the depth-dose profile was seen to be somewhat lower than without a magnetic field. In lung, the shape of the lateral (cross) profile was seen to be strongly influenced by the magnetic field. In spite of the depth-dose maximum being also located at shallower depths at 1.5 T and 3 T than at 0 T, in lung tissue the shape of the cross profile leads to locally higher dose values in the magnetic field, also beyond the dose maximum.

Generally, the warping results were in good agreement with reference Monte-Carlo simulations in the homogeneous part of the media investigated, such that it can be said that here, the warping method performs well. Especially in water and bone, deviations of the warping results from Monte Carlo simulations were seen to be minor and generally in the order of magnitude of statistical noise for all magnetic fields considered. In lung, only at 0.2 T was the agreement comparable with that in bone and water. At 1.5 T and 3 T, however, the warping is able to model the general shape of the dose deposition pattern but differences exist to the reference Monte Carlo simulations with respect to the exact magnitude, with deviations within around 5 %.

In heterogeneous regions, deviations between the warping and the reference simulations were observed to be severe. Not only can the electron return effect at interfaces to air not be adequately modelled by the method, but also in the build-up region, the warping results shown larger deviations from the reference simulations.

In terms of practical application in clinical settings, it need be asked at this point whether the deviations observed will be a serious obstacle for actual use of the method. At this point, it is concluded that this is not the case: On first sight, the electron return effect seems to be of major concern at the exit surface of the beam from the patient. Its absence in the dose distribution determined by means of the warping method will cause any fluence optimiser (cf. section 1.3) that makes use of the warping method for dose calculation, to underestimate the dose near the surface, and therefore create fluence patterns that in reality lead to a severe overdosage in this region. However, a mere addition of some bolus material at the exit surface of the beam from the patient will solve the issue. Some body cast or other immobilisation device can be used which may be considered a standard component of any better-equipped radiation therapy department, as long as the device's material is more-or-less water equivalent in terms of electron absorption. Irrespective of the dose calculation method applied, the use of additional material on the exit surface appears to be the procedure of choice for treatment in a magnetic field, since in this manner the high doses due to the ERE are avoided and cannot impair the quality of the dose distribution.

The second region where significant deviations of the warping results with respect to the Monte-Carlo simulations are observed, is in the build-up region. Generally, the warping method overestimates the dose in the dose maximum, i.e. close to the entrance surface. In the case that irradiation is from several directions, and some bolus material is used anyways for ERE compensation, the effect due to this overestimation will also be small. If no bolus material is used in the entrance channel of the beam, the optimiser may try

to reduce the dose unnecessarily which might result in a slightly suboptimal plan, but since the dose will always be lower in reality than what was determined by the warping-based dose calculation, no harm is expected in the tissues of the entrance channel.

However, in regard to inhomogeneities inside the human body, the answer towards applicability of the warping method is not straightforward, and the discussion will be resumed at the end of chapter 10, on the basis of the outcome of the phantoms studies presented there, and finally in chapter 12.

It was found later during the work on this thesis that for the water point interaction kernel at 3 T, as well as for the lung point interaction kernels at 1.5 T and 3 T, an energy conservation issue exists. In spite of the fact that for all point kernel simulations, the same number of photons with the same initial momenta were used, the energy deposited in the Monte-Carlo simulations differed depending on the magnetic field. For bone, the effect was generally below 1 % and the same is true for the water kernels at 0.2 T and 1.5 T. However, the energy deposited in the 3 T water kernel was lower by almost 2 % with respect to the 0 T kernel at 6 MV and by nearly 3 % at 3 MeV. In lung, the energy was lower by almost 3 % at 1.5 T and by almost 6 % at 3 T than at 0 T.

Regrettably, in the course of the work on the results presented in this chapter, only the 1.5 T water kernel had been used for verification of whether energy conservation is properly observed in the Monte-Carlo simulations, and the deviation below 1 % had been considered insignificant and not further been analysed. Due to the ERE, it was not expected that in the open field simulations the same amount of energy would be deposited in all settings, why here, it was not tested for energy conservation. Finally, since rather good agreement was found between the warping method and further Monte-Carlo simulation, and since these Monte-Carlo simulations are qualitatively consistent with the observations of other authors ([62], [44]), there had been no indication to doubt the results. Effects of the lack of energy in the 3 T warping kernel will be seen and discussed in chapter 11.

# Chapter 10

# Phantom Studies

Finding that the warping method was rather successful in homogeneous media and that the relevance of the deviations at tissue-air-interfaces is limited to certain cases, application is extended in this chapter to phantom studies of near-clinical cases. One brain and one lung tumour phantom were virtually constructed, and the dose effects of application of the warping method to them is described in the following.

Referring to section 9.3, a brain tumour case may benefit from MR-guidance in terms of better differentiation between tumour and brain tissues or visualisation of oedema and the like. The second reason why this geometry was chosen is that it represents a combination of bone and soft tissue which is considered a good candidate for application of the warping method, and which is, in variable geometries, present in many parts of the human body.

The advantage of MR-guidance over guidance by means of x-ray based methods in lung may be debated, since Hounsfield units between tumours and lung tissue differ enough to result in a reasonable x-ray contrast (except for the case of atelectasis, where MR-guidance may be of benefit). However, it is worthwhile considering that MRI will be one more useful means for image guidance of lung tumours. The lung tumour geometry was chosen to assess the effects of the magnetic fields on the dose in more detail, which are expected to be large Second, it was intended to investigate the performance of the warping method in such a heterogeneous geometry, after it was found in chapter 9 that the method showed large deviations from the reference simulations at tissue-air interfaces.

## 10.1 Material and Methods

For each phantom geometry, two beam settings are used, which is an open field encompassing the tumour, and a single beamlet for IMRT, respectively. Irradiation is simulated for a 6 MV beam of flat fluence, again using the spectrum of the central axis only.

As in chapter 9, a Monte-Carlo simulated dose distribution without magnetic field is warped using the kernels for 0.2 T, 1.5 T and 3.0 T and compared with the respective Monte Carlo simulation involving the magnetic field. The effect of the magnetic field on the dose distribution, i.e. the respective differences between the Monte-Carlo simulated 0 T dose distribution and those simulated with application of a magnetic field, are also analysed.

### 10.1.1 Irradiation of Brain Phantom using an Open Field

The skull and brain for the simulation were constructed as two concentric elliptical tube sections consisting of cortical bone (CB) and white matter (WM) which mimicks the situation above the skull base. The brain tumour was not explicitly constructed since in general, brain tumours do not differ a lot from the surrounding brain tissues in terms of mass and electron density and therefore photon interactions (cf. 2).

A sketch of the set up is shown in figure 10.1. The skull ellipse (black in the figure) has an outer major-semi axis of 10 cm and an outer minor-semi axis of 8.5 cm, in which the brain ellipse is embedded such as to have 0.5 cm skull bone uniformly around the brain. The semi axes of the brain ellipse are thus

9.5 cm and 8 cm (blue in the figure). Both the skull and the brain elliptical tube section have a height of 10 cm, and the whole structure is surrounded by air. A possible tumour outline is also given in the figure.

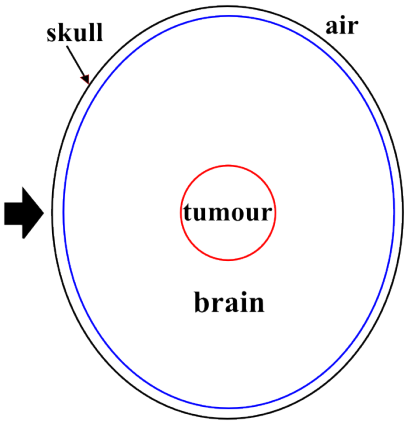


**Figure 10.1** Brain phantom cross section. Direction of beam incidence for simulations is indicated by the black arrow.

**Table 10.1** Mass fraction of chemical elements for brain phantom

| | density | H | C | N | O | P | Na | S | Mg | Ca | Cl | K |
|---|---|---|---|---|---|---|---|---|---|---|---|---|
| CB | 1.575 g/cm$^3$ | 0.034 | 0.155 | 0.042 | 0.435 | 0.103 | 0.001 | 0.003 | 0.002 | 0.225 | - | - |
| WM | 1.04 g/cm$^3$ | 0.106 | 0.194 | 0.025 | 0.661 | 0.004 | 0.002 | 0.002 | - | - | 0.003 | 0.003 |

The material composition for these simulations are taken from [70], and are given in table 10.1.

The simulated irradiation was by a (4.6 cm)$^2$ field, assuming a tumour volume of roughly 50 ml and warping was performed using the water kernel since the phantom is widely water equivalent from its radiological properties.

### 10.1.2 Irradiation of Brain Phantom using a Beamlet

The geometry is as described in the preceding section 10.1.1; however, the irradiation was by a beamlet (bixel) of (0.5 cm)$^2$ width which represents the smallest subunit, that an IMRT field can be composed of (cf. chapter 1.2 of the introduction).

### 10.1.3 Irradiation of Lung Phantom using an Open Field

A thorax was set up in Geant4, again using an elliptical tube section, and as shown in figure 10.2. The major and minor-semi axes were 14 cm and 8.5 cm, respectively, corresponding to the lateral and ventrodorsal directions. Into one side of the thorax, a lung was inserted as another elliptical tube in which a tumour was embedded.

The lung elliptical tube had its major-semi axis of 6.5 cm in ventrodorsal direction and its minor-semi axis of 4.5 cm in left-right lateral direction and is placed at 7 cm from the mid-sagittal axis of the thorax. Both elliptical tubes again cover 10 cm in the cranio-caudal direction. The lung tumour is constructed as a solid sphere of 1.25 cm radius and placed in the centre of the lung.

Soft tissue and lung are again defined according to [70] and their composition is given in table 10.2. The lung tumour is constructed to have the same elemental composition as lung tissue but a higher density is assigned using 0.88 g/cm$^3$ taken from [71].

A ventro-dorsal irradiation field of (2.5 cm)$^2$ is used such that it is exactly the size of the outer dimensions of the tumour. It has to be remarked that in clinical reality, a 1 cm margin would be chosen around the tumour.

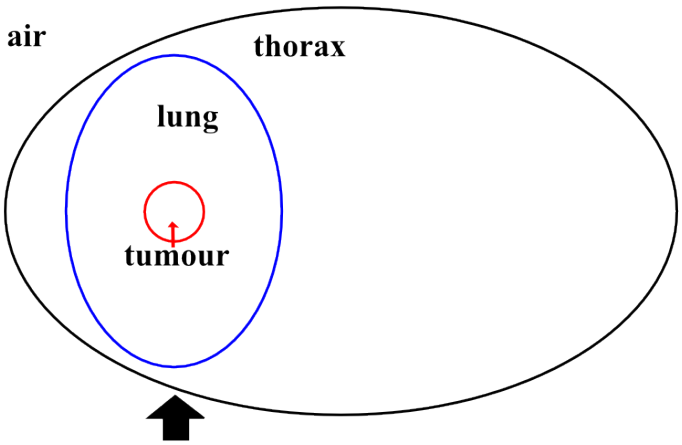


**Figure 10.2** Cross section of the lung phantom. The beam direction for simulation is indicated by the black arrow.

**Table 10.2** Mass fraction of chemical elements for lung phantom

| | **density** | **H** | **C** | **N** | **O** | **P** | **Na** | **S** | **Cl** | **K** |
|---|---|---|---|---|---|---|---|---|---|---|
| soft tissue | 1.05 g/cm$^3$ | 0.102 | 0.143 | 0.034 | 0.710 | 0.002 | 0.001 | 0.003 | 0.001 | 0.004 |
| lung | 0.26 g/cm$^3$ | 0.103 | 0.101 | 0.029 | 0.755 | 0.002 | 0.002 | 0.003 | 0.003 | 0.002 |

Warping was performed both with the water kernels and the lung kernels, where the lung kernels were used as calculated for the homogeneous test cases, in spite of the slightly different density used there (0.217 g/cm$^3$).

### 10.1.4 Irradiation of Lung Phantom using a Beamlet

Using the same set up as described in section 10.1.3 above, dose deposition from a beamlet (bixel) of (0.5 cm)$^2$ width was simulated also for the lung phantom to see the behaviour of the dose from an elemental IMRT field (cf. chapter 1.2 of the introduction)). For warping, again both the water and the lung kernels were employed.

## 10.2 Results

### 10.2.1 Irradiation of Brain Phantom using an Open Field

#### Brain - Open Field - 0.2 T

Two dimensional dose distributions of the Monte Carlo simulations and warping results for 0.2 T are displayed in figure 10.3 as well as difference plots which have been normalised by the dose at the virtual tumour position, i.e. the centre voxel at a depth of 91 mm. In the figure title, $D_G$ denotes the dose from the Geant4 simulation $D_w$ the warped dose and $D_T$ the dose in the tumour. While the colour coding of the left difference plot stretches over the full range of values, in the right plot, values above ±10 % have been cut off such that the details within the brain are visible, and comparison with the difference plots from warping to magnetic fields of other magnitude is facilitated. The beam is incident from the left and in all cases, the increase of dose in the skull is seen on both sides. Between the warping and the Monte Carlo dose at 0.2 T, the ERE is seen to be the most significant difference, and some smaller deviations are observed in the entrance region of the beam where also the skull is located.

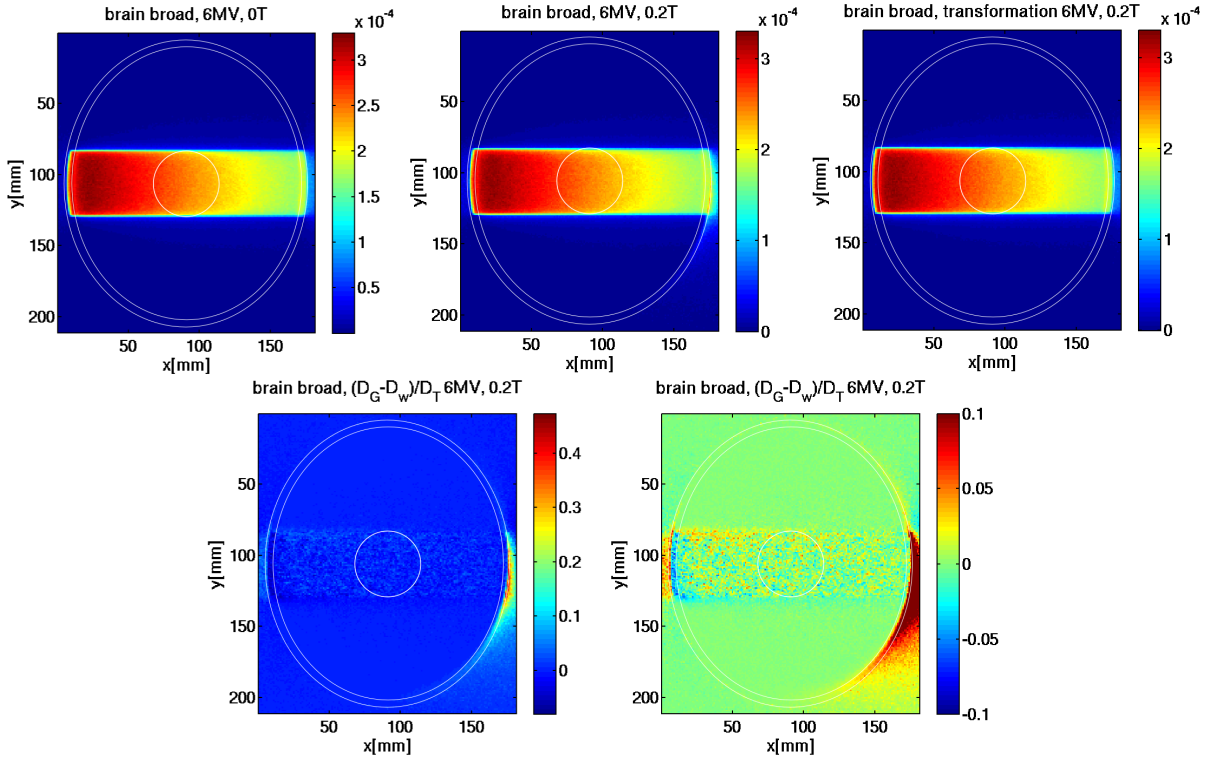


**Figure 10.3** Top: Monte Carlo simulations of brain phantom irradiation with an open field at 0 T (left) and 0.2 T (centre), and warping result (right). Dose values in Gy. Bottom: Difference plots between warping and simulation for 0.2 T, full range of values (left) and range restricted to values within ±10 % (right).

Depth-dose curves and cross profiles for the 0.2 T case are displayed in figure 10.4 both for the Monte Carlo simulations and the warping result, as well as for the difference between them which is again normalised by the tumour dose in the magnetic field. Despite the statistical noise on the Monte Carlo simulations, it can be seen that no major systematic deviations exist between the warping and the simulation, except for the ERE. Fluctuations within the high dose region are generally within 3-4 %. As already discussed in chapter 9.2 above, dose in a magnetic field is shifted upstream, and this is even more prominent in the bone layer of this case, where the backward-bent secondary electrons loose their energy over a shorter track length. Difference plots between Monte-Carlo simulated dose distributions at 0.2 T and 0 T are shown in figure 10.5, where $D_B$ and $D_0$ in the figure title denote the dose with and without a magnetic field applied, respectively, and $D_{TB}$ is the tumour dose in the magnetic field. Here, a systematic difference of up to around ±8 % is observed at the beam edges while in the beam centre, fluctuations are also within around 2-4 %.

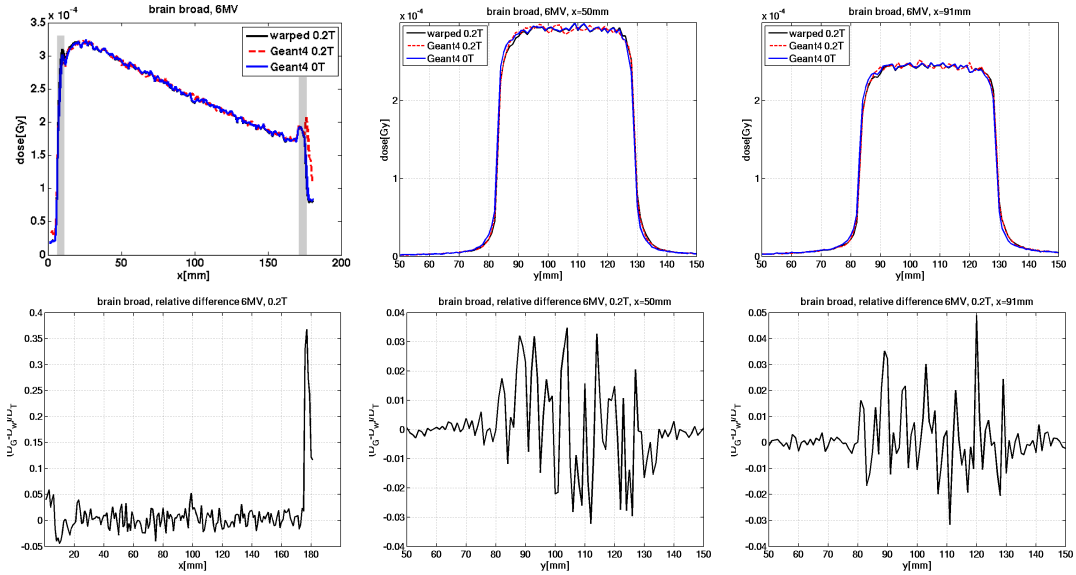


**Figure 10.4** Open field in brain phantom. Top: Depth-dose profile (left) and cross profiles at two different depths of the Monte Carlo simulation ('Geant4', red-dashed) at 0.2 T and the warping result (black). The profile at 0 T (blue) is given as a reference as well as the position of the skull in the depth-dose profile. Bottom: difference normalised by tumour dose.

It can thus be stated that even though a magnetic field of 0.2 T does not have a large influence on the dose distribution in this brain tumour case, the result of the warping method is significantly closer to the actual dose distribution produced at a magnetic field of this magnitude than if the effect of the magnetic field is not taken into account at all.

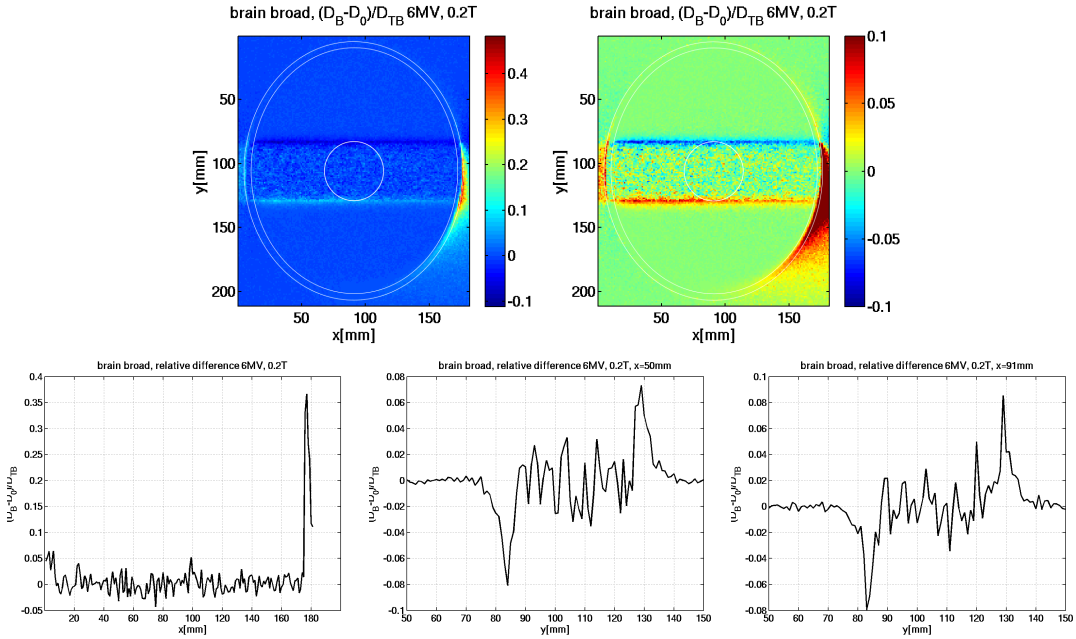


**Figure 10.5** Comparison of the Monte Carlo simulations at 0.2 T and 0 T: difference normalised by the tumour dose in the magnetic field. Top: 2D maps with full and restricted range of values; bottom: profiles along the beam direction (left) and across the beam at two different depths.

### Brain - Open Field - 1.5 T

The corresponding results for 1.5 T are displayed in figures 10.6, 10.7 and 10.8. It is evident that the ERE still constitutes the major difference and also in the entrance region warping and Monte Carlo simulation do not perfectly agree. However, also in the homogeneous region, systematic deviations between the warped and Monte-Carlo simulated dose distribution exist at the beam edges. They are seen to decrease with increasing depth in the rightmost plot of figure 10.6, with magnitudes of nearly 10 % at a depth value of 5 cm and 6 % at the virtual tumour depth value of 9 cm as the cross-sectional profiles in figure 10.7 reveal.

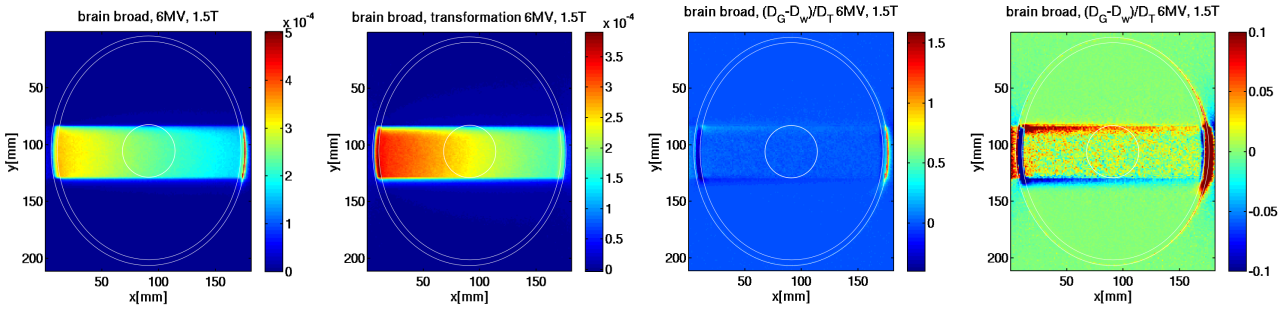


**Figure 10.6** From left to right: Monte Carlo simulation of brain phantom irradiation with an open field at 1.5 T and warping result (dose values in Gy) as well as difference plots between warping and simulation for 1.5 T, using the full range of values and a restricted range.

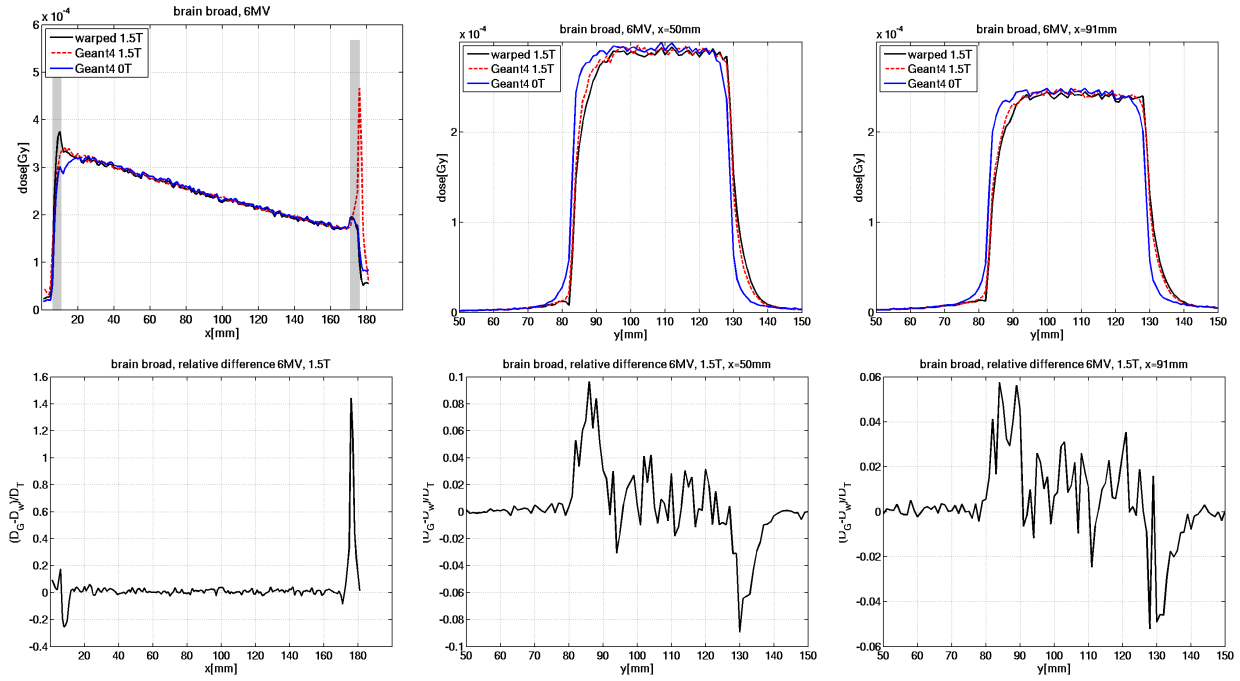


**Figure 10.7** Open field in brain phantom. Top: Depth-dose profile (left) and cross profiles at two different depths of the Monte Carlo simulation ('Geant4', red-dashed) at 1.5 T and the warping result (black). The profile at 0 T (blue) is given as a reference as well as the position of the skull in the depth-dose profile. Bottom: difference normalised by tumour dose.

Differences to 0 T are given for comparison in figure 10.8. Here, dose at the beam edges differs by almost ±30 % with smaller depth dependence of this value than in the warping case.

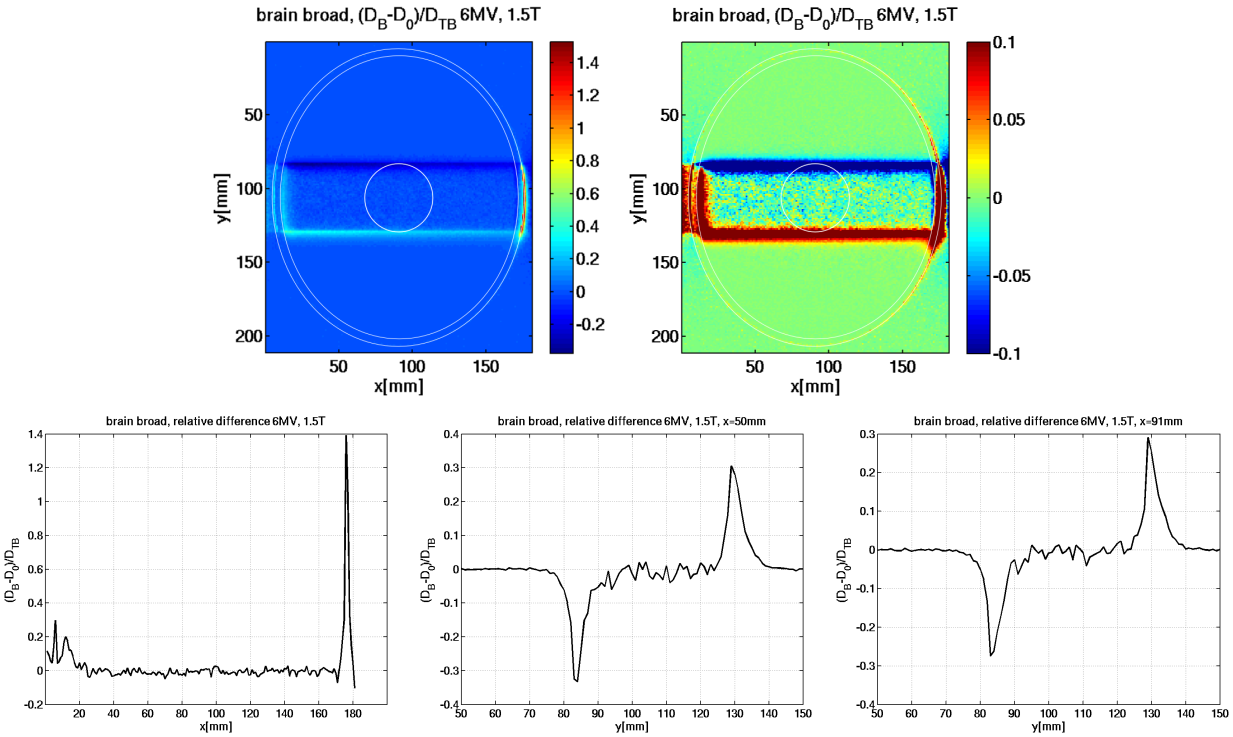


**Figure 10.8** Comparison of the Monte Carlo simulations at 1.5 T and 0 T: difference normalised by the tumour dose in the magnetic field. Top: 2D maps with full and restricted range of values; bottom: profiles along the beam direction (left) and across the beam at two different depths.

### Brain - Open Field - 3 T

For 3 T, observations are very similar as seen in figures 10.9, 10.10 and 10.11. Entrance and exit region are not well modelled by the warping but also in the homogeneous part, dose at the beam edges differs by up to around ±6 % where this value decreases with depth.

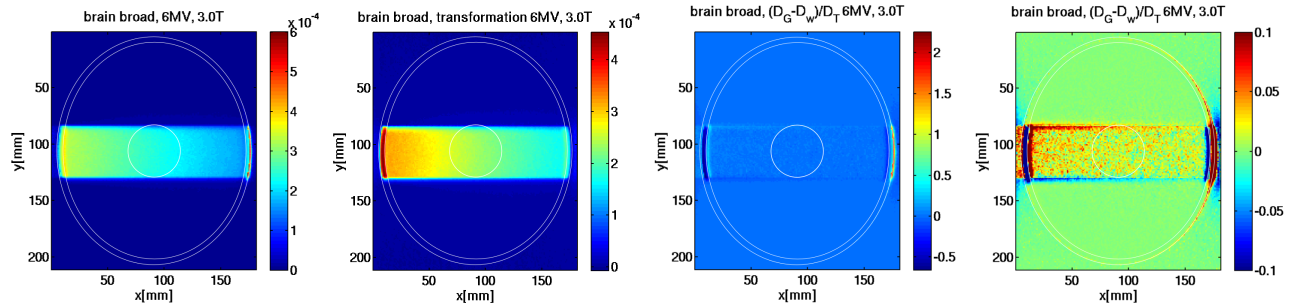


**Figure 10.9** From left to right: Monte Carlo simulation of brain phantom irradiation with an open field at 3 T, warping result (dose values in Gy) as well as difference plots between warping and simulation for 3 T, using the full range of values and a restricted range.

Deviations to the dose distribution without magnetic field are again much larger and range up to more than ±30 % as figure 10.11 shows.

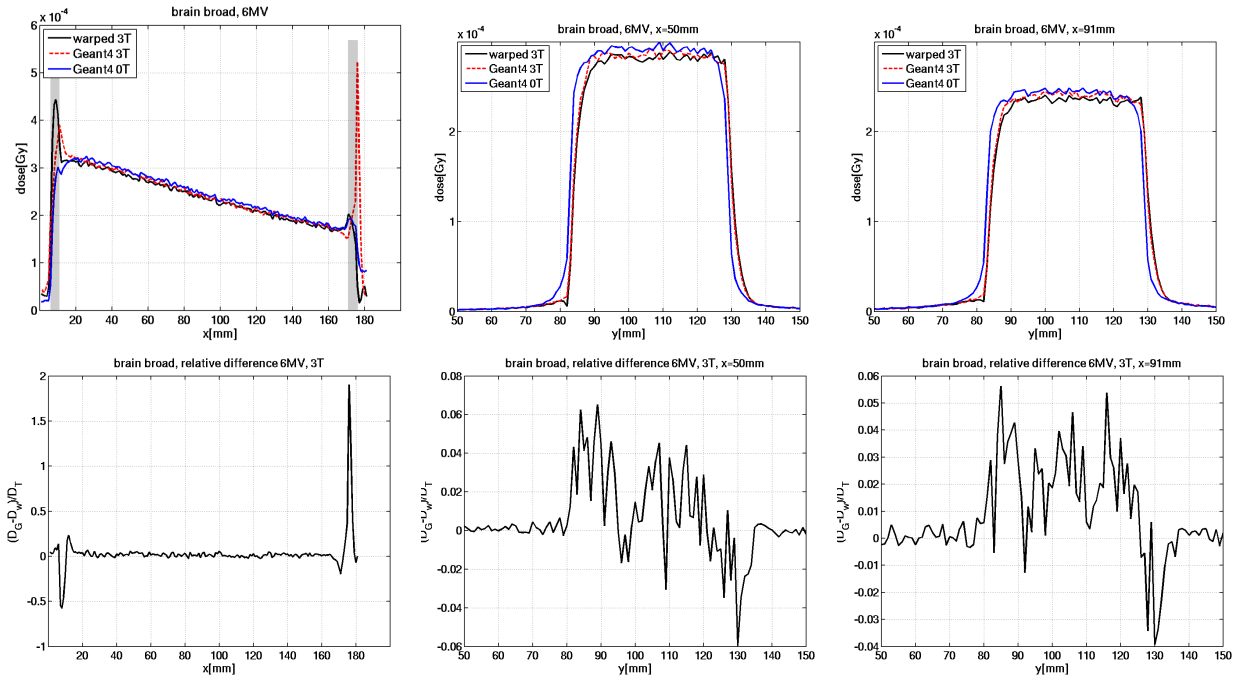


**Figure 10.10** Open field in brain phantom. Top: Depth-dose profile (left) and cross profiles at two different depths of the Monte Carlo simulation ('Geant4', red-dashed) at 3 T and the warping result (black). The profile at 0 T (blue) is given as a reference as well as the position of the skull in the depth-dose profile. Bottom: difference normalised by tumour dose.

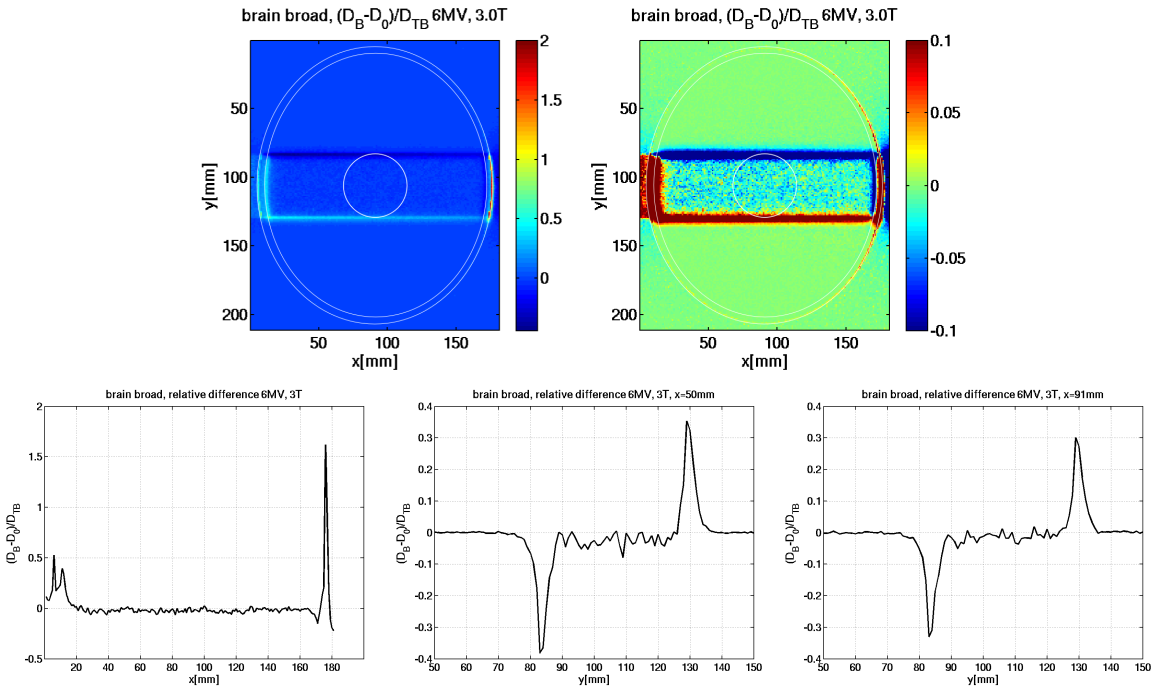


**Figure 10.11** Comparison of the Monte Carlo simulations at 3 T and 0 T: difference normalised by the tumour dose in the magnetic field. Top: 2D maps with full and restricted range of values; bottom: profiles along the beam direction (left) and across the beam at two different depths.

### 10.2.2 Irradiation of Brain Phantom using a Beamlet

#### Brain - Beamlet - 0.2 T

While hardly any difference can be seen between the two dimensional dose maps of the Monte Carlo simulations at 0 T and 0.2 T as well as the warping result in figure 10.12, the two difference plots reveal that also for the beamlet case, the prominent deviations are found close to the entrance and exit surfaces. The colour coding in the second difference plot is maintained to be between ±10 % for comparison purpose, although the actual maximum values are smaller.

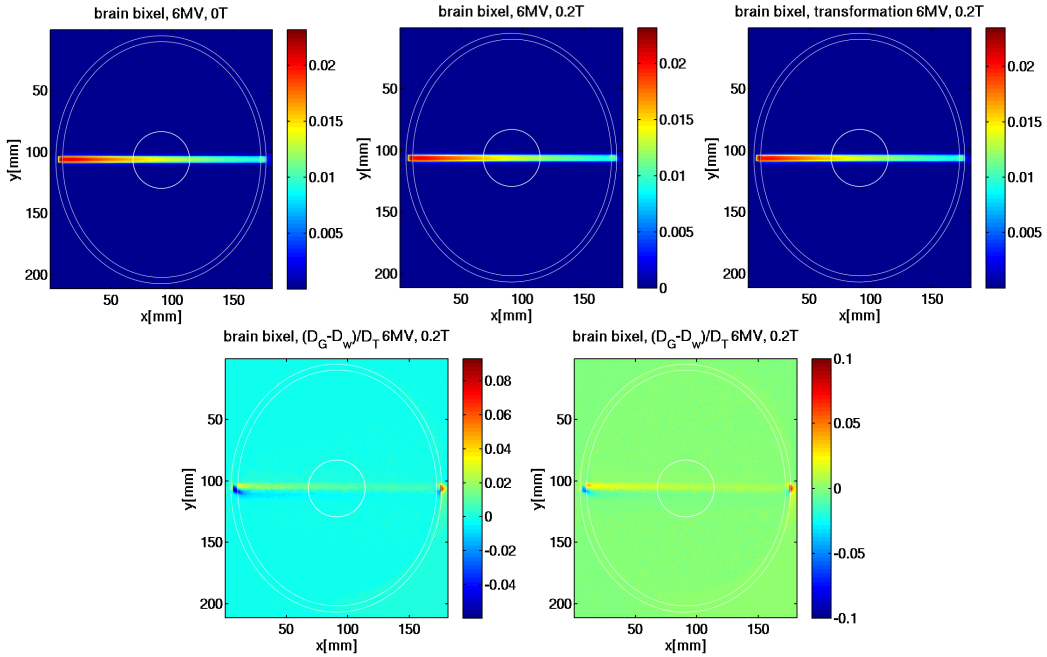


**Figure 10.12** Top: Monte Carlo simulations of brain phantom irradiation with a beamlet at 0 T (left) and 0.2 T (centre), and warping result (right). Dose values in Gy. Bottom: Difference plots between warping and simulation for 0.2 T, full range of values (left) and colour coding such as to display values within ±10 % (right).

In the depth-dose profile shown in figure 10.13, all curves almost coincide, where the magnetically deformed curves are slightly lower than the 0 T curve. In the difference depth-dose profiles, it is observed that in the homogeneous region and along the central axis of the beam at y=106 mm, the dose values of the Geant4 simulation are always higher than in the warping result by 1-2 %. In the entrance region, the warping overestimates the dose, and at the exit surface where the ERE is, it underestimates it.

The cross-sectional profiles show deviations at the beamlet edges of up to around 1.5 % between the warping result and the reference simulation. The comparision with the 0 T distribution is found in figure 10.14, where the sideward deformation of the beamlet is clearly seen. It leads to differences at the beamlet edges of around 6 % at the depths displayed in the figure. The fluctuations on the depth-dose curve of the difference to 0 T are centred at a negative value, showing that the magnetically deformed dose is generally lower than the 0 T dose in the central voxels at y=106 mm.

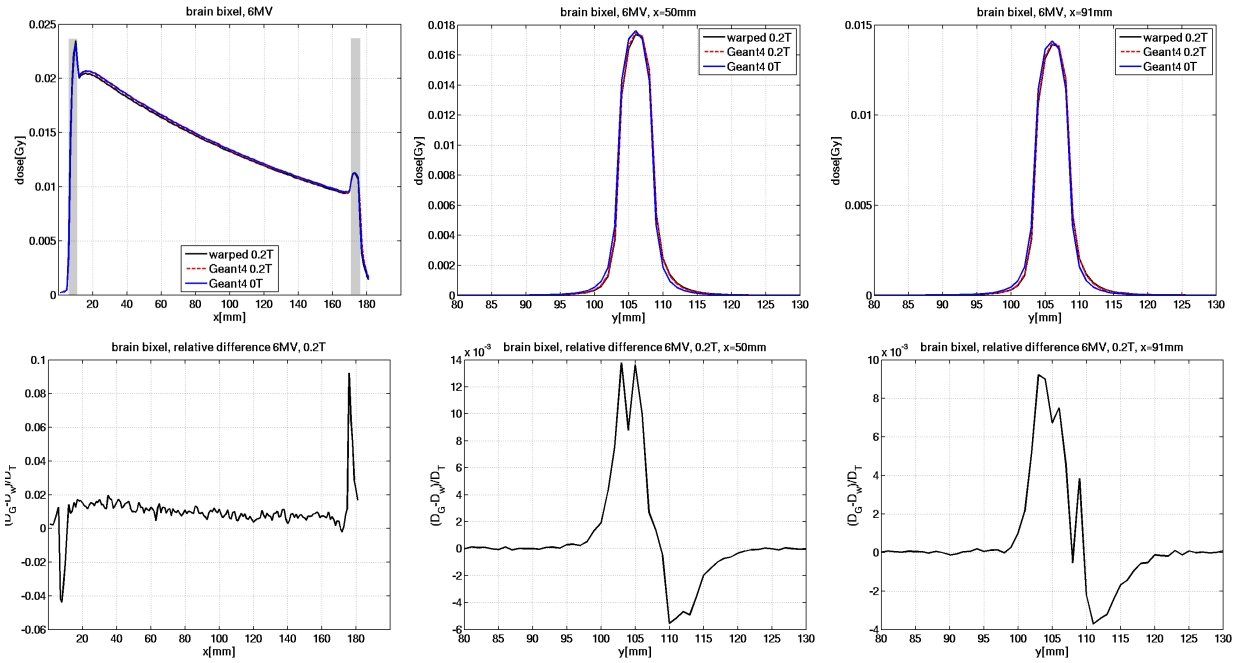


**Figure 10.13** Beamlet in brain phantom. Top: Depth-dose profile (left) and cross profiles at two different depths of the Monte Carlo simulation ('Geant4', red-dashed) at 0.2 T and the warping result (black). The profile at 0 T (blue) is given as a reference as well as the position of the skull in the depth-dose profile. Bottom: difference normalised by tumour dose.

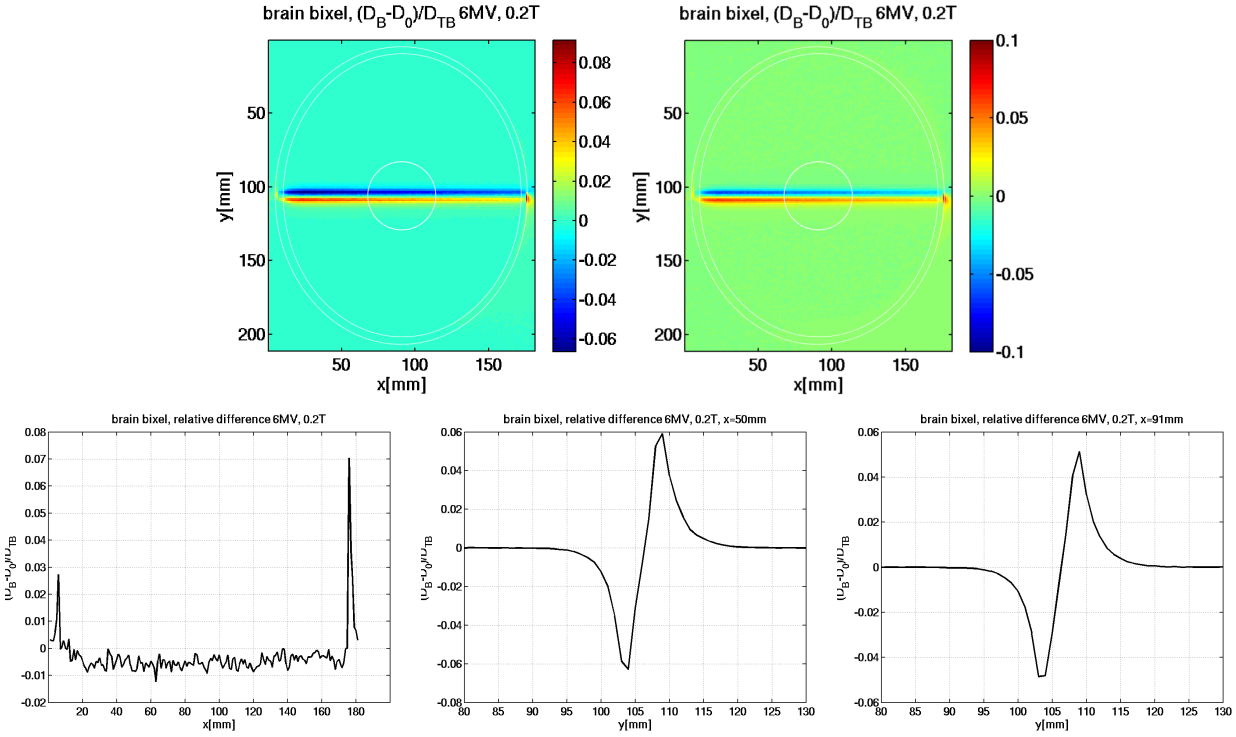


**Figure 10.14** Comparison of the Monte Carlo simulations at 0.2 T and 0 T: difference normalised by the tumour dose in the magnetic field. Top: 2D maps with full and restricted range of values; bottom: profiles along the beam direction (left) and across the beam at two different depths.

### Brain - Beamlet - 1.5 T

At 1.5 T, it is also in the difference plots of figure 10.15 that deviations become evident between the warping result and the reference simulation. Beside the discrepancies in the entrance and exit region of the beam, significant differences also exist again at the beamlet edges but decrease with increasing depth.

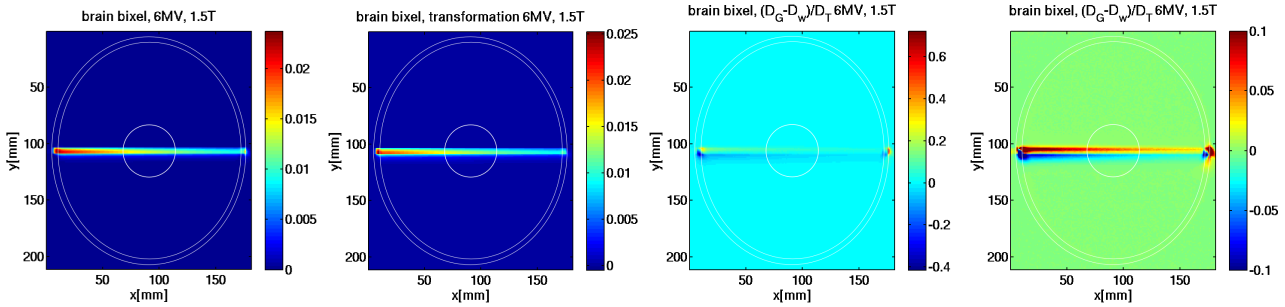


**Figure 10.15** From left to right: Monte Carlo simulation of brain phantom irradiation with a beamlet at 1.5 T, warping result (dose values in Gy) as well as difference plots between warping and simulation for 1.5 T, using the full range of values and a restricted range.

The cross profiles of the local difference normalised by the tumour dose in figure 10.16 reveal that they range up to 8 % at x=50 mm and 6 % at x=91 mm. In the depth-dose curves it is further observed that along the central axis of the beam, the warping widely underestimates the dose.

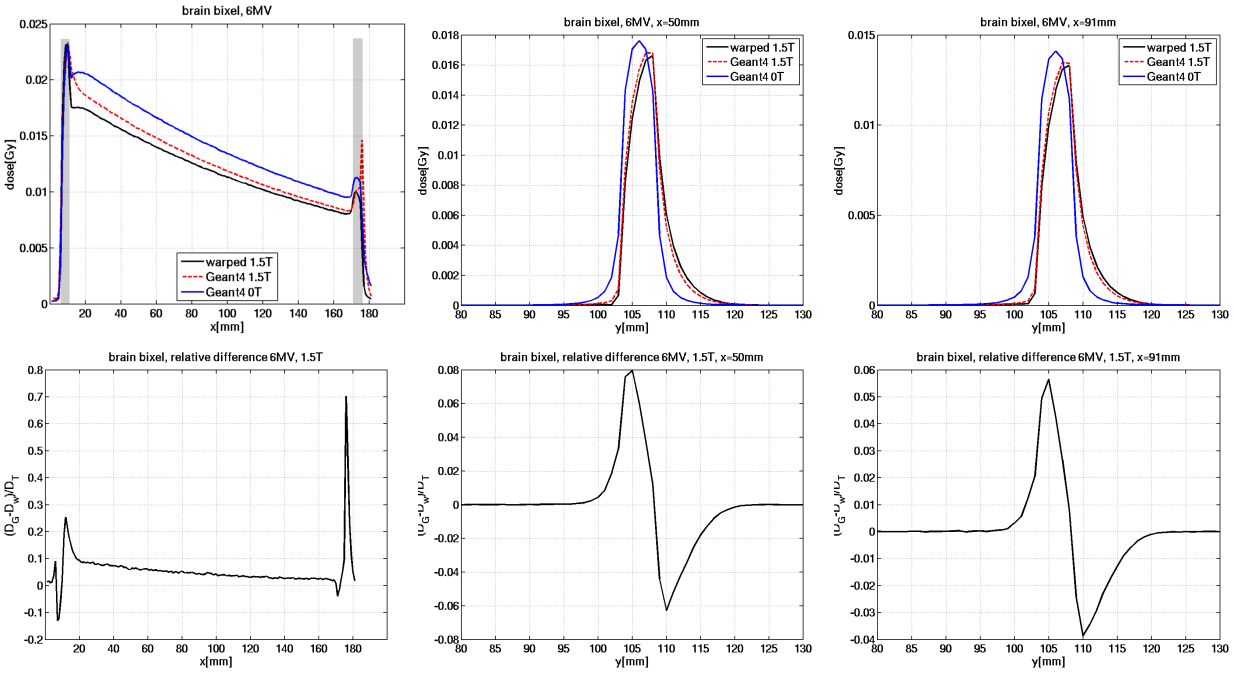


**Figure 10.16** Beamlet in brain phantom. Top: Depth-dose profile (left) and cross profiles at two different depths of the Monte Carlo simulation ('Geant4', red-dashed) at 1.5 T and the warping result (black). The profile at 0 T (blue) is given as a reference as well as the position of the skull in the depth-dose profile. Bottom: difference normalised by tumour dose.

Large discrepancies are again remarked when comparing the magnetically deformed dose with the dose at 0 T as seen in figure 10.17.
The difference map with colour coding between ±10 % shows that in hardly any point along the beam, deviations are below that threshold. From the cross profiles, it is observed that the actual difference values are of around 30 %.

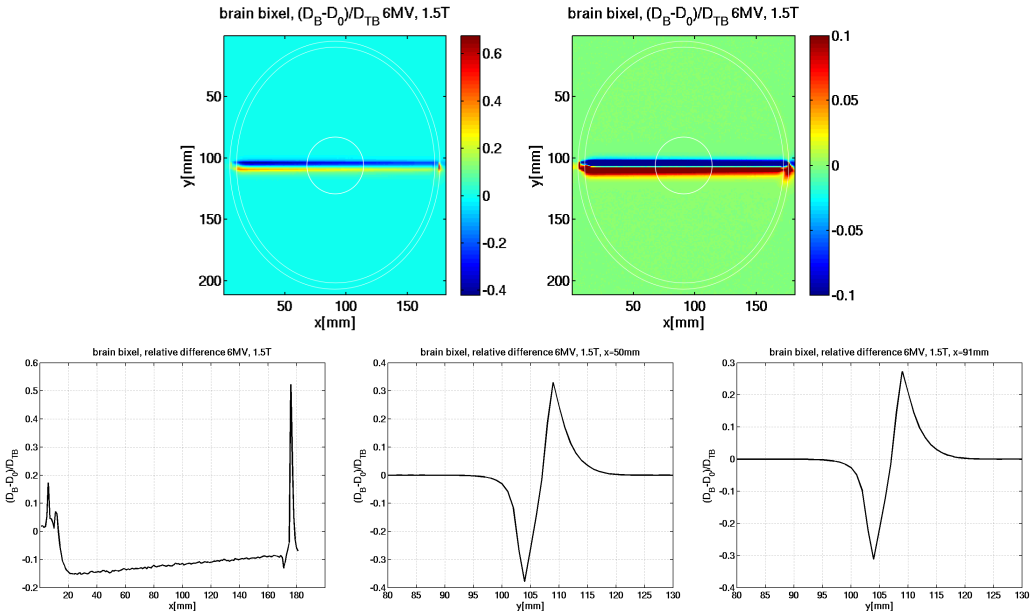


**Figure 10.17** Comparison of the Monte Carlo simulations at 1.5 T and 0 T: difference normalised by the tumour dose in the magnetic field. Top: 2D maps with full and restricted range of values; bottom: profiles along the beam direction (left) and across the beam at two different depths.

### Brain - Beamlet - 3 T

The results of warping at 3 T widely resemble the 1.5 T findings. Again, significant differences are observed in the heterogeneous regions as well as partially at the beamlet edges. This can be seen in the difference plot of figure 10.18, and from the profiles in figure 10.19. Difference values at the beamlet edges are up to around 7 % at x=50 mm and below 5 % at x=91 mm.

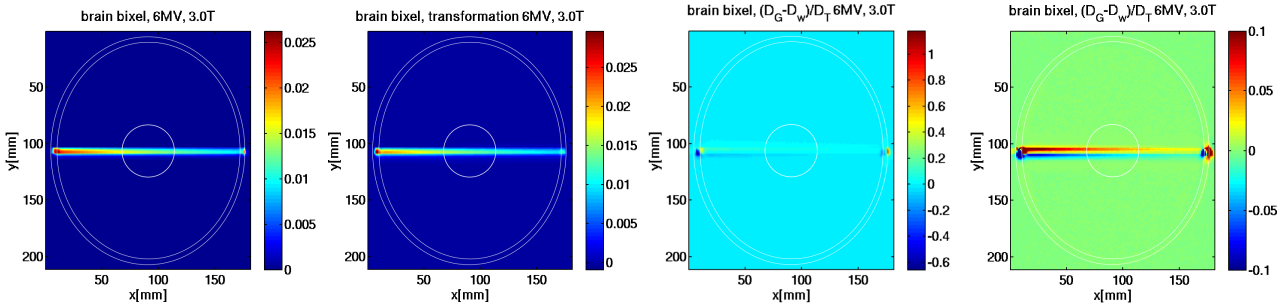


**Figure 10.18** From left to right: Monte Carlo simulation of brain phantom irradiation with a beamlet at 3 T, warping result (dose values in Gy) as well as difference plots between warping and simulation for 3 T, using the full range of values and a restricted range.

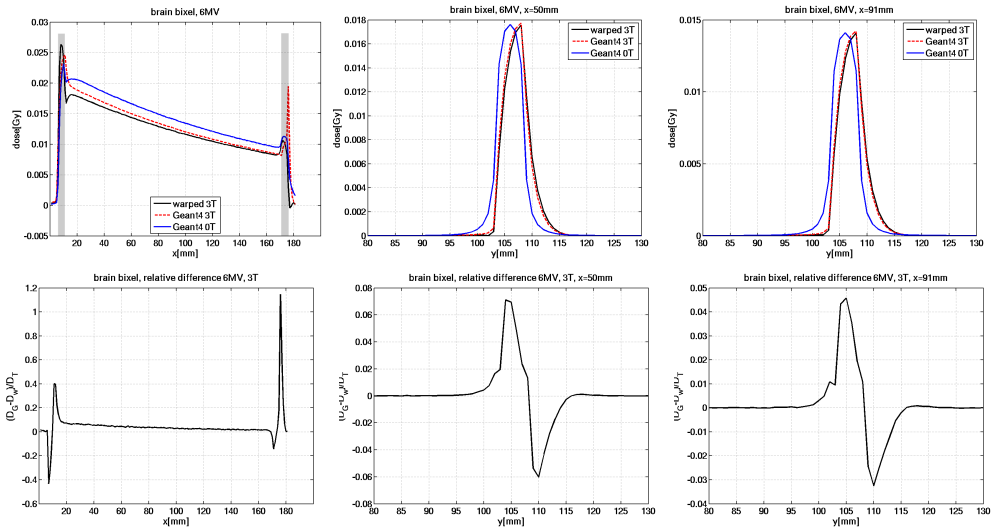


**Figure 10.19** Beamlet in brain phantom. Top: Depth-dose profile (left) and cross profiles at two different depths of the Monte Carlo simulation ('Geant4', red-dashed) at 3 T and the warping result (black). The profile at 0 T (blue) is given as a reference as well as the position of the skull in the depth-dose profile. Bottom relative difference normalised to tumour dose.

Again, the differences to the original 0 T dose distribution are enormous as figure 10.20 reveals. Basically the dose values at all points in the beam deviate by more than 10 % with peak values of ±40 % at x=50 mm.

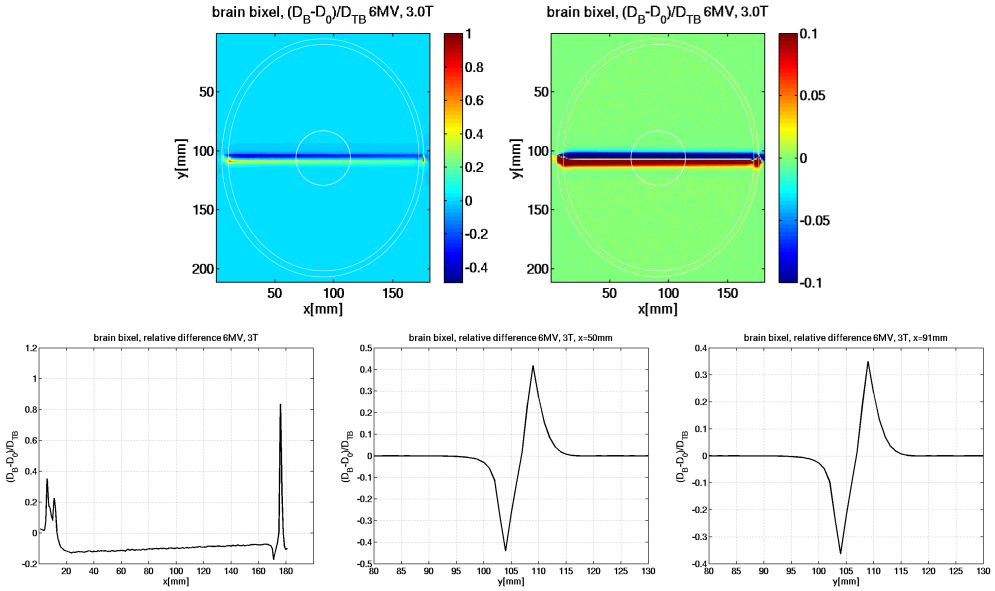


**Figure 10.20** Comparison of the Monte Carlo simulations at 3 T and 0 T: difference normalised by the tumour dose in the magnetic field. Top: 2D maps with full and restricted range of values; bottom: profiles along the beam direction (left) and across the beam at two different depths.

### 10.2.3 Irradiation of Lung Phantom using an Open Field

In this section, for each magnetic field the results from warping by means of the kernel generated from point interaction in water are presented, followed by the results from using the kernel based on point interactions in lung. For comparison, it is also illustration how big the effect of the magnetic field actually is.

#### Lung - Open Field - 0.2 T - Water Kernel

Figure 10.21 shows both the Monte Carlo simulations for 0 T and 0.2 T (top), the results from warping by means of the water kernel (middle) and the difference plots between warping and the corresponding Monte Carlo simulation (bottom). The difference plots are again displayed using the full range of values for colour coding (left) and restricting the range to ±10 % (right).

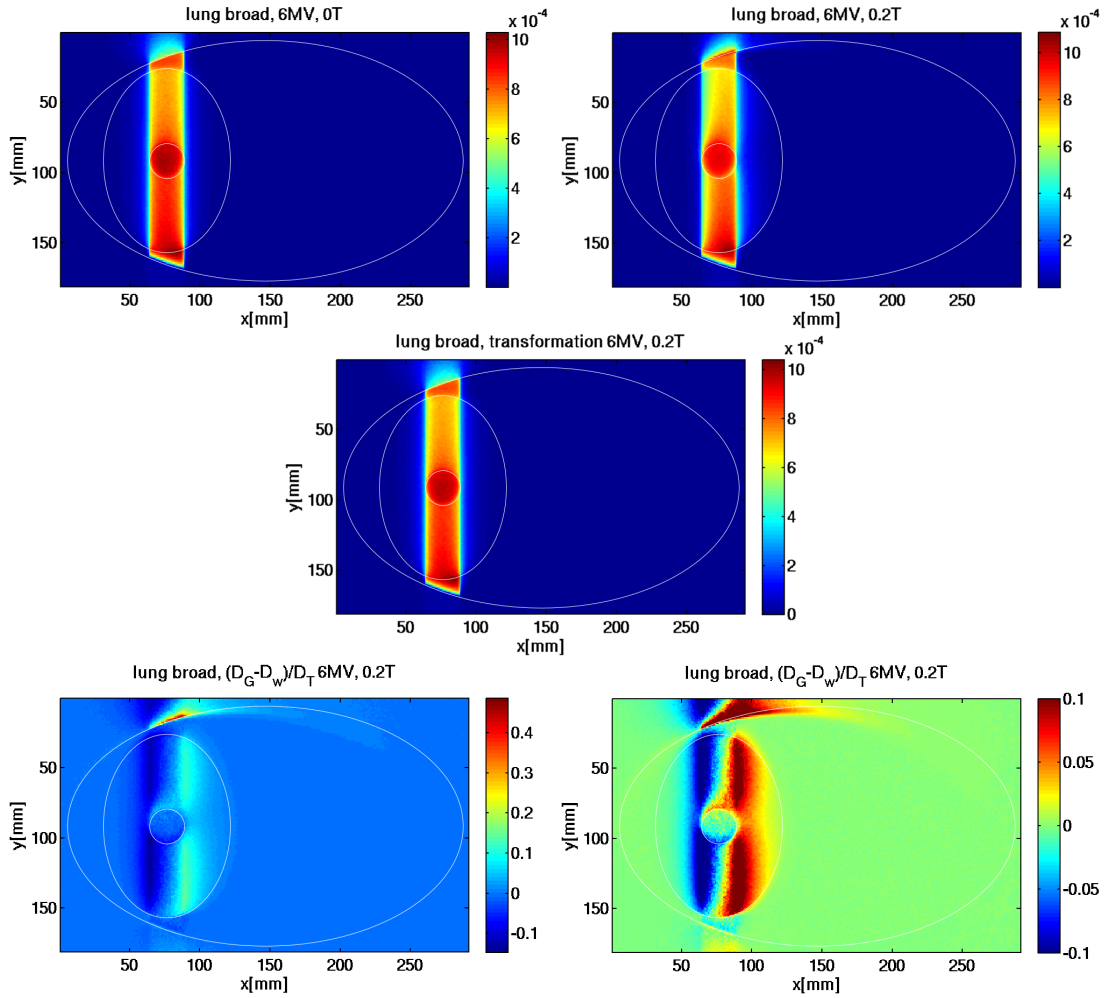


**Figure 10.21** Lung phantom irradiation with an open field. Direction of incidence is from below. Top: Monte Carlo simulations at 0 T and 0.2 T (dose values in Gy); middle: warping result using the water kernel (dose values in Gy); bottom: difference plots with two colour scales.

It is observed that even though numerically, the ERE is still the prominent effect, also in the lung and at the tumour boundaries large deviations exist. The dose profiles presented in the top row of figure 10.22 show that while the warping basically reproduces the 0 T behaviour, the actual dose in the 0.2 T reference Monte Carlo simulation is shifted more sideways. This behaviour is clearly seen in the cross profile in lung (middle) and less so in the cross profile in tumour (right), but also here, the profiles of the warping result (black line) and the 0 T simulation (blue) nearly superpose, while the red dashed line of the 0.2 T simulation exhibits a deformation especially at the beam edges.

Also in the depth-dose profiles displayed in the leftmost plot, the black line of the warping result is almost fully hidden by the blue 0 T line, while the red dashed line showing the 0.2 T simulation clearly disagrees. It should be noticed that since the beam direction is towards decreasing values of y, the ERE is seen toward the left of the curves.

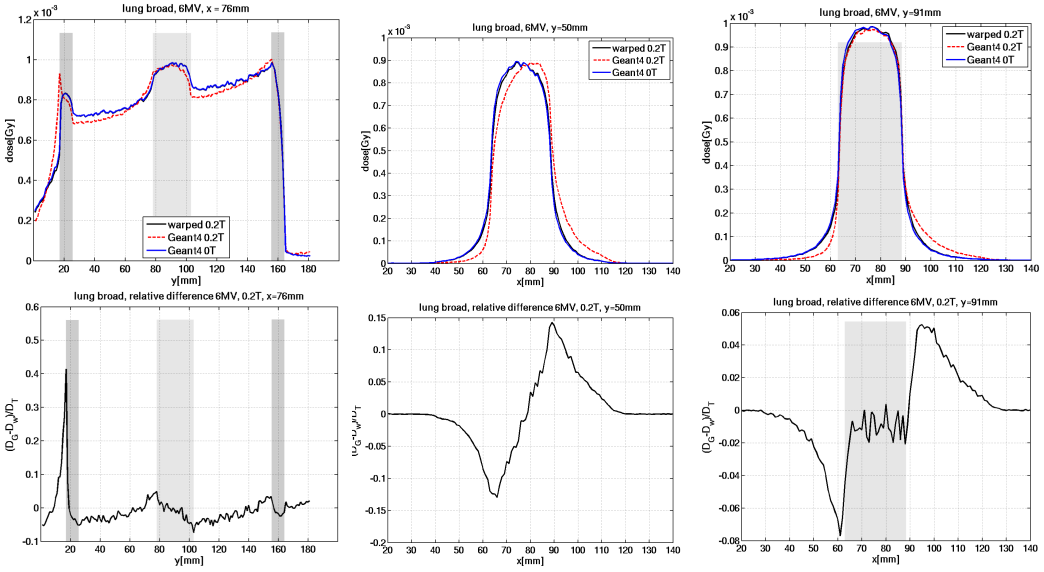


**Figure 10.22** Open field in lung phantom. Top: Depth-dose profile (left) and cross profiles at two different depths of the Monte Carlo simulation ('Geant4', red-dashed) at 0.2 T and the result from warping by means of the water kernel (black). The profile at 0 T (blue) is given as a reference. The position of the thoracic wall and the tumour are indicated by grey shading. Bottom: difference normalised by tumour dose.

The difference induced by this deformation ranges up to around ±15 % in lung as seen in the cross profile at y=50 mm. Across the tumour, the shape of the high dose region is rather preserved and at the beam edges, the differences are between around +5 % and -7 %. In the high dose region, the warping slightly overestimates the dose, such that in the cross profile through y=91 mm, the difference values in the tumour volume centre around -1 %. So while the water kernel produces large deviations in lung tissue, the results in the tumour consisting of soft tissue are rather acceptable.

### Lung - Open Field - 0.2 T - Lung Kernel

Warping by means of the lung kernel yields the exact opposite behaviour as figures 10.23 and 10.24 show: In the lung tissue, deviations are smaller and the shape of the dose is modelled well but not in the tumour volume. In lung, the differences stay below around ±6 % but in the tumour, they are as high as ±20 %.

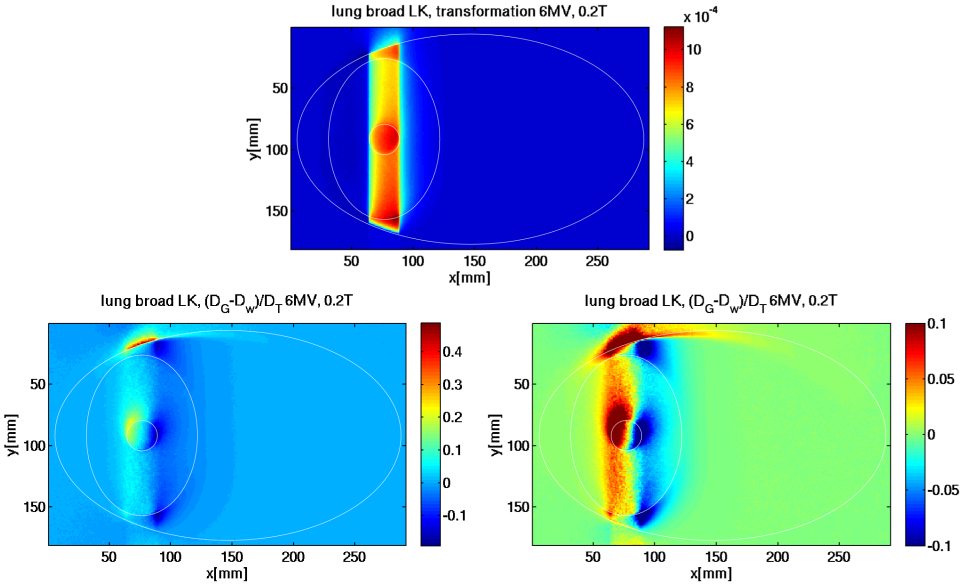


**Figure 10.23** Lung phantom irradiation with an open field. Direction of incidence is from below. Top: warping result using the lung kernel (dose values in Gy); bottom: difference plots with two colour scales.

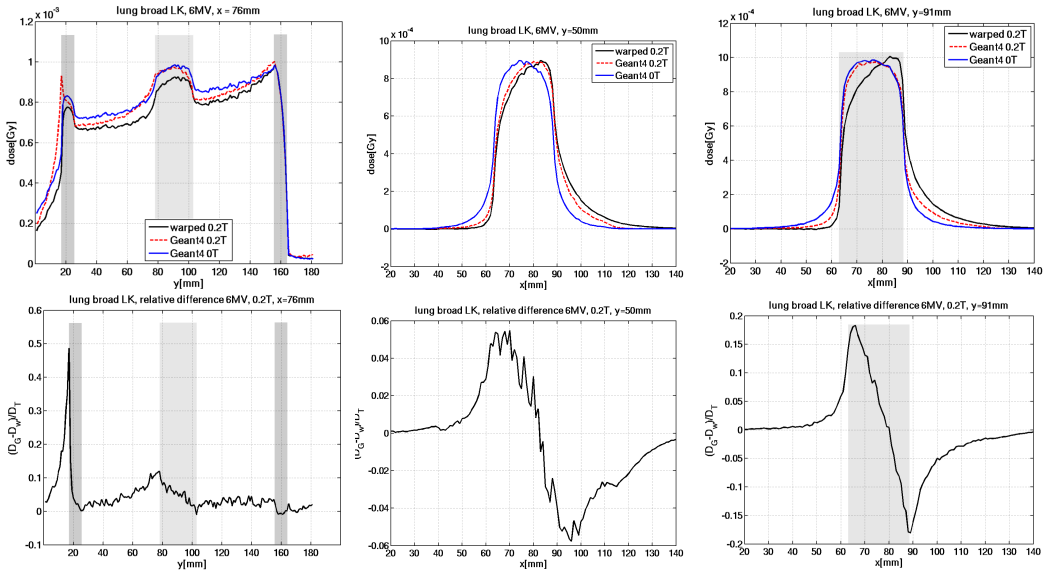


**Figure 10.24** Open field in lung phantom. Top: Depth-dose profile (left) and cross profiles at two different depths of the Monte Carlo simulation ('Geant4', red-dashed) at 0.2 T and the result from warping by means of the lung kernel (black). The profile at 0 T (blue) is given as a reference. The position of the thoracic wall and the tumour are indicated by grey shading. Bottom: difference normalised by tumour dose.

### Lung - Open Field - 0.2 T - Effect of the Magnetic Field

The results of comparing the dose in the magnetic field with the dose at 0 T widely resemble the warping results from using the water kernel as seen in figure 10.25. This is explainable with the rather minor deformation of the kernels in water at 0.2 T compared with the deviations that occur in lung.

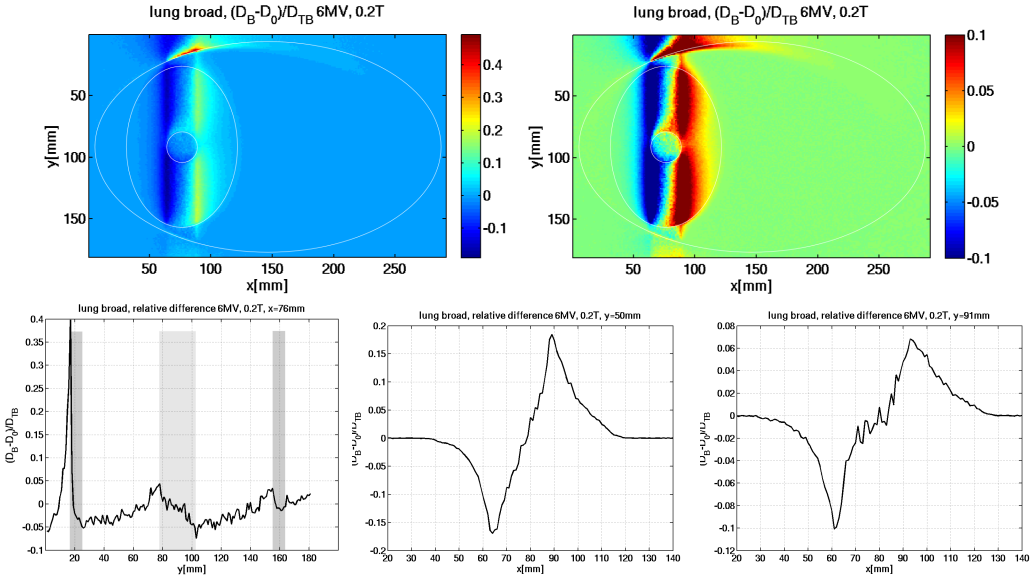


**Figure 10.25** Comparison of the Monte Carlo simulations at 0.2 T and 0 T: difference normalised by the tumour dose in the magnetic field. Top: 2D maps with full and restricted range of values; bottom: profiles along the beam direction (left) and across the beam at two different depths.

However, differences to 0 T are larger than to the warping result, with peak values in the lung cross profile of 20 % here vs. the 15 % reported in figure 10.22, and between +7 % and -10 % in the vicinity of the tumour, compared with +5 % and -7 % above.

### Lung - Open Field - 1.5 T - Water Kernel

At 1.5 T, the magnitude of the effects induced by the heterogeneities increases. Comparing the Monte Carlo simulation and the transformation results in figure 10.26, it can first be remarked that the maximum dose value in the simulation is around 50 % higher than in the warping result using the water kernel. High dose regions due to returning electrons exist at all boundaries from soft tissue to lung or air in the simulation result. From the difference plots in the same figure, it becomes evident that in addition to these ERE discrepancies, deviations also exist across the beam in the lung tissue. The cross profiles of figure 10.27 show that these deviations are of up to 15 % in the lung tissue and nearly 25 % in the vicinity of the tumour.

This time even in the tumour volume, the warping method by means of the water kernel does not suffice to describe the tumour dose accurately due to the overdosage at the tumour boundary caused by the ERE, as the cross profile at y=91 mm reveals. In the centre of the tumour though, the warping matches the simulation. In lung, the warping underestimates the dose in the high dose region and on the beam edge that the electrons get deflected towards, while on the beam edge that the electrons get deflected away from, the warping predicts a higher dose than observed in the simulation.

The depth-dose profiles are dominated by the heterogeneity effects, and it can be remarked that at the interfaces where the beam transits from lung tissue into the tumour or the soft tissue of the thorax, a new build-up effect exists. This is consistent with the findings of Raaynakers et al. in 2004 [27] as reported in section 4.3.

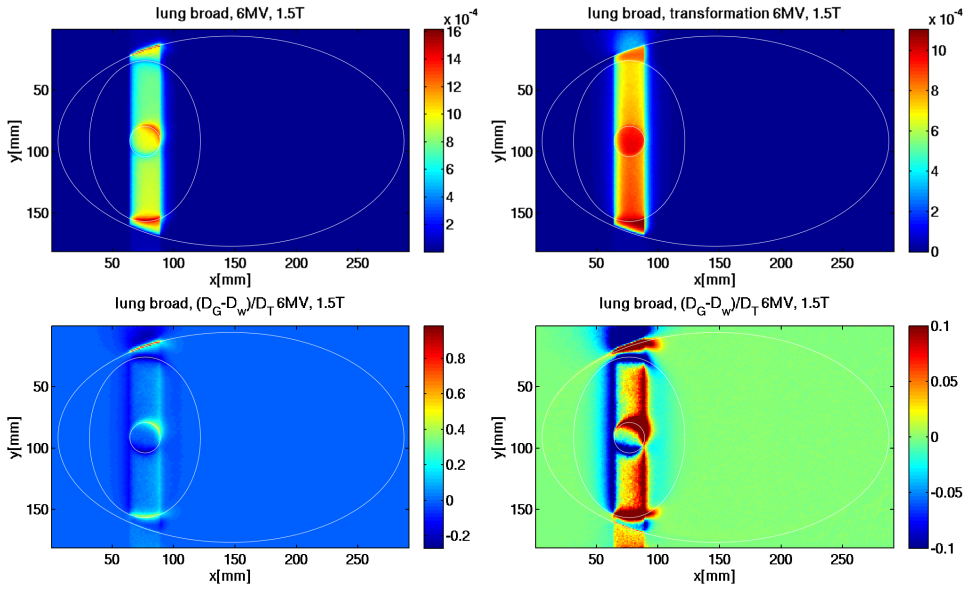


**Figure 10.26** Lung phantom irradiation with an open field. Direction of incidence is from below. Top: Monte Carlo simulation at 1.5 T and warping result using the water kernel (dose values in Gy); bottom: difference plots with two colour scales.

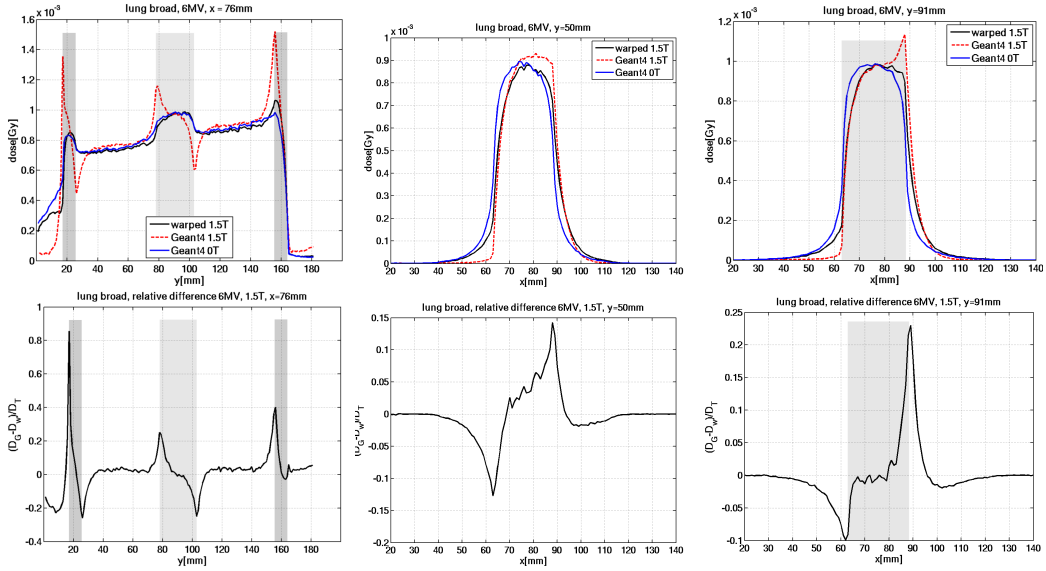


**Figure 10.27** Open field in lung phantom. Top: Depth-dose profile (left) and cross profiles at two different depths of the Monte Carlo simulation ('Geant4', red-dashed) at 1.5 T and the result from warping by means of the water kernel (black). The profile at 0 T (blue) is given as a reference. The position of the thoracic wall and the tumour are indicated by grey shading. Bottom: difference normalised by tumour dose.

### Lung - Open Field - 1.5 T - Lung Kernel

Warping by means of the lung kernel leads to differences of more than 10 % almost everywhere in the soft tissue, as figures 10.28 and 10.29 show. In the homogeneous lung tissue, the deviations are generally smaller; however, in the vicinity of tissue interfaces they are large.

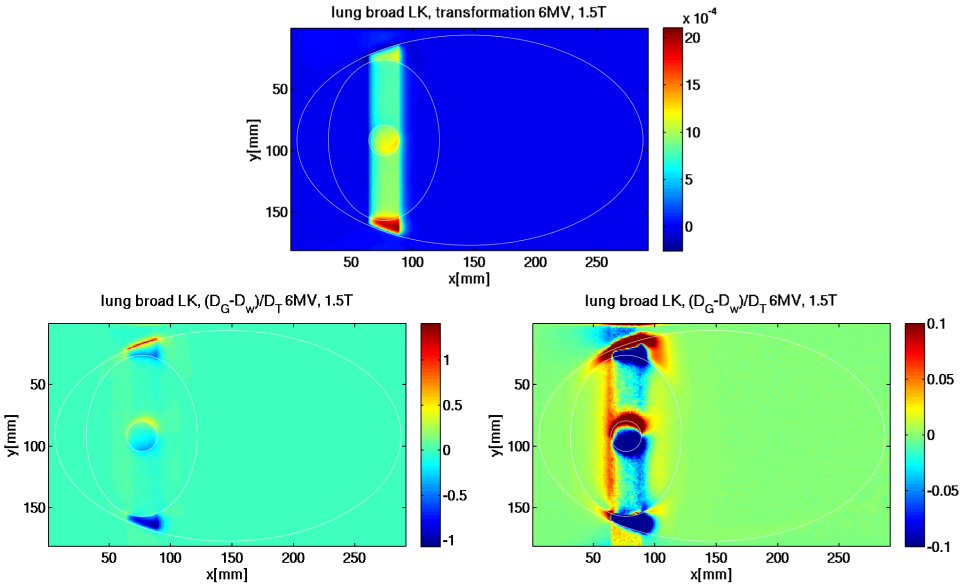


**Figure 10.28** Lung phantom irradiation with an open field. Direction of incidence is from below. Top: warping result using the lung kernel (dose values in Gy); bottom: difference plots with two colour scales.

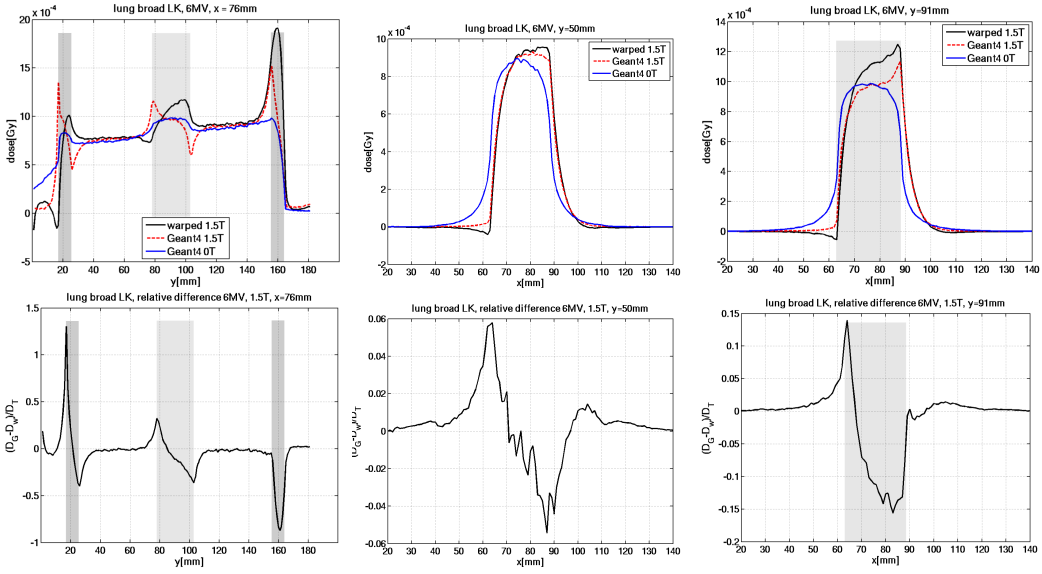


**Figure 10.29** Open field in lung phantom. Top: Depth-dose profile (left) and cross profiles at two different depths of the Monte Carlo simulation ('Geant4', red-dashed) at 1.5 T and the result from warping by means of the lung kernel (black). The profile at 0 T (blue) is given as a reference. The position of the thoracic wall and the tumour are indicated by grey shading. Bottom: difference normalised by tumour dose.

The depth-dose curves confirm these significant differences. In the cross profiles it is seen that in the homogeneous part of the lung, the shape of the warping result agrees rather well with the reference simulation (y=50 mm). However, at the beam edges deviations are observed of ±6 %.

In the tumour (y=91 mm), the shape is obtained whereas the magnitude is overestimated by 10 to 15 %

in most of the volume, and underestimated by the same amount at the beam edge that the electrons get deflected towards.

### Lung - Open Field - 1.5 T - Effect of the Magnetic Field

The comparison between the dose at 1.5 T and the original 0 T distribution is presented in figure 10.30. The magnetic field entirely alters the dose distribution with peak difference values of around 70 % at the tumour boundary.

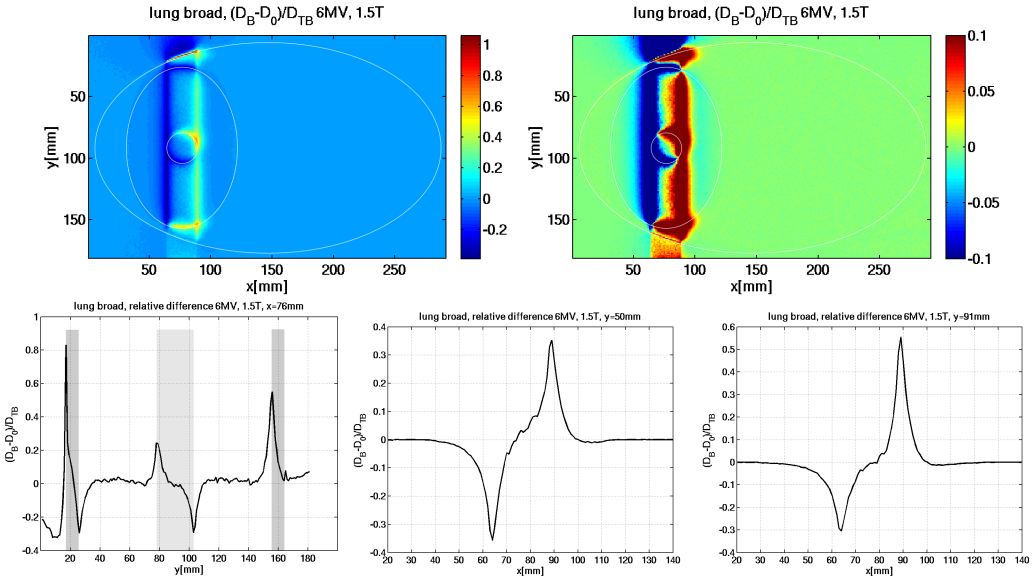


**Figure 10.30** Comparison of the Monte Carlo simulations at 1.5 T and 0 T: difference normalised by the tumour dose in the magnetic field. Top: 2D maps with full and restricted range of values; bottom: profiles along the beam direction (left) and across the beam at two different depths.

Looking at the depth-dose difference, it is remarked that not only the ERE at the exit surface of the beam from the body causes a spike in the dose distribution, but also the two other spikes are of significant magnitude: At the entrance surface of the beam into the lung from the soft tissue of the thorax, the spike is of more than 50 % and at the exit surface from the tumour tissue into the lung, it has a magnitude of more than 20 %. The two dips where the beam enters the tumour and the thorax from within the lung tissue, are almost -30 % in magnitude.

In the homogeneous lung tissue at y=50 mm, the difference cross profile shows values of nearly ±40 %, while the cross profile through the tumour at y=91 mm has its peak at almost 60 % on the side the electrons get deflected to, and -30 % on the beam edge the electrons get deflected away from. As for the 0.2 T case, these values are larger than the differences observed between the warping result and the Monte-Carlo simulation reported above.

In the vicinity of the tumour at y=91 mm, the effect of the 1.5 T magnetic field is very comparable with the effect of the 0.2 T magnetic field shown in figure 10.25, while in the homogeneous lung tissue the differences double with respect to the 0.2 T case.

### Lung - Open Field - 3 T - Water Kernel

At 3 T, deviations are comparable with those at 1.5 T with respect to their magnitude. However, with respect to their spacial pattern, figure 10.31 shows that now in lung tissue, both positiv and negative differences occur at both beam edges.

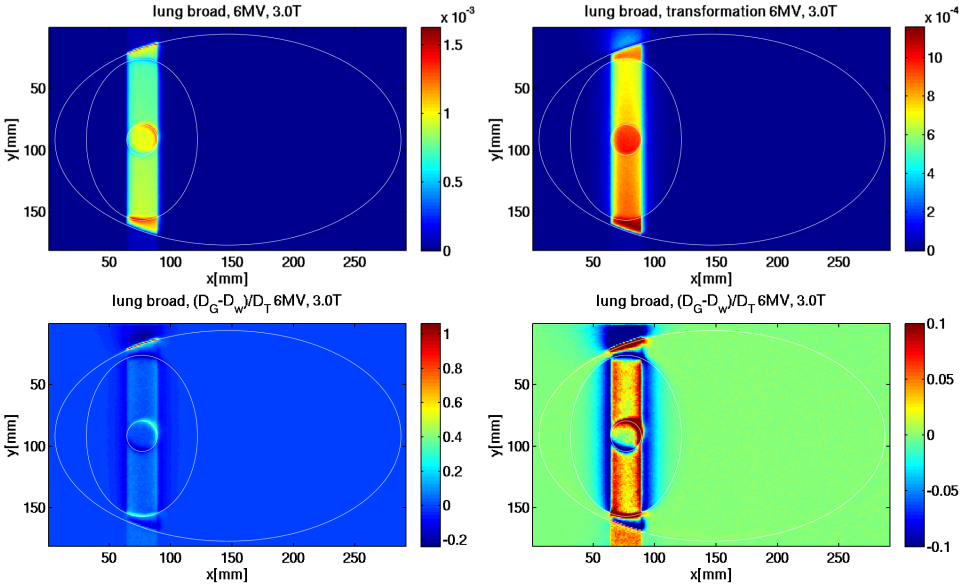


**Figure 10.31** Lung phantom irradiation with an open field. Direction of incidence is from below. Top: Monte Carlo simulation at 3 T and warping result using the water kernel (dose values in Gy); bottom: difference plots with two colour scales.

This pattern is observed in more details in the cross profiles at y=50 mm in the centre of figure 10.32. While in the middle portion of the beam, the warping generally underestimated the dose by 4-5 %, the underestimation reaches peak values of around 10 % before the two profiles cross, followed by an overestimation of the warping by the same amount.

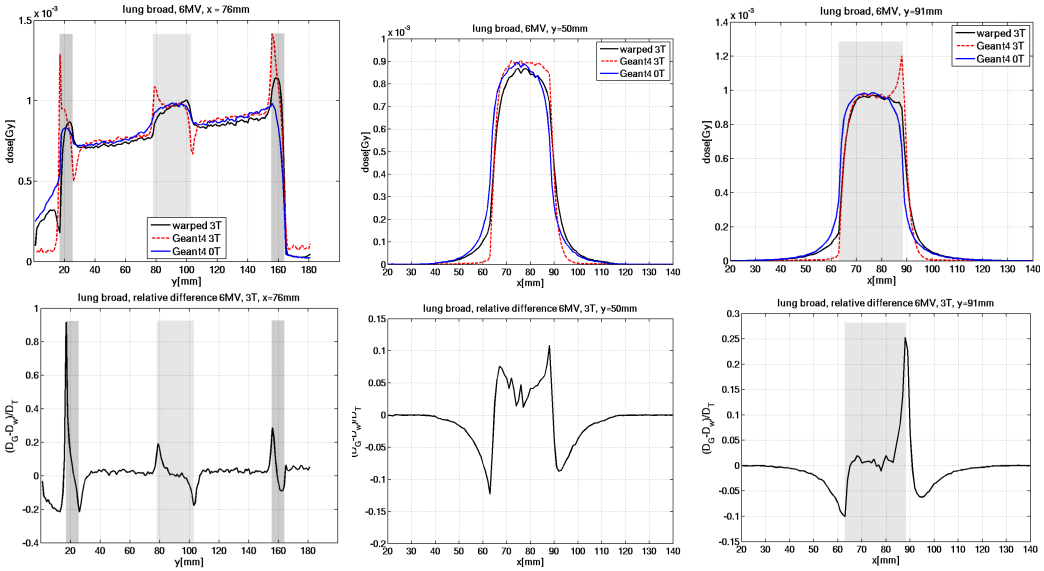


**Figure 10.32** Open field in lung phantom. Top: Depth-dose profile (left) and cross profiles at two different depths of the Monte Carlo simulation ('Geant4', red-dashed) at 3 T and the result from warping by means of the water kernel (black). The profile at 0 T (blue) is given as a reference. The position of the thoracic wall and the tumour are indicated by grey shading. Bottom: difference normalised by tumour dose.

In the tumour at y=91 mm, the cross profiles show that the ERE peak is at around 25 %, as it was for 1.5 T, and the dip on the other side is at around -10 %. It can be remarked, however, that next to the ERE peak and to the outside of the beam, a second dip is present which is not the case for 1.5 T.

### Lung - Open Field - 3 T - Lung Kernel

Warping by means of the lung kernel, it is noticed in figure 10.33 that a strong overdosage is produced in most of the tumour as well as in the thorax tissue. Only at the surfaces where the ERE takes place is the dose higher in the reference simulation.

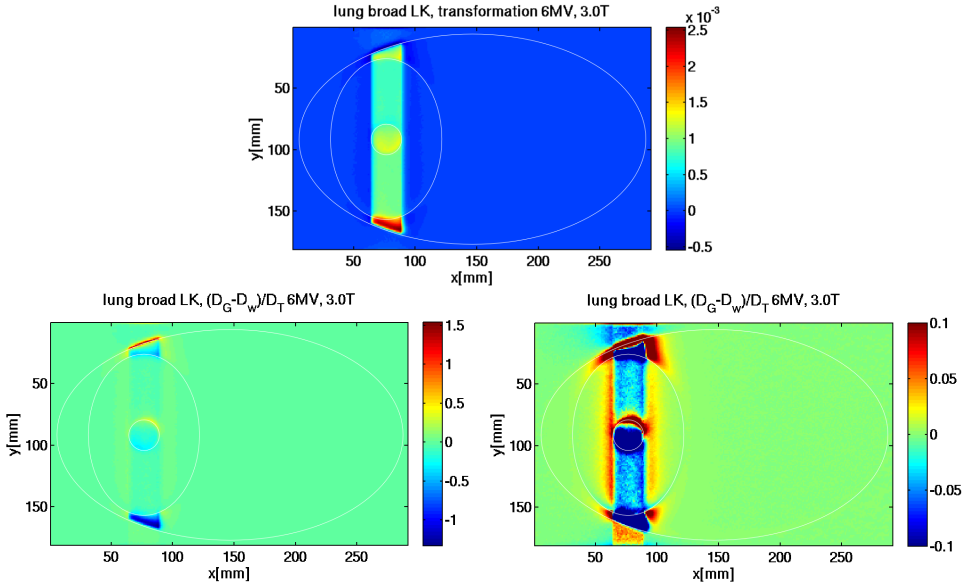


**Figure 10.33** Lung phantom irradiation with an open field. Direction of incidence is from below. Top: warping result using the lung kernel (dose values in Gy); bottom: difference plots with two colour scales.

In the lung tissue, there is again a somewhat symmetric pattern to the central axis, but in contrast to warping with the water kernel, dose is overestimated in the central part and underestimated on the beam edges. The depth-dose profile and the cross profiles in figure 10.34 show more details of the lung warping. The depth-dose behaviour is very similar to what is observed at 1.5 T with peaks and dips that are not modelled well at all tissue interfaces. The maximum deviations in the cross profile through lung tissue at y=50 mm are around +7 % and +3 % on the beam edges, i.e. underestimation of the warping method, and around -3 % to -7 % in the middle portion of the beam, corresponding to an overestimation by the warping method. Across the tumour at y=91 mm, the differences are higher with more than 10 % underestimation in the beam edges, and more than 15 % overestimation in the centre of the beam.

### Lung - Open Field - 3 T - Effect of the Magnetic Field

Looking at the overall impact of the magnetic field compared with the situation at 0 T in figure 10.35, it can be noticed that the differences along the central axis are partially smaller but over the lateral extension of the beam, there are big deviations. Peaks in the cross profile through the lung tissue are as high as ±30 %, and through the tumour, they range up to 60 %. Interestingly, these values are very similar to the 1.5 T results that were reported in figure 10.30, both in the homogeneous part of the lung and in the vicinity of the tumour.

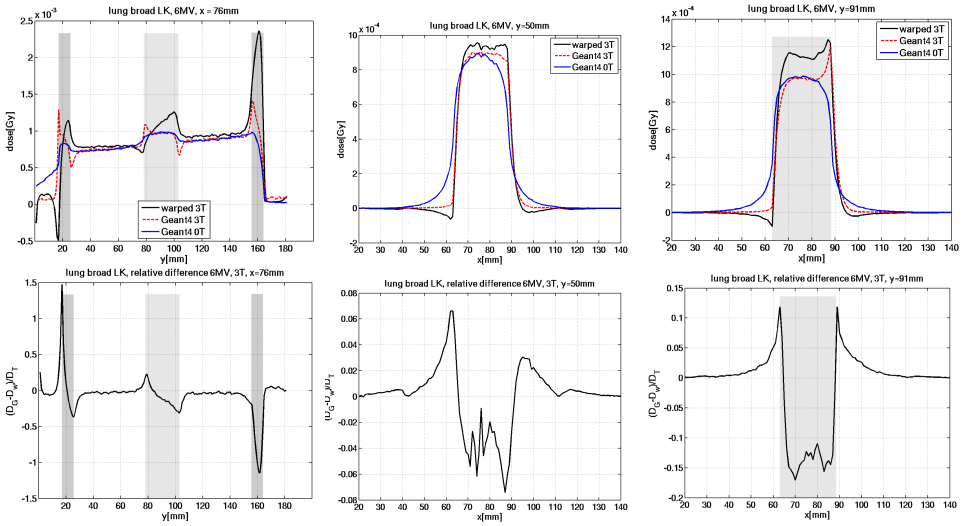


**Figure 10.34** Open field in lung phantom. Top: Depth-dose profile (left) and cross profiles at two different depths of the Monte Carlo simulation ('Geant4', red-dashed) at 3 T and the result from warping by means of the lung kernel (black). The profile at 0 T (blue) is given as a reference. The position of the thoracic wall and the tumour are indicated by grey shading. Bottom: difference normalised by tumour dose.

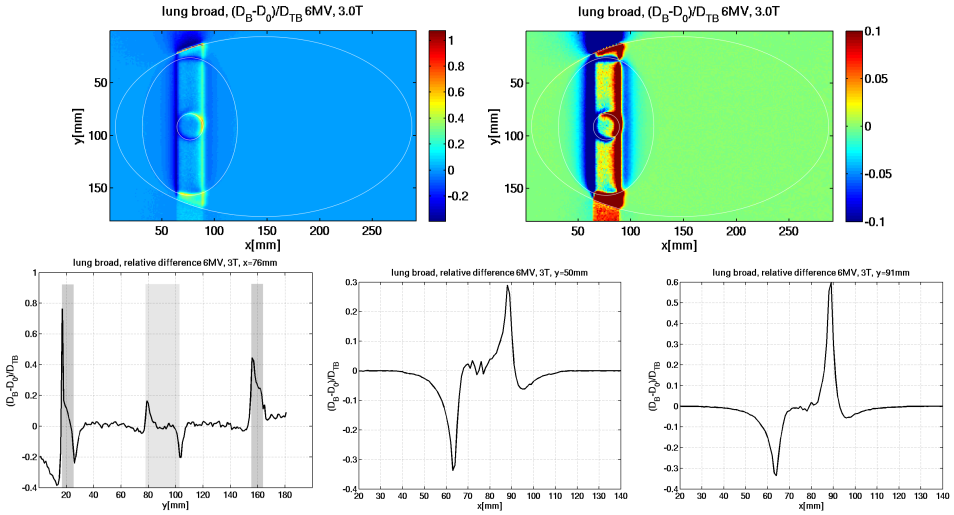


**Figure 10.35** Comparison of the Monte Carlo simulations at 3 T and 0 T: difference normalised by the tumour dose in the magnetic field. Top: 2D maps with full and restricted range of values; bottom: profiles along the beam direction (left) and across the beam at two different depths.

### 10.2.4 Irradiation of Lung Phantom using a Beamlet

In the following the results from warping the 0 T dose distribution of irradiation with one single beamlet in the lung phantom are described. Again, the results of warping by means of the water kernel and the lung kernel are presented, respectively, as well as the overall impact of the magnetic field reported.

#### Lung - Beamlet - 0.2 T - Water Kernel

Figure 10.36 shows two dimensional plots of the dose distributions from the Monte Carlo simulations at 0 T and 0.2 T as well as the warping result using the water kernel, and the difference to the reference simulation. The same colour coding as before is used, displaying the full range of values in the left-hand difference plot, and restricting the values displayed to ±10 % in the right-hand plot.

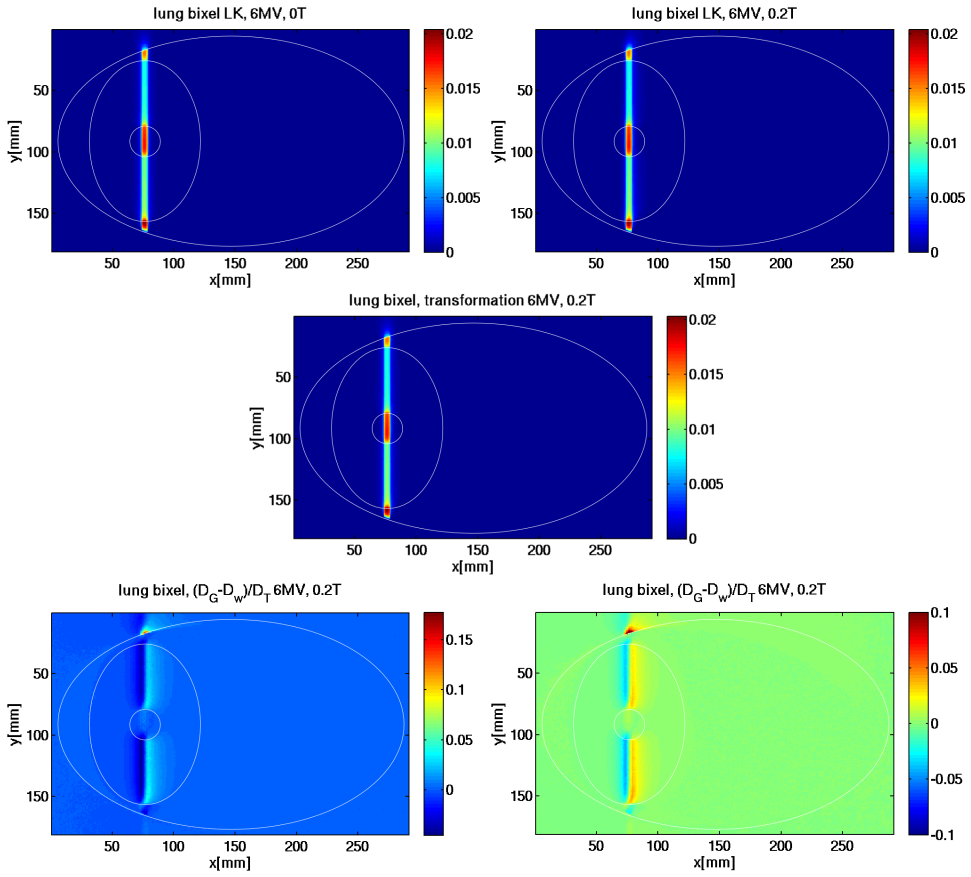


**Figure 10.36** Lung phantom irradiation with a beamlet. Direction of incidence is from below. Top: Monte Carlo simulation at 0 T and at 0.2 T (dose values in Gy); middle: warping result using the water kernel (dose values in Gy); bottom: difference plots with two colour scales.

While visually, hardly any difference can be seen between the Monte Carlo simulations and the warping result, the difference plots reveal that beside the deviation due to the ERE, also in the lung tissue dose differences of up to around ±5 % exist. In the tumour volume, the warping agrees well with the reference simulation.

Depth-dose curves and cross profiles displayed in figure 10.37 confirm the findings. It is observed that in the tumour at y=91 mm, the deviations between the warping and the reference simulation stay below 1 %. This is much better than what was observed in the case of the open field.

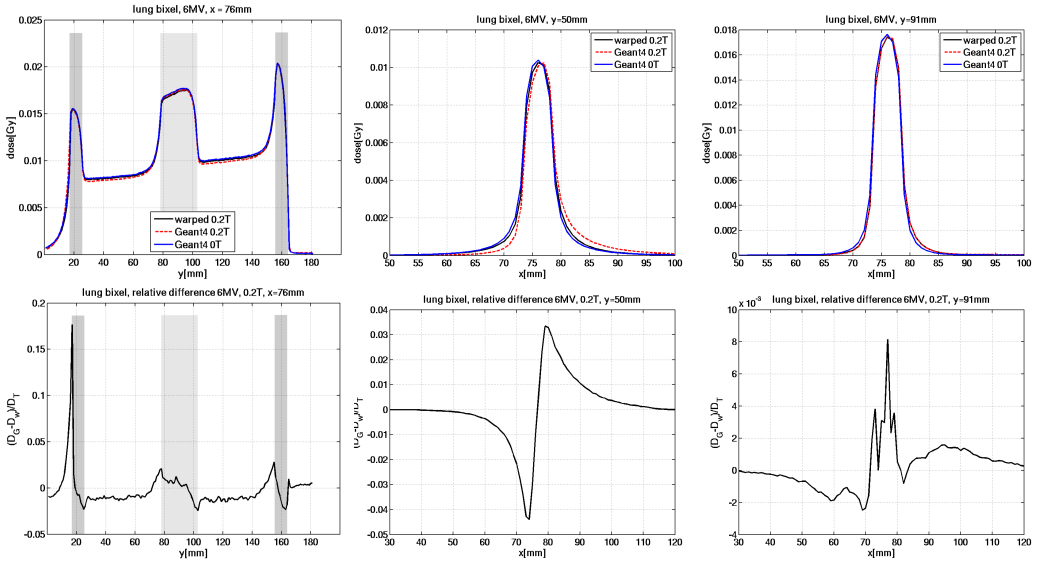


**Figure 10.37** Beamlet in lung phantom. Top: Depth-dose profile (left) and cross profiles at two different depths of the Monte Carlo simulation ('Geant4', red-dashed) at 0.2 T and the result from warping by means of the water kernel (black). The profile at 0 T (blue) is given as a reference. The position of the thoracic wall and the tumour are indicated by grey shading. Bottom: difference normalised by tumour dose.

### Lung - Beamlet - 0.2 T - Lung Kernel

Using the lung kernel instead for warping, the deviations are high in the tumour and smaller in the homogeneous part of the lung as figures 10.38 and 10.39 show. The same was observed when simulating the irradiation with an open field described above.

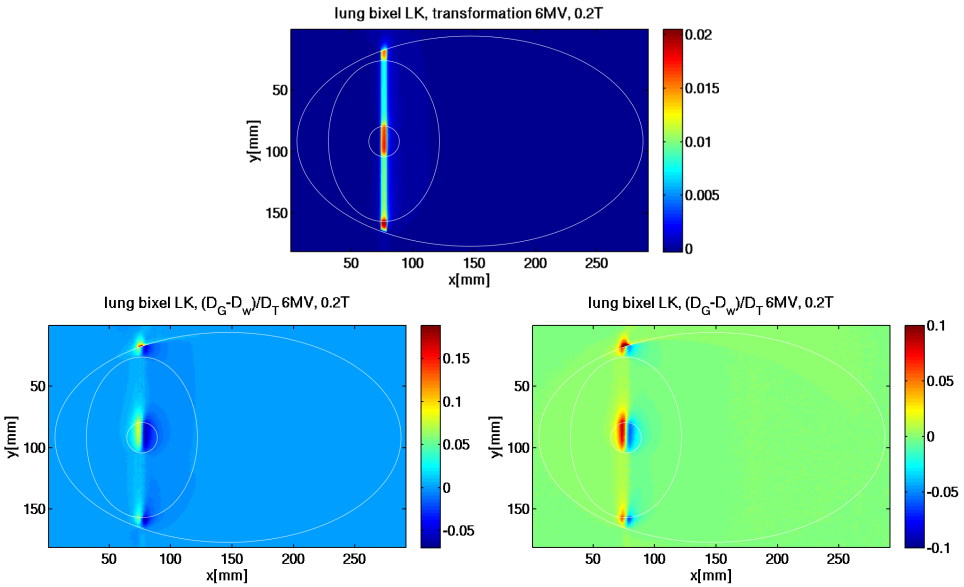


**Figure 10.38** Lung phantom irradiation with a beamlet. Direction of incidence is from below. Top: warping result at 0.2 T using the lung kernel (dose values in Gy); bottom: difference plots with two colour scales.

It can be seen in the cross profile plots that now, deviations in lung stay within 1 % whereas in the tumour they range up to 8 %.

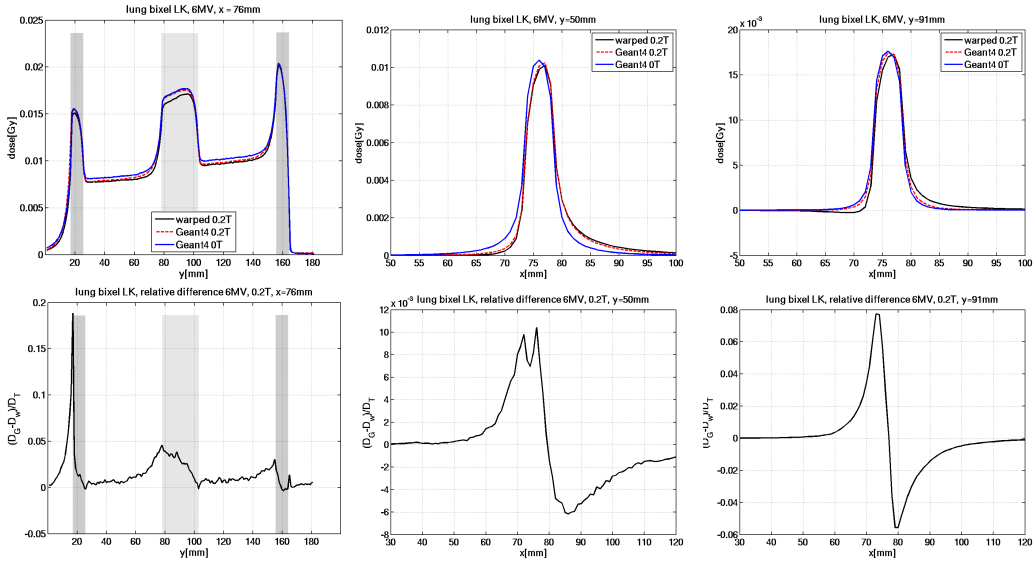


**Figure 10.39** Beamlet in lung phantom. Top: Depth-dose profile (left) and cross profiles at two different depths of the Monte Carlo simulation ('Geant4', red-dashed) at 0.2 T and the result from warping by means of the lung kernel (black). The profile at 0 T (blue) is given as a reference. The position of the thoracic wall and the tumour are indicated by grey shading. Bottom: difference normalised by tumour dose.

### Lung - Beamlet - 0.2 T - Effect of the Magnetic Field

In the comparison of the 0.2 T dose distribution with its 0 T counterpart as shown in figure 10.40, it is observed that both in lung as well as in the tumour, the deviations do not exceed ±6 %.

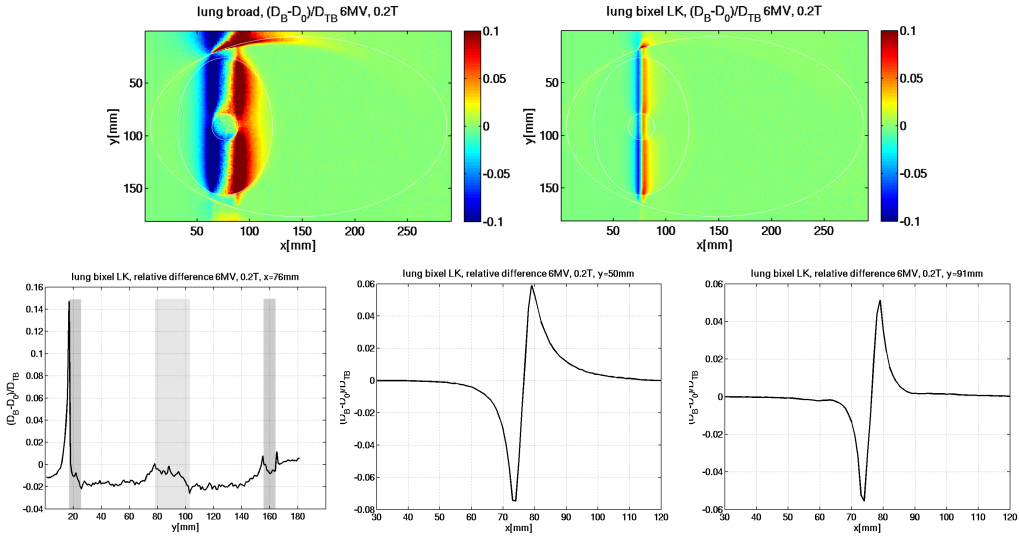


**Figure 10.40** Comparison of the Monte Carlo simulations at 0.2 T and 0 T: difference normalised by the tumour dose in the magnetic field. Top: 2D maps with full and restricted range of values; bottom: profiles along the beam direction (left) and across the beam at two different depths.

### Lung - Beamlet - 1.5 T - Water Kernel

At 1.5 T, deviations again get more pronounced, especially at the tissue interfaces. In the left difference plot in figure 10.41, the higher dose in the reference simulation at locations prone to ERE appears as bright spots. However, the right difference plot shows that differences of more than 10 % are not only observed at tissue heterogeneities but also along the beam.

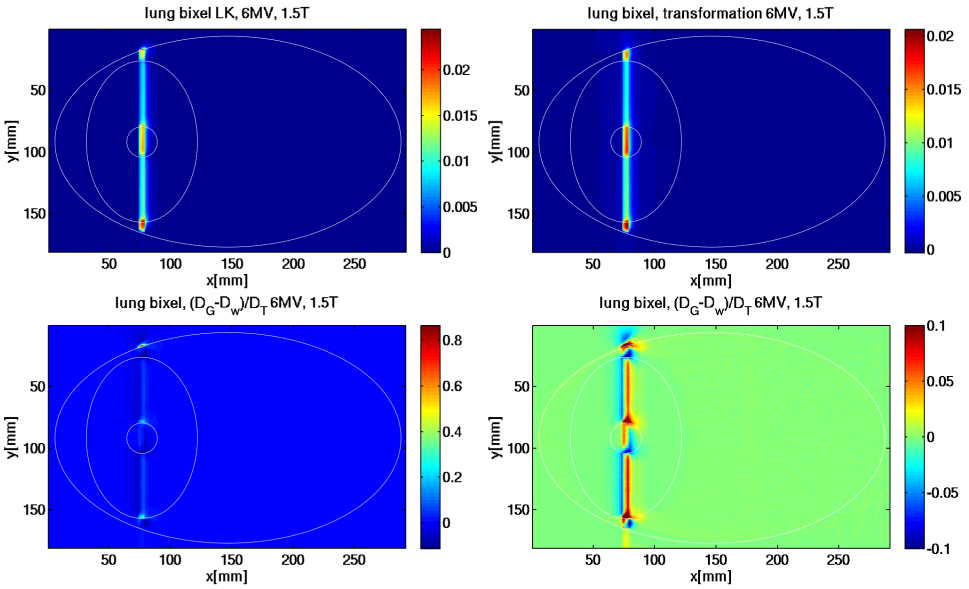


**Figure 10.41** Lung phantom irradiation with a beamlet. Direction of incidence is from below. Top: Monte Carlo simulation at 0 T and at 1.5 T (dose values in Gy). Bottom: warping result using the water kernel (dose values in Gy) and difference plot.

In the depth-dose curves and cross profiles of figure 10.42, it is observed that actually the shape of the dose distribution is modelled rather well by the warping, but in magnitude, deviations of up to 8 % are observed in the lung tissue and even across the tumour, they are of around 5 %.

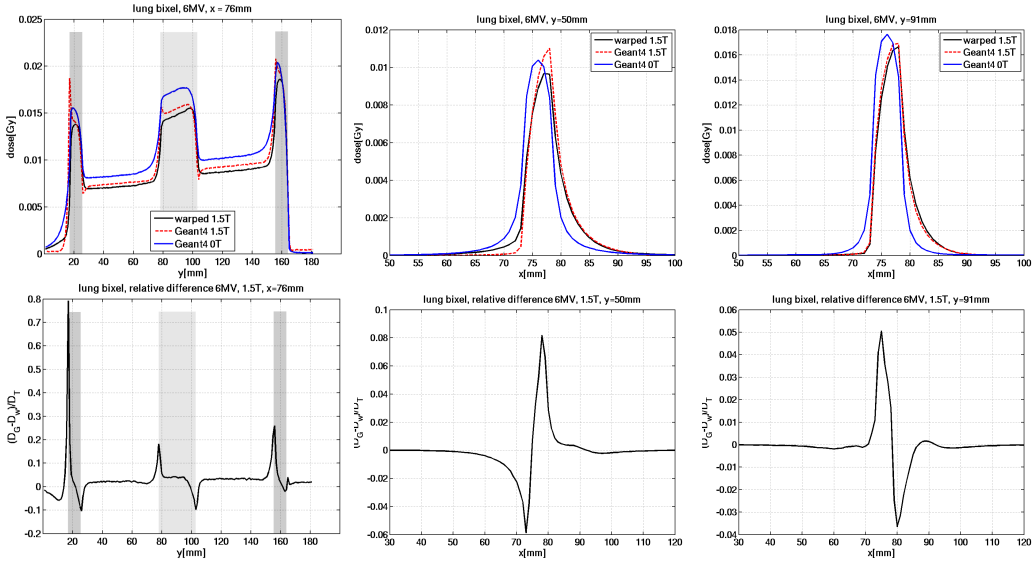


**Figure 10.42** Beamlet in lung phantom. Top: Depth-dose profile (left) and cross profiles at two different depths of the Monte Carlo simulation ('Geant4', red-dashed) at 1.5 T and the result from warping by means of the water kernel (black). The profile at 0 T (blue) is given as a reference. The position of the thoracic wall and the tumour are indicated by grey shading. Bottom: difference normalised by tumour dose.

### Lung - Beamlet - 1.5 T - Lung Kernel

Using the warping based on the lung kernels, observations for 1.5 T are consistent with those for 0.2 T: Maximum deviations occur in the solid tissues of tumour and thorax, while in lung, differences are smaller, as seen in figure 10.43.

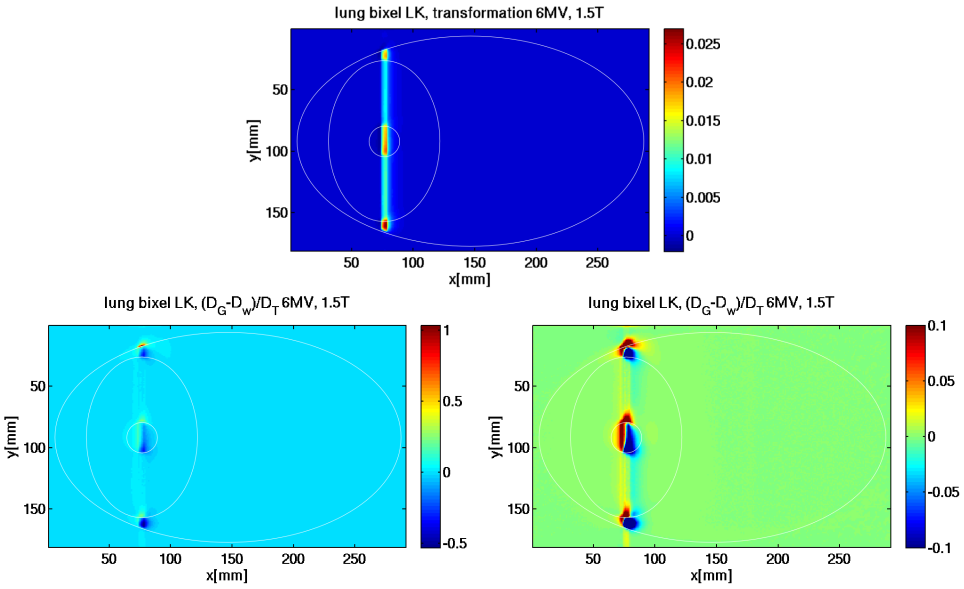


**Figure 10.43** Lung phantom irradiation with a beamlet. Direction of incidence is from below. Top: warping result at 1.5 T using the lung kernel (dose values in Gy); bottom: difference plots with two colour scales.

Depth-dose curve and cross profiles in figure 10.44 confirm this finding. While deviations in the lung tissue stay within ±2 %, the cross profile through the tumour exhibits peaks of up to ±15 %.

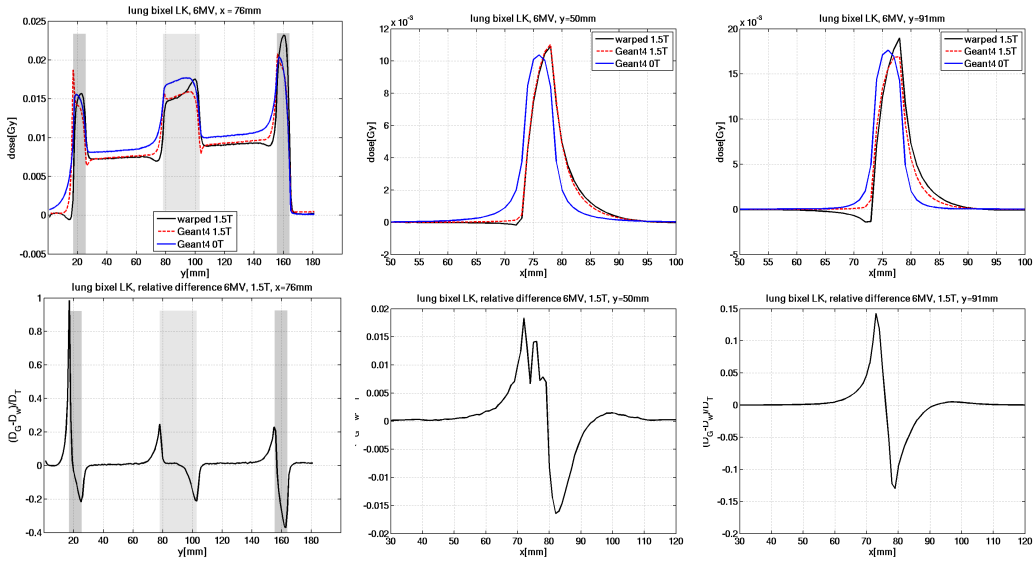


**Figure 10.44** Beamlet in lung phantom. Top: Depth-dose profile (left) and cross profiles at two different depths of the Monte Carlo simulation ('Geant4', red-dashed) at 1.5 T and the result from warping by means of the lung kernel (black). The profile at 0 T (blue) is given as a reference. The position of the thoracic wall and the tumour are indicated by grey shading. Bottom: difference normalised by tumour dose.

### Lung - Beamlet - 1.5 T - Effect of the Magnetic Field

Comparing the simulated dose distribution at 1.5 T with that at 0 T, it is seen that the magnetic field alters the dose deposition by around ±3 % almost everywhere along the beamlet. This is evident from figure 10.45 both from the two dimensional difference maps and the cross profiles.

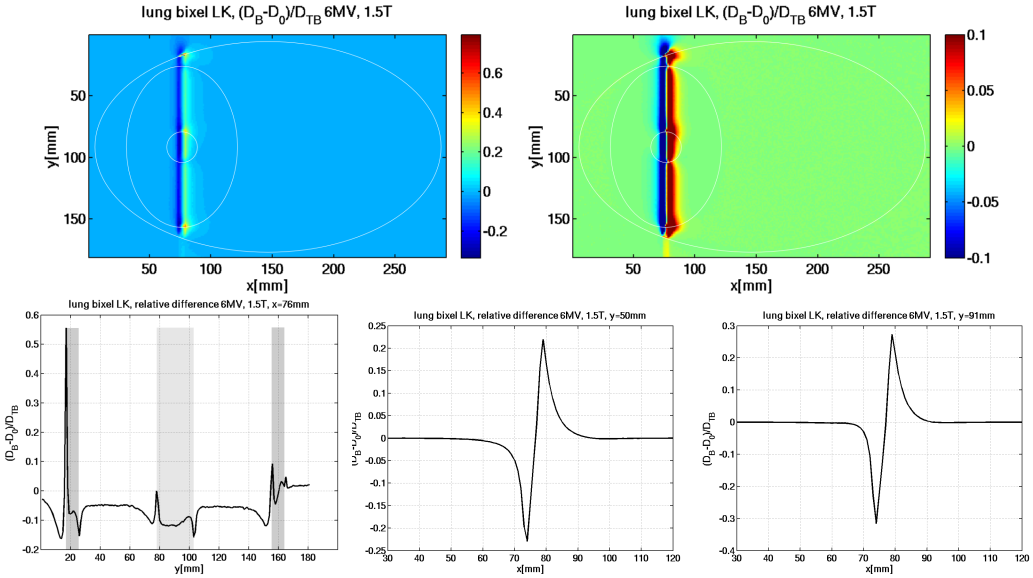


**Figure 10.45** Comparison of the Monte Carlo simulations at 1.5 T and 0 T: difference normalised by the tumour dose in the magnetic field. Top: 2D maps with full and restricted range of values; bottom: profiles along the beam direction (left) and across the beam at two different depths.

### Lung - Beamlet - 3 T - Water Kernel

At 3 T, the situation is very similar to the results at 1.5 T. In figures 10.46 and 10.47, it can be seen that while still the differences at the tissue interfaces are most significant, also in the more homogeneous parts, deviations of more than 10 % are observed.

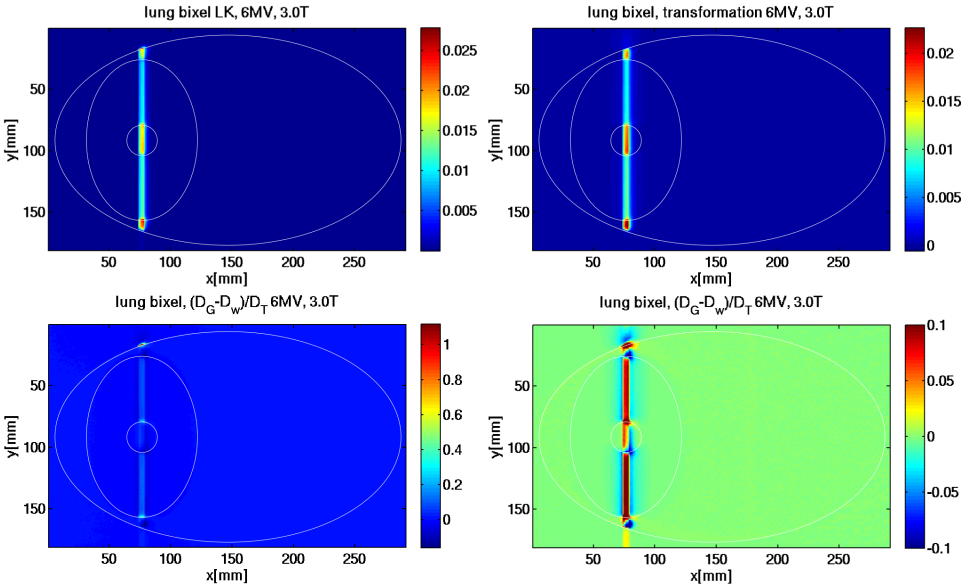


**Figure 10.46** Lung phantom irradiation with a beamlet. Direction of incidence is from below. Top: Monte Carlo simulation at 3 T and warping result using the water kernel (dose values in Gy); bottom: difference plots with two colour scales.

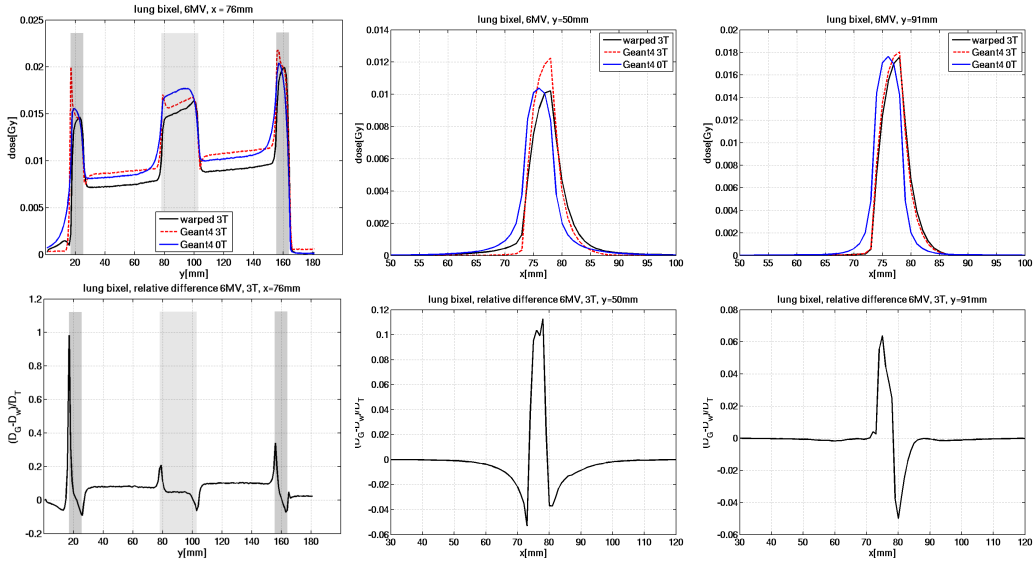


**Figure 10.47** Beamlet in lung phantom. Top: Depth-dose profile (left) and cross profiles at two different depths of the Monte Carlo simulation ('Geant4', red-dashed) at 3 T and the result from warping by means of the water kernel (black). The profile at 0 T (blue) is given as a reference. The position of the thoracic wall and the tumour are indicated by grey shading. Bottom: difference normalised by tumour dose.

The cross profiles through the lung show that in the central part of the beamlet, the warping strongly underestimates the dose by around 10 %. At the beamlet edges, however, it overestimates the dose by up to around 5 %. The cross profile through the tumour shows a smaller underestimation, namely by around 6 %, on the side of the beamlet that the electrons get deflected away from, and a very comparable overestimation of around 5 % at the side the electrons get deflected towards.

### Lung - Beamlet - 3 T - Lung Kernel

Also for warping by means of the lung kernel, the outcome is in line with the findings at 1.5 T. Figures 10.48 and 10.49 display the corresponding plots for this situation.

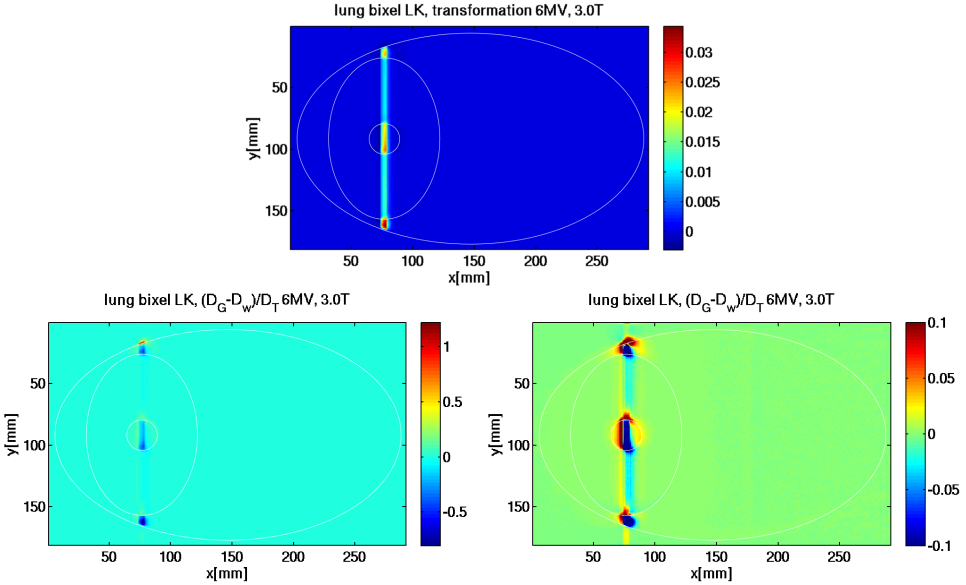


**Figure 10.48** Lung phantom irradiation with a beamlet. Direction of incidence is from below. Top: warping result at 1.5 T using the lung kernel (dose values in Gy); bottom: difference plots with two colour scales.

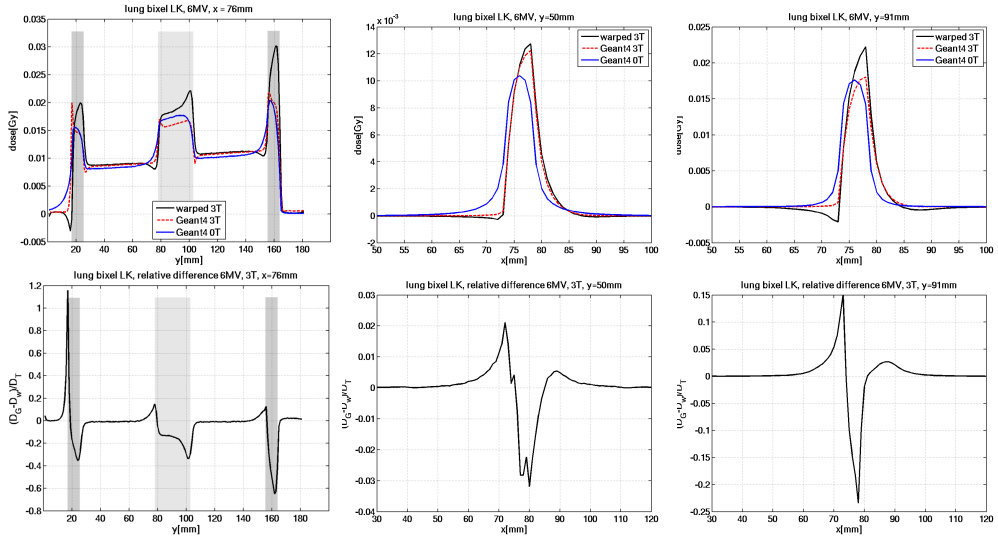


**Figure 10.49** Beamlet in lung phantom. Top: Depth-dose profile (left) and cross profiles at two different depths of the Monte Carlo simulation ('Geant4', red-dashed) at 3 T and the result from warping by means of the lung kernel (black). The profile at 0 T (blue) is given as a reference. The position of the thoracic wall and the tumour are indicated by grey shading. Bottom relative difference normalised to tumour dose.

Deviations at the interfaces are again large, whereas in the homogenous part of the lung, they range between +2 % and -3 %. Across the tumour, there is a strong overestimation of dose by the warping in the central portion of the beamlet which almost 25 % in magnitude, and a severe underestimation at one of the beamlet edges of 15 %.

### Lung - Beamlet - 3 T - Effect of the Magnetic Field

These deviations almost get into the range of difference values observed when comparing the dose in the magnetic field with that at 0 T as is done in figure 10.50. However here, basically everywhere in the high-dose region, deviations are significant and always exceed 10 %. Difference values seen on the cross profiles are around ±20 % in the homogeneous lung tissue, and more than ±30 % across the tumour.

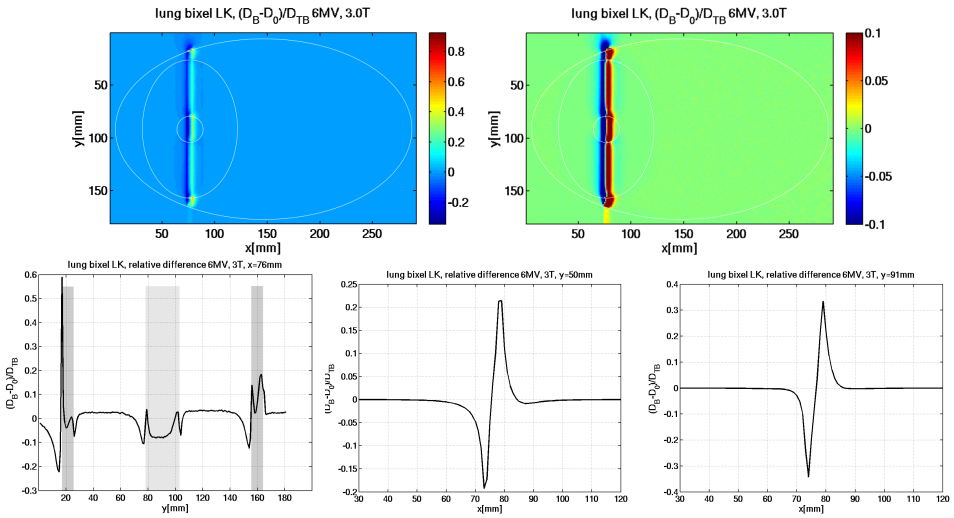


**Figure 10.50** Comparison of the Monte Carlo simulations at 3 T and 0 T: difference normalised by the tumour dose in the magnetic field. Top: 2D maps with full and restricted range of values; bottom: profiles along the beam direction (left) and across the beam at two different depths.

## 10.3 Summary and Conclusion

In this chapter, the warping method was applied to two phantom geometries, and it was seen that as expected, in the skull/brain case the warping performed rather well, while especially at the interfaces between soft tissue and lung, the ERE tremendously affects the dose distribution, and the warping definitely has limitations.

The most important quantitative results are summarised in tables 10.3 and 10.4. The maximum difference values observed with respect to the reference Monte-Carlo simulation are listed, where the data are condensed to one value each, which encompasses both the highest positive and negative deviations observed in the cross profiles at the given depths, normalised by the tumour doses.

**Table 10.3** Brain phantom: relative deviations from the reference simulation

| **brain open** | central beam | | beam edges | | **brain beamlet** | beam edges | |
|---|---|---|---|---|---|---|---|
| | warping | 0 T | warping | 0 T | | warping | 0 T |
| 0.2 T | ±5 % | ±4 % | ±4 % | ±8 % | 0.2 T | ±2 % | ±6 % |
| 1.5 T | ±4 % | ±4 % | ±10 % | ±30 % | 1.5 T | ±8 % | ±40 % |
| 3 T | ±6 % | ±6 % | ±6 % | ±30 % | 3 T | ±7 % | ±45 % |

**Table 10.4** Lung phantom: relative deviations from the reference simulation

| **lung open** | homogen. lung | | lung-tumour-lung | | **lung beamlet** | homogen. lung | | lung-tumour-lung | |
|---|---|---|---|---|---|---|---|---|---|
| | warping | 0 T | warping | 0 T | | warping | 0 T | warping | 0 T |
| 0.2 T<br>water kernel<br>lung kernel | <br>±15 %<br>±6 % | ±20 % | <br>±7 %<br>±20 % | ±10 % | 0.2 T<br>water kernel<br>lung kernel | <br>±5 %<br>±2 % | ±8 % | <br>±1 %<br>±8 % | ±6 % |
| 1.5 T<br>water kernel<br>lung kernel | <br>±15 %<br>±6 % | ±40 % | <br>±25 %<br>±16 % | ±60 % | 1.5 T<br>water kernel<br>lung kernel | <br>±8 %<br>±2 % | ±25 % | <br>±5 %<br>±15 % | ±31 % |
| 3 T<br>water kernel<br>lung kernel | <br>±11 %<br>±7 % | ±33 % | <br>±25 %<br>±17 % | ±60 % | 3 T<br>water kernel<br>lung kernel | <br>±12 %<br>±3 % | ±22 % | <br>±7 %<br>±25 % | ±35 % |

It has to be mentioned that the statistical fluctuations of the Monte-Carlo simulations themselves range up to ±4 % in the brain case using the open field. In the central portion of the beam, deviations between all dose distributions are small, and therefore it is not surprising that here, all difference values are within that statistical range. At the beam edges and in the other beam settings used, systematic deviations are much higher than the statistical noise.

In all settings, it is observed that application of the warping significantly improves the dose estimation, compared with the 0 T cases. The only exception is the dose across the tumour resulting from lung-kernel based warping in the lung open setting, where the warping exhibits deviations from the reference simulation that are twice as high as the difference to 0 T.

The good results in the lung tumour case are somewhat surprising, and it should not be forgotten that high local doses exist due to the ERE that are not listed in the table. It may also be remarked that no definite conclusion can be made on whether the use of the water or the lung kernel is beneficial in the cases studied. In the open field case at 0.2 T and in all beamlet cases, the lung warping performs better in the homogeneous part of the lung and the water kernel performs better across the tumour. However, in the 1.5 T and 3 T cases of the open field, the lung kernel is seen to generally yield better results than the water kernel.

Summarising, it may be said that in the phantom studies considered, the warping has serious issues in determining the exact dose but it is significantly closer to reality than if the magnetic field is not taken into account at all. The potential of the warping method may therefore lie in its use in optimisation as a fast means of dose calculation for multiple evaluation cycles of the objective function but may not be the method of choice if a highly exact dose distribution is desired.

In rather homogeneous regions though, warping was demonstrated in the preceeding chapter 9 to yield acceptable results, and deviations close to the patient surface may be compensated for or be of lower impact (cf. section 9.3).

# Chapter 11

# Optimisation of Treatment Plans

The warping method is finally applied to actual patient cases in a simulation study. In this manner, its applicability in the optimisation process is demonstrated. Based upon the above findings, it is known that the dose calculated in the framework of this demonstration will show deviations from the exact actual dose distributions. Especially will dose at interfaces with tissues of very low density or at the boundaries to air-filled cavities be more severely affected by the magnetic field in reality than what the warping predicts. Therefore, the results reported in this chapter should be seen to serve as a good estimation for the minimal impact - rather than exact determination of the effects - that inclusion of the magnetic field in the optimisation has on dose to the patient and on fluence pattern resulting from optimisation.

## 11.1 Material and Methods

As described in section 1.3, inverse planning for IMRT optimises fluence patterns which are composed of small beam elements, called bixels or beamlets. The dose distribution of such a beamlet in water was used in this study, both for 0 T and warped to magnetic fields of 0.2 T, 1.5 T and 3 T.

Two szenarios were investigated in each patient case considered. First, inverse planning was performed on the basis of the original 0 T beamlet and the warped beamlets, where the same optimisation constraints were used for all calculations such as to find out whether the same plan quality was basically achievable. Second, the fluence patterns resulting from the optimisation using the original 0 T beamlet were kept and the dose from these patterns was subsequently calculated by means of the warped beamlets. In this manner, it was possible to assess the effects that application of a magnetic field would impose on the dose from a conventional optimisation which does not have the capability to include a magnetic field.

The treatment planning system used for this investigation was VIRTUOS (VIRTUal RadiOtherapySimulator, Bendl et al. 1995 [72]) with the inverse planning module KonRadXP (Preiser et al. 1997 [9], Nill et al. 2004 [10]). KonRadXP uses a quadratic objective function (Oelfke and Bortfeld 2001 [11]).

Dose calculation is performed according to the method described by Bortfeld et al. in 1993 [31] and sketched in section 3.2. The input dose distribution used in this method is that of a beamlet of a parallel beam, and only later, the divergence according to the actual source-to-isocentre distance in the treatment situation is used for assignment of correct dose values to the point where dose is calculated.

It is not straight forward that this methodology can also be applied when a magnetic field is present. At 0 T, the dose deposition of secondary electrons is rotational symmetric around the photon beam, such that an interpolation to a divergent beam is possible, whereas in a magnetic field, the orientation of the electrons' initial momenta with respect to the field influences their pattern of motion. In the framework of this study, this was not further investigated but an almost parallel beam geometry was chosen by definition of a source-to-axis distance of 100 m.

A 5×5 mm$^2$ beamlet was used which had been dosimetrically validated for a state-of-the-art multileaf collimator (Siemens 160 MLC$^{TM}$, [73], Tacke et al. 2008 [74]) in combination with a Siemens ARTISTE$^{TM}$ linear accelerator [73]. Profiles of the original 0 T beamlet and the warped beamlets employed in optimisation and dose calculation are shown in figure 11.1 in the results section.

Due to the lack of divergence in the beamlets used and the resulting sharper gradients at the beam edges, the quality of the plans reported in the results section may be better than realistic plans that a patient would be treated with. In addition to that, no sequencing was performed on the fluences resulting from optimisation, such that other small deviations from an actual clinical plan are expected. This study aims at determining the effects of the warping method and cannot be compared with a clinical investigation.

### 11.1.1 Prostate

The first case investigated was a cancer of the prostate. In optimisation, 76 Gy were prescribed uniformly to the gross tumour volume (GTV, cf. section 1.2) and 70 Gy to the clinical target volume (CTV), except for where it included the GTV. Delineated structures are displayed in the results section (11.2.1) among with the dose distributions.

The dose prescription of 76 Gy was to the mean dose ($D_{mean}$) in the GTV which, in case of a Gaussian distribution in the target volume, is very close to the median dose, i.e. the dose that 50% of the volume receive $D_{50\%}$. In the results section, both values will be reported for clarity.

The maximum dose values used in the objective function for the organs at risk were: rectum: 40 Gy, bladder: 30 Gy, left/right femoral head: 40 Gy, normal tissue: 25 Gy.

The beam arrangement was chosen to consist of nine beams in the transverse plane meeting in the isocentre and spaced by 40° each, which is a set-up that is commonly referred to as a nine-beam equiangular coplanar plan. The magnetic field is directed parallel to the patient cranio-caudal axis as would be the case in a cylindrical MR-scanner with a ring gantry.

### 11.1.2 Head and Neck

The second case was a nasopharyngeal cancer. 66 Gy were uniformly prescribed to a boost volume of main tumour growth, while another target volume was defined such as to encompass the lymphatic vessels which present a major source of tumour spread. This volume was prescribed 54 Gy homogeneously. The prescription to the boost volume was again to $D_{mean}$.

The following maximum dose values to organs at risk were used in optimisation: brain stem: 45 Gy, left parotid gland: 20 Gy, right parotid gland: 18 Gy, left temporomandibular joint: 45 Gy, right temporomandibular joint: 45 Gy, spinal cord: 30 Gy (with high priority), normal tissue: 30 Gy (with low priority). In addition, helping volumes were defined in the lung and around the spinal cord. In lung, dose was not allowed to exceed 40 Gy, while in a volume that added a 5 mm margin around the spinal cord, the dose was restricted to below 33 Gy (with very high priority). Another larger volume around the spine has a maximum allowed dose of 30 Gy (with moderately high priority).

A nine-beam equiangular coplanar set up was also chosen in the head-and-neck case in combination with a magnetic field parallel to the patient cranio-caudal axis.

### 11.1.3 Abdomen

In the case of an abdominal cancer, only one target volume existed which was uniformly prescribed 60 Gy to $D_{mean}$.

Maximum dose values used for the organs at risk were 35 Gy to the spinal cord, 35 Gy to each of the kidneys, 35 Gy to the intestines and 20 Gy to the normal tissue.

For the abdominal cancer, the set up consisted of five equiangular coplanar beams, where the magnetic field was again in cranio-caudal direction.

### 11.1.4 Brain

In a meningeoma case, the target volume was prescribed 52.2 Gy, also to $D_{mean}$, where the non-integer dose value results from the original plan only having 29 fractions of 1.8 Gy each.

The organs at risk were allowed a maximum of 20 Gy to the right eye, 25 Gy to the left eye, 30 Gy to the spinal cord, 45 Gy each to the left and right temporomandibular joint, 9 Gy to the left lens, 6 Gy to the right lens, 37 Gy to the part of the brain stem that does not intersect the target volume, and 27 Gy to the normal tissue.

A total of ten beams were selected for the brain tumour, where a nine-beam equiangular coplanar set up was modified by shifting one of the beams by 5° and adding one extra non-coplanar beam. For the extra beam, a table angle of 85° was used in combination with a gantry angle of 300°, leading to the beam being incident approximately through the middle of the frontal bone of the skull. It need be mentioned that such a setting cannot be applied in a cylindrical MR-scanner with a ring gantry but rather with a double-donut MR design. Two magnetic field directions were used in this plan for dose calculation, namely a cranio-caudal field for the coplanar beams and a field perpendicular to the non-coplanar beam that is nearly parallel to the left-right lateral axis of the patient.

## 11.2 Results

### The Beamlets

The beamlets used in dose calculation and optimisation are shown in figure 11.1, where cross profiles through the original 0 T bixel dose are displayed along with the profiles through the warped 0.2 T, 1.5 T and 3 T bixel dose. It can be remarked that while the 1.5 T beamlet does not only get shallower but also broader in x direction, the 3 T beamlet basically has the same width as the 0 T beamlet and only its height is decreased.

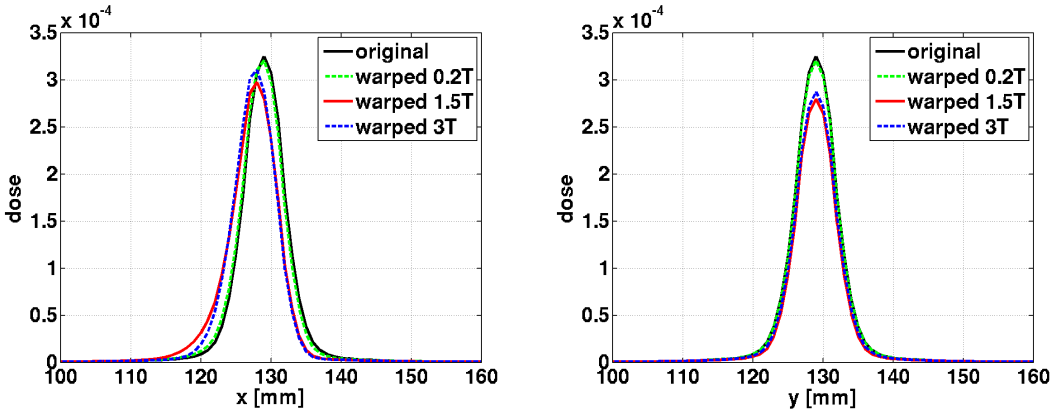


**Figure 11.1** Cross profiles of the bixels used in dose calculation at a depth of 9 cm.

Integrating over the dose values in the x-y plane at the given depth, it is seen that the total energy deposited in the plane is lower for the warped beamlets than for the original beamlets by less than 1 % at 0.2 T, around 1 % at 1.5 T and around 3 % at 3 T. The maximum dose values in the plane differ from the 0 T beamlet by 1 %, 8 % and 4 %, respectively, where both the maximum and integral dose values were averaged over the respective values at depths of 6 cm, 9 cm and 12 cm. These values correspond to the findings of chapter 9 above, where it was seen in figures 9.7 and 9.9 that beyond the depth-dose maximum, the depth-dose profile in case of the 3 T simulation was lower by around 4 % with respect to the 0 T profile. Bearing in mind that the total energy deposited in the 3 T point kernel was found to be lower by around 2 % than in the 0 T kernel (discussion in section 9.3), the actual value for the dose difference at depth is very likely to be 1-2 % only, but it is certain that the dose at depth is lower.

For the 1.5 T beamlet, the effect on the dose delivered by an actual irregular beam shape is not so clear considering the significant decrease in maximum dose value and the moderate decrease when looking at the energy deposited in the whole plane, since dose contributions from several beamlets will superimpose. In the 1.5 T cross profiles of figure 9.9 above, it was also seen that an open field of $(2\ \text{cm})^2$ (4×4 beamlets) causes a wider dose fall-off on one beamedge than on the other. In fact, this fall-off stretches over half of the profile, such that only after 1 cm, the maximum dose value is reached. Therefore, it is most reasonable to expect that at 1.5 T, regions will exist where resulting dose values at depth will be significantly smaller than the corresponding 0 T values, whereas in other regions the effects will be less pronounced. For any region in the fluence applied, where the fluence is high over a width of only 1 or 2 beamlets in x direction, but lower next to that high fluence pattern, the depth-dose profile caused by that part of the fluence will be lower than at 0 T.

### The Cases

For each of the cases reported below (prostate 11.2.1, head and neck 11.2.2, abdomen 11.2.3, brain 11.2.4), first the CT image is shown on which the delineated structures for treatment planning are seen, and which is overlaid with the 0 T dose distribution. Subsequently, dose volume histograms are reported as well as dose-volume measures, based on the current ICRU recommendations [75].

For the respective target volumes these were both the mean dose $D_{mean}$ that the dose was prescribed to and the median dose, which is the dose that 50 % of the volume receive ($D_{50\%}$). In addition, the near-maximum dose which only 2 % of the volume receive ($D_{2\%}$), and the near-minimum target dose which 98 % of the target volume receive, are reported. The homogeneity index HI=($D_{2\%}$-$D_{98\%}$)/$D_{50\%}$ is also given for the primary target structure. Images follow that visualise the effects on the dose distribution in more detail.

### 11.2.1 Prostate

Overview CT images overlaid with the dose distribution at 0 T are displayed in figure 11.2. More detailed images of dose distributions will be shown further below. Delineated volumes are the GTV and CTV in the prostate, along with the bladder, the rectum, both femoral heads and the outer contour of the patient.

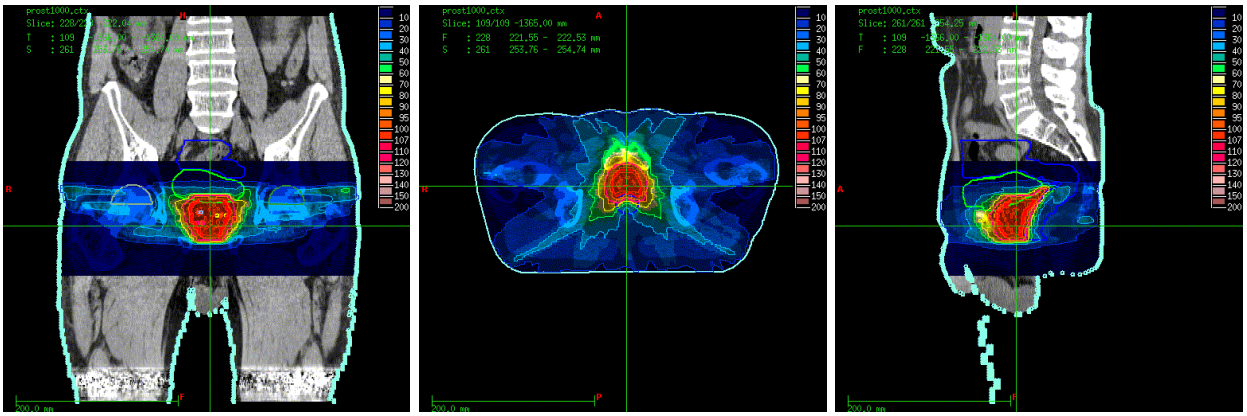

**Figure 11.2** CT images of the prostate case, overlaid with the dose distribution from optimisation using the original 0 T beamlet.

#### Optimisation using Warped Beamlets

Using the warped beamlets in optimisation, the target coverage achieved did not differ from the optimisation result using the original 0 T beamlets, irrespective of the magnetic field the beamlet was warped to. This can be seen from the dose-volume histograms displayed in figure 11.3, where no distinction is possible between the dashed and solid lines representing the results from optimisation using warped beamlets and with the original 0 T beamlet, respectively. Tables 11.1 and 11.2 further list the dose values in the GTV and CTV, and also here, the values agree.

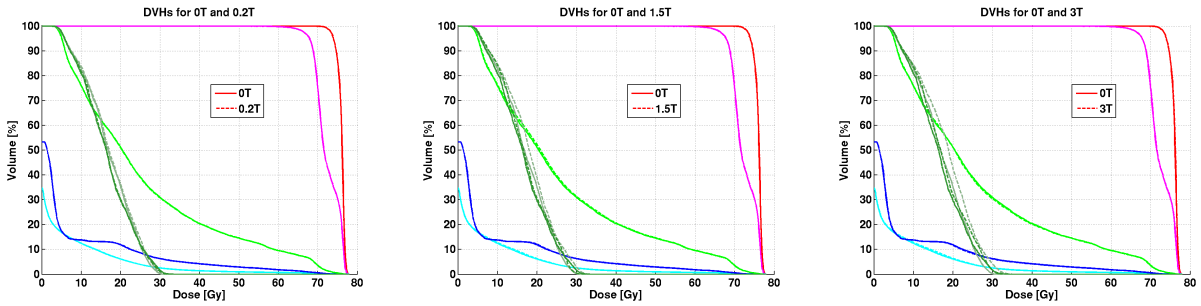


**Figure 11.3** Dose-volume histograms for plans optimised using the original (solid lines) and the warped (dashed lines) beamlets. From left to right: 0.2 T, 1.5 T, 3 T. The structures included are the GTV (red), CTV (magenta), bladder (bright green), rectum (blue), left (dark green) and right femoral head (grey green) and outer patient contour (cyan).

**Table 11.1** Dose-volume measures in the GTV of the prostate

| | $D_{98\%}$[%] | $D_{98\%}$[Gy] | $D_{50\%}$[%] | $D_{50\%}$[Gy] | $D_{mean}$[%] | $D_{mean}$[Gy] | $D_{2\%}$[%] | $D_{2\%}$[Gy] | HI |
|---|---|---|---|---|---|---|---|---|---|
| 0 T | 96.3 | 73.2 | 100.2 | 76.2 | 100.0 | 76.0 | 101.7 | 77.3 | 0.05 |
| 0.2 T | 96.2 | 73.1 | 100.2 | 76.1 | 100.0 | 76.0 | 101.7 | 77.3 | 0.05 |
| 1.5 T | 96.3 | 73.2 | 100.2 | 76.2 | 100.0 | 76.0 | 101.6 | 77.2 | 0.05 |
| 3 T | 96.3 | 73.2 | 100.3 | 76.2 | 100.0 | 76.0 | 101.7 | 77.3 | 0.05 |

**Table 11.2** Dose-volume measures in the CTV of the prostate

| | $D_{98\%}$[%] | $D_{98\%}$[Gy] | $D_{50\%}$[%] | $D_{50\%}$[Gy] | $D_{mean}$[%] | $D_{mean}$[Gy] | $D_{2\%}$[%] | $D_{2\%}$[Gy] |
|---|---|---|---|---|---|---|---|---|
| 0 T | 87.0 | 66.1 | 94.1 | 71.5 | 95.2 | 72.3 | 101.3 | 77.0 |
| 0.2 T | 86.9 | 66.1 | 94.1 | 71.5 | 95.2 | 72.3 | 101.3 | 77.0 |
| 1.5 T | 86.8 | 66.0 | 94.2 | 71.6 | 95.2 | 72.3 | 101.3 | 77.0 |
| 3 T | 86.9 | 66.1 | 94.2 | 71.6 | 95.2 | 72.4 | 101.4 | 77.0 |

Also in the organs at risk, differences are minor. Both in the rectum, in the bladder and in the left femoral head, the DVH curves of the optimisation using the original and the warped beamlet almost perfectly superpose in figure 11.3, and also the values in table 11.3 agree. The dose to the right femoral head shows a small increase for 1.5 T and 3 T which is seen in the DVH's. Here, the dashed lines are slightly shifted to the right, where the effect is stronger at 3 T than at 1.5 T. The shift also manifests in the dose-volume measures listed in table 11.3, where both the mean dose $D_{mean}$ and the near-maximum dose $D_{2\%}$ are increased by around 5 % at 1.5 T with respect to the 0 T result, and by 10 % at 3 T.

**Table 11.3** Dose-volume measures in the organs at risk for the prostate case

| | $D_{98\%}$[%] | $D_{98\%}$[Gy] | $D_{mean}$[%] | $D_{mean}$[Gy] | $D_{2\%}$[%] | $D_{2\%}$[Gy] |
|---|---|---|---|---|---|---|
| **rectum** | | | | | | |
| 0 T | - | - | 8.0 | 6.1 | 77.0 | 58.5 |
| 0.2 T | - | - | 8.0 | 6.1 | 77.3 | 58.7 |
| 1.5 T | - | - | 8.0 | 6.1 | 77.2 | 58.6 |
| 3 T | - | - | 7.9 | 6.0 | 77.3 | 58.8 |
| **bladder** | | | | | | |
| 0 T | 5.6 | 4.3 | 33.9 | 25.8 | 94.0 | 71.5 |
| 0.2 T | 5.6 | 4.3 | 33.9 | 25.7 | 94.0 | 71.4 |
| 1.5 T | 5.7 | 4.4 | 34.2 | 26.0 | 94.1 | 71.5 |
| 3 T | 5.7 | 4.4 | 33.8 | 25.7 | 94.0 | 71.5 |
| **l. femoral head** | | | | | | |
| 0 T | 6.4 | 4.8 | 21.6 | 16.4 | 39.1 | 29.7 |
| 0.2 T | 6.4 | 4.9 | 21.7 | 16.5 | 38.7 | 29.4 |
| 1.5 T | 6.6 | 5.0 | 22.1 | 16.8 | 37.7 | 28.6 |
| 3 T | 6.5 | 4.9 | 22.5 | 17.1 | 39.0 | 29.6 |
| **r. femoral head** | | | | | | |
| 0 T | 6.3 | 4.8 | 22.2 | 16.9 | 37.5 | 28.5 |
| 0.2 T | 6.4 | 4.9 | 22.6 | 17.2 | 38.2 | 29.0 |
| 1.5 T | 6.4 | 4.9 | 23.4 | 17.8 | 40.2 | 30.6 |
| 3 T | 6.2 | 4.7 | 24.0 | 18.2 | 41.3 | 31.4 |

Figure 11.4 shows differences between the plans from optimisation by means of the warped beamlet and the plan optimised using the 0 T beamlet, where the latter is used as reference. Local differences did not exceed 10 %, and only values between 1 and 10 % are displayed which is the standard representation of the VIRTUOS treatment planning system used [72]. Red colour means that in the plan optimised using the warped beamlet, the dose is higher than in the 0 T plan, while blue represents a lower dose. For each magnetic field, the distribution in the transverse plane is given at three different depths.

The difference plots are consistent with the findings from the DVH's and dose-volume measures de-

scribed above in that no difference of the dose to the target volumes is seen. It can be remarked that in order to achieve this same dose, partially other beamlets are chosen by the inverse planning program. Differences are minor at 0.2 T and get bigger at 1.5 T and 3 T.

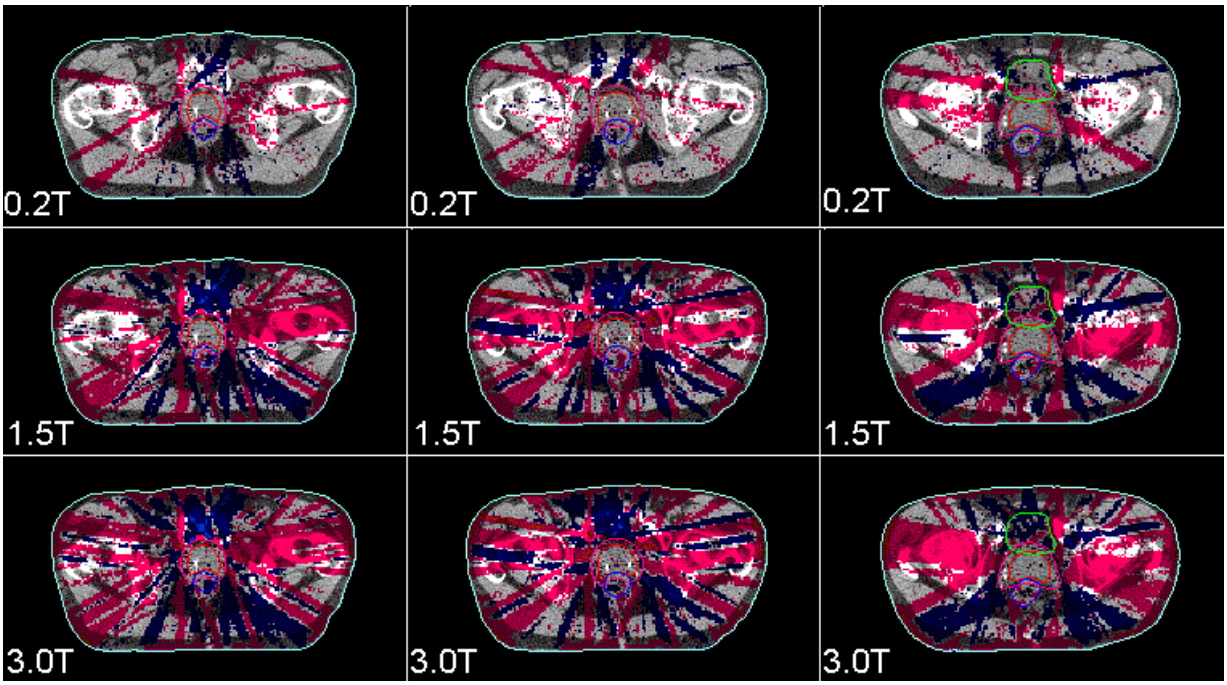


**Figure 11.4** Difference plots of the warped beamlet plans with respect to the 0 T plan at different depths (columns) for the prostate case. Deviations between 1 and 10 % are shown, where red represents an overdosage in the warped beamlet plan, and blue represents an underdosage.

At 1.5 T and 3 T, it is observed that generally, the dose right below the surface of the patient is higher in the plans optimised using the warped beamlets. This is in agreement with the findings from the homogeneous warping experiments described above. It was shown in figure 9.7 and 9.9, that due to the sideward deflection of the secondary electrons in a magnetic field, the dose maxima are at a shallower depth than if no field is present since dose is deposited closer to the entrance surface of the beam.

Beyond the dose maxima, the deflection results into a relatively lower depth-dose profile in the presence of a magnetic field which is also seen in the cross profile of the warped beamlet in figure 11.1. Therefore it is not surprising that patterns exist in the difference plots of figure 11.4 that show a higher dose close to the entrance surface but then a lower dose along the beam path.

Another consequence of the relatively lower depth-dose profile at the depth of the tumour is an increase of the total energy deposited in the patient. In order to obtain the same dose at the depth of the target, a higher fluence is required and thereby, more dose is deposited in the entrance region of the beam where in the presence of a magnetic field, sideward-deflected electrons deposit their energy.

Table 11.4 lists the integral dose of the optimsation results, which is given in the top row as the product of the mean dose and the total volume in which dose calculation was performed $D_{mean,tot}$ in units of gray, and the total volume $V_{tot}$ itself, in litres, such that $E_V = V_{tot} \cdot D_{mean,tot}$, where $V_{tot}$ was about 26 litres. (Defining integral dose by this product is in agreement with ICRU report 83 [75], and this value would agree with the total energy deposited if the patient consisted homogeneously of water with a density of 1kg/l.) The lower row of the table shows the quotient $E_{V,B}/E_{V,0T}$ of the integral dose in each plan, divided by the integral dose in the 0 T plan.

**Table 11.4** Integral dose for the different optimisation results, $V_{tot}$=26.1 litres

| | 0 T | B = 0.2 T | B = 1.5 T | B = 3 T |
|---|---|---|---|---|
| integral dose: $E_V$[Gy·l] | 95.4 | 95.6 | 96.7 | 97.5 |
| relative to 0 T: $E_{V,B}/E_{V,0T}$ | 1.000 | 1.003 | 1.014 | 1.022 |

### Differences in Fluence Patterns for Same Dose to the Tumour

In order to assess the increase in fluence required to produce the same dose in the tumour and which leads to the increase in integral dose described above, a summation of the beamlet weights resulting from the different optimisation procedures was chosen as a measure. Beamlet weights scale with the fluence that is delivered for each individual beamlet, and since all elemental beamlets are of same cross-sectional area, namely 5×5 mm$^2$ in the isocentre, and the same number of beamlets is used in each optimisation result, a ratio of the beamlet weights' sum, from optimisation using the warped and the original beamlet, respectively, may be used in this evaluation.

The sum was calculated over all beamlets from all beam directions, and if $N$ is the total number of beamlets, and $w_{0T,i}$, $w_{0.2T,i}$, $w_{1.5T,i}$ and $w_{3T,i}$ represent the weights of the i's beamlet of the 0 T, 0.2 T, 1.5 and 3 T optimisation result, respectively, the increase was found to be

$$\frac{\sum_{i=1}^{N} w_{0.2T,i}}{\sum_{i=1}^{N} w_{0T,i}} = 1.005, \quad \frac{\sum_{i=1}^{N} w_{1.5T,i}}{\sum_{i=1}^{N} w_{0T,i}} = 1.020 \quad \text{and} \quad \frac{\sum_{i=1}^{N} w_{3T,i}}{\sum_{i=1}^{N} w_{0T,i}} = 1.036.$$

This is in agreement with the lateral integration of the beamlet cross profiles given in figure 11.1 above and the findings of chapter 9 reported there, where it was seen that at greater depths, the 3 T dose in the kernel is lower by 4 % which probably corresponds to actual 2 %. These values are consistent with the increase in integral dose reported in table 11.4: a 4 % increase in fluence results only in a 2 % increase in total energy deposited, since 2 % of the energy are lost due to the energy issue in the warping kernel.

Maps of the beamlet weights resulting from the optimisation using the different beamlets are displayed in figure 11.5. The top row shows the 0 T ($F_{0T}$) result, where the patterns from all beam angles are seen, i.e. from 0° to 320°. In the following rows, the result from one optimisation procedure with a warped beamlet (e.g. $F_{0.2T}$) and the difference between this results and the 0 T result (e.g $F_{0.2T}$-$F_{0T}$) are given, respectively. The axes in the upper right corner shows the collimator x and y direction, according to which the beamlet weights are organised in each plot.

It is observed that even though the patterns are generally very alike for each individual angle, irrespective of the magnetic field that the beamlet is warped to, deviations become apparent from the difference plots. At 0.2 T, these deviations are insignificant, which is consistent with the fact that the dose profiles of 0 T and 0.2 T only show minor if any differences. For 1.5 T and 3 T the differences in the dose profile increase, and so do the differences in beamlet weight patterns.

A tendency can be remarked that beamlets in positive x direction rather have higher weights, and those in the opposite direction rather have lower weights. This observation also matches the direction of action of the magnetic field that deforms the beamlets into negative x direction as figure 11.1 reveals. In order to compensate for this deformation, the weights of beamlets of higher x position need to be higher.

### Differences in Dose for Same Fluence Patterns

Using the beamlet weight pattern and therefore also the fluence of the 0 T optimisation but performing the dose calculation by means of the warped beamlets, the DVH's shown in figure 11.6 result. Still no changes can be observed in the 0.2 T case; however, at 1.5 T and 3 T the effects on the target volume are significant. Also in some of the organs at risk, a slight drop in dose can be remarked.

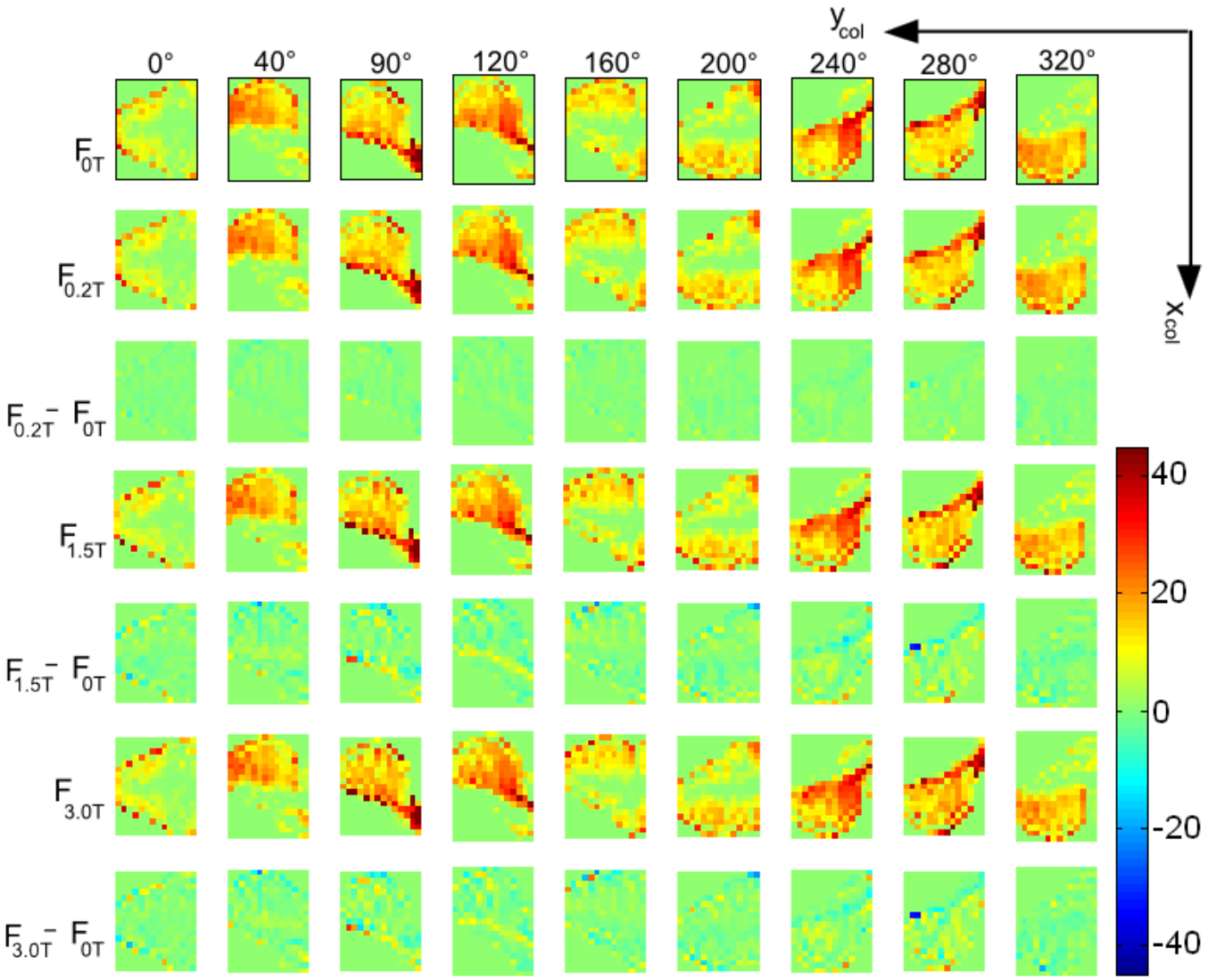


**Figure 11.5** Beamlet weight patterns of the optimisation using the original 0 T beamlet (top row), and the patterns from using the beamlets warped to 0.2 T (2nd row), 1.5 T (4th row) and 3 T (6th row), and the differences to the 0 T pattern (3rd, 5th and 7th row).

The effects on the target coverage become equally evident when looking at the dose-volume measures given in tables 11.5 and 11.6, where the 0 T values from tables 11.1 and 11.2 are repeated for the sake of better readability.

The drop in the near-minimum dose $D_{98\%}$ is most significant. While at 0.2 T, values agree with the 0 T original plan to within 0.4 % of the prescribed dose, the differences are around -3 % of the prescribed dose at 1.5 T, and up to nearly -5 % at 3 T.

The mean dose $D_{mean}$ differs by -1.6 % at 1.5 T and by -3.2 % at 3 T in the GTV, and by -1.8 % and -3.1 % of the prescribed dose in the CTV, respectively. Interestingly, the near-maximum dose $D_{2\%}$ agrees at 1.5 T and 0 T, but at 3 T, the $D_{2\%}$ exhibits differences of -1.7 % in the GTV and -1.9 % in CTV with respect to the 0 T prescribed dose.

Since all dose-volume measures are reduced, the effect on the homogeneity index HI in the GTV is of lower significance. However, with the stronger reduction in near-minimum dose than in near-maximum

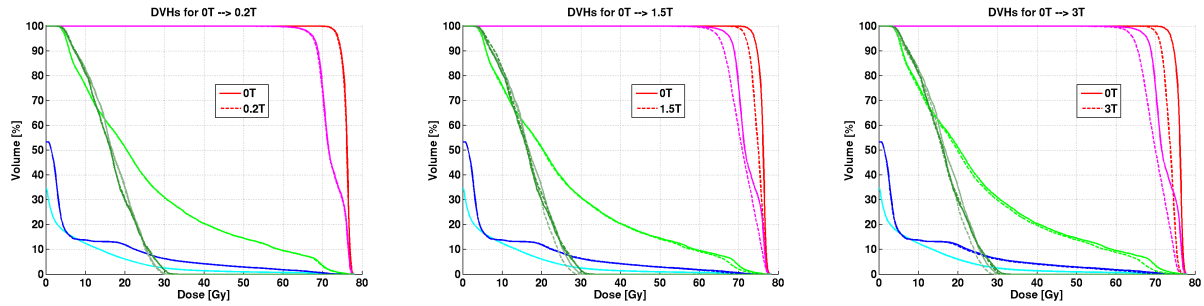


**Figure 11.6** DVH's from using the 0 T fluence together with the 0.2 T, 1.5 T and 3 T beamlet (from left to right). The 0 T DVH's are given as a reference as solid lines, while the DVH's from using the warped beamlets are displayed as dashed lines. The structures included are the GTV (red), CTV (magenta), bladder (bright green), rectum (blue), left (dark green) and right femoral head (grey green) and outer patient contour (cyan)

**Table 11.5** Dose-volume measures in the GTV of the prostate case, using the 0 T fluence with the warped beamlets for calculation

| | $D_{98\%}$[%] | $D_{98\%}$[Gy] | $D_{50\%}$[%] | $D_{50\%}$[Gy] | $D_{mean}$[%] | $D_{mean}$[Gy] | $D_{2\%}$[%] | $D_{2\%}$[Gy] | HI |
|---|---|---|---|---|---|---|---|---|---|
| 0 T | 96.3 | 73.2 | 100.2 | 76.2 | 100.0 | 76.0 | 101.7 | 77.3 | 0.05 |
| 0 T→0.2 T | 96.1 | 73.0 | 100.1 | 76.1 | 99.9 | 75.9 | 101.8 | 77.3 | 0.06 |
| 0 T → 1.5 T | 93.3 | 70.9 | 98.6 | 74.9 | 98.4 | 74.7 | 101.7 | 77.3 | 0.08 |
| 0 T → 3 T | 91.8 | 69.8 | 97.0 | 73.7 | 96.8 | 73.5 | 100.0 | 76.0 | 0.08 |

dose, a corresponding increase of the HI can be observed.

In the organs at risk, not much change is seen in the near-minimum dose $D_{98\%}$ and rather moderated changes of up to 1 % of the prescribed dose are seen in the mean dose $D_{mean}$ as table 11.7 shows. Here, it is the near-maximum dose $D_{2\%}$ of the organs adjacent to the target volumes where the most significant effects are noticed, with a difference of -2 % of the prescribed dose in the rectum and -3 % in the bladder.

This is a very probable result considering that the near-minimum dose is most likely produced by beams from a single direction of incidence, while in the vicinity of the target volumes, beams from several directions superimpose such that the dose effects add.

It is interesting to see that in the left femoral head, $D_{2\%}$ values agree at 1.5 T and 0 T and differ between 3 T and 0 T, while in the right femoral head, the $D_{2\%}$ value of both the 1.5 T and 3 T dose distribution deviate from the 0 T value by around 2 % of the prescribed dose.

Two-dimensional difference maps of the corresponding dose distributions in the transverse plane are shown in figure 11.7. As in the previous results, at 0.2 T the effects are minor, while they are significant at 1.5 T and 3 T. In the middle plot of 1.5 T, yellow lines have been added to show the directions of incidence of the treatment beams. In can be seen that except for the 0°, i.e. ventral, direction, there is always a red stripe of overdosage to the right of each yellow line, and a blue stripe of underdosage to the left of the line, where left and right are used with respect to the direction of beam incidence.

**Table 11.6** Dose-volume measures in the CTV of the prostate case, using the 0 T fluence with the warped beamlets for calculation

| | $D_{98\%}$[%] | $D_{98\%}$[Gy] | $D_{50\%}$[%] | $D_{50\%}$[Gy] | $D_{mean}$[%] | $D_{mean}$[Gy] | $D_{2\%}$[%] | $D_{2\%}$[Gy] |
|---|---|---|---|---|---|---|---|---|
| 0 T | 87.0 | 66.1 | 94.1 | 71.5 | 95.2 | 72.3 | 101.3 | 77.0 |
| 0 T→0.2 T | 86.6 | 65.8 | 94.1 | 71.5 | 95.0 | 72.2 | 101.4 | 77.1 |
| 0 T→1.5 T | 83.5 | 63.5 | 93.2 | 70.9 | 93.4 | 70.9 | 101.2 | 76.9 |
| 0 T→3 T | 82.7 | 62.8 | 92.0 | 69.9 | 92.1 | 70.0 | 99.4 | 75.6 |

**Table 11.7** Dose-volume measures in the organs at risk of the prostate case, using the 0 T fluence with the warped beamlets for calculation

| | $D_{98\%}$[%] | $D_{98\%}$[Gy] | $D_{mean}$[%] | $D_{mean}$[Gy] | $D_{2\%}$[%] | $D_{2\%}$[Gy] |
|---|---|---|---|---|---|---|
| **rectum** | | | | | | |
| 0 T | - | - | 8.0 | 6.1 | 77.0 | 58.5 |
| 0 T→0.2 T | - | - | 8.0 | 6.1 | 77.0 | 58.5 |
| 0 T→1.5 T | - | - | 7.9 | 6.0 | 75.9 | 57.7 |
| 0 T→3 T | - | - | 7.8 | 5.9 | 75.0 | 57.0 |
| **bladder** | | | | | | |
| 0 T | 5.6 | 4.3 | 33.9 | 25.8 | 94.0 | 71.5 |
| 0 T→0.2 T | 5.6 | 4.3 | 33.9 | 25.7 | 93.8 | 71.3 |
| 0 T→1.5 T | 5.5 | 4.2 | 33.5 | 25.4 | 92.2 | 70.1 |
| 0 T→3 T | 5.5 | 4.2 | 32.9 | 25.0 | 91.0 | 69.1 |
| **l. femoral head** | | | | | | |
| 0 T | 6.4 | 4.8 | 21.6 | 16.4 | 39.1 | 29.7 |
| 0 T→0.2 T | 6.6 | 5.0 | 22.0 | 16.8 | 39.2 | 29.8 |
| 0 T→1.5 T | 6.6 | 5.0 | 21.3 | 16.2 | 39.1 | 29.7 |
| 0 T→3 T | 6.4 | 4.9 | 21.0 | 15.9 | 38.4 | 29.1 |
| **r. femoral head** | | | | | | |
| 0 T | 6.3 | 4.8 | 22.2 | 16.9 | 37.5 | 28.5 |
| 0 T→0.2 T | 6.2 | 4.7 | 21.8 | 16.5 | 37.1 | 28.2 |
| 0 T→1.5 T | 6.0 | 4.5 | 22.1 | 16.8 | 35.6 | 27.1 |
| 0 T→3 T | 5.8 | 4.4 | 21.6 | 16.4 | 35.4 | 26.9 |

These stripes can be understood to describe the behaviour of the dose distribution on the edges of the beams. In fact, they nicely illustrate the deformation of the beams' dose profiles by the magnetic field: With the magnetic field being parallel to the patient's cranio-caudal axis, the beamlets get deformed towards the right with respect to the beam's direction of incidence. In this direction, therefore higher values exist in the dose distributions calculated using the warped beamlets. These dose values constitute the red margins in the difference plots, while on the left edge of the beam, blue margins of negative dose differences are observed. It may be mentioned as a matter of completeness that the direction of deformation, is the negative x direction of the beam collimator which was termed -$x_{col}$ before.

Obviously, dose contributions from several beamlets partially cancel out the effect in the more central portions of the beams, since here, no differences above 1 % are present, while towards the edges of the beams, the respective over- and underdosage is more pronounced. Similar behaviour is present in the other 1.5 T and 3 T plots of figure 11.7 as well.

The absence of edge patterns for the beam at 0° can be understood referring back to the fluence maps of figure 11.5, where it is seen that the optimiser widely avoids the 0° direction which is most likely due to both bladder and rectum being aligned along it. The edge patterns are also less clear in the two dorsal beams, corresponding to directions 160° and 200° in the fluence map. The beamlet weight patterns for these two directions actually differ from the others in that not one single, "bulk" region of high weights is observed but rather one cluster at lower, and one cluster at higher values of $x_{col}$. From this observation, a more alternating pattern of over- and underdosage as found along these beam directions, is not surprising.

In addition to the edge patterns, it may again be remarked that below the entrance surface of the beam, generally the dose is higher for the warped beamlet calculation which is, as described above, due to the upstream shift of the dose profile.

It is consistent with the DVH's and other dose-volume measures reported above, that the dose to the target is significantly impaired in the 1.5 T and 3 T case. A close-up view of the target in one transverse, sagittal and frontal plane each is displayed in figures 11.8 and 11.9 for 1.5 T and 3 T, respectively. The top

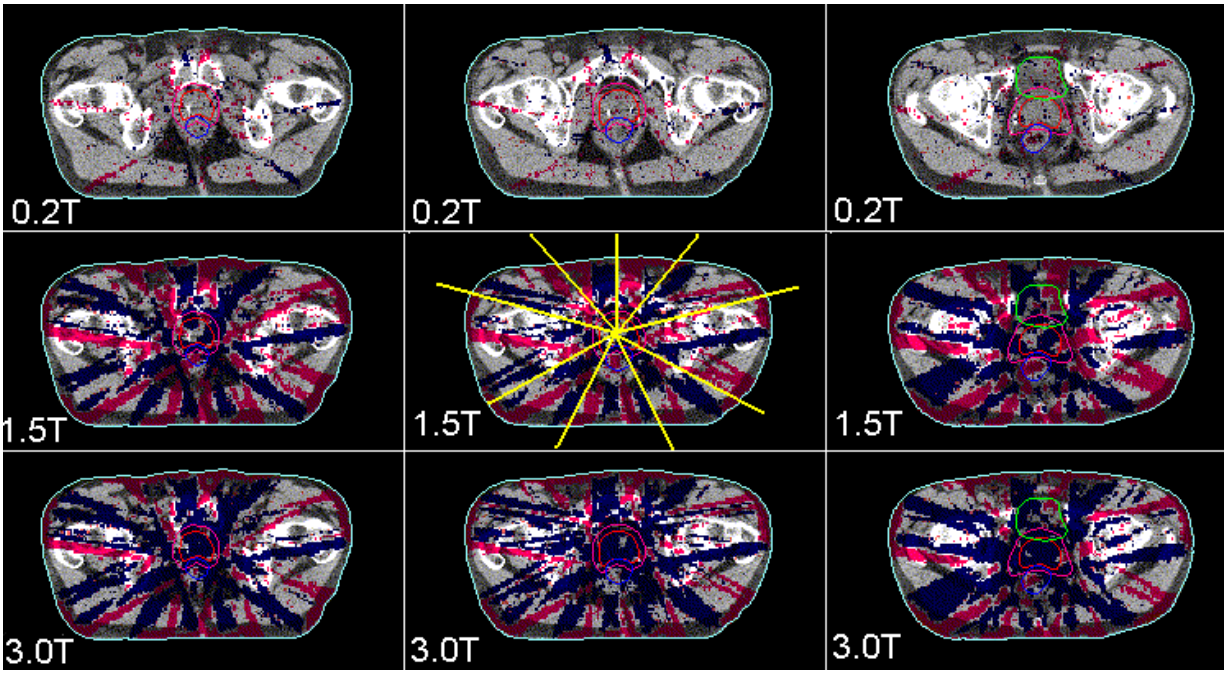


**Figure 11.7** Difference plots of the prostate case, from using the 0 T fluence with the warped beamlets. The transverse plane is shown at different depths (columns) with deviations between 1 and 10 %, where red represents an overdosage in the warped beamlet plan, and blue represents an underdosage.

row shows the calculation result using the warped beamlet, in the middle row the result of 0 T is found, and in the bottom row the difference between both is again displayed for the sake of clarity.

The effects are most evident in the transverse planes. In the left column of figure 11.8, it can be observed that while the 100 % isodose line nicely covers most of the GTV in the 0 T plan, it shrinks to an island not even half the size of the GTV in the 1.5 T calculation. The 95 % isodose line still covers most of the GTV but it is seen to extend further left (in patient coordinates, right side in the plot) into the CTV, and a severe inward displacement of the 90 % isodose line is remarked, leaving wide parts of the CTV uncovered.

The shrinkage of the area covered by the 100 % isodose line is also clearly visible in both the sagittal and frontal plane. The difference patterns in the bottom row are consistent in that blue regions are found in large parts of the GTV and a red region can be noticed where the 95 % isodose line extends into the CTV in the transverse plane.

At 3 T, effects are even more severe as seen in figure 11.9. In the top row, the 100 % isodose line has entirely disappeared, and even the 95 % isodose line does not cover all of the GTV. Larger portions of the CTV remain at below 90 %. Consequently, almost all parts of the targets exhibit underdosage values between 1 and 10 % as the blue colour in the difference plots reveals.

Looking finally into the integral dose to the full volume irradiated, the values listed in table 11.8 can be observed. It is seen that the energy deposited in the patient decreases exactly by the amount that was seen in the warped kernels and discussed in the beginning of the results section around figure 11.1.

**Table 11.8** Integral dose for 0 T fluence in combination with warped beamlets, $V_{tot}$=26.1 litres

| | 0 T | B = 0.2 T | B = 1.5 T | B = 3 T |
|---|---|---|---|---|
| integral dose: $E_V$[Gy·l] | 95.4 | 95.1 | 94.6 | 93.6 |
| relative to 0 T: $E_{V,B}/E_{V,0T}$ | 1.000 | 0.997 | 0.992 | 0.981 |

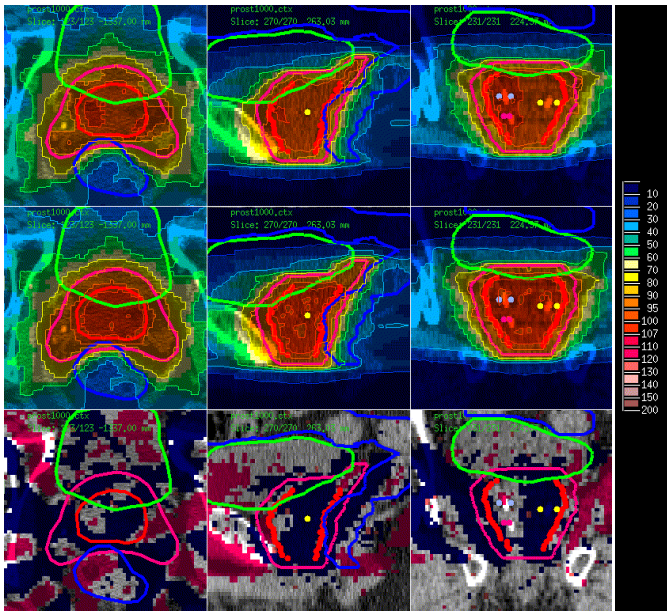


**Figure 11.8** Close up of the target coverage of the prostate case using the 0 T fluence with the 1.5 T beamlet (top) and the 0 T beamlet (middle), as well as the difference between both.

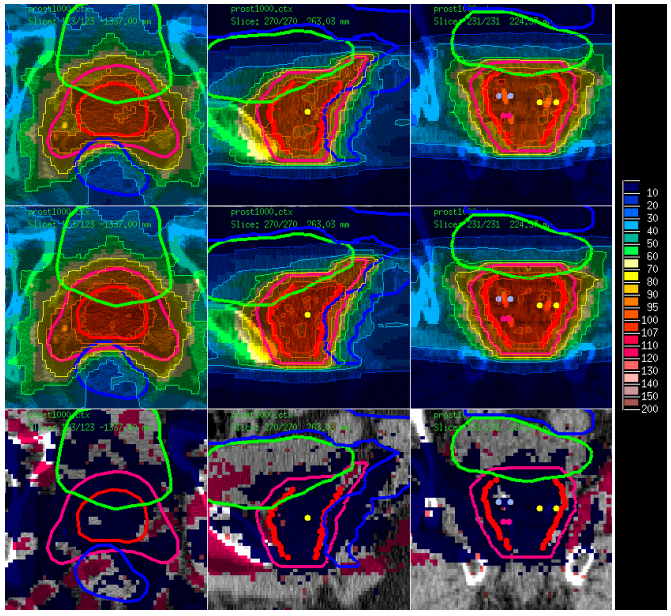


**Figure 11.9** Close up of the target coverage of the prostate case using the 0 T fluence with the 3 T beamlet (top) and the 0 T beamlet (middle), as well as the difference between both.

### 11.2.2 Head and Neck

Figure 11.10 shows the CT of the nasopharyngeal cancer case which is overlaid with the dose distribution of optimisation by means of the 0 T beamlet. The region of main tumour growth is seen to be covered homogeneously in red while the target region encompassing also the lymphatic vessels is evenly coloured in yellow.

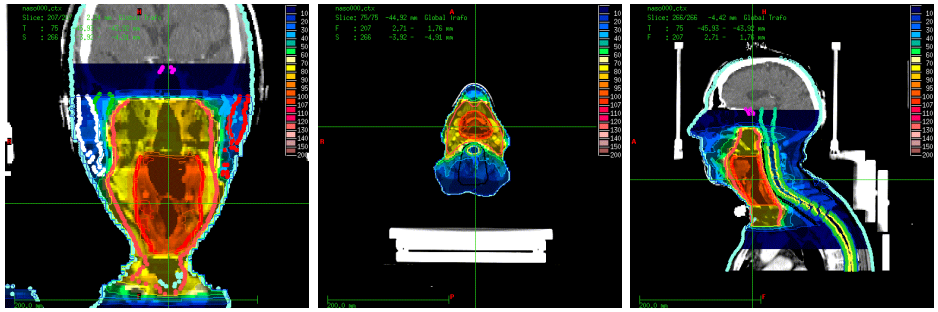

**Figure 11.10** CT image of the head-and-neck case, overlaid with the dose distribution from optimisation using the 0 T beamlet.

#### Optimisation using Warped Beamlets

The DVH's of the plans optimised using the warped beamlets are displayed in figure 11.11 as dashed lines which are partially covered by the solid lines respresenting the 0 T optimisation result which is given for the purpose of comparison.

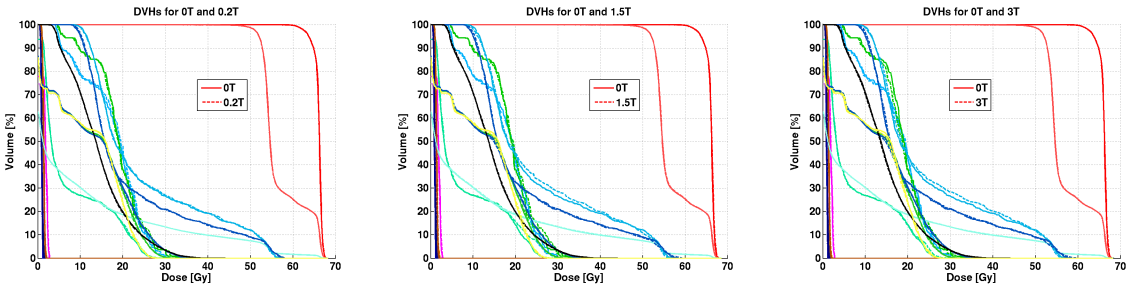


**Figure 11.11** Dose-volume histograms of the optimisation results using the original and warped beamlets. In each diagram, the 0 T results is given by solid lines, while the 0.2 T (left), 1.5 T (middle) and 3 T (right) results are represented by dashed lines. The colour coding of the volumes of interest is: boost (red), target including lymphatic vessels (red), right/left parotid gland (blue/light blue), right/left temporomandibular joint (green/light blue), larger spine (**black**), spinal cord (+3 mm/+5 mm) (yellow (green/blue)), outer patient contour (turquoise), brain stem (mint). The DVH lines of the right/left eye, right/left lens and right/left optic nerve superpose behind the line of the optic chiasm (pink).

It is seen that as in the case of the prostate cancer described above, the target coverage is not impaired by the use of the warped beamlets. At 0.2 T, no effect is observed on any of the DVH lines, while at 1.5 T and 3 T, slight shifts to higher doses can be remarked for the left parotid gland. Overall, the quality of the DVH's is highly comparable with the 0 T result.

Consequently, also the dose-volume measures in the target structures agree, and minor changes are seen in the organs at risk. The exact values are listed in the appendix in tables B.1, B.2, B.3 and B.4, but they are omitted here to avoid lengthiness.

Overview plots of the differences between the dose distributions are displayed in figure 11.12. Again, the dose difference to the 0 T plan is shown where red illustrates regions of higher dose in the warped beamlet plans, and blue refers to regions of lower dose. Only values deviating by 1 to 10 % are given as above. Also

for the head-and-neck case, differences for 0.2 T are marginal but get more significant at 1.5 T and 3 T. No dose differences are observed in the target structures but only in the surrounding tissues.

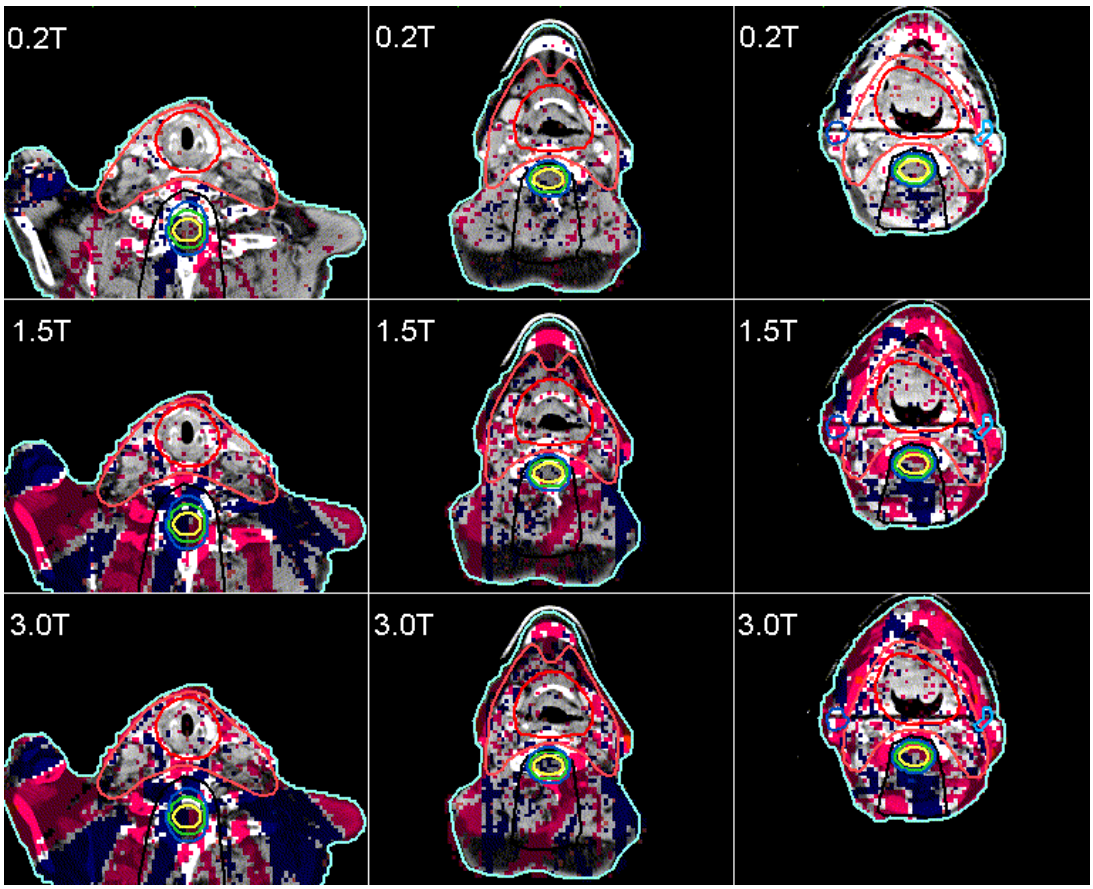


**Figure 11.12** Difference plots of the head-and-neck warped beamlet plans with respect to the 0 T plan at different depths (columns). Deviations between 1 and 10 % are shown, where red represents an overdosage in the warped beamlet plan, and blue represents an underdosage.

Looking at the integral dose values listed in table 11.9, it can be remarked that the increase is generally smaller than in the prostate case, and within 1 % in all cases. One can speculate that this may be due to the fact that big portions of the target volumes are located closer to the patient surface where the depth-dose curve in the magnetic field is actually higher and not lower than its 0 T counterpart. Considering that at 3 T, optimisation only leads to a 0.6 % increase in dose in spite of the insufficient energy deposition in the corresponding beamlet, this implies that the fluence must be higher by 2-3 %.

**Table 11.9** Integral dose for the different optimisation results, $V_{tot}$=10.2 litres

| | 0 T | B = 0.2 T | B = 1.5 T | B = 3 T |
|---|---|---|---|---|
| integral dose: $E_V$[Gy·l] | 105.1 | 105.2 | 106.2 | 105.7 |
| relative to 0 T: $E_{V,B}/E_{V,0T}$ | 1.000 | 1.001 | 1.010 | 1.006 |

### Differences in Fluence Patterns for Same Dose to the Tumour

The beamlet weight patterns found by the optimisation are shown in figure 11.13. As before, patterns are similar for all settings but single beamlet weights with high deviations occur as well as a larger number of smaller beamlet weight deviations. A tendency seems to be present that beamlets with higher weights rather appear towards higher values of x (downward in the figure), while beamlets with lower weights are

rather present towards lower values of x.

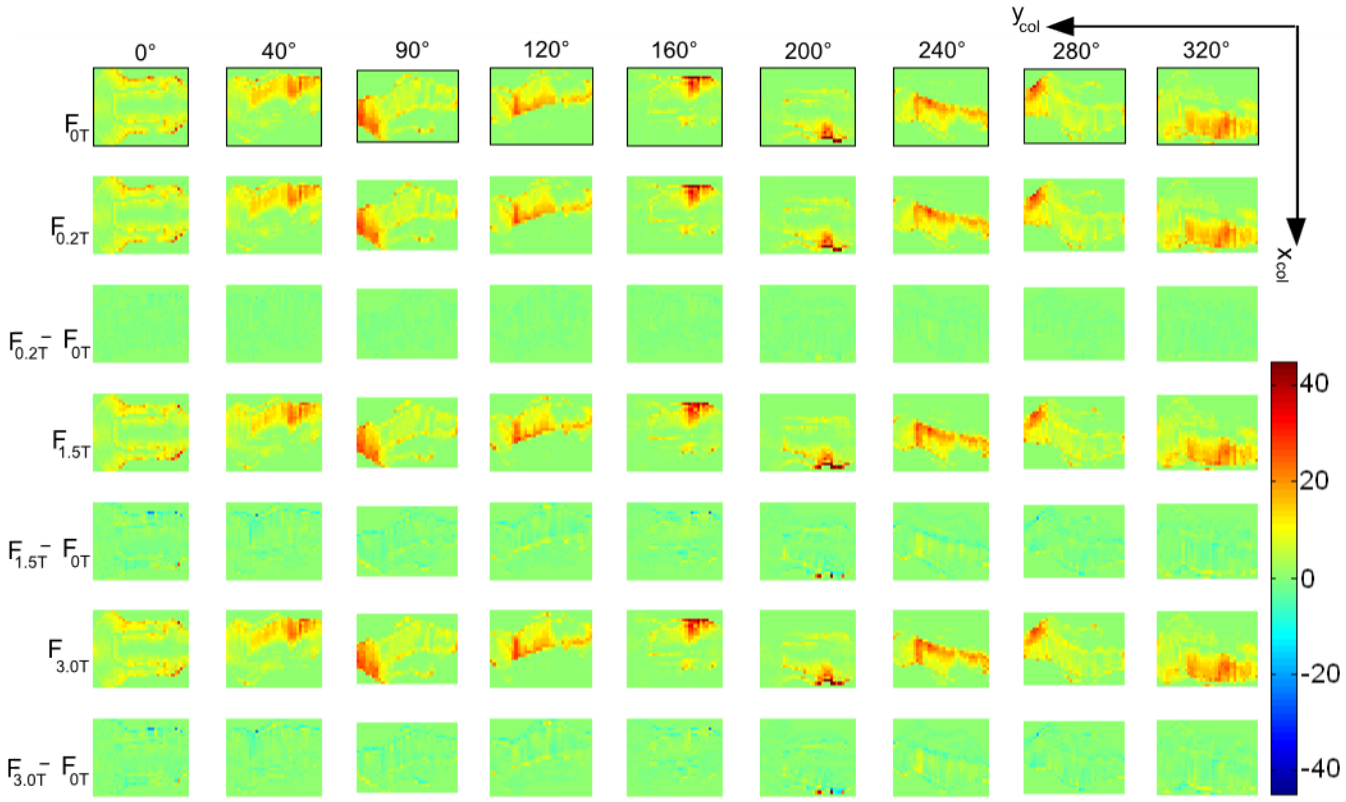


**Figure 11.13** Beamlet weight patterns of the optimisation using the original 0 T beamlet (top row), and the patterns from using the beamlets warped to 0.2 T (2nd row), 1.5 T (4th row) and 3 T (6th row), and the differences to the 0 T pattern (3rd, 5th and 7th row).

Summing again over all beamlets from all beam directions, also for the nasopharyngeal cancer case, an increase can be seen in that

$$\frac{\sum_{i=1}^{N} w_{0.2T,i}}{\sum_{i=1}^{N} w_{0T,i}} = 1.003, \quad \frac{\sum_{i=1}^{N} w_{1.5T,i}}{\sum_{i=1}^{N} w_{0T,i}} = 1.015 \quad \text{and} \quad \frac{\sum_{i=1}^{N} w_{3T,i}}{\sum_{i=1}^{N} w_{0T,i}} = 1.023,$$

where again $N$ is the total number of beamlets, and the weights of the i's beamlet of the 0 T, 0.2 T, 1.5 and 3 T optimisation result are denoted as $w_{0T,i}$, $w_{0.2T,i}$, $w_{1.5T,i}$ and $w_{3T,i}$, respectively.

The 2.3 % increase observed in the 3 T case is in perfect agreement to what was predicted from the values of table 11.9, and also the 0.2 T and 1.5 T values match.

### Differences in Dose for Same Fluence Patterns

Using the fluence from the 0 T optimisation in combination with the warped beamlets, the effects were again very similar to the prostate case. Figure 11.14 shows the respective DVH's. It is seen that the dose to the target structures is significantly impaired at 1.5 T and 3 T, whereas changes in the dose to the organs at risk are smaller.

The dose-volume measures for the targets are given in tables 11.10 and 11.11. Also for the head-and-neck case, the strongest effect is on the near-minimum dose, followed by the mean dose and the relatively smallest effect on the near-maximum dose, both in the boost volume of major tumour growth and in the

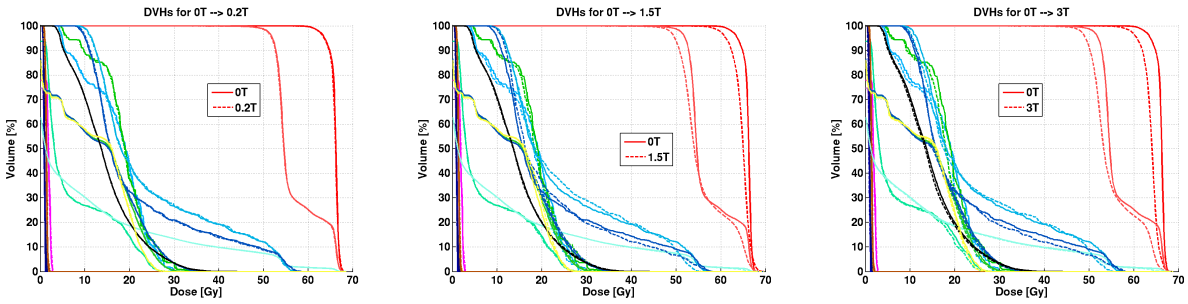


**Figure 11.14** DVH's from using the 0 T fluence together with the 0.2 T, 1.5 T and 3 T beamlet (from left to right). The 0 T DVH's are given as a reference as solid lines, while the DVH's from using the warped beamlets are displayed as dashed lines. The volumes of interest are colour-coded as: boost (red), target including lymphatic vessels (red), right/left parotid gland (blue/light blue), right/left temporomandibular joint (green/light blue), larger spine (**black**), spinal cord (+3 mm/+5 mm) (yellow (green/blue)), outer patient contour (turquoise), brain stem (mint). The DVH lines of the right/left eye, right/left lens and right/left optic nerve superpose behind the line of the optic chiasm (pink).

target including the lymphatic vessels. The $D_{98\%}$ is reduced by 3 % of the prescribed dose, $D_{mean}$ is reduced by 2 %, and $D_{2\%}$ differs by around 1 %. This is less difference than in the prostate case. The corresponding values for the organs at risk are found in tables B.5 and B.6 in the appendix.

Table 11.12 shows the integral dose values. Again, the energy deposition in the warped beamlets is reflected in the numbers, with the difference in integral dose being below 1 % for 0.2 T and 1.5 T in contrast to the 2 % in the 3 T case.

**Table 11.10** Dose-volume measures for the boost volume of major tumour growth

| | $D_{98\%}$[%] | $D_{98\%}$[Gy] | $D_{50\%}$[%] | $D_{50\%}$[Gy] | $D_{mean}$[%] | $D_{mean}$[Gy] | $D_{2\%}$[%] | $D_{2\%}$[Gy] | HI |
|---|---|---|---|---|---|---|---|---|---|
| 0 T | 94.4 | 62.3 | 100.3 | 66.2 | 100.0 | 66.0 | 102.0 | 67.3 | 0.08 |
| 0 T→0.2 T | 94.3 | 62.2 | 100.2 | 66.1 | 99.9 | 65.9 | 102.2 | 67.5 | 0.08 |
| 0 T→1.5 T | 90.4 | 59.7 | 98.4 | 65.0 | 98.0 | 64.7 | 102.7 | 67.8 | 0.12 |
| 0 T→3 T | 89.8 | 59.2 | 97.0 | 64.0 | 96.7 | 63.9 | 101.1 | 66.7 | 0.12 |

**Table 11.11** Dose-volume measures for the target including the lymphatic vessels

| | $D_{98\%}$[%] | $D_{98\%}$[Gy] | $D_{50\%}$[%] | $D_{50\%}$[Gy] | $D_{mean}$[%] | $D_{mean}$[Gy] | $D_{2\%}$[%] | $D_{2\%}$[Gy] |
|---|---|---|---|---|---|---|---|---|
| 0 T | 77.0 | 50.8 | 82.7 | 54.6 | 86.3 | 57.0 | 101.3 | 66.9 |
| 0 T→0.2 T | 76.8 | 50.7 | 82.7 | 54.6 | 86.2 | 56.9 | 101.4 | 66.9 |
| 0 T→1.5 T | 73.5 | 48.5 | 81.9 | 54.0 | 84.8 | 55.9 | 101.1 | 66.7 |
| 0 T→3 T | 72.8 | 48.0 | 80.7 | 53.3 | 83.7 | 55.2 | 99.5 | 65.7 |

Overviews of the differences are displayed in figure 11.15, where again the direction of action of the magnetic field on the secondary electrons can be remarked. Again, effects are small at 0.2 T and larger at 1.5 T and 3 T.

A severe underdosage in parts of the target volumes is seen but indeed, the images in the left column reveal that in some parts of the target volume which are close to the surface, an increase in dose is observed when the warped beamlets are used. This supports the earlier assumption that in the head-and-neck case, the action of the magnetic field does not only lead to lower doses being delivered at the depth of the tumour but the upstream shift of the dose maximum causes an increase in dose in more superficial regions of the target.

Close-up views of the effect on target coverage are seen for 1.5 T and 3 T in figures 11.16 and 11.17,

**Table 11.12** Integral dose for 0 T fluence in combination with warped beamlets, $V_{tot}$=10.2 litres

| | 0 T | B = 0.2 T | B = 1.5 T | B = 3 T |
|---|---|---|---|---|
| integral dose: $E_V$[Gy·l] | 105.1 | 105.1 | 104.3 | 103.1 |
| relative to 0 T: $E_{V,B}/E_{V,0T}$ | 1.000 | 1.000 | 0.992 | 0.981 |

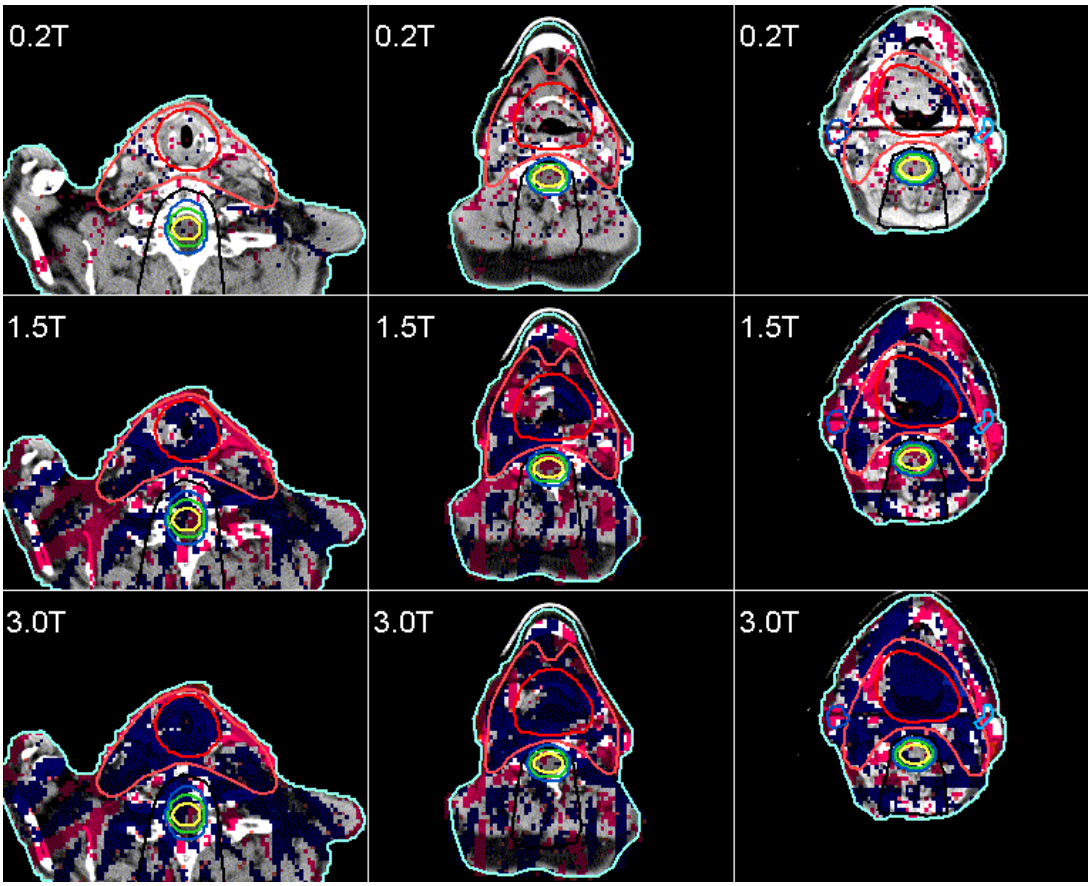


**Figure 11.15** Difference plots of the head-and-neck case, from using the 0 T fluence with the warped beamlets. The transverse plane is shown at different depths (columns) with deviations between 1 and 10 %, where red represents an overdosage in the warped beamlet plan, and blue represents an underdosage.

respectively. Observations resemble the prostate case in that the high-dose region surrounded by the 100 % isodose line shrinks to smaller islands at 1.5 T. In agreement with the red overdosage regions of the difference plots, however, is the inverse noticed in certain parts of the dose distribution.

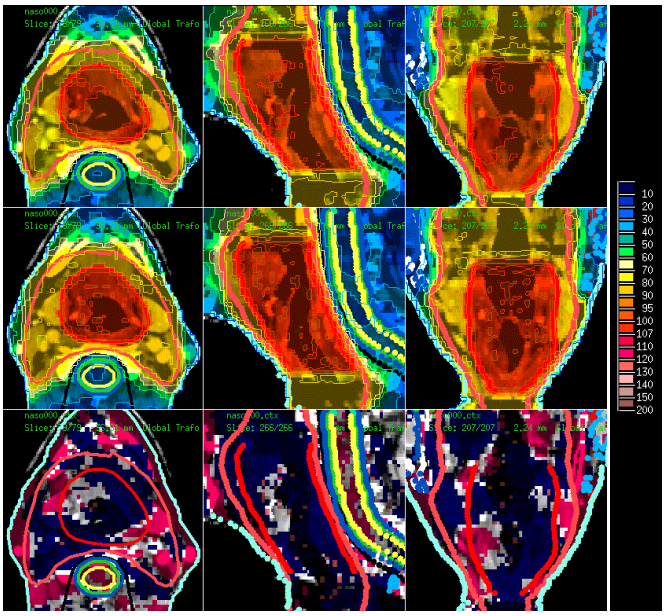


**Figure 11.16** Close up of the target coverage of the head-and-neck case using the 0 T fluence with the 1.5 T beamlet (top) and the 0 T beamlet (middle), as well as the difference between both.

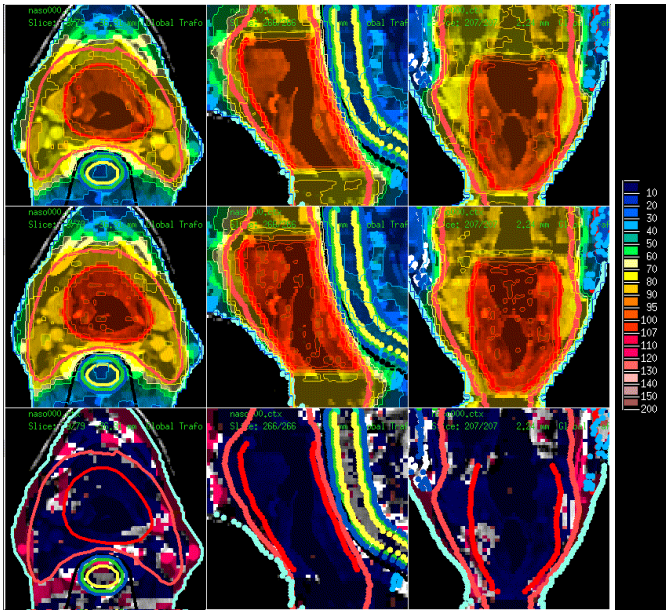


**Figure 11.17** Close up of the target coverage of the head-and-neck case using the 0 T fluence with the 3 T beamlet (top) and the 0 T beamlet (middle), as well as the difference between both.

### 11.2.3 Abdomen

The CT of the abdominal case overlaid with the dose distribution at 0 T is shown in figure 11.18. It has to be mentioned that metal implants, such that the exact patient would most likely not be a candidate for MR-guidance. Nevertheless, the patient data are included here since the target shape wrapping around the spine is found rather often.

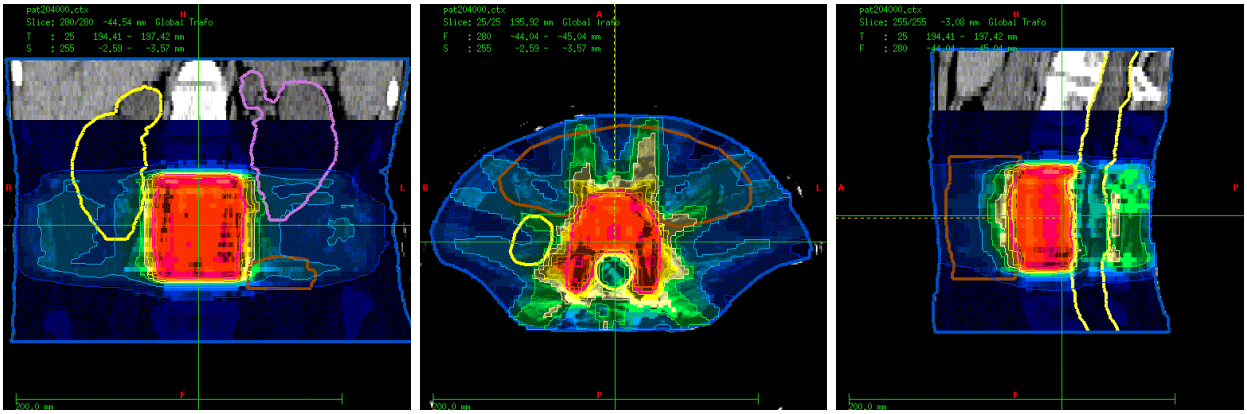

**Figure 11.18** CT images of the abdominal cancer case overlaid with the 0 T dose distribution: frontal, transverse and sagittal plane (from left to right).

#### Optimisation using Warped Beamlets

For the abdominal cancer case, in none of the DVH's can any difference be observed between the 0 T optimisation result and the results of using the warped beamlets for optimisation. In figure 11.19, all DVH's are seen to be identical, and the dashed lines from optimising by means of the warped beamlets are fully covered by the solid lines representing the 0 T optimisation result. It may be remarked that in the abdominal cancer case, the DVH for the target is not very steep, i.e. the dose to the target is rather inhomogeneous.

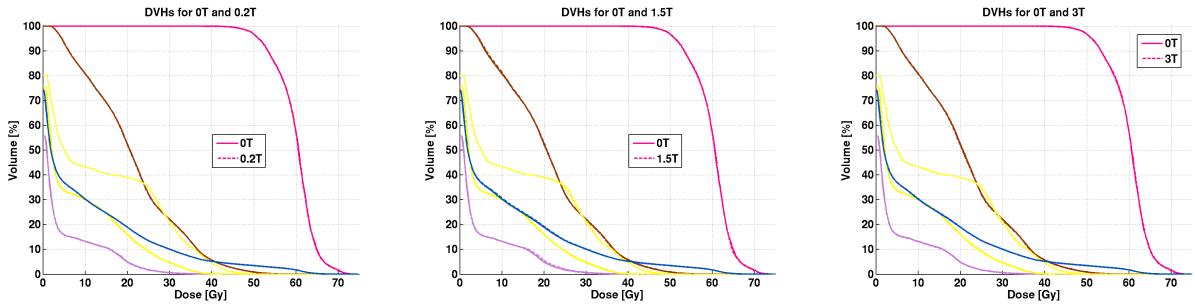


**Figure 11.19** Dose-volume histograms for the abdominal cancer case: target (magenta), intestine (brown), spinal cord (yellow), patient contour (blue), left/right kidney (purple/yellow). DVH's of optimisation by means of the warped beamlets superposes with the 0 T result.

The dose-volume measures are listed in the appendix in tables B.7 and B.8, and an overview of the dose differences in the transverse plane is displayed in figure 11.20. The figure gives an insight to why the treatment plans are identical in quality: Hardly any beam direction exists where the target is not in line with an organ at risk. Obviously, partially other beamlets weights are chosen for the beamlets, and throughout the transverse planes red and blue patterns of over- or underdosage (1 to 10 %) alternate also in the organs at risk, such that it is likely that the overall dose to these organs dose not differ much.

The increase in integral dose is at 1 % for 1.5 T and less at 3 T, as table 11.13 reveals. This is very comparable to the head-and-neck cancer described above but lower for 3 T than in the prostate case.

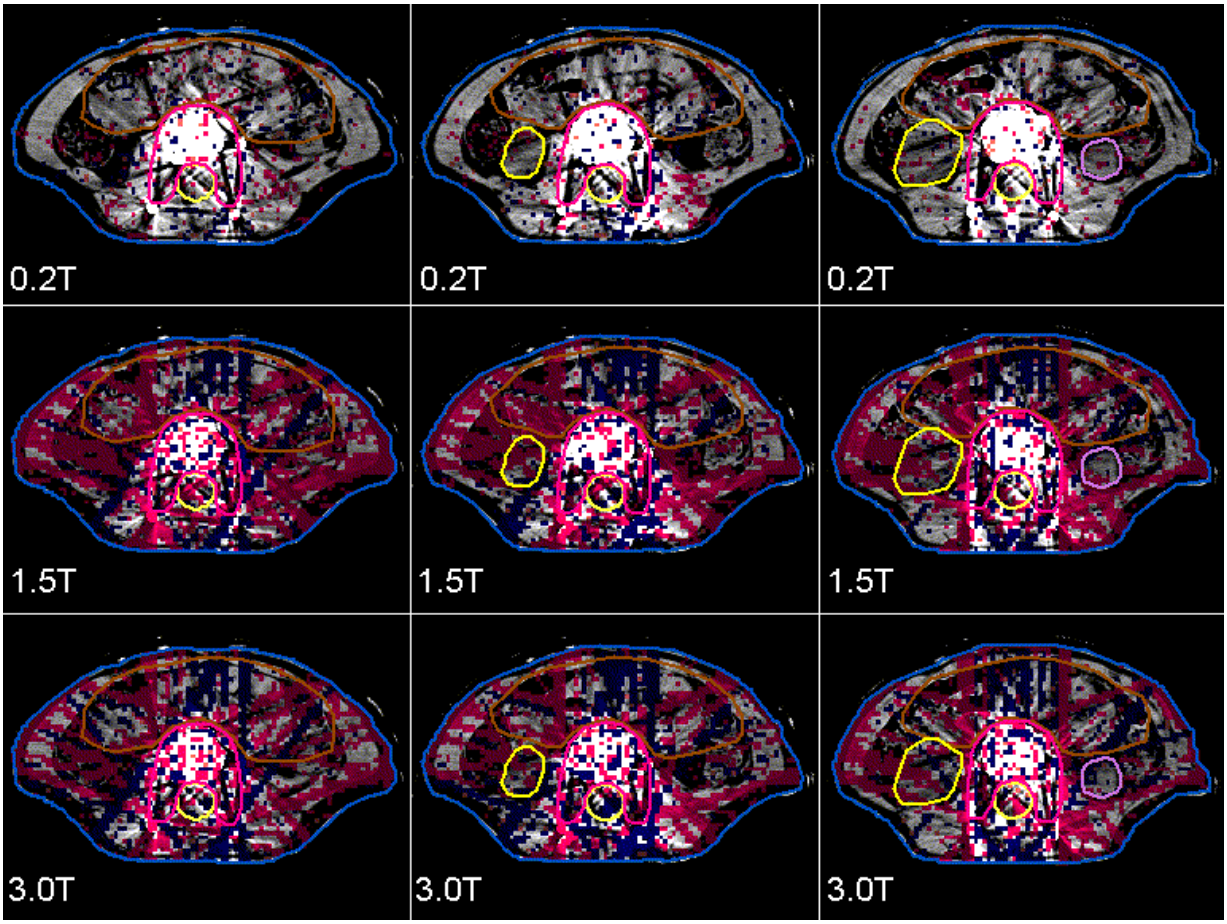


**Figure 11.20** Difference plots between the dose from optimisation by means of the warped beamlets and the 0 T result, for the abdominal cancer case.

**Table 11.13** Integral dose for the different optimisation results, $V_{tot}$=4.6 litres

| | 0 T | B = 0.2 T | B = 1.5 T | B = 3 T |
|---|---|---|---|---|
| integral dose: $E_V$[Gy·l] | 43.6 | 43.6 | 44.1 | 43.8 |
| relative to 0 T: $E_{V,B}/E_{V,0T}$ | 1.000 | 1.000 | 1.011 | 1.005 |

### Differences in Fluence Patterns for Same Dose to the Tumour

The sums over the beamlets from all beam directions read

$$\frac{\sum_{i=1}^{N} w_{0.2T,i}}{\sum_{i=1}^{N} w_{0T,i}} = 1.001, \quad \frac{\sum_{i=1}^{N} w_{1.5T,i}}{\sum_{i=1}^{N} w_{0T,i}} = 1.018 \quad \text{and} \quad \frac{\sum_{i=1}^{N} w_{3T,i}}{\sum_{i=1}^{N} w_{0T,i}} = 1.030,$$

with $N$ being the total number of beamlets, and $w_{0T,i}$, $w_{0.2T,i}$, $w_{1.5T,i}$ and $w_{3T,i}$ denoting the weights of the i's beamlet of the 0 T, 0.2 T, 1.5 and 3 T optimisation result, respectively.

In magnitude, these values are again comparable with the nasopharyngeal cancer case, but lower than for the prostate cancer. They are consistent with the integral dose values reported in table 11.13, considering the lack of energy in the 3 T kernel of around 2 %.

The patterns of beamlet weights are seen in figure 11.21 where again a tendency is seen that beamlets at higher x values get higher weights.

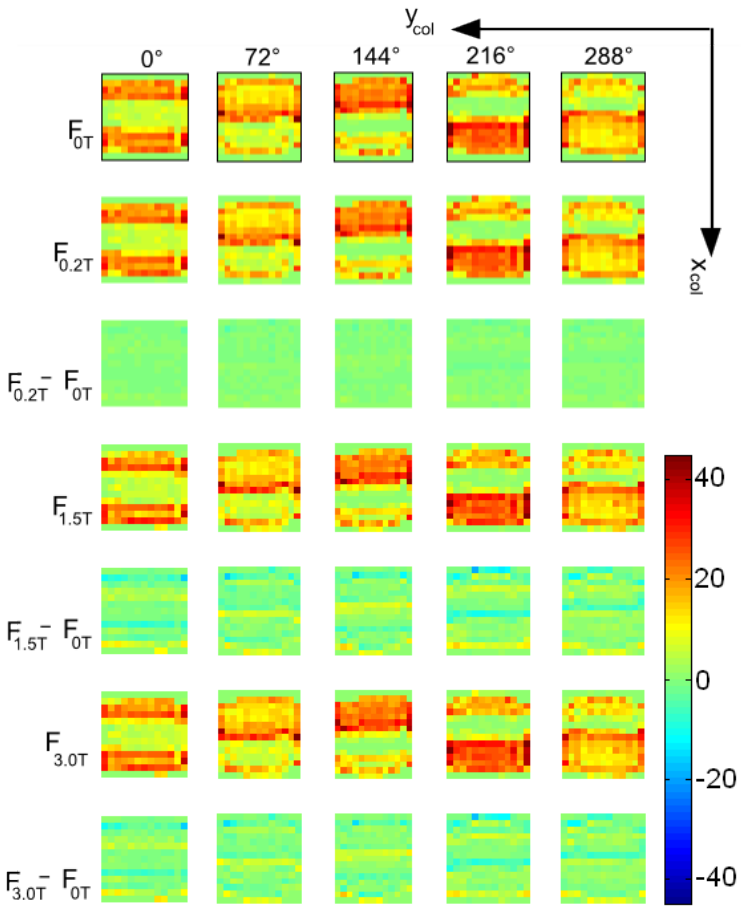


**Figure 11.21** Beamlet weight patterns of the optimisation using the original 0 T beamlet (top row), and the patterns from using the beamlets warped to 0.2 T (2nd row), 1.5 T (4th row) and 3 T (6th row), and the differences to the 0 T pattern (3rd, 5th and 7th row).

### Differences in Dose for Same Fluence Patterns

Looking at the DVH's from using the 0 T fluence in combination with the warped beamlets in figure 11.22, it is apparent that the findings from the prostate and head-and-neck case also repoduce in the case of the abdominal cancer. The dose to the target is significantly affected at 1.5 T and 3 T, while no actual change is seen at 0.2 T.

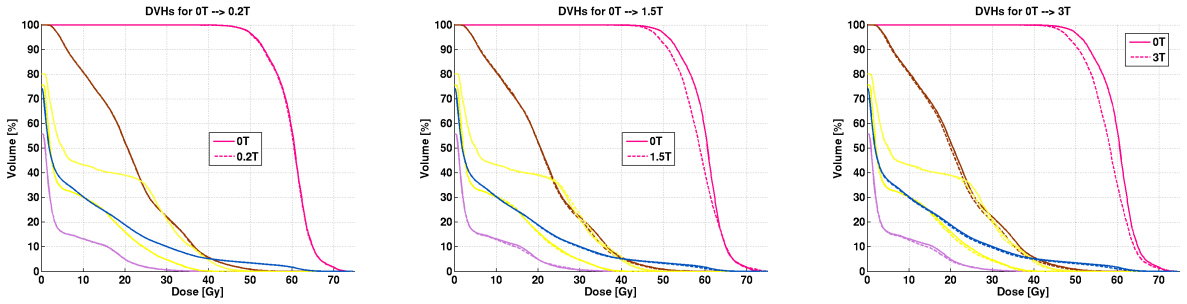


**Figure 11.22** target (magenta), intestine (brown), spinal cord (yellow), patient contour (blue), left/right kidney (purple/yellow).

Table 11.14 shows that the $D_{98\%}$, the median dose $D_{50\%}$ and the $D_{mean}$ drop by 3-4 % of the prescribed dose at 3 T, while the $D_{2\%}$ is less affected and only decreases by less than 2 %.

**Table 11.14** Dose-volume measures in the target in the abdominal cancer case

| | $D_{98\%}$[%] | $D_{98\%}$[Gy] | $D_{50\%}$[%] | $D_{50\%}$[Gy] | $D_{mean}$[%] | $D_{mean}$[Gy] | $D_{2\%}$[%] | $D_{2\%}$[Gy] | HI |
|---|---|---|---|---|---|---|---|---|---|
| 0 T | 81.5 | 48.9 | 101.0 | 60.6 | 100.0 | 60.0 | 116.0 | 69.6 | 0.34 |
| 0 T→0.2 T | 81.2 | 48.7 | 100.3 | 60.5 | 99.8 | 59.9 | 116.0 | 69.6 | 0.34 |
| 0 T→1.5 T | 77.3 | 46.7 | 98.0 | 58.8 | 97.6 | 58.5 | 115.3 | 69.2 | 0.38 |
| 0 T→3 T | 77.2 | 46.3 | 97.2 | 58.3 | 96.5 | 57.9 | 114.3 | 68.6 | 0.38 |

The integral dose values listed in table 11.15 are in agreement with the above cases in that the total energy deposited in the 0.2 T and 1.5 T case does not differ significantly from the energy in the 0 T plan but at 3 T, the lack of energy in the 3 T kernel shows.

**Table 11.15** Integral dose for 0 T fluence in combination with warped beamlets, $V_{tot}$=4.6 litres

| | 0 T | B = 0.2 T | B = 1.5 T | B = 3 T |
|---|---|---|---|---|
| integral dose: $E_V$[Gy·l] | 43.6 | 43.6 | 43.2 | 42.4 |
| relative to 0 T: $E_{V,B}/E_{V,0T}$ | 1.000 | 1.000 | 0.991 | 0.972 |

Difference plots of the dose distribution are seen in figure 11.23. It can be remarked that in the abdominal cancer case, even at 0.2 T exist differences exceeding ±1 % in the target. The differences get more pronounced at 1.5 T and 3 T, where they even range between 10 and 20 % which is represented by the brighter blue colour in the plots.

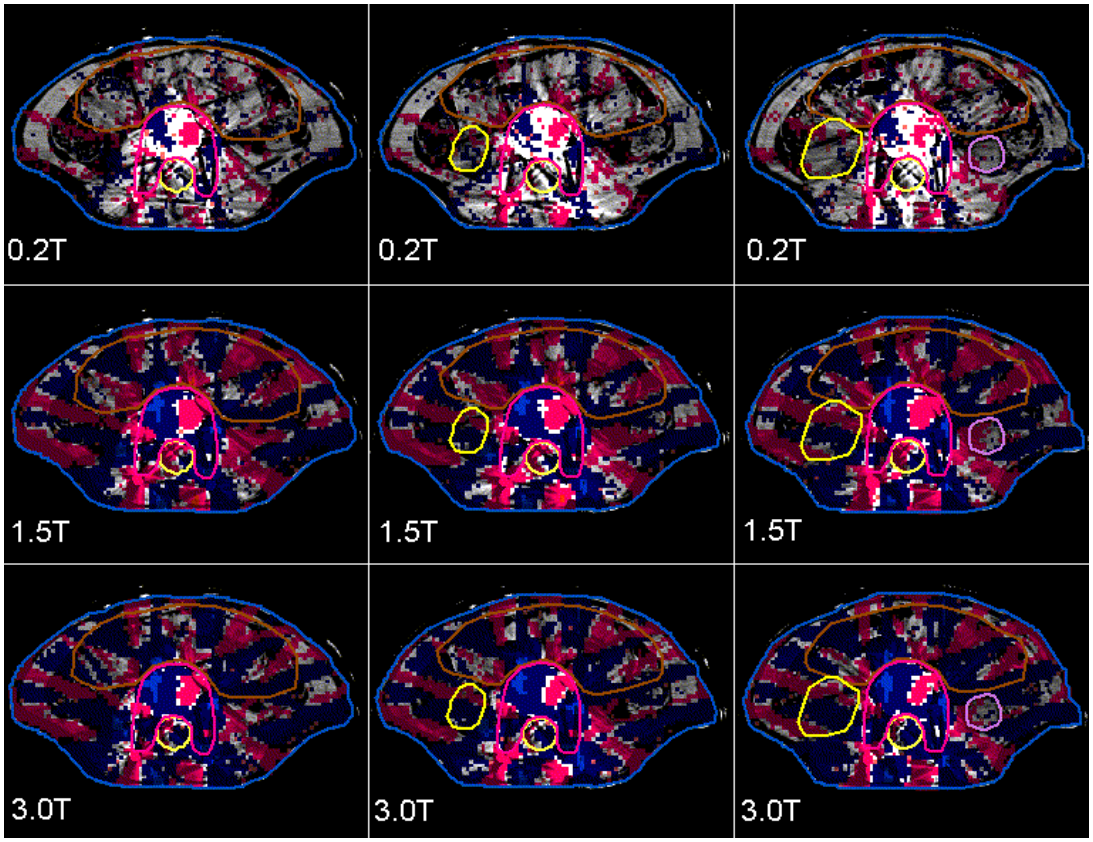


**Figure 11.23** Difference plots of the abdominal cancer case, from using the 0 T fluence with the warped beamlets. The transverse plane is shown at different depths (columns) with deviations between 1 and 10 %, where red represents an overdosage in the warped beamlet plan, and blue represents an underdosage.

In addition close-up views of the dose to the target are seen for all magnetic fields in figures 11.24, 11.25 and 11.26. In the frontal views shown in the respective right columns, it is evident that the severe over-

and underdosage is present throughout the entire cranio-caudal dimension of the target.

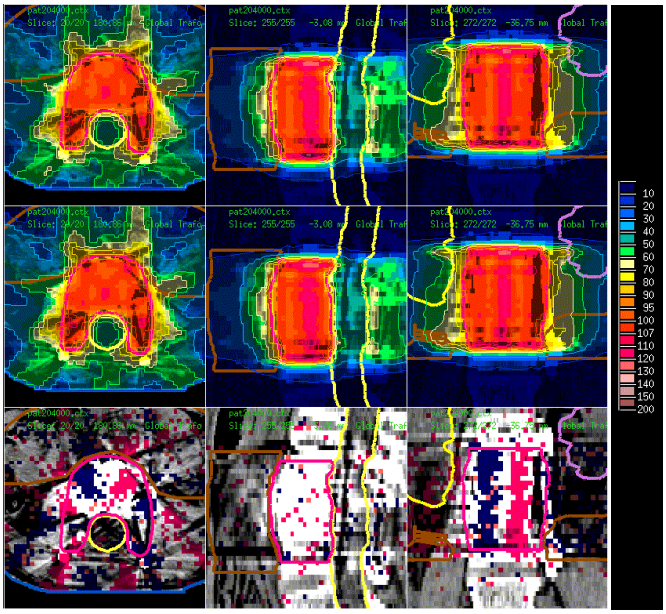

**Figure 11.24** Close up of the target coverage of the abdominal cancer case using the 0 T fluence with the 0.2 T beamlet (top) and the 0 T beamlet (middle), as well as the difference between both.

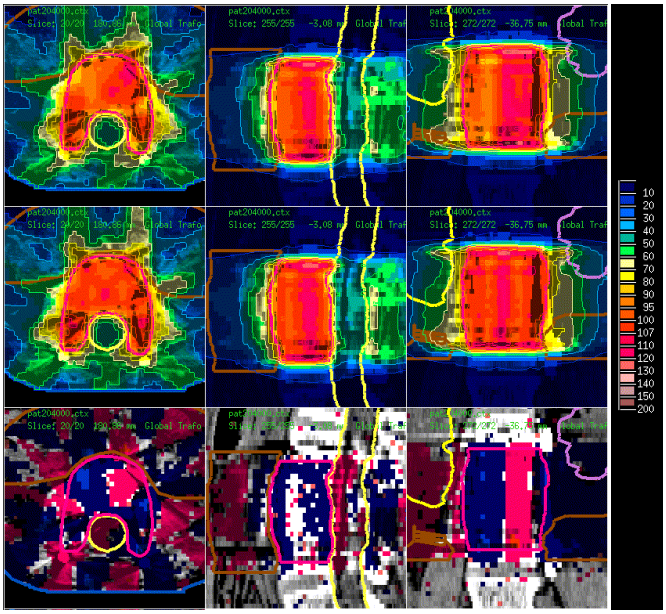

**Figure 11.25** Close up of the target coverage of the abdominal cancer case using the 0 T fluence with the 1.5 T beamlet (top) and the 0 T beamlet (middle), as well as the difference between both.

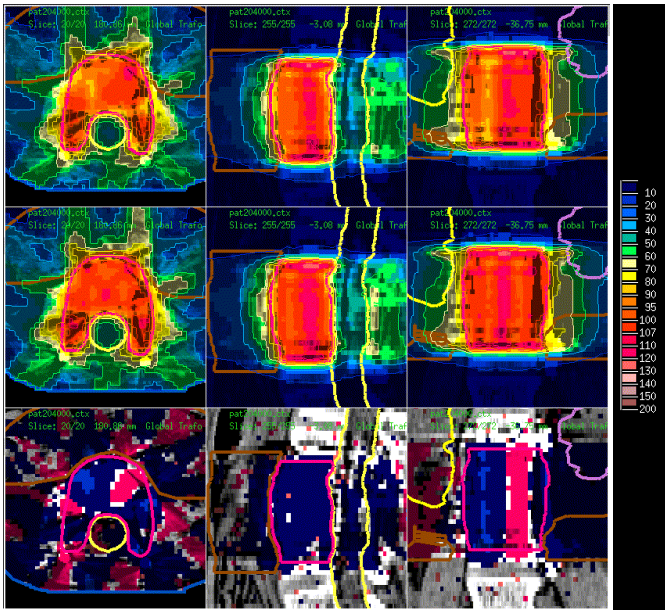


**Figure 11.26** Close up of the target coverage of the abdominal cancer case using the 0 T fluence with the 3 T beamlet (top) and the 0 T beamlet (middle), as well as the difference between both.

### 11.2.4 Brain

The last case discussed in this work is a meningeoma, i.e. a cancer of the brain. The dose distribution along with the CT is seen in figure 11.27. In the sagittal view (right), the dose along the non-coplanar beam may be noticed that cannot be delivered by a cylindrical MR design but rather requires a double-donut design.

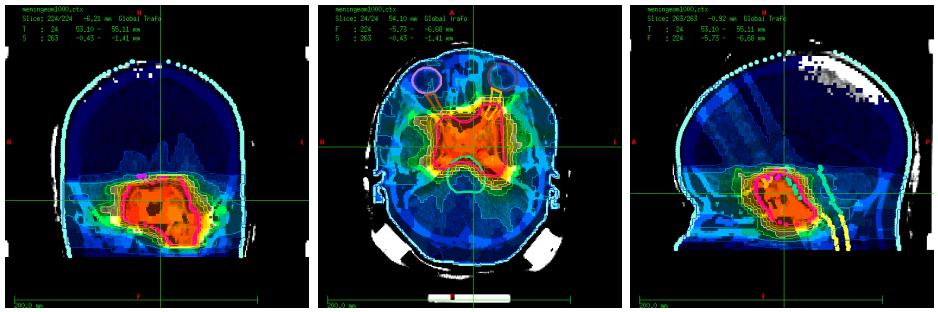

**Figure 11.27** CT images of the brain cancer case overlaid with the 0 T dose distribution: frontal, transverse and sagittal plane (from left to right).

#### Optimisation using Warped Beamlets

The DVH's from optimisation using the warped beamlets and displayed in figure 11.28 show that changes in target coverage do not occur for any of the warped beamlets; however, dose changes in some of the organs at risk. Especially in the optic nerves (brown/orange) a partial increase of dose is observed at 1.5 T and 3 T. However, these are very small structures where only few voxels contribute to the DVH. The dose to the spinal cord (yellow) is partially somewhat higher, but lower for another part. At 1.5 T and 3 T, the dose to the right temporomandibular joint (blue) is slightly increased, whereas to the left temporomandibular joint, a decrease is seen. At 0.2 T, however, the optimisation results in a lower dose to the right temporomandibular joint than at 0 T with the other organs receiving almost identical dose to the 0 T case.

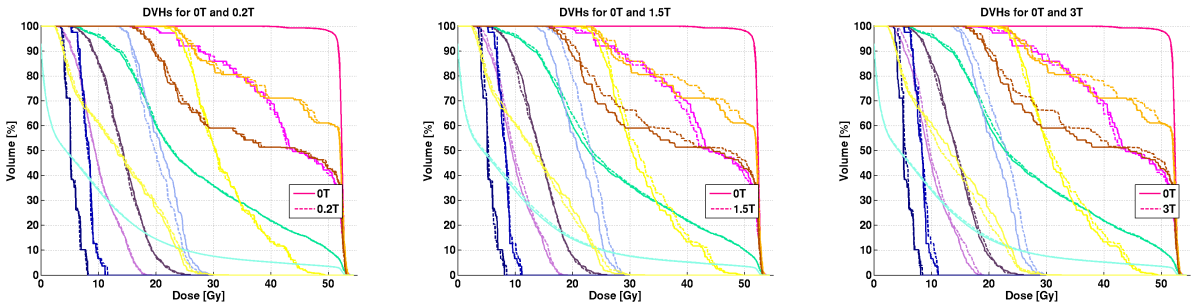


**Figure 11.28** target (magenta), optic chiasm (pink), right/left optic nerve (brown/orange), spinal cord (yellow), brain stem (mint), right/left temporomandibular joint (blue/yellow), right/left eye (purple/purple), right/left lens (blue/blue), patient contour (turquoise)

The table with the dose-volume measures of the target volume is omitted here but found in table B.10 of the appendix. Dose-volume measures of the above-mentioned organs at risk are displayed in table 11.16 while the respective values of other delineated structures are listed in table B.11 in the appendix. It can be remarked that the increase in dose to the right and left optic nerves is mainly in terms of $D_{mean}$. In addition to what can be noticed from the DVH's, the near-minimum dose $D_{98\%}$ to the optic chiasm

The integral dose values are displayed in table 11.17, and it can be seen that both for 1.5 T and 3 T, it is slightly increased.

**Table 11.16** Dose-volume measures in the organs at risk for the brain cancer case

| | $D_{98\%}$[%] | $D_{98\%}$[Gy] | $D_{mean}$[%] | $D_{mean}$[Gy] | $D_{2\%}$[%] | $D_{2\%}$[Gy] |
|---|---|---|---|---|---|---|
| **r. opt. nerve** | | | | | | |
| 0 T | 33.1 | 17.3 | 73.5 | 38.4 | 101.5 | 53.0 |
| 0.2 T | 34.2 | 17.9 | 73.9 | 38.6 | 101.4 | 52.9 |
| 1.5 T | 34.6 | 18.1 | 75.8 | 39.5 | 101.7 | 53.1 |
| 3 T | 33.4 | 17.5 | 75.7 | 39.5 | 101.7 | 53.1 |
| **l. opt. nerve** | | | | | | |
| 0 T | 45.7 | 23.9 | 86.8 | 45.3 | 101.8 | 53.1 |
| 0.2 T | 45.9 | 23.9 | 87.4 | 45.6 | 102.1 | 53.2 |
| 1.5 T | 46.3 | 24.2 | 88.6 | 46.2 | 101.5 | 53.0 |
| 3 T | 44.8 | 23.4 | 88.3 | 46.1 | 101.6 | 53.0 |
| **spinal cord** | | | | | | |
| 0 T | 5.3 | 2.8 | 25.8 | 13.5 | 48.6 | 25.4 |
| 0.2 T | 5.5 | 2.9 | 26.5 | 13.8 | 50.2 | 26.2 |
| 1.5 T | 5.9 | 3.1 | 25.8 | 13.5 | 51.7 | 27.0 |
| 3 T | 5.4 | 2.8 | 24.6 | 12.8 | 50.2 | 26.2 |
| **l. temporomandib. j.** | | | | | | |
| 0 T | 43.8 | 22.9 | 61.3 | 32.0 | 87.3 | 45.6 |
| 0.2 T | 46.5 | 24.3 | 61.4 | 32.1 | 88.0 | 46.0 |
| 1.5 T | 47.2 | 24.6 | 63.0 | 32.9 | 88.5 | 46.2 |
| 3 T | 45.5 | 23.7 | 62.2 | 32.5 | 88.7 | 46.3 |
| **r. temporomandib. j.** | | | | | | |
| 0 T | 28.7 | 15.0 | 40.3 | 21.0 | 53.0 | 27.7 |
| 0.2 T | 28.2 | 14.7 | 38.7 | 20.2 | 51.8 | 27.1 |
| 1.5 T | 31.6 | 16.5 | 42.9 | 23.0 | 54.2 | 28.3 |
| 3 T | 29.4 | 15.4 | 42.9 | 22.4 | 54.2 | 28.3 |
| **opt. chiasm** | | | | | | |
| 0 T | 39.3 | 20.5 | 83.0 | 43.3 | 101.8 | 53.1 |
| 0.2 T | 39.4 | 20.6 | 83.0 | 43.3 | 101.6 | 53.0 |
| 1.5 T | 41.5 | 21.6 | 82.4 | 43.0 | 101.7 | 53.1 |
| 3 T | 43.3 | 22.6 | 82.9 | 43.3 | 101.8 | 53.1 |

**Table 11.17** Integral dose for the different optimisation results, $V_{tot}$=2.9 litres

| | 0 T | B = 0.2 T | B = 1.5 T | B = 3 T |
|---|---|---|---|---|
| integral dose: $E_V$[Gy·l] | 27.5 | 27.6 | 28.2 | 28.0 |
| relative to 0 T: $E_{V,B}/E_{V,0T}$ | 1.000 | 1.004 | 1.025 | 1.018 |

Difference plot are shown in figure 11.29, and no deviations above 1 % can be observed in the target but only in the surrounding tissues.

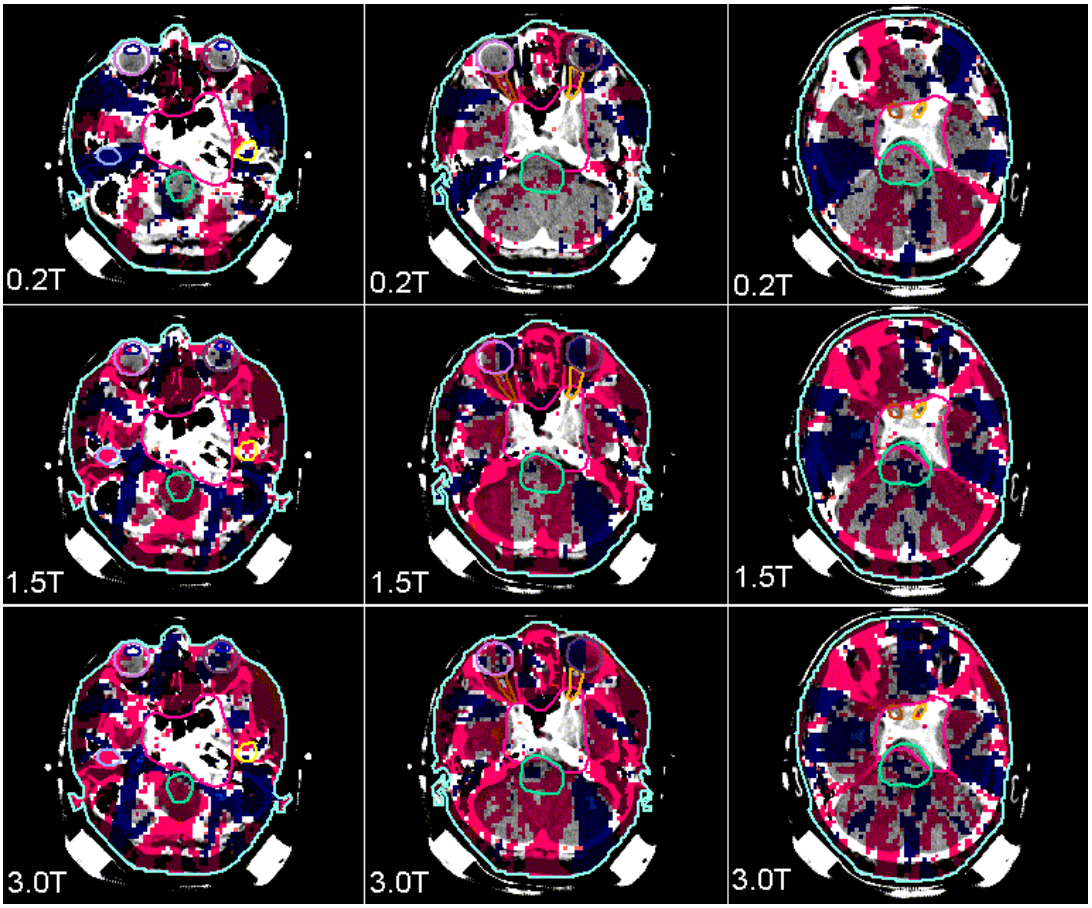


**Figure 11.29** Difference plots of the brain warped beamlet plans with respect to the 0 T plan at different depths (columns). Deviations between 1 and 10 % are shown, where red represents an overdosage in the warped beamlet plan, and blue represents an underdosage.

### Differences in Fluence Patterns for Same Dose to the Tumour

Also in the meningeoma case, an increase in fluence can be noticed for the plans optimised using the warped beamlets. Summation of the beamlet weights leads to the following figures:

$$\frac{\sum_{i=1}^{N} w_{0.2T,i}}{\sum_{i=1}^{N} w_{0T,i}} = 1.006, \quad \frac{\sum_{i=1}^{N} w_{1.5T,i}}{\sum_{i=1}^{N} w_{0T,i}} = 1.032 \quad \text{and} \quad \frac{\sum_{i=1}^{N} w_{3T,i}}{\sum_{i=1}^{N} w_{0T,i}} = 1.040,$$

where $N$ is the total number of beamlets, and $w_{0T,i}$, $w_{0.2T,i}$, $w_{1.5T,i}$ and $w_{3T,i}$ are the weights of the i's beamlet of the 0 T, 0.2 T, 1.5 and 3 T optimisation result, respectively.

Among the four cases considered, these are the highest difference values, and they are very comparable with the values for the prostate. They are again in agreement with the integral dose vlues reported in table 11.17 above, considering the lack of around 2 % of the energy in the 3 T kernel.

The significant increase in beamlet weights is not directly apparent from the plots of figure 11.30 where the differences rather look less pronounced than in other cases.

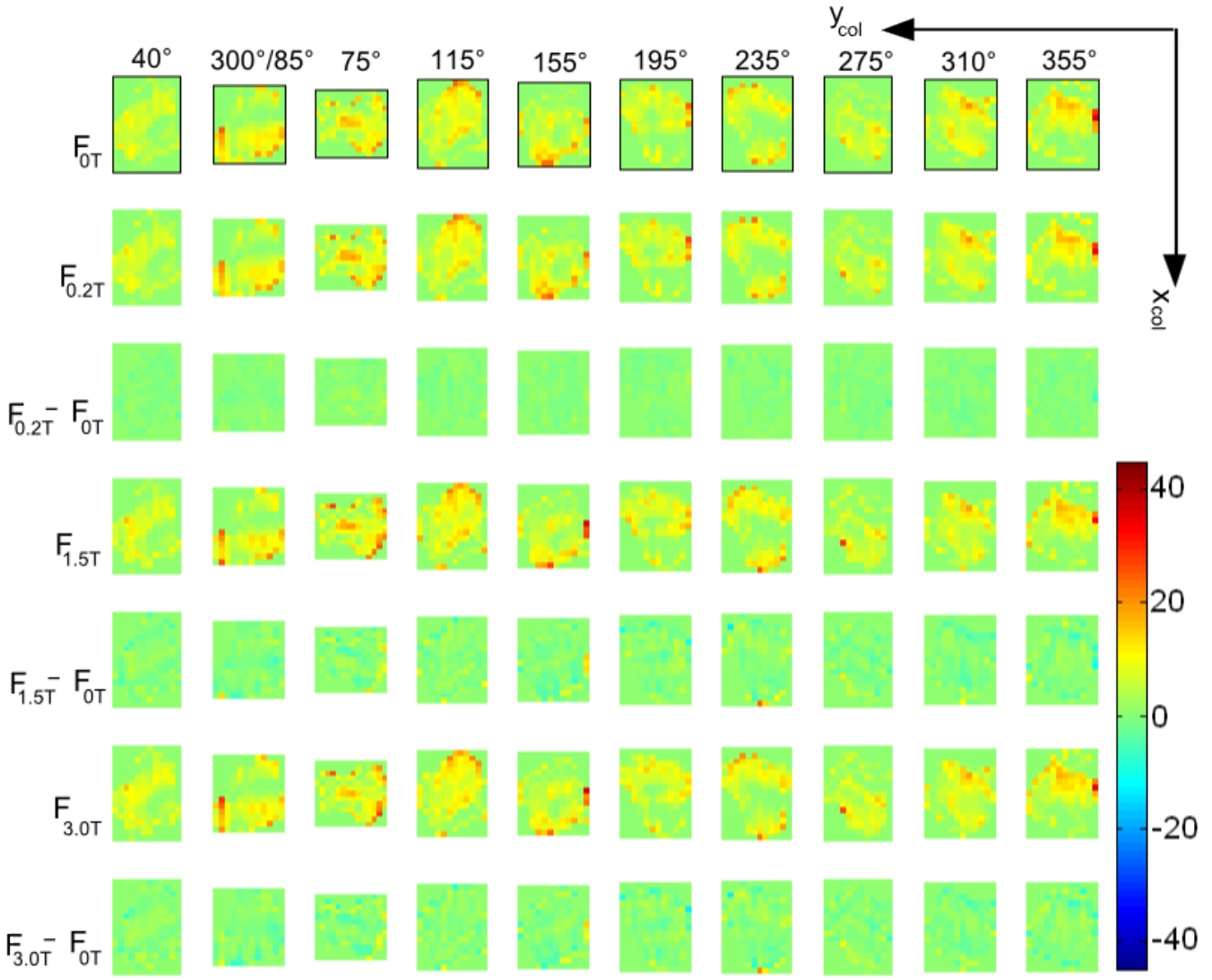


**Figure 11.30** Beamlet weight patterns of the optimisation using the original 0 T beamlet (top row), and the patterns from using the beamlets warped to 0.2 T (2nd row), 1.5 T (4th row) and 3 T (6th row), and the differences to the 0 T pattern (3rd, 5th and 7th row).

### Differences in Dose for Same Fluence Patterns

Using the 0 T fluence in combination with the magnetically deformed beamlets, a strong impairment of the target dose is observed for the meningeoma case as well, as figure 11.31 reveals. Also some organs at risk receive a lower dose than in the 0 T plan.

Dose-volume measures reporting the impact on the target dose are found in table 11.18, and it can be seen than the near-minimum dose $D_{98\%}$ drops by up to 6 % of the prescribed dose when calculation is performed by means of the 3 T beamlet. Also the median and mean dose are reduced by more than 3 % of the prescribed dose in the 3 T case, whereas the near-maximum dose $D_{2\%}$ slightly increases at 3 T and even more so at 1.5 T. It is likely that the increase is due to positive superposition of the dose of several beamlets in areas to which, at 0 T, dose from fewer beamlets contributes.

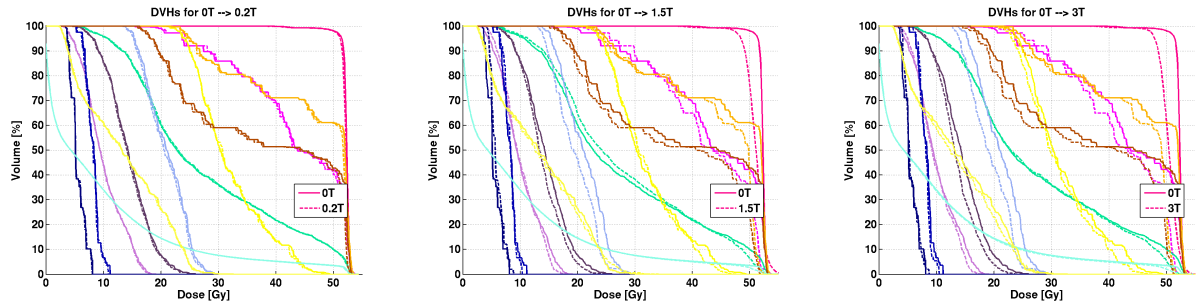


**Figure 11.31** target (magenta), optic chiasm (pink), right/left optic nerve (brown/orange), spinal cord (yellow), brain stem (mint), right/left temporomandibular joint (blue/yellow), right/left eye (purple/purple), right/left lens (blue/blue), patient contour (turquoise)

**Table 11.18** Dose-volume measures in the target of the brain cancer case

| | $D_{98\%}$[%] | $D_{98\%}$[Gy] | $D_{50\%}$[%] | $D_{50\%}$[Gy] | $D_{mean}$[%] | $D_{mean}$[Gy] | $D_{2\%}$[%] | $D_{2\%}$[Gy] | HI |
|---|---|---|---|---|---|---|---|---|---|
| 0 T | 96.2 | 50.2 | 100.2 | 52.3 | 100.0 | 52.2 | 101.7 | 53.1 | 0.05 |
| 0 T→0.2 T | 95.4 | 50.1 | 100.0 | 52.2 | 99.8 | 52.1 | 101.3 | 53.2 | 0.06 |
| 0 T→1.5 T | 90.3 | 47.4 | 97.4 | 51.1 | 97.8 | 51.0 | 103.6 | 54.1 | 0.13 |
| 0 T→3 T | 90.2 | 47.1 | 96.6 | 50.4 | 96.5 | 50.4 | 102.3 | 53.4 | 0.12 |

The decrease in dose to the organs at risk is reflected in the dose-volume measures displayed in table 11.19, whereas values for organs with little or no change have been included in table B.12 in the appendix.

The integral dose values are listed in table 11.20, and they reflect the energy deposition in the warping kernels, i.e. insignificant changes for 0.2 T and 1.5 T, and 2 % at 3 T.

The difference plots of figure 11.32 reveal that beside larger regions of underdosage to the target, islands of overdosage exist as well in the dose distributions calculated by means of the warped beamlets. It may be noticed throughout the transverse planes displayed, that over- and underdosage pattern alternate.

Close-up views of target coverage at 1.5 T and 3 T are displayed in figure 11.33 and 11.34.

**Table 11.19** Dose-volume measures for the organs at risk in the brain cancer case

| | $D_{98\%}$[%] | $D_{98\%}$[Gy] | $D_{mean}$[%] | $D_{mean}$[Gy] | $D_{2\%}$[%] | $D_{2\%}$[Gy] |
|---|---|---|---|---|---|---|
| **r. opt. nerve** | | | | | | |
| 0 T | 33.1 | 17.3 | 73.5 | 38.4 | 101.5 | 53.0 |
| 0 T → 0.2 T | 33.7 | 17.6 | 72.8 | 38.0 | 101.0 | 52.7 |
| 0 T → 1.5 T | 32.8 | 17.1 | 69.5 | 36.3 | 98.9 | 51.7 |
| 0 T → 3 T | 32.4 | 16.9 | 68.8 | 35.9 | 97.7 | 51.0 |
| **l. opt. nerve** | | | | | | |
| 0 T | 45.7 | 23.9 | 86.8 | 45.3 | 101.8 | 53.1 |
| 0 T → 0.2 T | 45.6 | 23.8 | 86.4 | 45.1 | 101.3 | 52.9 |
| 0 T → 1.5 T | 45.1 | 23.5 | 83.9 | 43.8 | 99.3 | 51.9 |
| 0 T → 3 T | 44.7 | 23.3 | 83.1 | 43.4 | 98.4 | 16.9 |
| **spinal cord** | | | | | | |
| 0 T | 5.3 | 2.8 | 25.8 | 13.5 | 48.6 | 25.4 |
| 0 T → 0.2 T | 5.4 | 2.8 | 25.8 | 13.5 | 49.7 | 25.9 |
| 0 T → 1.5 T | 5.6 | 2.9 | 25.6 | 13.3 | 52.5 | 27.4 |
| 0 T → 3 T | 5.5 | 2.9 | 24.9 | 13.0 | 50.5 | 26.3 |
| **r. temporomandib. j.** | | | | | | |
| 0 T | 28.7 | 15.0 | 40.3 | 21.0 | 53.0 | 27.7 |
| 0 T → 0.2 T | 28.0 | 14.6 | 39.7 | 20.7 | 52.8 | 27.5 |
| 0 T → 1.5 T | 26.2 | 13.7 | 37.4 | 19.5 | 52.6 | 27.4 |
| 0 T → 3 T | 25.7 | 13.4 | 36.9 | 19.3 | 52.0 | 27.2 |
| **opt. chiasm** | | | | | | |
| 0 T | 39.3 | 20.5 | 83.0 | 43.3 | 101.8 | 53.1 |
| 0 T → 0.2 T | 40.0 | 20.9 | 82.8 | 43.2 | 101.5 | 53.0 |
| 0 T → 1.5 T | 45.8 | 23.9 | 81.4 | 42.5 | 100.5 | 52.4 |
| 0 T → 3 T | 44.4 | 23.2 | 80.3 | 41.9 | 98.7 | 51.5 |
| **l. eye** | | | | | | |
| 0 T | 13.2 | 6.9 | 27.5 | 14.3 | 43.5 | 22.7 |
| 0 T → 0.2 T | 13.0 | 6.8 | 27.2 | 14.2 | 43.2 | 22.6 |
| 0 T → 1.5 T | 14.1 | 7.3 | 26.4 | 13.8 | 40.7 | 21.2 |
| 0 T → 3 T | 13.8 | 7.2 | 25.9 | 13.5 | 40.4 | 21.1 |
| **brain stem** | | | | | | |
| 0 T | 14.6 | 7.6 | 52.5 | 27.4 | 101.0 | 53.1 |
| 0 T → 0.2 T | 15.2 | 7.9 | 52.8 | 27.6 | 100.9 | 52.7 |
| 0 T → 1.5 T | 15.6 | 8.2 | 53.6 | 28.0 | 99.8 | 52.1 |
| 0 T → 3 T | 14.8 | 7.7 | 52.1 | 27.2 | 98.4 | 51.4 |

**Table 11.20** Integral dose for 0 T fluence in combination with warped beamlets, $V_{tot}$=2.9 litres

| | 0 T | B = 0.2 T | B = 1.5 T | B = 3 T |
|---|---|---|---|---|
| integral dose: $E_V$[Gy·l] | 27.5 | 27.5 | 27.3 | 26.9 |
| relative to 0 T: $E_{V,B}/E_{V,0T}$ | 1.000 | 1.000 | 0.993 | 0.978 |

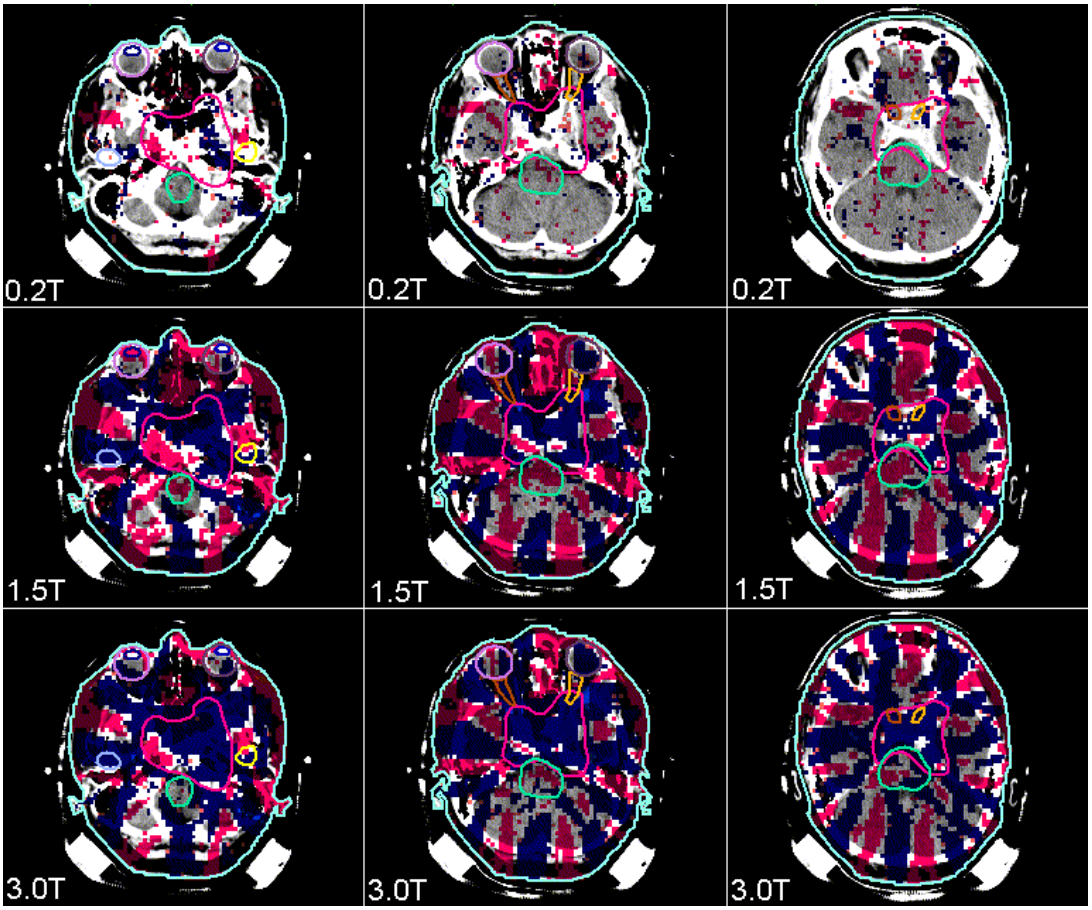


**Figure 11.32** Difference plots of the brain case, from using the 0 T fluence with the warped beamlets. The transverse plane is shown at different depths (columns) with deviations between 1 and 10 %, where red represents an overdosage in the warped beamlet plan, and blue represents an underdosage.

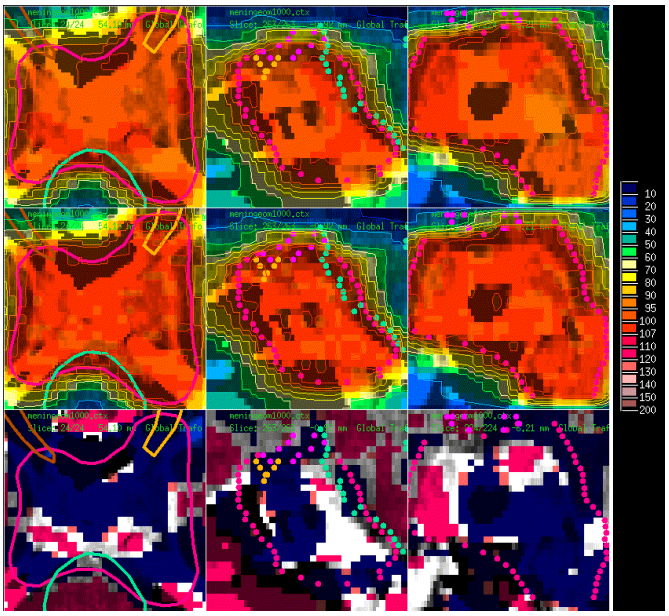


**Figure 11.33** Close up of the target coverage of the brain case using the 0 T fluence with the 1.5 T beamlet (top) and the 0 T beamlet (middle), as well as the difference between both.

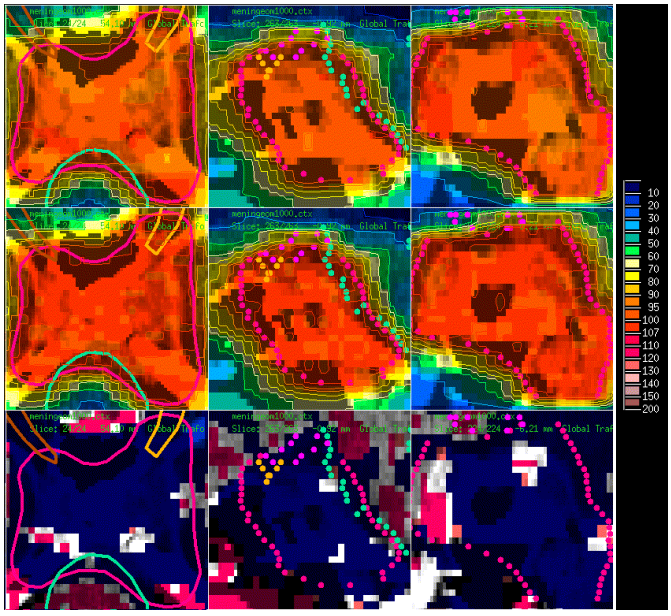


**Figure 11.34** Close up of the target coverage of the brain case using the 0 T fluence with the 3 T beamlet (top) and the 0 T beamlet (middle), as well as the difference between both.

## 11.3 Summary and Conclusion

Dose warping was applied to four patient cases in a treatment plan optimisation study. For each of the cases, first the effects of using warped beamlets directly in the optimisation process were investigated in terms of plan quality, along with the overall impact on the dose distribution in the patient and the differences in fluence profiles determined by the optimiser. Subsequently, it was discussed for all cases how usage of warped beamlets affects the dose distribution if a fluence is applied that does not take into account the effects of a magnetic field.

The cancer sites studied were the prostate, head and neck, abdomen, and brain, and for each site warping kernels for magnetic fields of 0.2 T, 1.5 T and 3 T were used. The findings were very consistent among the different sites: Application of a warped beamlet in optimisation did not impair target coverage in any of the sites, irrespective of the magnetic field that was used.

At 0.2 T, the effects on the dose to organs at risk were negligible for basically all patient cases, while at 1.5 T and 3 T, a slight increase of dose to certain organs at risk could be noticed. This increase is thought to be partially attributed to the relatively lower depth-dose profiles observed at magnetic fields of this magnitude at greater depths which originate from secondary electrons depositing their energy rather sideways from the beam than along the depth of it. A higher photon fluence is therefore required to transport the same dose into a given depth as without a magnetic field, and the overall energy deposited in the patient increases.

Table 11.21 summarises these findings: In the first row, the beamlet weight ratio (BWR) is reported that results from dividing the sum of the beamlet weights from optimisation based on the warped beamlets by the sum of the beamlet weights from the 0 T optimisation. As was discussed in the results section, this value is slightly too high since the warped beamlets contain less energy than the 0 T beamlet. Therefore, the second row of the table lists the ratio of integral dose values from using the warped beamlets for dose calcuation based on the 0 T fluence and the 0 T result ($IDR_{0TF}$) which reflects the energy ratio in the warped beamlets with respect to the 0 T beamlet: In the 0.2 T kernel, the same amount of energy is deposited as in the 0 T kernel, while the energy in the 1.5 T kernel and the 3 T kernel differs by <1 % and around 2 %, respectively, from the 0 T kernel. In the third row, the ratio of integral dose values from optimising by means of the warped beamlets and by means of the 0 T beamlet are displayed. This last row represents the actual energy increase that is needed to generate a dose distribution in the target that is comparable with the 0 T solution, and consistently, it is given approximately by the product of the values in the upper two rows.

**Table 11.21** Beam weight ratio (BWR) and integral dose ratio (IDR) between the warping plans and the 0 T plan. $IDR_{0TF}$ denotes the result from using the warped beamlets with the 0 T fluence, and $IDR_{opt}$ denotes the result from optimisation by means of the warped beamlets.

| | **prostate** | | | **head and neck** | | | **abdomen** | | | **brain** | | |
|---|---|---|---|---|---|---|---|---|---|---|---|---|
| | **0.2 T** | **1.5 T** | **3 T** | **0.2 T** | **1.5 T** | **3 T** | **0.2 T** | **1.5 T** | **3 T** | **0.2 T** | **1.5 T** | **3 T** |
| BWR | 1.005 | 1.020 | 1.036 | 1.003 | 1.015 | 1.023 | 1.001 | 1.018 | 1.030 | 1.006 | 1.032 | 1.040 |
| $IDR_{0TF}$ | 0.997 | 0.992 | 0.981 | 1.000 | 0.992 | 0.981 | 1.000 | 0.991 | 0.971 | 1.000 | 0.993 | 0.978 |
| $IDR_{opt}$ | 1.003 | 1.014 | 1.022 | 1.001 | 1.010 | 1.006 | 1.000 | 1.011 | 1.005 | 1.004 | 1.025 | 1.018 |

It can be seen that the increase is higher in the prostate and brain cases than in the two other ones, and it can be speculated that this is related to the fact that the radiological depth to be penetrated before the target is reached, is rather high in these two cases. In the head-and-neck case, parts of the target were close to the surface, where the upstream shift of the depth-dose profile in a magnetic field leads to increased dose values which may be the reason why the increase in integral dose is not so pronounced.

In spite of the differences in dose deposition, fluence patterns found by optimisation using the warped beamlets still resemble the patterns from optimisation using the original 0 T beamlet. However, deviations

could be observed.

When combining the 0 T fluence with the warped beamlets in dose calculation, a degradation of target coverage is seen in all patient cases for 1.5 T and 3 T, whereas at 0.2 T this is only slightly the case for the abdominal cancer. In the prostate cancer case, the dose to the target is basically reduced, while for the other cases, also regions of increased dose are remarked in the target structures. In all cases, however, are the near-minimum dose $D_{98\%}$ and the mean dose reduced as can be seen in table 11.22, where the change of dose-volume measures with respect to the 0 T results are listed.

**Table 11.22** Change of dose-volume measures in the main target when using the 0 T fluence in combination with the warped beamlets. Values are in percent of the prescribed dose.

| | **prostate** | | | **head and neck** | | | **abdomen** | | | **brain** | | |
|---|---|---|---|---|---|---|---|---|---|---|---|---|
| | **0.2 T** | **1.5 T** | **3 T** | **0.2 T** | **1.5 T** | **3 T** | **0.2 T** | **1.5 T** | **3 T** | **0.2 T** | **1.5 T** | **3 T** |
| $D_{98\%}$[%] | -0.2 | -3.0 | -4.5 | -0.1 | -4.0 | -4.6 | -0.3 | -4.2 | -4.3 | -0.8 | -5.9 | -6.0 |
| $D_{\text{mean}}$[%] | -0.1 | -1.6 | -3.2 | -0.1 | -2.0 | -3.3 | -0.2 | -2.4 | -3.5 | -0.2 | -2.2 | -3.5 |
| $D_{2\%}$[%] | -0.1 | 0.0 | -1.7 | +0.2 | +0.7 | -0.9 | 0.0 | -0.7 | -1.7 | -0.4 | +1.9 | +0.6 |

On the other hand, the near-maximum dose $D_{2\%}$ was less affected and in some cases even increased. It is likely that this increase is caused by the superposition of dose contributions from different beamlets in areas where at 0 T, less beamlets contributes.

For all results, the time required in optimisation and dose calculation was not higher than for a conventional pencil-beam optimisation, except for one warping operation applied prior to the actual optimisation process, to the beamlet dose distribution. The warping implemented in a MATLAB routine (v7.11) [66] needed a maximum of 34 seconds for Fourier transformation of the beamlet dose distribution, multiplication by the warping kernel and backtransformation to obtain the warped beamlet, on either one of three computer systems tested in order to obtain a (256×256×510) voxel beamlet dose distribution. These were two Intel Xeon systems with two four-core processors each (X5450, E5345), adding up to 8 cores each, and one AMD system consisting of 4 Quad-Core Opteron (8350) processors, adding up to a total of 16 cores, with the default parallelisation of MATLAB. Application of fftw [76] optimisation reduced the time to 25 seconds (E5345) and 19 seconds (X5450) on the Intel Xeon systems. The generation of a warping kernel from MC-simulated point kernels took around 20 seconds, where the point kernel generation itself was in the range of hours using the Geant4 toolkit ([21][22], cf. section 3.1).

It can be concluded from this chapter that the applicability of the warping method in treatment plan optimisation was demonstrated and non-negligible impacts were seen on the resulting dose distributions. For a further discussion about the potential and the limitations of the warping method it may be referred to chapter 12.

# Chapter 12

# Discussion of the Warping Method

The method of dose warping presents a means to include magnetic field effects into photon dose calculation. By convolution with an appropriate warping kernel, a conventional dose distribution from irradiation in the absence of any magnetic field is transformed into one that incorporates magnetic deflection of secondary electrons.

The potential of such a method arises from its computational simplicity if compared with Monte-Carlo simulations. Monte-Carlo simulations constitute the only other means for dose calculation in a magnetic field that is seriously considered for radiation treatment planning [62][44][57]. Having a faster means of dose calculation at hand, real-time online replanning on the basis of the MR imaging may become possible. What is more, warping may be combined with any available conventional dose calculation method and is therefore flexible in terms of wide applicability.

In this work, the performance of the method was investigated in homogeneous media (cf. chapter 9) and in phantom studies (cf. chapter 10), where Monte-Carlo simulations were used as the reference method for evaluation. This was followed by a demonstration of the applicability of dose warping in treatment plan optimisation (cf. chapter 11).

In homogeneous media, dose warping was capable of modelling the magnetic field effects nearly perfectly in terms of the shape of the deformed dose distribution. In water and bone, also the height of the dose profiles agreed, and only in lung were deviations with respect to the exact magnitude of dose observed at 1.5 T and 3 T. The electron return effect at the exit surface of the beam from the tissue was not modelled by the warping method but it has been argued in section 9.3 already that this issue can easily be overcome by addition of some bolus material on the skin of the patient which is generally considered advisable for irradiation in a magnetic field.

For the phantom studies, one geometry each was chosen in which the warping method was expected to perform well (brain) and to yield larger deviations (lung). Indeed are the results in the brain phantom promising for the applicability of the warping method, whereas in the lung tumour phantom, returning electrons cause patterns of dose increment that the warping does not model. However, also in the lung tumour phantom did the warping significantly reduce differences to the reference simulation if compared with not taking into account the magnetic field at all, such that even here, a potential of the warping method could be identified. It was concluded in section 10.3 at the end of the chapter, that in cases involving larger heterogeneities, the value of dose warping may lie in its application in optimisation rather than in presenting the sole means of dose calculation, while in more homogeneous situations dose warping is expected to yield acceptable results.

In fact, a closer look has to be taken on the exact geometry under consideration. One aspect with regard to air-filled cavities is that the amount of dose due to the ERE is strongly affected by the size of the cavity

with respect to the radius of electron deflection which itself depends on both the magnitude of the magnetic field and the photon spectrum used. If the cavity is small compared with the electron radius, electrons will not return to their exit surface but reach the opposite side of the cavity. So for air-filled cavities, there may be good reasons not to employ the warping method as the sole dose calculation method, depending on the precise anatomy. On the other hand, Raaijmakers et al. [59] report that the use of opposing fields across an air-filled volume will basically lead to a compensation of the ERE from one beam direction by the new build up from the opposing beam direction. Therefore, it may be a matter of beam setup to avoid regions of strong ERE influence, and the performance of the warping method in this respect would have to be separately analysed. Besides, some air-filled cavities like intestinal loops may change their shape and location on a daily basis such that it is unlikely that ERE doses will add up over the course of a fractionated treatment. In this case, the continuous imaging information from the MR-scanner will be helpful to monitor daily changes and retrospectively analyse the actual dose deposition.

Another aspect when judging whether or not the warping method presents an appropriate means for dose calculation, is to consider which cases are deemed to benefit from application of MR-guidance. The real benefit over x-ray based procedures will come where the difference in Hounsfield units between neighbouring structures of interest is small. The varying location of nerves, lymph nodes, seminal vesicles, the exact boundaries between organs or the position of a lung tumour in a collapsed lung can be identified on an MR image but not necessarily on a CT image. Also for an update on histological information, MR will be useful to differentiate between tumour and surrounding tissues, e.g. in liver or breast tissue, to identify inflammatory processes, or to obtain more detailed anatomical information by means of methods like diffusion tensor imaging. The advantage expected from MR guidance is therefore rather in soft tissues where the warping models the situation well. However, it will depend on the exact anatomy whether application of the method is considered advisable. Considering the use of dose warping as a fast online re-planning tool, a practical approach may be to assess the uncertainties posed by the method on the basis of an offline Monte-Carlo simulation during the treatment planning process and take an informed decision towards the applicability of the method in the specific case under consideration.

In conclusion, two cases can be identified that are expected to benefit from dose warping but need to be regarded separately in terms of the manner in which dose warping may be applied: On the one hand, heterogeneities may be so large that dose warping cannot be considered the only dose calculation method. If this is the case, still the fluence patterns found by optimisation based on warped beamlets will be closer to reality than if the magnetic field influence is not taken into account. An optimisation strategy can be used then that combines pencil-beam and Monte-Carlo dose calculation methods [77] to achieve a high accuracy in short calculation time, where dose warping would be applied to the pencil beam kernel used.

If, on the other hand, the irradiated tissue is rather homogeneous with respect to its electron density, dose warping has, beside its regular use for optimisation and dose calculation, the potential to be developed into a fast online re-planning tool. The MR imaging information acquired during treatment could be used directly to check the validity of the planned dose distribution for the given patient anatomy, and in case of deviations a new plan could be created. Also changes due to intrafraction organ motion could be incorporated by calculating regular updates of the dose distribution and optional adaption of the plan. For this potential to be exploited, necessarily an increase in the overall speed for dose calculation and optimisation is required and it remains to be determined how warping can be integrated in other strategies directed at this aim (e.g. Siggel et al. [33]).

In general, other intelligent strategies may also be considered to reduce tissue heterogeneity where dose calculation is needed. This could for example be achieved by means of beam angle selection [78][79][80], where beam directions penetrating low-density tissues or air could be penalised and therefore avoided.

Summarising, by the method of dose warping, a means for dose calculation in a magnetic field has been developed in this work and its performance has been investigated. It is expected that its potential prevails

over the limitations that have been found, although it need be mentioned that situations exist where dose warping will not suffice as a sole means of dose calculation. For actual implementation in a clinical setting, however, several issues still have to be addressed, e.g. with respect to determining the appropriate warping kernels for the spectrum and geometry used, incorporating beam divergence and validating the results dosimetrically.

# Part IV

# General Discussion and Suggestions for Further Work

In this work, two approaches are presented towards kernel-based dose calculation for an MRI-integrated irradiation device for radiation therapy with photons. The potential of an MRI-integrated irradiation device arises from the availability of images of excellent quality online, i.e. during the treatment procedure (cf. chapter 4). In order to fully exploit the potential and react to anatomical or physiological changes that occur throughout the treatment, a fast adaptation of the treatment plan to the actual situation is required.

Kernel-based dose calculation methods generally have the advantage of a higher speed when compared with Monte Carlo methods, which achieve a very high accuracy at the cost of longer calculation times (cf. chapter 3). For MRI-integrated devices involving a magnetic field in which dose is deposited, no kernel-based method has been published yet.

The analytical approach described in part II samples secondary Compton electrons due to photon interaction with tissue which are known to be the major cause of dose in the tissue, and uses a formulation of their tracks in matter to deposit energy according to the continuous slowing down approximation and thereby generate photon point interaction kernels. It is seen that the neglect of scatter in the approximation yields significant artefacts already in homogeneous medium, when creating pencil beams from the point kernels. The application of the energy and track information from the kernels generated in a superposition algorithm (cf. section 3.2) that would perform a density scaling on the basis of this information, is rejected due to the artefacts observed.

The second method presented is that of dose warping which transforms a dose distribution as observed without a magnetic field, into one that is observed under the influence of a magnetic field. It is seen to yield good results in rather homogeneous tissue, but in lung, the deviations between the warping results and reference Monte Carlo simulations are as high as 25 %. This accuracy is very comparable with that of a pencil beam algorithm showing deviations of up to 20 % in lung which is widely applied in radiation therapy dose calculation, either alone or complemented with Monte Carlo calculations (cf. chapter 3). It was found that the dose determined by dose warping is always closer to the reference simulation than if the magnetic field is not taken into considerations for 1.5 T and 3 T fields, where the magnetic field effects are very pronounced.

It was further demonstrated in this work that dose warping can be included in the optimisation process, and it was applied in a treatment planning study of four patient cases in combination with a pencil beam algorithm. Dose distributions generated by optimisation with warped beamlets were of the same quality as with the original 0 T beamlet; however, when calculating the dose due to the fluence from the 0 T optimisation, by means of the warped beamlets, a significant reduction of plan quality in terms of target coverage was observed with a decrease in $D_{98\ \%}$ of up to 6 % (cf. section 11.3). Based on the above findings, it is expected that the plans optimised by means of the warped beamlets are closer to the actual dose distribution than if the magnetic field is not taken into account.

The findings lead to the conclusion presented in chapter 12 that in situations involving larger heterogeneities, dose warping in combination with a pencil beam or superposition dose calculation algorithm may be a valuable method to be applied in optimisation, which is faster than Monte Carlo methods, but which should be complemented with one or more final Monte Carlo steps in order to achieve the desired accuracy. In more homogeneous geometries, it may even be used as the sole means of dose calculation with the potential to be developed into a real-time tool for on-the-flight dose calculations when computational speed further increases.

Calculation time for Monte Carlo methods is getting into the range of online applicability with values of 2.5 minutes reported by Bol et al. [1] to account for interfraction changes; however, kernel-based methods are likely to remain faster and thus can be imagined to open up possibilities for intrafraction motion mitigation on the basis of real-time dose calculation on real-time imaging data, and account for the motion of both the tumour and surrounding tissues.

Considering further the aim of optimisation to find the best treatment plan for the patient, it is desired to explore as many degrees of freedom as may influence the dose distribution. Traditionally, e.g. the beam angles for an IMRT treatment are manually selected by the treatment planner, and only the fluence patterns are optimised, whereas also the selection of the angle has an influence on the quality on the dose distribution achieved [80]. An ideal optimisation would know the contributions of all possible beamlets from all possible angles and be able to handle the information, such that also here, a potential for an increased speed due to kernel-based dose calculation may exist.

Another general aspect to be discussed here is that still in a magnetic field, dosimetry is not yet well-established [81], such that the benchmarking of any Monte Carlo algorithm is subject to further uncertainties which is also true for the determination of any dose calculation kernel. Additional tasks involve the modelling of the treatment head to determine the photon phase space the calculation is based on. Also with respect to the magnitude of the magnetic field to be used in MRI-integrated devices, different approaches exist (cf. chapter 4), and it may depend on this parameter as well, which type of dose calculation algorithm is best suited for a given device.

MRI-integration with irradiation units is currently in its beginnings, and methods for use with these promising devices are just evolving. The method of dose warping in combination with a pencil beam algorithm provides a second method for dose calculation in a magnetic field beside Monte Carlo simulations, where the latter are significantly more accurate particularly in heterogeneous tissues, but they exhibit longer calculation times. Hybrid use of both methods may be considered as well as the selection of the appropriate method for a given situation.

In the current state of the work, the performance of dose warping has been investigated and its applicability in the treatment planning process has been demonstrated. Using Monte Carlo simulations as the reference method, actual experimental validation has not been performed, although the dose distributions are basically consistent with publications of other authors. As mentioned in the discussion of the warping method (chapter 12) already, also beam divergence remains to be incorporated. Conduction of a treatment planning study comparing the warping-based and Monte-Carlo based optimisation, and differences of the warping-based optimisation results to Monte Carlo calculations is another task that has not been covered in this work but will be valuable to further assess the capabilities of the method.

# Appendix A

# Point Kernels

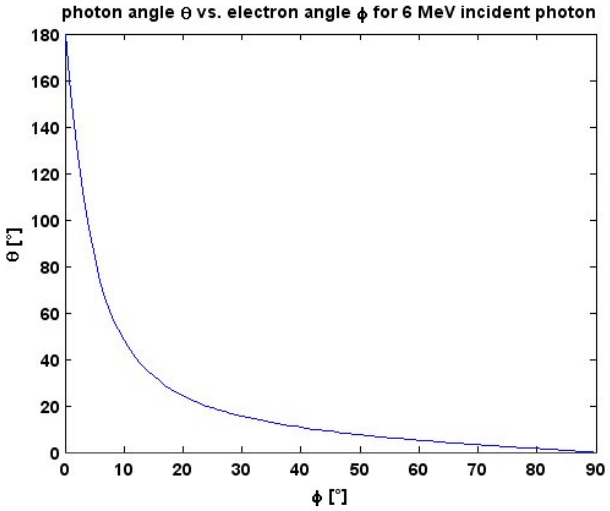


**Figure A.1** Photon and electron angle after Compton interaction according to equation 2.4.

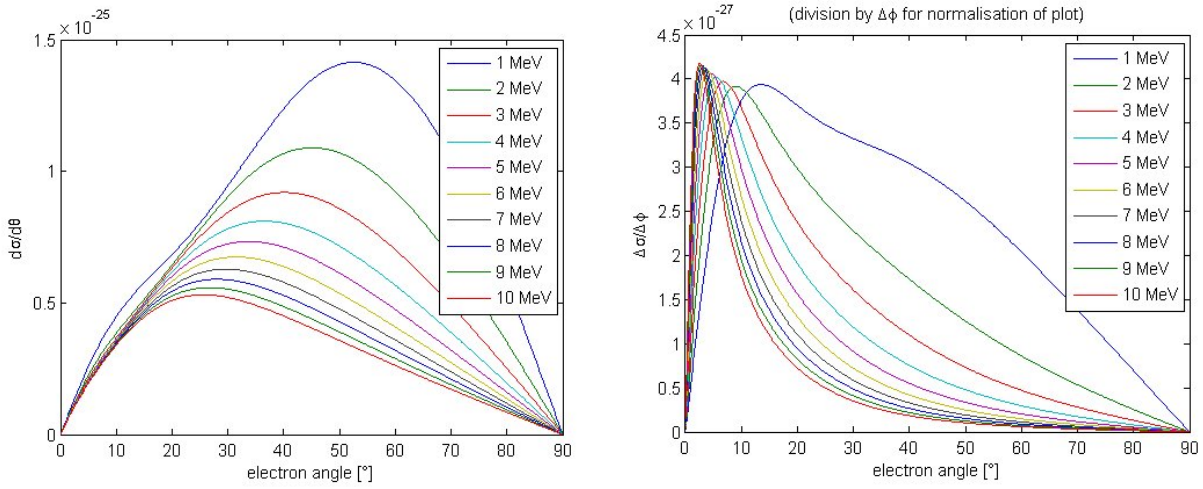


**Figure A.2** Differential Compton cross section according to equation 2.7 (left) and divided by corresponding angular interval of electron scatter angle (right). The photon angle interval $\Delta\theta$ corresponding to an electron angle interval of constant size $\Delta\phi$ is bigger for small values of $\phi$ (cf. figure A.1), so $\Delta\sigma$ relatively larger than $\frac{d\sigma}{d\theta}$ at low angles.

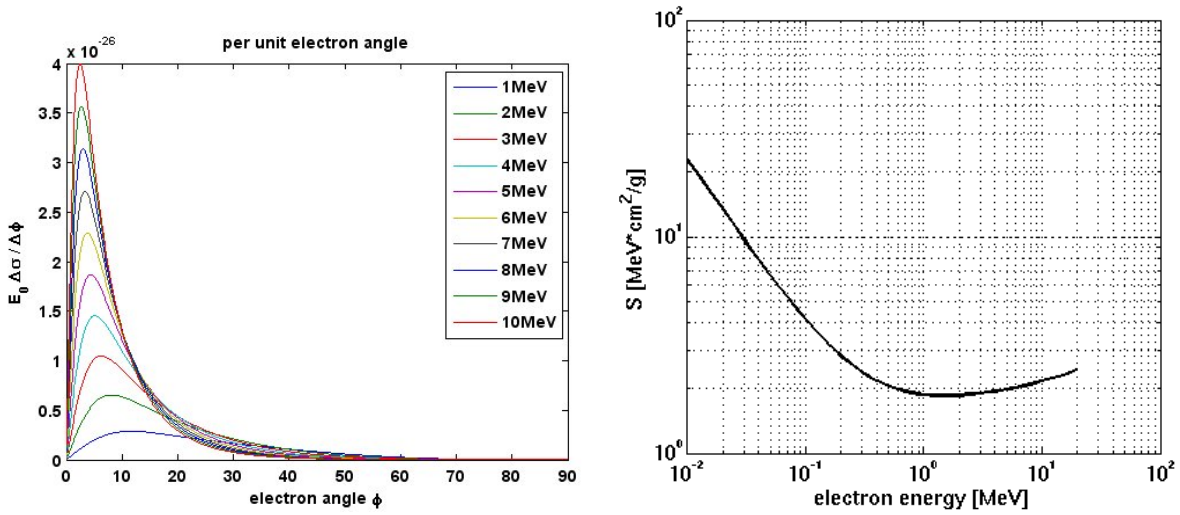


**Figure A.3** Product of the initial electron energy and the cross section of the respective angular interval (left). Electrons stopping powers from the ESTAR database (right) [65].

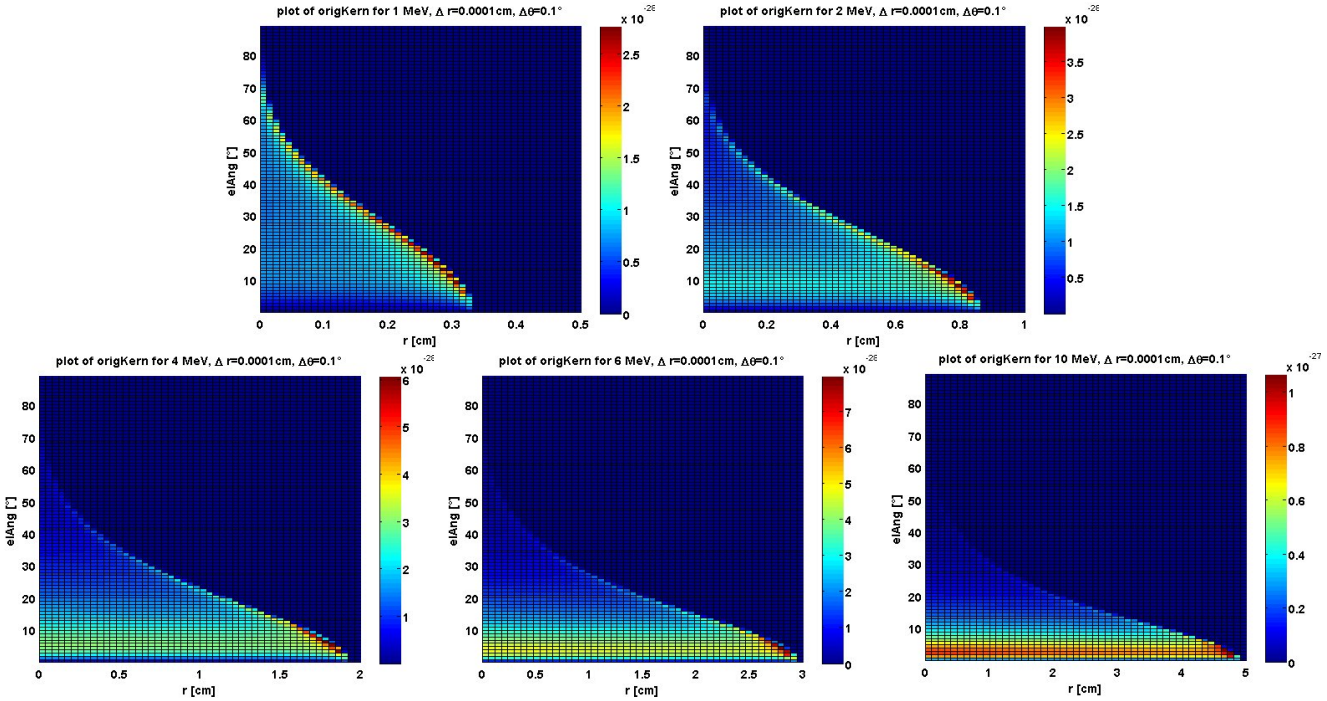


**Figure A.4** Energy deposition after csda is carried out for each interval of electron zenith angle, in total azimuthal angle of $2pi$, for 1 MeV, 2 MeV (top, left to right), 4 MeV, 6 MeV, 10 MeV (bottom, left to tight). For display, bigger pixels are used than for calculation.

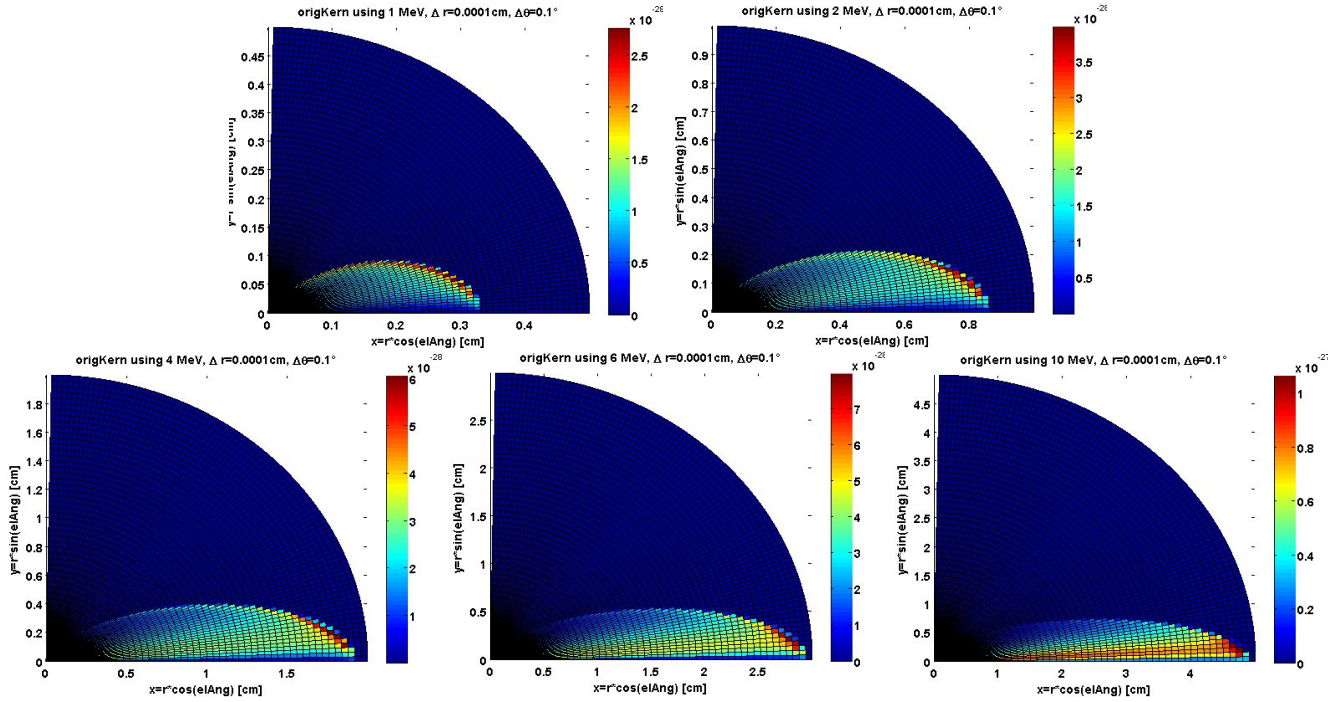


**Figure A.5** Polar plots of energy deposition after csda for each interval of electron zenith angle, in total azimuthal angle of $2pi$, for 1 MeV, 2 MeV (top, left to right), 4 MeV, 6 MeV, 10 MeV (bottom, left to tight). For display, bigger pixels are used than for calculation. In the point kernels presented in section 6.1.1, the energy is distributed in the full solid angle.

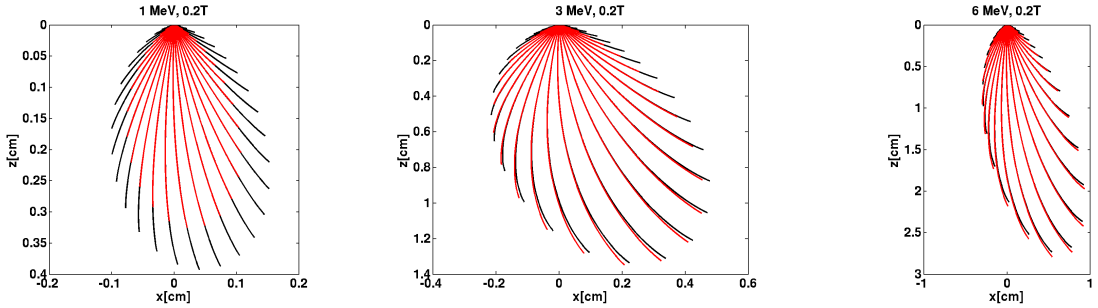


**Figure A.6** Analytical tracks for a 0.2 T magnetic field that were not part of the analysis in section 6.1.1 but may be used for comparison with the point kernels for warping.

# Appendix B

# Dose-volume measures

**Table B.1** Head and Neck: Warped beamlet optimisation: BOOST

| | $D_{98\%}$[%] | $D_{98\%}$[Gy] | $D_{50\%}$[%] | $D_{50\%}$[Gy] | $D_{mean}$[%] | $D_{mean}$[Gy] | $D_{2\%}$[%] | $D_{2\%}$[Gy] | HI |
|---|---|---|---|---|---|---|---|---|---|
| 0 T | 94.2 | 62.3 | 100.3 | 66.2 | 100.0 | 66.0 | 102.0 | 67.3 | 0.08 |
| 0.2 T | 94.4 | 62.3 | 100.3 | 66.2 | 100.0 | 66.0 | 102.0 | 67.3 | 0.08 |
| 1.5 T | 94.5 | 62.4 | 100.4 | 66.3 | 100.0 | 66.0 | 102.1 | 67.4 | 0.08 |
| 3 T | 94.4 | 62.3 | 100.4 | 66.2 | 100.0 | 66.0 | 102.1 | 67.3 | 0.08 |

**Table B.2** Head and Neck: Warped beamlet optimisation: target including the lymphatic vessels

| | $D_{98\%}$[%] | $D_{98\%}$[Gy] | $D_{50\%}$[%] | $D_{50\%}$[Gy] | $D_{mean}$[%] | $D_{mean}$[Gy] | $D_{2\%}$[%] | $D_{2\%}$[Gy] |
|---|---|---|---|---|---|---|---|---|
| 0 T | 77.0 | 50.8 | 82.7 | 54.6 | 86.3 | 57.0 | 101.3 | 66.9 |
| 0.2 T | 77.0 | 50.8 | 82.7 | 54.6 | 86.3 | 56.9 | 101.3 | 66.9 |
| 1.5 T | 76.9 | 50.7 | 101.5 | 54.6 | 86.4 | 57.0 | 101.5 | 67.0 |
| 3 T | 77.0 | 50.8 | 82.7 | 54.6 | 86.4 | 57.0 | 101.4 | 67.0 |

**Table B.3** Head and Neck: Warped beamlet optimisation: organs at risk

| | $D_{98\%}$[%] | $D_{98\%}$[Gy] | $D_{mean}$[%] | $D_{mean}$[Gy] | $D_{2\%}$[%] | $D_{2\%}$[Gy] |
|---|---|---|---|---|---|---|
| **r. eye 0 T** | 0.0 | 0.0 | 1.3 | 0.9 | 2.9 | 1.9 |
| 0.2 T | 0.0 | 0.0 | 1.3 | 0.9 | 2.8 | 1.9 |
| 1.5 T | 0.0 | 0.0 | 1.4 | 0.9 | 3.1 | 2.0 |
| 3 T | 0.0 | 0.0 | 1.3 | 0.9 | 2.9 | 1.9 |
| **l. eye 0 T** | 0.0 | 0.0 | 1.0 | 0.6 | 2.3 | 1.5 |
| 0.2 T | 0.0 | 0.0 | 1.0 | 0.6 | 2.3 | 1.5 |
| 1.5 T | 0.0 | 0.0 | 1.0 | 0.7 | 2.4 | 1.6 |
| 3 T | 0.0 | 0.0 | 1.0 | 0.7 | 2.3 | 1.5 |
| **opt. chiasm 0 T** | 0.0 | 0.0 | 2.3 | 1.5 | 4.0 | 2.7 |
| 0.2 T | 0.0 | 0.0 | 2.4 | 1.6 | 4.0 | 2.6 |
| 1.5 T | 0.0 | 0.0 | 2.4 | 1.6 | 4.1 | 2.7 |
| 3 T | 0.0 | 0.0 | 2.4 | 1.6 | 4.1 | 2.7 |
| **brain stem 0 T** | 0.0 | 0.0 | 11.3 | 7.4 | 38.0 | 25.1 |
| 0.2 T | 0.0 | 0.0 | 11.4 | 7.5 | 38.6 | 25.5 |
| 1.5 T | 0.0 | 0.0 | 11.8 | 7.8 | 42.3 | 27.9 |
| 3 T | 0.0 | 0.0 | 11.4 | 7.5 | 39.2 | 25.9 |
| **l. temporomand. j. 0 T** | 6.7 | 4.4 | 26.5 | 17.5 | 42.4 | 28.0 |
| 0.2 T | 6.9 | 4.6 | 27.0 | 17.8 | 43.8 | 28.9 |
| 1.5 T | 6.7 | 4.4 | 26.1 | 17.2 | 41.0 | 27.0 |
| 3 T | 6.8 | 4.5 | 26.3 | 17.4 | 42.0 | 27.7 |
| **r. temporomand. j. 0 T** | 7.8 | 5.1 | 28.4 | 18.7 | 42.4 | 30.1 |
| 0.2 T | 7.5 | 5.0 | 24.5 | 18.8 | 46.9 | 31.0 |
| 1.5 T | 7.7 | 5.1 | 29.0 | 19.1 | 45.0 | 29.7 |
| 3 T | 7.5 | 4.9 | 28.0 | 18.5 | 44.4 | 29.3 |
| **l. lens 0 T** | 0.8 | 0.5 | 1.3 | 0.9 | 1.6 | 1.1 |
| 0.2 T | 0.8 | 0.5 | 1.3 | 0.9 | 1.8 | 1.2 |
| 1.5 T | 0.8 | 0.5 | 1.4 | 0.9 | 1.9 | 1.2 |
| 3 T | 0.9 | 0.6 | 1.4 | 0.9 | 1.9 | 1.2 |
| **r. lens 0 T** | 0.8 | 0.5 | 1.5 | 1.0 | 2.1 | 1.4 |
| 0.2 T | 0.9 | 0.6 | 1.5 | 1.0 | 2.0 | 1.3 |
| 1.5 T | 1.1 | 0.7 | 1.5 | 1.0 | 2.0 | 1.3 |
| 3 T | 1.2 | 0.5 | 1.5 | 1.0 | 1.9 | 1.2 |

**Table B.4** Head and Neck: Warped beamlet optimisation: organs at risk

| | $D_{98\%}$[%] | $D_{98\%}$[Gy] | $D_{mean}$[%] | $D_{mean}$[Gy] | $D_{2\%}$[%] | $D_{2\%}$[Gy] |
|---|---|---|---|---|---|---|
| **l. opt. nerve 0 T** | 1.4 | 0.9 | 2.1 | 1.4 | 2.9 | 1.9 |
| 0.2 T | 1.3 | 0.8 | 2.1 | 1.4 | 2.8 | 1.8 |
| 1.5 T | 1.4 | 0.9 | 2.1 | 1.4 | 3.1 | 2.0 |
| 3 T | 1.3 | 0.9 | 2.1 | 1.4 | 3.0 | 1.9 |
| **r. opt. nerve 0 T** | 1.3 | 0.9 | 2.1 | 1.4 | 2.7 | 1.8 |
| 0.2 T | 2.8 | 0.9 | 2.1 | 1.4 | 1.9 | 1.8 |
| 1.5 T | 1.5 | 1.0 | 2.1 | 1.4 | 2.9 | 1.9 |
| 3 T | 1.2 | 0.8 | 2.1 | 1.4 | 2.9 | 1.9 |
| **l. parotid g. 0 T** | 16.1 | 10.6 | 37.4 | 24.7 | 83.7 | 55.2 |
| 0.2 T | 15.7 | 10.4 | 37.6 | 24.8 | 83.1 | 55.1 |
| 1.5 T | 15.2 | 10.0 | 38.0 | 25.1 | 83.1 | 54.8 |
| 3 T | 15.7 | 10.4 | 38.2 | 25.2 | 83.0 | 54.8 |
| **r. parotid g. 0 T** | 13.8 | 9.1 | 33.1 | 21.8 | 90.0 | 56.1 |
| 0.2 T | 14.4 | 9.5 | 33.1 | 21.9 | 10.4 | 55.9 |
| 1.5 T | 14.4 | 9.5 | 33.2 | 21.9 | 83.1 | 55.9 |
| 3 T | 14.6 | 9.6 | 33.3 | 22.0 | 84.8 | 56.0 |
| **spinal cord +3 mm 0 T** | 0.0 | 0.0 | 19.1 | 12.6 | 42.3 | 27.9 |
| 0.2 T | 0.0 | 0.0 | 19.0 | 12.5 | 42.3 | 27.9 |
| 1.5 T | 0.0 | 0.0 | 19.1 | 13.0 | 42.5 | 28.1 |
| 3 T | 0.0 | 0.0 | 18.9 | 12.5 | 42.5 | 28.0 |
| **spinal cord +5 mm 0 T** | 0.0 | 0.0 | 19.7 | 13.0 | 47.8 | 31.6 |
| 0.2 T | 0.0 | 0.0 | 19.6 | 13.0 | 47.8 | 31.5 |
| 1.5 T | 0.0 | 0.0 | 19.7 | 13.0 | 47.6 | 31.4 |
| 3 T | 0.0 | 0.0 | 19.6 | 12.9 | 47.7 | 31.5 |
| **larger spine 0 T** | 5.9 | 3.9 | 21.8 | 14.4 | 48.4 | 32.0 |
| 0.2 T | 6.0 | 4.0 | 21.8 | 14.4 | 48.3 | 31.9 |
| 1.5 T | 6.2 | 4.1 | 21.9 | 14.5 | 48.0 | 31.7 |
| 3 T | 6.3 | 4.1 | 21.7 | 14.4 | 48.0 | 31.7 |
| **spinal cord 0 T** | 0.0 | 0.0 | 18.3 | 12.1 | 38.4 | 25.3 |
| 0.2 T | 0.0 | 0.0 | 18.2 | 12.0 | 38.6 | 25.4 |
| 1.5 T | 0.0 | 0.0 | 18.3 | 12.1 | 38.3 | 25.3 |
| 3 T | 0.0 | 0.0 | 18.1 | 12.0 | 38.0 | 25.1 |

**Table B.5** Head and Neck: 0 T fluence: organs at risk

| | $D_{98\%}$[%] | $D_{98\%}$[Gy] | $D_{mean}$[%] | $D_{mean}$[Gy] | $D_{2\%}$[%] | $D_{2\%}$[Gy] |
|---|---|---|---|---|---|---|
| **r. eye 0 T** | 0.0 | 0.0 | 1.3 | 0.9 | 2.9 | 1.9 |
| 0 T → 0.2 T | 0.0 | 0.0 | 1.3 | 0.9 | 2.9 | 1.9 |
| 0 T → 1.5 T | 0.0 | 0.0 | 1.3 | 0.9 | 2.9 | 1.9 |
| 0 T → 3 T | 0.0 | 0.0 | 1.3 | 0.9 | 2.9 | 1.9 |
| **l. eye 0 T** | 0.0 | 0.0 | 1.0 | 0.6 | 2.3 | 1.5 |
| 0 T → 0.2 T | 0.0 | 0.0 | 1.0 | 0.6 | 2.3 | 1.5 |
| 0 T → 1.5 T | 0.0 | 0.0 | 1.0 | 0.6 | 2.2 | 1.5 |
| 0 T → 3 T | 0.0 | 0.0 | 1.0 | 0.6 | 2.2 | 1.4 |
| **opt. chiasm 0 T** | 0.0 | 0.0 | 2.3 | 1.5 | 4.0 | 2.7 |
| 0 T → 0.2 T | 0.0 | 0.0 | 2.4 | 1.6 | 4.0 | 2.7 |
| 0 T → 1.5 T | 0.0 | 0.0 | 2.4 | 1.6 | 4.2 | 2.8 |
| 0 T → 3 T | 0.0 | 0.0 | 2.3 | 1.5 | 4.0 | 2.6 |
| **brain stem 0 T** | 0.0 | 0.0 | 11.3 | 7.4 | 38.0 | 25.1 |
| 0 T → 0.2 T | 0.0 | 0.0 | 11.3 | 7.4 | 37.9 | 25.0 |
| 0 T → 1.5 T | 0.0 | 0.0 | 11.2 | 7.4 | 37.7 | 24.9 |
| 0 T → 3 T | 0.0 | 0.0 | 10.9 | 7.2 | 36.5 | 24.1 |
| **l. temporomand. j. 0 T** | 6.7 | 4.4 | 26.5 | 17.5 | 42.4 | 28.0 |
| 0 T → 0.2 T | 6.6 | 4.3 | 26.2 | 17.3 | 41.8 | 27.6 |
| 0 T → 1.5 T | 6.4 | 4.3 | 25.2 | 16.6 | 42.4 | 28.0 |
| 0 T → 3 T | 6.5 | 4.3 | 24.8 | 16.4 | 41.7 | 27.5 |
| **r. temporomand. j. 0 T** | 7.8 | 5.1 | 28.4 | 18.7 | 42.4 | 30.1 |
| 0 T → 0.2 T | 7.8 | 5.2 | 28.3 | 18.7 | 46.1 | 30.4 |
| 0 T → 1.5 T | 7.6 | 5.0 | 28.3 | 18.7 | 48.4 | 32.0 |
| 0 T → 3 T | 7.4 | 4.9 | 27.4 | 18.1 | 47.2 | 31.2 |
| **l. lens 0 T** | 0.8 | 0.5 | 1.3 | 0.9 | 1.6 | 1.1 |
| 0 T → 0.2 T | 0.9 | 0.6 | 1.3 | 0.9 | 1.8 | 1.2 |
| 0 T → 1.5 T | 0.9 | 0.6 | 1.3 | 0.9 | 1.8 | 1.2 |
| 0 T → 3 T | 0.8 | 0.5 | 1.3 | 0.8 | 1.9 | 1.3 |
| **r. lens 0 T** | 0.8 | 0.5 | 1.5 | 1.0 | 2.1 | 1.4 |
| 0 T → 0.2 T | 0.9 | 0.6 | 1.4 | 0.9 | 1.9 | 1.2 |
| 0 T → 1.5 T | 1.0 | 0.6 | 1.4 | 0.9 | 1.9 | 1.3 |
| 0 T → 3 T | 1.1 | 0.7 | 1.5 | 1.0 | 2.3 | 1.5 |

**Table B.6** Head and Neck: 0 T fluence: organs at risk

| | $D_{98\%}$[%] | $D_{98\%}$[Gy] | $D_{mean}$[%] | $D_{mean}$[Gy] | $D_{2\%}$[%] | $D_{2\%}$[Gy] |
|---|---|---|---|---|---|---|
| **l. opt. nerve 0 T** | 1.4 | 0.9 | 2.1 | 1.4 | 2.9 | 1.9 |
| 0 T → 0.2 T | 1.3 | 0.8 | 2.0 | 1.3 | 2.8 | 1.9 |
| 0 T → 1.5 T | 1.3 | 0.9 | 2.1 | 1.4 | 2.8 | 1.9 |
| 0 T → 3 T | 1.2 | 0.8 | 2.0 | 1.3 | 2.6 | 1.7 |
| **r. opt. nerve 0 T** | 1.3 | 0.9 | 2.1 | 1.4 | 2.7 | 1.8 |
| 0 T → 0.2 T | 1.4 | 0.9 | 2.1 | 1.4 | 2.9 | 1.9 |
| 0 T → 1.5 T | 1.3 | 0.9 | 2.1 | 1.4 | 2.9 | 1.9 |
| 0 T → 3 T | 1.5 | 1.0 | 2.1 | 1.4 | 2.8 | 1.8 |
| **l. parotid g. 0 T** | 16.1 | 10.6 | 37.4 | 24.7 | 83.7 | 55.2 |
| 0 T → 0.2 T | 15.8 | 10.5 | 37.5 | 24.8 | 83.6 | 55.2 |
| 0 T → 1.5 T | 15.6 | 10.3 | 37.8 | 24.9 | 80.7 | 53.3 |
| 0 T → 3 T | 14.7 | 9.7 | 36.7 | 24.2 | 80.9 | 53.4 |
| **r. parotid g. 0 T** | 13.8 | 9.1 | 33.1 | 21.8 | 90.0 | 56.1 |
| 0 T → 0.2 T | 14.3 | 9.4 | 33.1 | 21.9 | 84.7 | 55.9 |
| 0 T → 1.5 T | 15.5 | 10.2 | 33.3 | 22.0 | 83.6 | 55.2 |
| 0 T → 3 T | 14.4 | 9.5 | 32.3 | 21.3 | 84.2 | 55.6 |
| **spinal cord +3 mm 0 T** | 0.0 | 0.0 | 19.1 | 12.6 | 42.3 | 27.9 |
| 0 T → 0.2 T | 0.0 | 0.0 | 19.1 | 12.6 | 42.4 | 28.0 |
| 0 T → 1.5 T | 0.0 | 0.0 | 19.4 | 12.8 | 43.1 | 28.4 |
| 0 T → 3 T | 0.0 | 0.0 | 18.7 | 12.4 | 41.7 | 27.5 |
| **spinal cord +5 mm 0 T** | 0.0 | 0.0 | 19.1 | 12.6 | 42.3 | 27.9 |
| 0 T | 0.0 | 0.0 | 19.7 | 13.0 | 47.8 | 31.6 |
| 0 T → 0.2 T | 0.0 | 0.0 | 19.8 | 13.0 | 47.9 | 31.6 |
| 0 T → 1.5 T | 0.0 | 0.0 | 20.0 | 13.2 | 48.7 | 32.1 |
| 0 T → 3 T | 0.0 | 0.0 | 19.4 | 12.8 | 47.1 | 31.1 |
| **larger spine 0 T** | 5.9 | 3.9 | 21.8 | 14.4 | 48.4 | 32.0 |
| 0 T → 0.2 T | 5.9 | 3.9 | 21.9 | 14.4 | 48.5 | 32.0 |
| 0 T → 1.5 T | 5.8 | 3.8 | 21.8 | 14.4 | 48.9 | 32.2 |
| 0 T → 3 T | 5.7 | 3.8 | 21.3 | 14.1 | 47.7 | 31.5 |
| **spinal cord 0 T** | 0.0 | 0.0 | 18.3 | 12.1 | 38.4 | 25.3 |
| 0 T → 0.2 T | 0.0 | 0.0 | 18.3 | 12.1 | 38.4 | 25.4 |
| 0 T → 1.5 T | 0.0 | 0.0 | 18.6 | 12.3 | 38.0 | 25.1 |
| 0 T → 3 T | 0.0 | 0.0 | 18.0 | 11.9 | 37.1 | 24.5 |

**Table B.7** Abdomen: Warped beamlet optimisation: target

| | $D_{98\%}$[%] | $D_{98\%}$[Gy] | $D_{50\%}$[%] | $D_{50\%}$[Gy] | $D_{mean}$[%] | $D_{mean}$[Gy] | $D_{2\%}$[%] | $D_{2\%}$[Gy] | HI |
|---|---|---|---|---|---|---|---|---|---|
| 0 T | 81.6 | 48.9 | 101.0 | 60.6 | 100.0 | 60.0 | 116.0 | 69.6 | 0.34 |
| 0.2 T | 81.5 | 48.9 | 100.9 | 60.6 | 99.9 | 59.9 | 116.0 | 69.6 | 0.34 |
| 1.5 T | 81.3 | 48.8 | 101.0 | 60.6 | 100.0 | 60.0 | 115.8 | 69.5 | 0.34 |
| 3 T | 81.6 | 49.0 | 101.0 | 60.6 | 100.1 | 60.0 | 115.7 | 69.4 | 0.34 |

**Table B.8** Abdomen: Warped beamlet optimisation: organs at risk

| | $D_{98\%}$[%] | $D_{98\%}$[Gy] | $D_{mean}$[%] | $D_{mean}$[Gy] | $D_{2\%}$[%] | $D_{2\%}$[Gy] |
|---|---|---|---|---|---|---|
| **intestine** 0 T | 5.3 | 3.2 | 35.5 | 21.3 | 77.5 | 46.5 |
| 0.2 T | 5.4 | 3.2 | 35.5 | 21.3 | 77.5 | 46.5 |
| 1.5 T | 5.4 | 3.2 | 35.6 | 21.4 | 78.1 | 46.9 |
| 3 T | 5.3 | 3.2 | 35.4 | 21.3 | 77.9 | 46.7 |
| **spinal cord** 0 T | 0.0 | 0.0 | 23.8 | 14.3 | 71.6 | 43.0 |
| 0.2 T | 0.0 | 0.0 | 23.8 | 14.3 | 71.5 | 42.9 |
| 1.5 T | 0.0 | 0.0 | 23.9 | 14.4 | 71.4 | 42.8 |
| 3 T | 0.0 | 0.0 | 23.7 | 14.2 | 71.3 | 42.8 |
| **l. kidney** 0 T | 0.0 | 0.0 | 5.9 | 3.5 | 40.8 | 24.5 |
| 0.2 T | 0.0 | 0.0 | 5.9 | 3.5 | 40.9 | 24.6 |
| 1.5 T | 0.0 | 0.0 | 6.0 | 3.6 | 42.0 | 25.2 |
| 3 T | 0.0 | 0.0 | 5.9 | 3.5 | 40.9 | 24.5 |
| **r. kidney** 0 T | 0.0 | 0.0 | 12.8 | 7.7 | 57.0 | 34.2 |
| 0.2 T | 0.0 | 0.0 | 12.8 | 7.7 | 56.9 | 34.1 |
| 1.5 T | 0.0 | 0.0 | 12.9 | 7.7 | 57.6 | 34.5 |
| 3 T | 0.0 | 0.0 | 12.8 | 7.7 | 57.5 | 34.5 |

**Table B.9** Abdomen: 0 T fluence: organs at risk

| | $D_{98\%}$[%] | $D_{98\%}$[Gy] | $D_{mean}$[%] | $D_{mean}$[Gy] | $D_{2\%}$[%] | $D_{2\%}$[Gy] |
|---|---|---|---|---|---|---|
| **intestine** 0 T | 5.3 | 3.2 | 35.5 | 21.3 | 77.5 | 46.5 |
| 0 T → 0.2 T | 5.4 | 3.2 | 35.5 | 21.3 | 77.3 | 46.4 |
| 0 T → 1.5 T | 5.3 | 3.2 | 35.2 | 21.1 | 76.5 | 45.9 |
| 0 T → 3 T | 5.1 | 3.1 | 34.4 | 20.7 | 75.7 | 45.4 |
| **spinal cord** 0 T | 0.0 | 0.0 | 23.8 | 14.3 | 71.6 | 43.0 |
| 0 T → 0.2 T | 0.0 | 0.0 | 23.8 | 14.3 | 71.4 | 42.9 |
| 0 T → 1.5 T | 0.0 | 0.0 | 24.3 | 14.6 | 72.1 | 43.3 |
| 0 T → 3 T | 0.0 | 0.0 | 23.2 | 13.9 | 69.9 | 42.0 |
| **l. kidney** 0 T | 0.0 | 0.0 | 5.9 | 3.5 | 40.8 | 24.5 |
| 0 T → 0.2 T | 0.0 | 0.0 | 5.8 | 3.5 | 41.3 | 24.8 |
| 0 T → 1.5 T | 0.0 | 0.0 | 5.8 | 3.5 | 42.3 | 25.4 |
| 0 T → 3 T | 0.0 | 0.0 | 5.6 | 3.4 | 41.0 | 24.6 |
| **r. kidney** 0 T | 0.0 | 0.0 | 12.8 | 7.7 | 57.0 | 34.2 |
| 0 T → 0.2 T | 0.0 | 0.0 | 12.9 | 7.7 | 57.3 | 34.4 |
| 0 T → 1.5 T | 0.0 | 0.0 | 12.8 | 7.7 | 57.0 | 34.2 |
| 0 T → 3 T | 0.0 | 0.0 | 12.5 | 7.5 | 56.4 | 33.8 |

**Table B.10** Brain: Warped beamlet optimisation: target

| | $D_{98\%}$[%] | $D_{98\%}$[Gy] | $D_{50\%}$[%] | $D_{50\%}$[Gy] | $D_{mean}$[%] | $D_{mean}$[Gy] | $D_{2\%}$[%] | $D_{2\%}$[Gy] | HI |
|---|---|---|---|---|---|---|---|---|---|
| 0 T | 96.2 | 50.2 | 100.2 | 52.3 | 100.0 | 52.2 | 101.7 | 53.1 | 0.05 |
| 0.2 T | 96.2 | 50.2 | 100.2 | 52.3 | 100.0 | 52.2 | 101.7 | 53.1 | 0.06 |
| 1.5 T | 96.3 | 50.3 | 100.3 | 52.3 | 100.0 | 52.2 | 101.7 | 53.1 | 0.05 |
| 3 T | 96.3 | 50.3 | 100.2 | 52.3 | 100.0 | 52.2 | 101.8 | 53.1 | 0.05 |

**Table B.11** Brain: Warped beamlet optimisation: OARs

| | | $D_{98\%}$[%] | $D_{98\%}$[Gy] | $D_{mean}$[%] | $D_{mean}$[Gy] | $D_{2\%}$[%] | $D_{2\%}$[Gy] |
|---|---|---|---|---|---|---|---|
| **r. eye** | 0 T | 7.1 | 3.7 | 19.1 | 9.9 | 33.1 | 17.3 |
| | 0.2 T | 7.5 | 3.9 | 19.1 | 10.0 | 32.8 | 17.1 |
| | 1.5 T | 8.6 | 4.5 | 19.8 | 10.3 | 32.8 | 17.1 |
| | 3 T | 8.9 | 4.6 | 20.2 | 10.5 | 34.5 | 18.0 |
| **l. eye** | 0 T | 13.2 | 6.9 | 27.5 | 14.3 | 43.5 | 22.7 |
| | 0.2 T | 13.1 | 6.8 | 27.2 | 14.2 | 43.2 | 22.5 |
| | 1.5 T | 13.9 | 7.2 | 27.3 | 14.3 | 42.8 | 22.4 |
| | 3 T | 13.3 | 7.0 | 27.7 | 14.4 | 42.8 | 22.3 |
| **brain stem** | 0 T | 14.6 | 7.6 | 52.5 | 27.4 | 101.0 | 53.1 |
| | 0.2 T | 15.4 | 8.0 | 52.9 | 27.6 | 100.9 | 52.7 |
| | 1.5 T | 15.4 | 8.1 | 53.3 | 27.8 | 101.0 | 52.7 |
| | 3 T | 15.4 | 8.0 | 53.1 | 27.7 | 101.1 | 52.8 |
| **l. lens** | 0 T | 10.1 | 5.3 | 15.7 | 8.2 | 21.3 | 11.1 |
| | 0.2 T | 10.4 | 5.5 | 15.5 | 8.1 | 22.1 | 11.5 |
| | 1.5 T | 11.5 | 6.0 | 16.0 | 8.4 | 20.8 | 10.9 |
| | 3 T | 12.4 | 6.4 | 16.2 | 8.4 | 21.0 | 11.0 |
| **r. lens** | 0 T | 6.9 | 3.6 | 10.5 | 5.5 | 15.5 | 8.1 |
| | 0.2 T | 7.0 | 3.7 | 10.5 | 5.5 | 15.2 | 8.0 |
| | 1.5 T | 7.8 | 4.1 | 10.7 | 5.6 | 4.1 | 8.5 |
| | 3 T | 7.9 | 4.1 | 11.1 | 5.8 | 16.1 | 8.4 |

**Table B.12** Brain: 0 T fluence: organs at risk

| | $D_{98\%}$[%] | $D_{98\%}$[Gy] | $D_{mean}$[%] | $D_{mean}$[Gy] | $D_{2\%}$[%] | $D_{2\%}$[Gy] |
|---|---|---|---|---|---|---|
| **r. eye** 0 T | 7.1 | 3.7 | 19.1 | 9.9 | 33.1 | 17.3 |
| 0 T → 0.2 T | 7.4 | 3.9 | 19.0 | 9.9 | 32.5 | 17.0 |
| 0 T → 1.5 T | 8.8 | 4.6 | 19.2 | 10.0 | 30.4 | 15.9 |
| 0 T → 3 T | 8.2 | 4.3 | 18.7 | 9.7 | 30.7 | 16.0 |
| **l. jaw** 0 T | 43.8 | 22.9 | 61.3 | 32.0 | 87.3 | 45.6 |
| 0 T → 0.2 T | 43.8 | 22.9 | 61.3 | 32.0 | 87.0 | 45.4 |
| 0 T → 1.5 T | 43.8 | 22.9 | 61.0 | 31.9 | 85.0 | 44.4 |
| 0 T → 3 T | 42.3 | 22.1 | 59.6 | 31.1 | 84.3 | 44.0 |
| **l. lens** 0 T | 10.1 | 5.3 | 15.7 | 8.2 | 21.3 | 11.1 |
| 0 T | 10.1 | 5.3 | 15.7 | 8.2 | 21.3 | 11.1 |
| 0 T → 0.2 T | 10.3 | 5.3 | 15.5 | 8.1 | 20.6 | 10.8 |
| 0 T → 1.5 T | 11.4 | 6.0 | 15.7 | 8.2 | 19.7 | 10.3 |
| 0 T → 3 T | 11.4 | 5.9 | 15.4 | 8.1 | 20.0 | 10.4 |
| **r. lens** 0 T | 6.9 | 3.6 | 10.5 | 5.5 | 15.5 | 8.1 |
| 0 T → 0.2 T | 7.0 | 3.6 | 10.5 | 5.5 | 15.3 | 8.0 |
| 0 T → 1.5 T | 8.3 | 4.3 | 11.3 | 5.9 | 15.7 | 8.2 |
| 0 T → 3 T | 7.7 | 4.0 | 10.7 | 5.6 | 15.6 | 8.1 |

# Appendix C

# Computer tools used

- Virtuos DKFZ treatment planning software [72]
- KonRadXP DKFZ inverse planning module [9][10]
- Geant4 Monte Carlo simulation toolkit [21][22]
- MATLAB [66] including FFTW [76]
- MikTeX 2.9
- TeXnicCenter
- Inkscape (www.inkscape.org)
- Linux operating systems
- Microsoft Windows operating systems
- Microsoft Office, Paint
- Adobe Acrobat Pro
- Mozilla Firefox
- ... and other standard computer tools

# Bibliography


[1] G.H. Bol, S. Hissoiny, J.J.W. Lagendijk, and B.W. Raaymakers. Fast online monte carlo-based imrt planning for the mri linear accelerator. *Phys Med Biol*, 57:1375–1385, 2012.

[2] K.M. Langen and D.T.L. Jones. Organ motion and its management. *Int J Radiat Oncol Biol Phys*, 50(1):265–278, 2001.

[3] P.J. Keall, G.S. Mageras, J.M. Balter, R.S. Emery, K.M. Forster, S.B. Jiang, J.M. Kapatoes, D.A. Low, M.J. Murphy, B.R. Murray, C.R. Ramsey, M.B. van Herk, S.S. Vedam, J. Wong, and E.Yorke. The management of respiratory motion in radiation oncology report of the aapm task group 76. *Med Phys*, 33(10):3874–3900, 2006.

[4] C.C. Ling, J. Humm, S. Larson, H. Amols, Z. Fuks, S. Leibel, and J.A. Koutcher. Towards multidimensional radiotherapy (md-crt): biological imaging and biological conformality. *Int Journal Radiat Oncol Biol Phys*, 47(3):551 – 560, 2000.

[5] ICRU. International commission on radiation units and measurements report no. 62: "prescribing, recording and reporting photon beam therapy (supplement to icru report 50)". *Journal of the ICRU*, 4(1):21–24, 2004.

[6] M. van Herk. Errors and margin in radiotherapy. *Semin Radiat Oncol*, 14:52–64, 2004.

[7] M.J. Murphy, J. Balter, S. Balter, Jr. J.A. BenComo, I.J. Das, S.B. Jiang, C.-M. Ma, G.H. Olivera, R.F. Rodebaugh, K.J. Ruchala, H. Shirato, and F.-F. Yin. The management of imaging dose during image-guided radiotherapy: Report of the aapm task group 75. *Medical Physics*, 34(10):4041–4063, 2007.

[8] RaySearch Laboratories AB, Stockholm.

[9] K. Preiser, T. Bortfeld, K. Hartwig, W. Schlegel, and J. Stein. A new program for inverse radiotherapy planning. In D. Leavitt and G. Starkschall, editors, *XIIth International Conference on the Use of Computers in Radiation Therapy*, pages 425–428. Madison: Medical Physics Publishing, 1997.

[10] S. Nill, T. Bortfeld, and U. Oelfke. Inverse planning of intensity modulated proton therapy. *Z Med Phys*, 14(1):35–40, 2004.

[11] U. Oelfke and T. Bortfeld. Inverse planning for photon and proton beams. *Med Dosim*, 26(2):113–124, 2001.

[12] S. Nill. *Development and application of a multi-modality inverse treatment planning system.* PhD thesis, Ruprecht-Karls-Universität Heidelberg, 2001.

[13] H.Reich, editor. *Dosimetrie ionisierender Strahlung.* B.G. Teubner Stuttgart, 1990.

[14] J.H. Hubbell and S.M. Seltzer. *Tables of X-Ray Mass Attenuation Coefficients and Mass Energy-Absorption Coefficients (version 1.4).* National Institute of Standards and Technology, Gaithersburg, MD, 2004. [Online] Available: http://physics.nist.gov/xaamdi [2009, June 29].

[15] F.M. Khan. *The physics of radiation therapy.* Williams and Wilkins, Baltimore, MD, 1984.

[16] H.E. Johns and J.R. Cunningham. *The Physics of Radiology.* Charles C Thomas Pub Ltd, 1983.

[17] D. Jette. Photon dose calculation based on electron multiple-scattering theory: Practical representation of dose and particle transport integrals. *Med Phys*, 26(6):924–930, 1999.

[18] ICRU. *International Commission on Radiation Units and Measurements Report No. 35: "Radiation dosimetry: electron beams with energies between 1 and 50 MeV".* International Commission on Radiation Units and Measurements, Bethesda, Maryland, 1984.

[19] I.J. Chetty, B. Curran, J.E. Cygler, J.J. DeMarco, G. Ezzell, B.A. Faddegon, I. Kawrakow, P.J. Keall, H. Liu, Ma C.C., D.W.O Rogers, J. Seuntjens, D. Sheikh-Bagheri, and J.V. Siebers. Report of the aapm task group no. 105: Issues associated with clinical implementation of monte carlo-based photon and electron external beam treatment planning. *Med Phys*, 34:4818–4853, 2007.

[20] D.W.O. Rogers and A.F. Bielajew. Monte carlo techniques of electron and photon transport for radiation dosimetry. In B. Bjarngard, K. Kase, and F. Attix, editors, *The Dosimetry of Ionizing Radiation*, volume III, pages 427–539. Academic, New York, 1990.

[21] S. Agostinelli, J. Allison, K. Amako, J. Apostolakis, H. Araujo, P. Arce, M. Asai, D. Axen, S. Banerjee, G. Barrand, F. Behner, L. Bellagamba, J. Boudreau, L. Broglia, A. Brunengo, H. Burkhardt, S. Chauvie, J. Chuma, R. Chytracek, G. Cooperman, G. Cosmo, P. Degtyarenko, A. Dell'Acqua, G. Depaola, D. Dietrich, R. Enami, A. Feliciello, C. Ferguson, H. Fesefeldt, G. Folger, F. Foppiano, A. Forti, S. Garelli, S. Giani, R. Giannitrapani, D. Gibin, J.J. Gómez Cadenas, I. González, G. Gracia Abril, G. Greeniaus, W. Greiner, V. Grichine, A. Grossheim, S. Guatelli, P. Gumplinger, R. Hamatsu, K. Hashimoto, H. Hasui, A. Heikkinen, A. Howard, V. Ivanchenko, A. Johnson, F.W. Jones, J. Kallenbach, N. Kanaya, M. Kawabata, Y. Kawabata, M. Kawaguti, S. Kelner, P. Kent, A. Kimura, T. Kodama, R. Kokoulin, M. Kossov, H. Kurashige, E. Lamanna, T. Lampén, V. Lara, V. Lefebure, F. Lei, M. Liendl, W. Lockman, F. Longo, S. Magni, M. Maire, E. Medernach, K. Minamimoto, P. Mora de Freitas, Y. Morita, K. Murakami, M. Nagamatu, R. Nartallo, P. Nieminen, T. Nishimura, K. Ohtsubo, M. Okamura, S. O'Neale, Y. Oohata, K. Paech, J. Perl, A. Pfeiffer, M.G. Pia, F. Ranjard, A. Rybin, S. Sadilov, E. Di Salvo, G. Santin, T. Sasaki, N. Savvas, Y. Sawada, S. Scherer, S. Sei, V. Sirotenko, D. Smith, N. Starkov, H. Stoecker, J. Sulkimo, M. Takahata, S. Tanaka, E. Tcherniaev, E. Safai Tehrani, M. Tropeano, P. Truscott, H. Uno, L. Urban, P. Urban, M. Verderi, A. Walkden, W. Wander, H. Weber, J.P. Wellisch, T. Wenaus, D.C. Williams, D. Wright, T. Yamada, H. Yoshida, and D. Zschiesche. Geant4 - a simulation toolkit. *Nuclear Instruments and Methods in Physics Research Section A: Accelerators, Spectrometers, Detectors and Associated Equipment*, 506(3):250–303, 2003. Geant4 website: http://geant4.cern.ch/.

[22] J. Allison, K. Amako, J. Apostolakis, H. Araujo, P.A. Dubois, M. Asai, G. Barrand, R. Capra, S. Chauvie, R. Chytracek, G.A.P. Cirrone, G. Cooperman, G. Cosmo, G. Cuttone, G.G. Daquino, M. Donszelmann, M. Dressel, G. Folger, F. Foppiano, J. Generowicz, V. Grichine, S. Guatelli, P. Gumplinger, A. Heikkinen, I. Hrivnacova, A. Howard, S. Incerti, V. Ivanchenko, T. Johnson, F. Jones, T. Koi, R. Kokoulin, M. Kossov, H. Kurashige, V. Lara, S. Larsson, F. Lei, O. Link, F. Longo, M. Maire, A. Mantero, B. Mascialino, I. McLaren, P.M. Lorenzo, K. Minamimoto, K. Murakami, P. Nieminen, L. Pandola, S. Parlati, L. Peralta, J. Perl, A. Pfeiffer, M.G. Pia, A. Ribon, P. Rodrigues, G. Russo, S. Sadilov, G. Santin, T. Sasaki, D. Smith, N. Starkov, S. Tanaka, E. Tcherniaev, B. Tome, A. Trindade, P. Truscott, L. Urban, M. Verderi, A. Walkden, J.P. Wellisch, D.C. Williams, D. Wright, and H. Yoshida. Geant4 developments and applications. *Nuclear Science, IEEE Transactions on*, 53(1):270–278, 2006.

[23] J.F. Briesmeister. Mcnp: a general monte carlo n-particle transport code-version 4b. Technical Report LA-12625, Los Alamos National Laboratories, Los Alamos, NM, 1997.

[24] W.R. Nelson, H. Hirayama, and D.W.O. Rogers. The egs4 code system. Technical Report Stanford Linear Accelerator Center Report 265, Stanford University Stanford, CA, USA, 1985.

[25] I. Kawrakow. Accurate condensed history monte carlo simulation of electron transport: I. egsnrc, the new egs4 version. *Med Phys*, 27:485–498, 2000.

[26] D.W. Litzenberg, B.A. Fraass, D.L. McShan, T.W. ODonnel, D.A. Roberts, F.D. Becchetti, A.F. Bielajew, and J.M. Moran. An apparatus for applying strong longitudinal magnetic fields to clinical photon and electron beams. *Phys Med Biol*, 46:N105–N115, 2001.

[27] B.W. Raaymakers, A.J.E. Raaijmakers, A.N.T.J. Kotte, D. Jette, and J.J.W. Lagendijk. Integrating a mri scanner with a 6 mv radiotherapy accelerator: dose deposition in a transverse magnetic field. *Phys Med Biol*, 49:4109–4118, 2004.

[28] R. Mohan and C. Chui. Use of fast fourier transforms in calculating dose distributions of irregularly shaped for three-dimensional treatment planning. *Med Phys*, 14:70–77, 1987.

[29] A. Boyer and E. Mok. A photon dose model employing convolution calculations. *Med Phys*, 12:169–177, 1985.

[30] T.R. Mackie, J.W. Scrimger, and J.J. Battista. A convolution method of calculating dose for 15-mv x-ray. *Med Phys*, 12:188–196, 1985.

[31] T. Bortfeld, W. Schlegel, and B. Rhein. Decomposition of pencil beam kernels for fast dose calculations in three-dimensional treatment planning. *Med Phys*, 20(2):311–318, 1993. http://dx.doi.org/10.1118/1.597070.

[32] C. Scholz, S. Nill, and U. Oelfke. Comparison of imrt optimization based on a pencil beam and a superposition algorithm. *Med Phys*, 30(7):1909–1913, 2003.

[33] S. Siggel, P. Ziegenhein, S. Nill, and U. Oelfke. Boosting runtime-performance of photon pencil beam algorithms for radiotherapy treatment planning. *Phys Med*, 28(4):273–280, 2012.

[34] A. Ahnesjö, P. Andreo, and A. Brahme. Calculation and application of point spread functions for treatment planning with high energy photon beams. *Acta Oncol*, 26:49–56, 1987.

[35] R. Mohan, C. Chui, and L. Lidofsky. Differential pencil beam dose computation model for photons. *Med Phys*, 13:64–73, 1986.

[36] J.E. O'Connor. The variation of scattered x-rays with density in an irradiated body. *PMB*, 1:352–269, 1957.

[37] C. Scholz. *Development and Evaluation of Advanced Dose Calculations for Modern Radiation Therapy Techniques*. PhD thesis, Ruprecht-Karls-Universität Heidelberg, 2004.

[38] S. Hissoiny, B. Ozell, and P. Després. A convolution-superposition dose calculation engine for gpus. *Med Phys*, 37(3):1029–1037, 2010.

[39] J.J.W. Lagendijk, B.W. Raaymakers, U.A. Van Der Heide, R. Topolnjak, H. Dehnad, P. Hofman, A.J. Nederveen, I.M. Schulz, J. Welleweerd, and C.J.G. Bakker. Mri guided radiotherapy: Mri as position verification system for imrt. *Radiother Oncol*, 64 (Suppl 1):224, 2002.

[40] J. Dempsey, B. Dionne, J. Fitzsimmons, A. Haghigat, J. Li, D. Low, S. Mutic, J. Palta, H. Romeijn, and G. Sjoden. A real-time mri guided external beam radiotherapy delivery system. *Med Phys*, 33:2254, 2006.

[41] ViewRay™ Incorporated, Cleveland, Ohio; www.viewray.com.

[42] T. Kron, D. Eyles, J.L. Schreiner, and J. Battista. Magnetic resonance imaging for adaptive cobalt tomotherapy: A proposal. *J Med Phys*, 31(4):242–254, 2006. Online available from: http://www.jmp.org.in/text.asp?2006/31/4/242/29194.

[43] B. Fallone, M.Carlone, B. Murray, S. Rathee, T. Stanescu, S. Steciw, K. Wachowitz, and C. Kirkby. Development of a linac-mri system for real-time art. *Med Phys*, 34:2547, 2007.

[44] C. Kirkby, T. Stanescu, S. Rathee, M. Carlone, B. Murray, and B.G. Fallone. Patient dosimetry for hybrid mri-radiotherapy systems. *Med Phys*, 35(3):1019–1027, 2008.

[45] D.E. Constantin, R. Fahrig, and P.J. Keall. A study of the effect of in-line and perpendicular magnetic fields on beam characteristics of electron guns in medical linear accelerators. *Med Phys*, 38(7):4174–4185, 2011.

[46] http://www.inghaminstitute.org.au/Mri-linac.html.

[47] M.K. Stam, S.P.M. Crijns, B.A. Zonnenberg, M.M. Barendrecht, M. van Vulpen, J.J.W. Lagendijk, and B.W. Raaymakers. Navigators for motion detection during real-time mri-guided radiotherapy. *Phys Med Biol*, 57:6797–6805, 2012.

[48] J. Yun, Y. Eugene, K. Wachowitz, S.Rathee, M. Mackenzie, D. Robinson, and B.G. Fallone. Evaluation of a lung tumor autocontouring algorithm for intrafractional tumor tracking using low-field mri: A phantom study. *Med Phys*, 39(3):1481–1494, 2012.

[49] S.P.M. Crijns, J.G.M. Kok, J.J.W. Lagendijk, and B.W. Raaymakers. Towards mri-guided linear accelerator control: gating on an mri accelerator. *Phys Med Biol*, 56:4815–4825, 2011.

[50] S.A. Nehmeh, N.Y. Lee, H. Schröder, O. Squire, P.B. Zanzonico, Y.E. Erdi, C. Greco, G. Mageras, H.S. Pham, S.M. Larson, C.C. Ling, and J.L. Humm. Reproducibility of intratumor distribution of $^{18}$f-fluoromisonidazole in had and neck cancer. *Int J Radiat Oncol Biol Phys*, 2008:235–242, 2008.

[51] S.J. Price and J.H. Gillard. Imaging biomarkers of brain tumour margin and tumour invasion. *British Journal of Radiology*, 84(Special Issue 2):S159–S167, 2011.

[52] International Atomic Energy Agency. *Radiation Biology: A Handbook for Teachers and Students*. IAEA, Vienna Austria, 2010. Available online: http://www-pub.iaea.org/MTCD/publications/PDF/TCS-42_web.pdf.

[53] B.W. Raaymakers, J.J.W. Lagendijk, J.Overweg, J.G.M. Kok, A.J.E. Raaijmakers, E.M. Kerkhof, R.W. van der Put, I. Meijsing, S.P.M. Crijns, F. Benedosso, M. van Vulpen, C.H.W. de Graaff, J. Allen, and K.J. Brown. Integrating a 1.5 t mri scanner with a 6 mv accelerator: proof of concept. *Phys Med Biol*, 54:N229–N237, 2009.

[54] J.St. Aubin, D.M. Santos, S.Steciw, and B.G.Fallone. Effect of longitudinal magnetic fields on a simulated in-line 6 mv linac. *Med Phys*, 37:4916–4923, 2010.

[55] B. Fallone, B. Murray, S. Rathee, T. Stanescu, S. Steciw, S. Vidakovic, E. Blosser, and D. Tymofichuk. First mr images obtained during megavoltage photon irradiation from a prototype integrated linac-mr system. *Med Phys*, 36(6):2084–2088, 2009.

[56] B.M. Oborn, P.E. Metcalfe, M.J. Butson, and A.B. Rosenfeld. High resolution entry and exit monte carlo dose calculations from a linear accelerator 6 mv beam under influence of transverse magnetic fields. *Med Phys*, 36(8):3549–3559, 2009.

[57] B.M. Oborn, P.E. Metcalfe, M.J. Butson, A.B. Rosenfeld, and P.J. Keall. Electron contamination modeling and skin dose in 6 mv longitudinal field mrigrt: Impact of the mri and mri fringe field. *Med Phys*, 39(2):874–890, 2012.

[58] C. Kirkby, B. Murray, S. Rathee, and B.G. Fallone. Lung dosimetry in a linac-mri radiotherapy unit with a longitudinal magnetic field. *Med Phys*, 37(9):4722–4732, 2010.

[59] A.J.E. Raaijmakers, B.W. Raaymakers, and J.J.W. Lagendijk. Integrating a mri scanner with a 6 mv radiotherapy accelerator: dose increase at tissueair interfaces in a lateral magnetic field due to returning electrons. *Phys Med Biol*, 50:1363–1376, 2005.

[60] A.J.E. Raaijmakers, B.W. Raaymakers, S. van der Meer, and J.J.W. Lagendijk. Integrating a mri scanner with a 6 mv radiotherapy accelerator: impact of the surface orientation on the entrance and exit dose due to the transverse magnetic field. *Phys Med Biol*, 52:929–939, 2007.

[61] Stanley Humphries Jr. *Principles of charged particle acceleration*. John Wiley and Sons, 1999. Available online: http://www.fieldp.com/freeware/principles_acceleration.pdf.

[62] A.J.E. Raaijmakers, B.W. Raaymakers, and J.J.W. Lagendijk. Magnetic-field-induced dose effects in mr-guided radiotherapy systems: dependence on the magnetic field strength. *Phys Med Biol*, 53:909–923, 2008.

[63] D. Jette. Magnetic fields with photon beams: Dose calculation using electron multiple-scattering theory. *Med Phys*, 27(8):1705–1716, 2000.

[64] D. Harder. Energiespektren schneller elektronen in verschiedenen tiefen. In A. Zuppinger and G. Poretti, editors, *Symposium on High Energy Electrons*, pages 26–33. Springer Berlin, 1965.

[65] M.J. Berger, J.S. Coursey, M.A. Zucker, and J. Chang. *ESTAR, PSTAR, and ASTAR: Computer Programs for Calculating Stopping-Power and Range Tables for Electrons, Protons, and Helium Ions (version 1.2.3)*. National Institute of Standards and Technology, Gaithersburg, MD, 2005. [Online] Available: http://physics.nist.gov/Star [2009, June 29].

[66] MATLAB, The MathWorks, Inc., Natick, MA, USA.

[67] M.B. Tacke, H. Szymanowski, C. Schulze, S. Nuss, E. Wehrwein, S. Leidenberger, and U. Oelfke. Assessment of a new multileaf collimator concept using geant4 monte carlo simulations. *Med Phys*, 33:1125–1132, 2006.

[68] C. Scholz. Implementierung eines superpositionsalgorithmus zur berechnung der strahlendosis in inhomogenem gewebe. Master's thesis, Ruprecht-Karls-Universität Heidelberg, 2001.

[69] ICRU. *International Commission on Radiation Units and Measurements Report No. 46: "Photon, Electron, Proton and Neutron Interaction Data for Body Tissues"*. International Commission on Radiation Units and Measurements, Bethesda, Maryland, 1992.

[70] H.Q. Woodard and D.R. White. The composition of body tissues. *Br J Radiol*, 59(708):1209–1218, 1986.

[71] G.S. Mageras, A. Pevsner, E.D. Yorke, K.E. Rosenzweig, E.C. Ford, A. Hertanto, S.M. Larson, D.M. Lovelock, Y.E. Erdi, S.A. Nehmeh, J.L. Humm, and C.C. Ling. Measurements of lung tumor motion using respiration-correlated ct. *Int J Radiat Oncol Biol Phys*, 60(3):933–941, 2004.

[72] R. Bendl, A. Hoess, and W. Schlegel. *Computer Vision, Virtual Reality and Robotics in Medicine*, volume 905, chapter Virtual simulation in radiotherapy planning, pages 287–292. Berlin, Heidelberg: Springer, 1995.

[73] Siemens AG Healthcare, Erlangen, Germany.

[74] M.B. Tacke, S. Nill, P. Häring, and U. Oelfke. 6 mv dosimetric characterization of the 160 mlc, the new siemens multileaf collimator. *Med Phys*, 35(5):1634–1642, 2008.

[75] ICRU. International commission on radiation units and measurements report no. 83: "prescribing, recording, and reporting photon-beam intensity-modulated radiation therapy (imrt)". *Journal of the ICRU*, 10(1), 2010. doi:10.1093/jicru/ndq008.

[76] M. Frigo and S.G. Johnson. Fftw: An adaptive software architecture for the fft,. In *Proceedings of the International Conference on Acoustics, Speech, and Signal Processing*, volume 3, pages 1381–1384, 1998. http://www.fftw.org.

[77] M. Siggel. *Concepts for the effcient Monte Carlo-based treatment plan optimization in radiotherapy.* PhD thesis, Ruprecht-Karls-Universität Heidelberg, 2012.

[78] J. Stein, R. Mohan, X.H. Wang, T. Bortfeld, Q. Wu, K. Preiser, C.C. Ling, and W. Schlegel. Number and orientations of beams in intensity-modulated radiation treatments. *Medical Physics*, 24:149, 1997.

[79] M. Bangert, P. Ziegenhein, and U. Oelfke. Characterizing the combinatorial beam angle selection problem. *Physics in Medicine and Biology*, 57(20):6707, 2012.

[80] P.W.J. Voet, M.L.P. Dirkx, S. Breedveld, D. Fransen, P.C. Levendag, and B.J.M. Heijmen. Toward fully automated multicriterial plan generation: A prospective clinical study. *International Journal of Radiation Oncology* Biology* Physics*, 2012.

[81] I. Meijsing, B.W. Raaymakers, A.J.E. Raaijmakers, J.G.M. Kok, L. Hogeweg, B. Liu, and J.J.W. Lagendijk. Dosimetry for the mri accelerator: the impact of a magnetic field on the response of a farmer ne2571 ionization chamber. *Phys Med Biol*, 54:2993–3002, 2009.

# Acknowledgements

First of all, I would like to express my sincere gratitude towards Prof. Dr. Uwe Oelfke for his supervision and support throughout my thesis. Prof. Dr. Wolfgang Schlegel I wish to thank deeply for continuously providing conditions that really helped me a lot to complete this thesis.

Special thanks go to Dr. Simeon Nill, not only for technical help and suggestions but also for the many discussion we had, both of professional and of personal kind.

Further, I would like to thank Dr. Silke Ulrich for proof-reading of this thesis and for many other pleasant personal encounters, and both Dr. Hanitra Szymanowski and Dr. Martin Tacke for helping me with my first steps in Geant4. Thanks go also to all other group members of E0401, former and present, and I would like to mention Hendrik Heinrich for providing me with a code snippet for the fluence evaluation while I was collecting my last results.

I am also grateful to Prof. Dr. Björn Poppe and Prof. Dr. Michael Bock who agreed to be members in my thesis advisory commitee and Prof. Dr. Makoto Asain from the Geant4 collaboration who also shared some code and was always very helpful answering questions about the toolkit.

Last but not least, I would like to thank Naved for his support in various ways.